TECHNISCHE UNIVERSITÄT WIEN
Vienna | Austria

Dissertation

CONTROLLING THE THIRD DIMENSION

CRITICAL QUALITY PARAMETERS OF STATIC AND DYNAMIC SPHEROID CULTURES FOR DRUG SCREENING APPLICATIONS

carried out for the purpose of obtaining the degree of Doctor technicae (Dr. techn.), submitted at TU Wien, Faculty of Technical Chemistry, by

Dipl.-Ing. Christoph Eilenberger

Mat.Nr.: 00800591

under the supervision of

Univ. Prof. Dipl.-Ing. Dr. Peter Ertl

Institute of Applied Synthetic Chemistry and Institute of Chemical Technologies and Analytics

Vienna, July 2021

This work was supported by the Christian-Doppler Gesellschaft within the framework of the Josef Ressel Center for Phytogenic Drug Research

Affidavit

I declare in lieu of oath, that I wrote this thesis and performed the associated research myself, using only literature cited in this volume. If text passages from sources are used literally, they are marked as such. I confirm that this work is original and has not been submitted elsewhere for any examination, nor is it currently under consideration for a thesis elsewhere.

Vienna, July 2021

Signature

Acknowledgements

I would like to express my sincerest gratitude to the whole CellChip Group for their friendship and support during the past years. I especially want to thank my thesis adviser Prof. Peter Ertl for his guidance, help and constant support during the whole research work. Thank you for letting me persuade you to start my thesis in my preferred field and to give me the freedom in my research.

I thank my fellow labmates Dr. Barbara Bachmann, Dipl.-Ing. Sarah Spitz, Dr. Sebastian Kratz, and Dr. Helene Zirath for fruitful discussions about life and science either in the laboratory, during coffee breaks before deadlines or in a cocktail bar in Amsterdam. Thank you for your friendship, sleepless nights and encouraging words throughout the years. It was a pleasure working with you!

Furthermore, I would like to give my thanks to Dr. Mario Rothbauer and Dr. Seta Küpcü for the extensive support throughout the work of my thesis and beyond.

I would like to express my gratitude to FH-Prof. Dr. Julian Weghuber and the Josef Ressel Center for Phytogenic Drug Research, funded by Christian-Doppler Gesellschaft for letting me be part of this network. Without their precious support it would not be possible to conduct this research.

My sincere thanks also go to Dr. Rudolf Zinell, who gave me the opportunity to join SAICO Biosystems KG, and who supported me constantly during my studies.

Many thanks go to the Austrian Marshall Plan Foundation as well as to the OeAD-GmbH and the Austrian Federal Ministry of Education, Science and Research (BMBWF) for the possibility of a research stay in the USA. I also want to thank Dr.

Taru Muranen and her research group for their support and the opportunity to work in their laboratory at the Harvard Medical School.

Last but not the least, I would like to thank my family: my parents and friends for supporting me throughout the years and my life in general.

Thank you!

Abstract

Three-dimensional (3D) multicellular spheroid systems, mimicking human physiology and diseases, are a promising solution to close the gap between pre-clinical trials and human *in vivo* scenarios. Implementing 3D spheroids into mainstream pharmaceutical procedures is considered to achieve representative test results leading to reduced development costs and drug attrition rates. Despite the rise of spheroid culture in the last decades, the lack of reproducibility and variations in screening procedures influence drug safety and efficacy outcomes, impeding a full incorporation of 3D cell culture systems into current drug discovery programs.

In this thesis, critical spheroid parameters are identified, evaluated, and controlled regarding their impact on pre-clinical drug screening results. Quality factors as spheroid morphology, viability, microarchitecture, functionality, drug sensitivity, and compound penetration are assessed by a range of colorimetric, microscopic, and spectroscopic techniques. To validate the spheroid technology in an industrial setting, a) the potential therapeutic effect and clearance of a pre-clinical nanodrug are investigated in a fully characterized static 3D liver spheroid culture model, and b) a versatile dynamic high-throughput spheroid-on-a-chip system is established to manipulate and screen spheroid size effects for anti-cancer drug testing and paracellular compound transport across the blood-brain barrier. Substantial changes in viability assay precision, as well as in IC_{50} values between spheroids of different ages (e.g., 118% between 3- day and 12- days post-seeding) and spheroid sizes (e.g., 160% between spheroid of 900 µm and 90 µm in diameter), can be observed and demonstrate the importance of validating quality parameters of 3D spheroids to select

the most appropriate condition for each pharmaceutical screening routine. To achieve these objectives, valuable insights for spheroid cultivation and screening procedures are obtained to increase data robustness in early-stage studies and ultimately enhance significance in biomedical and pre-clinical research.

Kurzfassung

Dreidimensionale (3D) Sphäroidmodelle ermöglichen durch ihre biologischen Eigenschaften, Physiologie und Funktionalität von menschliche Gewebe außerhalb des Körpers zu reproduzieren. Dadurch können vielversprechende Prognosen zu neuen Therapiemöglichkeiten getroffen werden. Eine breite Anwendung von 3D-Sphäroiden in gängige pharmazeutische Prozesse verspricht daher eine frühere Selektierung von potenziellen Wirkstoffkandidaten sowie eine Reduktion der ohnehin schon sehr hohen Entwicklungskosten und Ausfallquoten in der Medikamentenentwicklung. Trotz des Aufschwunges der Sphäroidtechnologie in den letzten Jahrzehnten, beeinflussen vor allem mangelnde Reproduzierbarkeit die Ergebnisse unterschiedlichster Studien erheblich wodurch eine vollständige Implementierung dieser Zellmodelle in gängige Testprogramme verhindert wird.

In dieser Arbeit werden daher kritische Sphäroidparameter identifiziert und hinsichtlich ihres Einflusses auf Resultate von präklinischen Wirkstoffscreenings untersucht. Qualitätsfaktoren wie Sphäroidmorphologie, Viabilität, Mikroarchitektur, Funktionalität, Arzneimittelempfindlichkeit und -transport werden durch eine Reihe kolorimetrischer, mikroskopischer und spektroskopischer Techniken geprüft und bewertet. Um die Sphäroid-Technologie in einem industriellen Umfeld zu validieren, werden a) die möglichen therapeutischen Wirkungen sowie die Clearance eines präklinischen Nanotherapeuthikums in einem charakterisierten statischen 3D-Leber-Sphäroid-Kulturmodell untersucht und b) ein dynamisches Sphäroid-on-a-Chip-System etabliert, um Sphäroidgrößeneffekte für Krebsmedikamententests und den parazellulären Transport von Wirkstoffen über die Blut-Hirn-Schranke zu untersuchen. Signifikante Unterschiede in der Präzision von Zellviabilitätsassays als

auch in den IC_{50}-Werten zwischen Sphäroiden unterschiedlichen Alters (z. B. 118% zwischen 3 und 12 Tagen nach Aussaat) und Größen (z. B. 160% zwischen 900 µm und 90 µm Durchmesser) kann verifiziert werden und zeigt die Bedeutsamkeit kritische Qualitätsparameter von Sphäroiden zu validieren. Zu diesem Zweck werden in dieser Dissertation wertvolle Erkenntnisse zur Charakterisierung von Sphäroiden vorgestellt, um die Robustheit komplexer Zellsysteme zu erhöhen und deren Bedeutung in der präklinischen Forschung zu steigern.

Table of Contents

List of Figures

List of Tables

List of Abbreviations

2D	Two-dimensional
3D	Three-dimensional
4D	Four-dimensional
AO-LLSM	Adaptive optics lattice light-sheet microscopy
ATP	Adenosine triphosphate
BBB	Blood-brain barrier
CFD	Computational fluid dynamics
CLSM	Confocal laser scanning microscopy
CNC	Computerized numerical control
CQA	Critical quality attributes
DSC	Differential scanning calorimetry
DSL	Dynamic light scattering
DNA	Deoxyribonucleic acid
ECM	Extracellular matrix
ELISA	Enzyme linked immunosorbent assay
EMA	European Medicines Agency
FDA	Food and Drug Administration
FT-IR	Fourier transform infrared
GMP	Good manufacturing practice
HCS	High-content screening
H&E	Hematoxylin and eosin
HTS	High-throughput screening
IC_{50}	Half-maximal inhibitory concentration
ICP-MS	Inductively coupled plasma mass spectrometry

LA-ICP-MS	Laser ablation inductively coupled plasma mass spectrometry
LSFM	Light-sheet-based fluorescence microscopy
MCS	Multicellular spheroids
MCTS	Multicellular tumor spheroids
MPC	(Methacryloyoxy)ethyl phosphorylcholine
MPS	Microphysiological systems
NDA/BLA	New drug application/Biologics license applications
NIH	National Institutes of Health
PDMS	Polydimethylsiloxane
PIXE	Proton induced X-ray emission
PMMA	Polymethylmethacrylate
qPCR	Quantitative polymerase chain reaction
R&D	Research and development
SD	Standard deviation
SDS	Sodium do-decylsulfate
SEM	Scanning electron microscope
S-layer	Surface –layer
SMC	Supramolecular complex
TDS	Tissue dynamic spectroscopy
TEM	Transmission electron microscopy
ULA	Ultra-low attachment

Highlights

1. In this thesis, key quality parameters of multicellular spheroids are identified.
2. Cell viability assay performance, spheroidal age, as well as spheroid size, are defined as crucial factors influencing compound penetration, drug response and thus, the outcome of drug screening results.
3. The therapeutic capacity of a pharmaceutical nano-drug is evaluated in a defined static 3D liver spheroid model by advanced spectrometric techniques as ICP-MS to show spatiotemporal distribution and clearance mechanisms.
4. To enhance screening throughput and precise spheroid size manipulation, a microfluidic spheroid biochip-platform is established, accelerating the generation of reproducible *in vitro* screening data.

"*If people never did silly things nothing intelligent would ever get done.*"

– Ludwig Wittgenstein

CHAPTER 1

Introduction

1.1 Problem and Motivation

1.1.1 The Old Trilemma

Pharmaceutical research and development (R&D) has enabled unprecedented progress for human health over the past century.[1] Advances in medicine and technology have come with falling mortality rates, extended life expectancy, and improving people's living conditions. Despite these extensive achievements, new challenges for the 21st century are immense; with antibiotic resistance on the horizon, cancer, neurodegenerative disorders, or infectious diseases as COVID-19, pharmaceutical solutions are desperately in need at a time of global aging and expanding populations. For example, since only one-third of all known 30,000 human disorders can be adequately treated, the demand for innovative advances is undiminished to increase screening efficiency and reduce development time during drug discovery.[2]

Ideally, these approaches have to be implemented in early-stage discovery to target and select substances that are less likely to fail due to complications with safety-related issues to avoid economic and healthwise damage.[3,4] With substantial drop-out rates of up to 90% and average costs of 1.8 billion dollars, new drug development takes approximately 12 years to get a therapeutic to the market (see Figure 1).[5,6] To date, high drug attrition is partly associated with poorly validated pre-clinical cellular models with weak relevance to human diseases.[7]

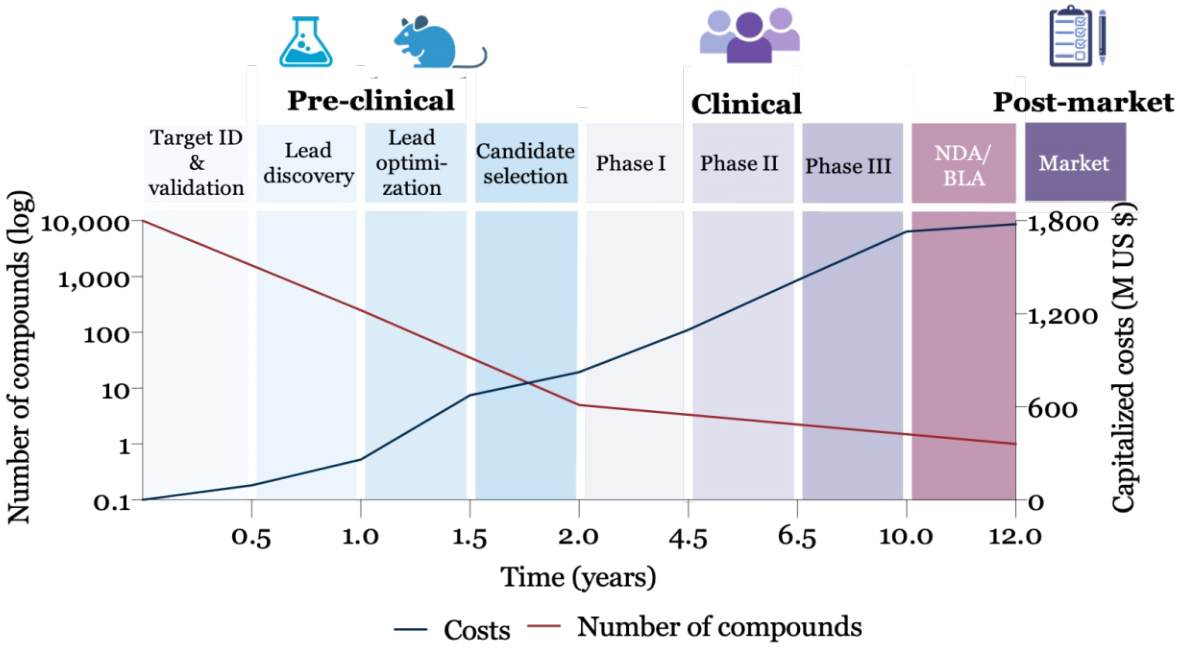

Figure 1: Stages of drug development with associated capitalized costs and the number of potential compounds (NDA/BLA, New drug application/Biologics License Applications). Created with BioRender.com.

For instance, the overall primary causes for termination in drug development between 2000 and 2010 were toxicologic issues (40%), as well as lack of clinical safety (11%) and efficacy (9%).[8] Breaking this down by development phase revealed that substantial safety failures were still apparent in clinical Phase II, suggesting that safety-related attrition remains a key area for improvement (see Figure 2). This demonstrates a clear inability to reproduce relevant states in early drug development for efficient target and compound selection.

Novel approaches and solutions are in need of developing more predictive assays to address this critical problem. Therefore, one fundamental question raises: How do we capture human biology's complexity in robust *in vitro* assays to mitigate late-stage termination of drug discovery programs?

The answer is to be found in translational processes itself: Higher predictability of potential drug effects in humans before clinical trials would lower the failure rate of new medications. Historically, two-dimensional (2D) cellular monolayers cultured on planar substrates were, for a long time, the only convenient approach to discover drug candidates. However, it is evident that these 2D cultures do not reproduce tissue-specific functionality, thus making them a relatively unpredictable model to investigate human drug response. Despite the shortcomings of this approach, 2D culture often turns out as the method of choice for cell-based drug screening.[9,10] For instance, once a biological target for a potential compound is identified, the pharmacokinetics (how the body processes the drug) and pharmacodynamics (what the drug does to body functions) must be profiled before translating to animal studies. During these stages, much of the current testing is still done in 2D cell cultures, often leading to unpredictable results.[11]

Another area of particular importance is the difference between animal tests and clinical studies carried out in humans. A prominent example of the discrepancies between species impacting the

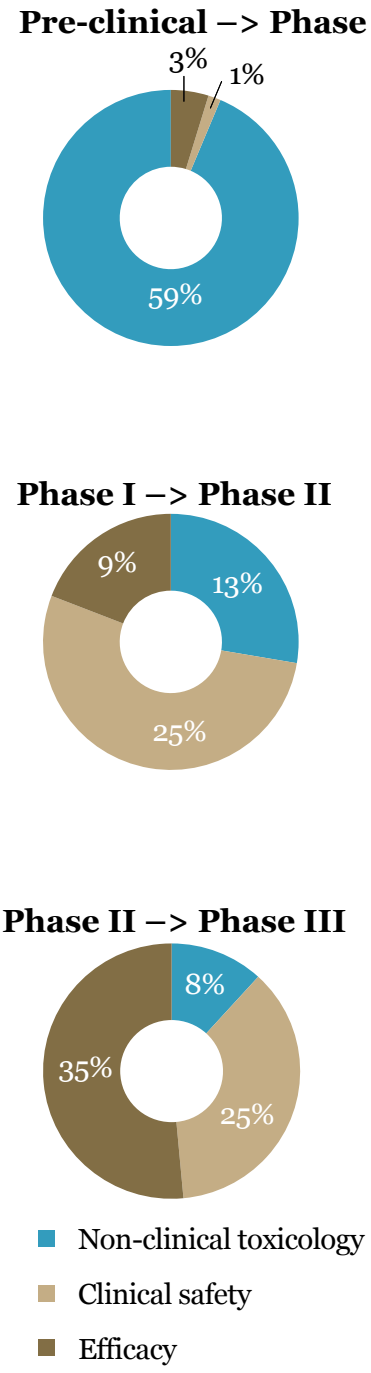

Figure 2: Primary cause of failure for terminated compounds during drug discovery. Reproduced from [8].

development pathway is found in cholesterol-lowering statins. Merck's lovastatin was approved by the Food and Drug Administration (FDA), but years later, many adverse effects in the original animal studies were not detected in the clinic. In contrast, serious side effects as muscle damage in humans were not observed in animal studies.[12]

Hence, preventing these problems earlier would reduce development costs and the time-to-market. A recent study involving data analysis on a set of 3,290 approved drugs reported 1,637,449 adverse events in regulatory submissions over a period of more than 70 years, indicating an insufficient translation of animal studies (from rat, dog, mouse, rabbit, and cynomolgus monkey) to predicting human response.[13]

Such cases make an old trilemma unambiguously apparent: How can unpredictable animal – and cell models be reduced, R&D efficiency increased, and incurring unsustainable costs avoided at the same time?[8,14,15]

1.1.2 Out of Complexity, Find Simplicity

The key to tackling these challenges and to pose new advances in healthcare is to substantially rethink the old dogmas of the pharmaceutical industry for the 21st century. Over the past decade, cell-based screening technologies in this area have therefore rapidly developed in three primary directions: (1) novel analytical technologies are used to analyze cell responses in high-throughput screening (HTS) or high-content screening (HCS) formats, (2) new approaches were established to generate and genetically manipulate cells, for example, CRISPR-Cas9-genome engineering, and (3) biological systems of cell models are gaining complexity to mimic the human *in vivo* situation.[16]

In particular, the rise of three-dimensional (3D) cell cultures in pre-clinical research is strongly supported by the need to continuously improve the productivity of R&D.[17,18] 3D spheroid cultures combined with advanced cell models (e.g., stem cells and primary human cells) would enable higher predictability in humans before drugs move into clinical trials and, in turn, decrease the failure rates of novel therapeutics significantly.[10,19] Multicellular spheroids, which reproduce human tissue - function and - architecture, are therefore considered as an advantageous model since they allow the screening of drugs in a more *in vivo* – like environment than traditional 2D cell cultures and exclude species-specific differences by testing novel compounds in a human cell system directly.

However, the progression of cell-based models to *in vivo*-like conditions is associated with increasing biological complexity by recreating physiological environments, such as 3D geometry, cell-to-cell interactions, and the presence of a dynamic micromilieu.

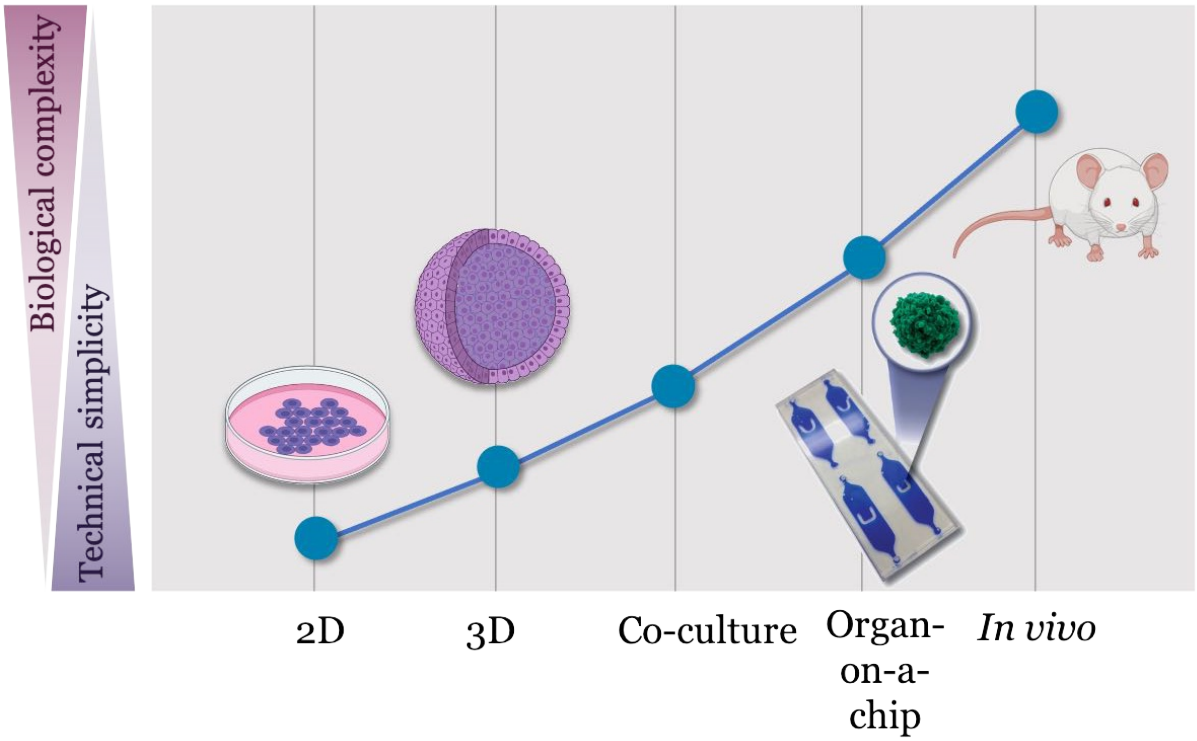

Figure 3: Progression of *in vitro* cell-based models as an alternative to animal models. The integration of more biological complex models decreases the level of technical and analytical simplicity. Created with BioRender.com. Reproduced from [20].

To correctly reproduce *in vivo* features, all of these factors must engage with each other, but often have to be included in a stepwise manner.[20]

As shown in Figure 3, each step causes an increase in *in vitro* model complexity. At the same time, this increase is accompanied by rising analytical- and technical issues. For example, the addition of dimensionality to current 2D cell culture models implement other important *in vivo* factors (as e.g., diffusion barriers and superior cell-to-cell interactions), recreating a better approximation to the human body, but also requiring systematic assessment in analytical tools and culture conditions (as e.g., specialized microtiter plates, imaging modality, changes in assay parameters). In order to find simplicity in 3D spheroid screening, complex spheroid parameters and optimal

experimental settings have to be identified, described, evaluated and controlled to streamline 3D-cell-based readouts and techniques for e.g., high-throughput screening to address the challenges of declining R&D efficiency.

In addition, since simple and complex systems have their respective advantages and disadvantages, the most appropriate complexity level has to be evaluated for each study. For instance, cancer spheroids containing only an epithelial component can be sufficient for toxicity testing but may lack relevance for more complex immuno-oncology therapy studies, requiring the presence of immune cells, mesenchymal, and/or endothelial cells. Unfortunately, standardized protocols or guidelines concerning these matters are still missing, so individual researchers are left to determine the most appropriate system for themselves. Together with batch-to-batch inconsistency of experimental materials, these circumstances often lead to protocol variability, limiting researchers' ability to compare experimental results. In this context, improvements in experimental design and the definition of specific strategies in compliance with quality and regulatory guidelines are needed.

In this thesis, main aspects and limitations for a broad adoption of 3D spheroid cultures in drug screening procedures are classified, validated, and discussed. Specific features of the 3D spheroid technology, potential applications in drug discovery as well as critical parameters for assaying, production, analysis, and scale-up to reduce data variability are described in more detail in the next upcoming sections of this work.

1.1.3 Key Characteristics of 3D Spheroid Cultures

Since the beginning of the 20th century, three-dimensional cell cultures have been employed in biomedical research to investigate the in-depth mechanisms of organogenesis. Multicellular spheroids as cellular aggregates are one of the most common and versatile way to culture cells in 3D.[21-23] The term 'multicellular spheroid', abbreviated to 'spheroid', refers to three-dimensional, spherical micromasses that consist of multiple single cells (epithelial, mesenchymal, endothelial, etc.).

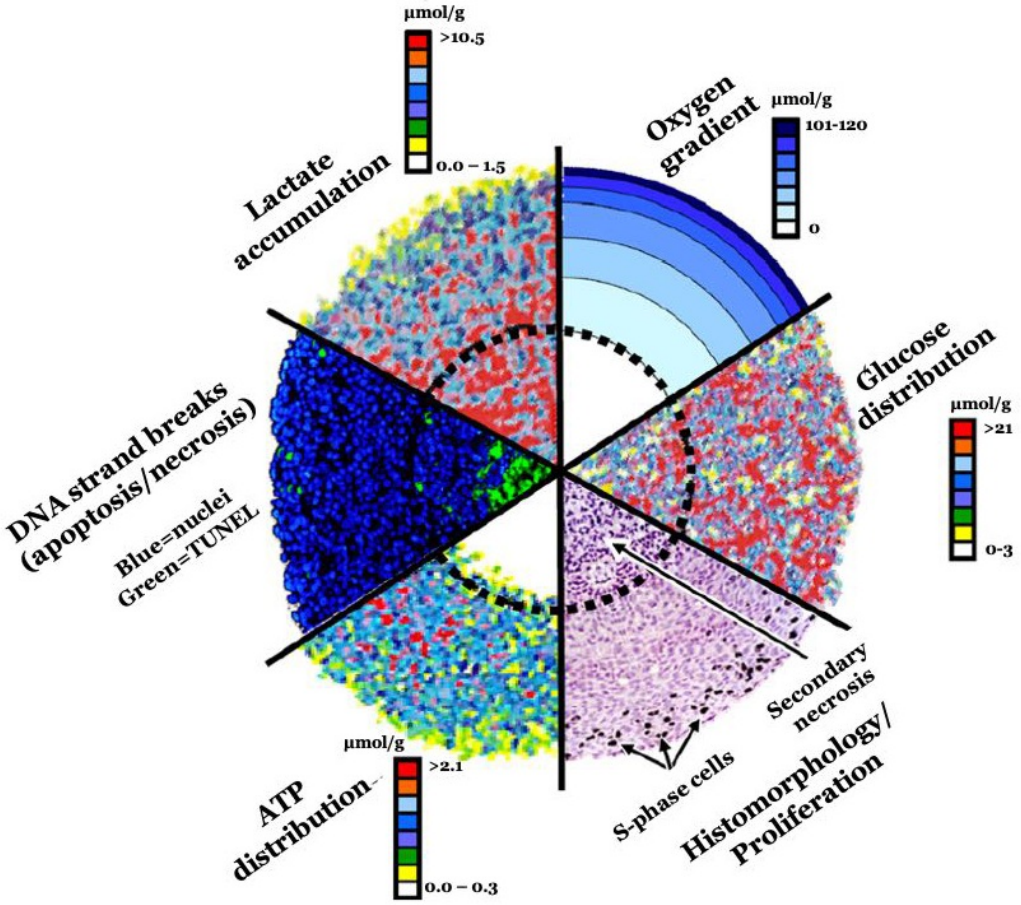

Figure 4: Characteristic microarchitecture and arrangement of proliferation, apoptosis, and metabolic gradients in multicellular spheroids. Reproduced from [25].

Examples of spheroid models in literature include multicellular tumor spheroids (from cancer cells), neurospheres (from neural stem cells), mammospheres (from mammary epithelial cells), hepatospheres (from hepatocytes), and embryoid bodies (from embryonal stem cells).[24-27] Compared to 2D cultures, 3D spheroids are characterized by numerous unique features making them tremendously relevant models for *in vitro* drug screening. A cross-section of spheroids displays concentric rings of heterogeneous cell populations, whereas the inner layer is composed of necrotic and hypoxic cells, surrounded by an intermediate stratum of quiescent inactive cells and an outermost layer of a highly proliferative and migratory cell population (see Figure 4).[28,29] This generates steep, physiologically relevant gradients resulting in transport barriers and limited exchange and permeability of nutrients and gases. Such diffusion mode causes cells at different depths to be in distinct nutritional states and, thus, at different cell cycle stages.[30] Furthermore, in hypoxic environments, cells convert pyruvate to lactate to obtain energy through a process known as the Warburg effect.[31] This accumulation of lactate in spheroids is responsible for acidifying its interior (pH of 6.5–7.2), which also occurs in e.g., solid tumors. Moreover, gene expression levels for stress-responses, signal transduction, and cellular transport are often upregulated in spheroids compared to 2D-cultured cells, which lead to, e.g., increased chemoresistance.[32] Additionally, cell–to-cell and cell-to-extracellular matrix (ECM) interactions differ from 2D cultures to 3D spheroids resulting in alterations in drug binding and transport as well as the interactions with bioassays.

However, these unique features of spheroids significantly contribute to overcome the current challenges of 2D cultures and animal models (see Table 1). For instance, 3D spheroids enable to study aspects of human development and disease that are not easily modeled in animals.[33] The use of animal studies for disease modeling and

therapeutic development is not only expensive and time-consuming but also do not mimic physiological responses in human beings.[34-36]

Considering these limitations of animal studies and 2D cell culture systems, more efficient and physiological-relevant *in vitro* tissue models by using spheroids with their promise of better predictability have the potential to improve drug screening outcomes in pre-clinical studies.

A plethora of production methods with significant variations in throughput, costs, and versatility have been developed during the past decades to accomplish these tasks. Since the choice of the production method is a critical question in spheroid experimental design strategies, the following section gives an overview of static and perfused dynamic spheroid generation methods, which have been reported throughout the last years.

Table 1: Comparative summary of cellular functions and screening performance of 2D cultures, 3D spheroid cultures, and animal models. Reproduced from [36].

	2D	**3D**	**Animal models**
Physiology	Limited	Semi-physiological	Physiological
Genetic profile	Cellular adhesion, proliferation and gene expression are modified compared to *in vivo*	Better representation of human growth factors, pro-angiogenic and adhesion molecule genes	Inter-species differences of genetic profiles
Disease modelling	Poor	Good	Good
High-throughput screening	Excellent	Good	Poor
Manageability	Excellent	Good	Limited
Multicellular studies	Poor	Suitable for the study of cell-cell communication, morphogenesis	Excellent
Vascularization and immune system	No	Limited	Yes
Costs	Low	Low	High

1.1.4 Generation of 3D Spheroids: Techniques-Devices-Systems

Traditionally, spheroids are mostly generated under static conditions using plastic culture dishes with non-adhesive surfaces or scaffolds. The type of 3D cell culture technique strongly varies on the used cell type, the aim of the study, costs, laboratory equipment, and the need for high-throughput capabilities.

Figure 5: Schemes of spheroid generation techniques under static conditions. Created with BioRender.com.

1.1.4.1 Static spheroid generation and culture

Commercially available culturing platforms for static 3D spheroid formation can be mainly classified into scaffold-based and scaffold-free procedures, as shown in Figure 5. Spheroid complexity, as size, depends on growth kinetics, cell density, duration of culture, and spatial limitations, such as the culture well diameter.[8] Since spheroid size heterogeneity can influence the robustness of endpoint assays, it is critical to generate spheroids of uniform size and -complexity for biochemical assays and high-throughput screening. Various methods with their advantages and disadvantages (see Table 2) have been established, which are as follows:

Scaffold-based:

Matrix-on-top and matrix-embedded. In the matrix-on-top method, cells are seeded on top of a solidified matrix, followed by agitation during incubation. The cells spontaneously aggregate to spheroids while remaining attached to the matrix. When using the matrix-embedded technique, cells are suspended in a liquefied matrix (e.g., agarose, Matrigel®, fibrin, or synthetic polymers) and dispensed into microwells or petri dishes and get embedded within the matrix upon gelation.[37,38]

Spinner flask. Cells are forced to aggregate in a dynamic bioreactor by continuous agitation. This method allows the large-scale production of spheroids, on the other hand, high flow-induced shear stress can lead to negative effects on microtissue growth as well as heterogeneity in spheroid size.[39,40]

Micro-/nano-patterned surfaces. Nano-scale scaffolds are imprinted onto a substrate similar to ultra-low attachment plates.

These micropatterned platform designs in standard plate formats making them compliant with HTS. However, a technological limitation includes the sensitivity of the nano-patterned interface in terms of pipetting induced damages.[41,42]

Scaffold-free:

Pellet culture. Due to centrifugal force, cells concentrate at the bottom of a tube, which maximizes cell-to-cell contact and ultimately leading to spheroid formation.[43,44]

Liquid overlay culture. Liquid overlay culture is described as one of most straightforward and simplest spheroid generation techniques. 3D spheroids are created by covering the surface of an, e.g., cell culture petri dish with a thin film of an inert, hydrophobic, cell-repellent substrate such as agar or agarose.[45,46]

Ultra-low-attachment (ULA) plate. Plates of different formats (48-, 96-, 384-well) are coated with an ultra-low attachment surface coating (e.g., neutrally charged hydrogels, lipid bilayers, or synthetic biopolymers) to minimize cell adherence. Additionally, these platforms are available with a wide range of geometries (e.g., round, tapered, or V-shaped bottom) to force and locate a single spheroid within each well. The essential advantage of this approach is to generate, cultivate, and assay spheroids within the same plate, thus enabling HTS or HCS.[47,48]

Hanging drop. Small droplets (20-60 µl) of cell suspension are dispensed onto the bottom of a petri dish lid, aiming to aggregate cells into a discrete media droplet, and ultimately forming spheroids on the liquid-air interface. However, an explicit limitation of this approach is that spheroids are required to be transfered to an additional plate for assaying.[49,50]

External forces. The external force method uses any force to concentrate single cells at high density to facilitate cell aggregation. External forces as electric fields, magnetic force, or ultrasound are commonly used for this method.[51-53]

3D-bioprinting. Bioprinting usually implicates layer-by-layer positioning of biological materials, biochemicals, and living cells. 3D bioprinting has been used to produce scaffolds for 3D cell cultures and tissue constructs for drug screening applications. However, the main concerns are the requirement of an expensive 3D bioprinting machine and the harmful effects on sensitive cells during the printing process.[54,55]

Table 2: Overview of static spheroid generation techniques.

Type	Technique	Advantages	Disadvantages	References
Scaffold-based	**Matrix on top and matrix embedded**	Cells can be recovered post-culture	Hydrogels require special handling Heterogeneous spheroids require sorting before assay Challenging to stain and image matrix-embedded spheroids Can be expensive for large-scale	37,38
	Spinner flask	High yield Minimal labor Fluid movement aids mass transport in spheroids Can easily be scaled up	Due to shear forces, this method is not useful for cells that are sensitive to shear Due to constant mixing, cells cannot be visualized as they aggregate	39,40
	Micro-/nanopatterned plate	Spheroids can be imaged with relative ease Post-culture recovery possible ECM component is present	Well surface needs to be coated to create low adhesion surface Generates spheroids of variable sizes Multiple spheroids in a well can overwhelm assay chemistry	41,42
Scaffold-free	**Pellet culture**	Simple Rapid	Shear stress from centrifugation can damage cells Cannot be scaled up for mass production Can mainly form larger spheroids	43,44
	Liquid overlay	Easy Cheap Rapid screening	Produce only a small number of spheroids Heterogeneous in size and shape	45,46
	Ultra-low attachment plates	Cheap and easy to handle Large number of spheroids can be obtained End-point analysis on the same plate Easy post-culture recovery Can generate single spheroid per well Can be multiplexed with imaging and other biochemical assays	Spheroids of variable sizes May have a mixture of variable cells and spheroids, since to batch-to-batch variation of the anti-adhesive coating	47,48
	Hanging drop	Good size control Low shear stress Inexpensive Large number of spheroids obtained in a limited space Reduced reagent consumption Post culture recovery possible	Labor intensive if preparing plates in-house Difficult medium exchange Spheroids are transferred to a secondary plate for end-point analysis	49,50
	External force	Low shear stress Culture of multiple cell types	Nonspecific cell adhesion Difficult to control spheroid size Physiological changes to the cells caused by external forces are not well characterized	51-53
	3D-bioprinting	Custom-made microarchitecture High-throughput capability	Expensive Process may damage cells	54,55

Despite the advances in static spheroid generation techniques, the non-dynamic microenvironment of conventional culture plates is known to cause fast reduction of oxygen and nutrients while increasing metabolic waste and osmolality in 3D aggregates, influencing subsequent results in drug testing.[56] The use of more superior technologies such as microfluidics has therefore gained increasing interest to produce more advanced spheroid models from diverse cell origins.

1.1.4.2 Dynamic microfluidic spheroid cultures

The semiconductor industry significantly contributed to microfabrication methods using e.g., photolithography to define microscale material patterns. These fabrication techniques were later adopted for applications in the life sciences and further developed to soft lithography for the 3D replication of elastomeric microstructures.[57] Due to the hydrophobic nature, gas permeability, optical transparency, and biocompatibility, the elastomer polydimethylsiloxane (PDMS) is an ideal material for microfluidic chip fabrication, spheroid formation, and long-term perfusion of cell cultures.[58] In the last years, a compendium of microfluidic technologies have begun to impact life sciences with relevant applications such as cell patterning[59,60] or the spatiotemporal manipulation of the cellular microenvironment.[61] A remarkable feature of microfluidic devices includes cell culturing in a dynamic microenvironment to recapitulate the tissue environment and to enhance spheroid formation and size control, allowing rapid aggregation, requiring minimal user interaction, and replacing manual handling with engineered and automated procedures (see Figure 6).[62]

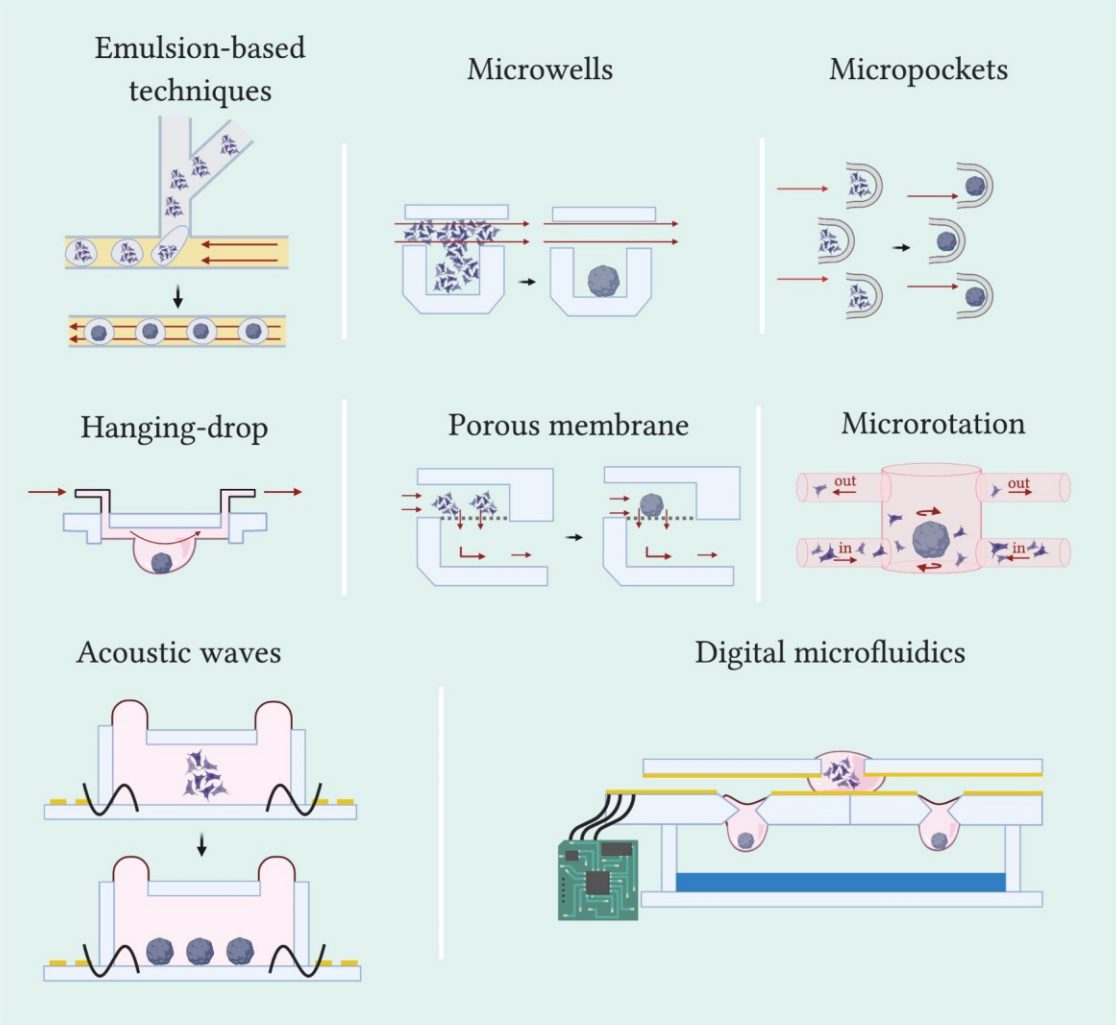

Figure 6: Overview of microfluidic dynamic spheroid generation methods. Created with BioRender.com.

This trend was also supported by an initiative on Advancing Regulatory Science in 2010 by the National Institutes of Health (NIH) and the FDA to address the need for new tools, standards and approaches to evaluate medical product safety, efficacy, and quality. A major focus of the program was the development of advanced microphysiological systems (MPS), to predict drug safety and efficacy in humans more accurately. The rapid growth of synergistic engineering by the convergence of MPS and 3D models as spheroids can lead to more a streamlined drug discovery.[63] In this

section, a panel of the most common spheroid generation techniques using microfluidic devices and systems are described.

Emulsion-based techniques: Single-, double- and triple-emulsion droplet generation techniques have been utilized in chip-based spheroid encapsulation. The fast production of microdroplets and high-throughput spheroid formation can be facilitated. This method involves (a) the generation of e.g., collagen or alginate droplets containing cells in suspension and (b) on-chip gelation and incubation of spheroid-containing droplets.[64,65] For instance, droplet generation frequencies of up to 200 droplets per minute have already been achieved.[66]

Microwells: The applied cell suspension fills microchannels and vertically aligned (perpendicular to flow direction) microwells due to microfluidic flow and initiate cell depositing on the bottom of microwells. Cell culture medium flows through the culturing channels and rinses excess cells without disturbing the cells on the microwell bottom. Anti-adhesive surface coatings induce cell aggregation on microwell bottoms and, thus to the formation of 3D spheroids.[67,68]

Micropockets. Horizontally aligned (parallel to flow direction) U-shaped micropockets act as hydrodynamic traps that accumulate cells to spheroids in a microfluidic chip. Spheroid diameters depend on microstructure dimensions, while the relative position of those structures is essential for efficient cell trapping.[69,70]

Hanging drop. Open hydrophobic rim structures restrict wetted areas, and liquid is guided through the network by capillary forces. Cell suspension is introduced, capillary forces form droplets, and cells aggregate to 3D spheroids at the air-liquid interface. Since holes structures are interconnected with each other, microfluidic perfusion can be applied by connecting pumps.[71,72]

Porous membrane. These microfluidic devices are composed of two layers of microchannels separated by a semi-porous membrane. The upper channel is designed with a dead-end to facilitate cell capture, whereas the lower channel is continuous to allow medium perfusion. Cells are introduced into the upper channel to cover the membrane fully. Since the membrane is treated with an anti-adhesive coating, cells self-aggregate to form 3D spheroids. The compartmentalization afforded by the membrane allows subsequent exposure to different culture scenarios with minimal perturbation of spheroid positions.[73,74]

Microrotation: Each microchamber is connected to two tangential inlet channels at the base and two outlet channels at the top. Microrotational perfusion is generated by the fluid flowing from the two inlet channels to the microchambers. Cells accumulate near the center of the chamber and form spheroids. The closed region fluidically maintains the spheroids in the center of the chamber and remove cells that had not been formed into spheroids.[75,76]

Acoustic waves. Spheroids are formed in microchannels where a potential field exists. Acoustic waves leak into the chamber and form a Gor'kov potential field. Cells aggregate in the areas of minimal Gor'kov potential and are levitated to trapping nodes in vertical direction by the balance of acoustic radiation force, facilitating cell–to-cell communication in a geometrically confined space.[77,78]

Digital microfluidics: Liquid droplets can be directed to specific locations using mechanisms such as magnetic fields, optical actuation, or electrostatic forces. Reagents, drugs, and any other liquid solutions are delivered to the anchored droplets on the chip without any pumps or valves. Liquid droplets of cell suspension are added to the chip to form sub-droplets and guided to open holes or hydrophilic sites to be

anchored. The sub-droplets take the shape of hanging drops, leading to cell aggregation to 3D spheroids in each droplet.[79,80]

To summarize the information presented in this section, Table 3 recapitulates the most common microfluidic spheroid formation designs with their respective advantages and disadvantages.

Table 3: Overview of advantages and limitations of microfluidic generation techniques.

Technique	Advantages	Disadvantages	References
Emulsion based techniques	High throughput spheroid formation Adjustable droplet frequency and droplet sizes	Hydrogels require special handling High concentrations of hydrogels may disturb cell proliferation Mechanical stress affects spheroid size and viability	64,65
Microwell based structures	Easy handling Variety of design options	Limited applications for HTS Limited prediction of nutrient and oxygen supply	67,68
Micropockets	Controllable spheroid sizes High yield Droplets and cells can be trapped	Easy to lose spheroids	69,70
Hanging drop	Allows high-throughput screening	Laborious Liquid evaporation can impact cell viability	71,72
Porous membranes	Spheroids can be imaged with relative ease Post-culture recovery possible ECM component is present	Well surface needs to be coated to create low adhesion surface Generates spheroids of variable sizes	73,74
Acoustic waves	Rapid No shear stress	Produce only a small number of spheroids Heterogeneous in both size and shape	77,78
Microrotation	Rapid Controllable spheroid sizes	Limited cultivation time Needs high volume flow rates	75,76
Digital microfluidics	Small amount of reagents Precise liquid handling	Liquid evaporation, Lack of continuous perfusion Complex control and fabrication biofouling	79,80

Overall, static and dynamic generation techniques offer various technical and analytical possibilities with differences in complexity, reproducibility, and duration. As shown in Figure 7, static methods as liquid overlay have much higher standard deviations (SD) compared to perfused dynamic methods as emulsion-based techniques or microwells. Dynamic solutions, as e.g., microrotational flow devices facilitate spheroid formation in a much shorter time due to the specific flow than any other static approach, which reveals, in general, the vast potential of microfluidic spheroid systems in manipulating key spheroid characteristics in a precise, high-quality, and time-effective manner.[81]

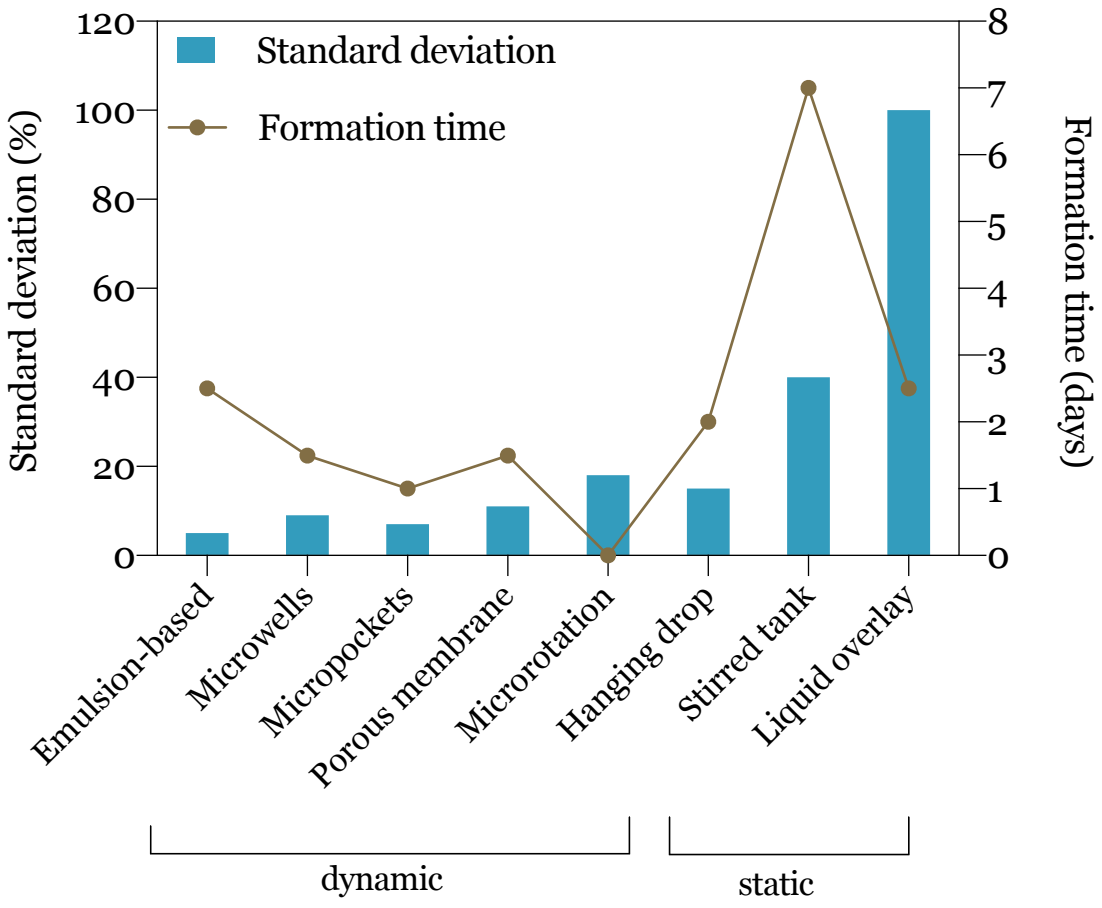

Figure 7: Spheroid diameter standard deviation versus formation times in literature. Reproduced from [80].

Despite advancements in the field of microfabrication, these processes are still considered expensive and need to become more robust and easier to handle. Remarkably, dynamic spheroid-chip approaches are accelerating in the field of drug screening, indicating that the impact of these platforms is likely to expand across life science.

As mentioned above, besides the different generation methods, further improvements of commercial assays, imaging, data acquisition, and throughput are necessary for a broad acceptance of 3D spheroid models in drug screening. Detailed analysis methods are described in the upcoming section to shed light on the respective applications and limitations of on-and off-chip spheroid detection technologies.

1.1.5 Under Investigation: Characterization and Analysis of 3D Spheroids

A variety of techniques are employed to study (a) morphology, (b) topography, (c) size, (d) cellular organization, and (e) protein and gene expression patterns of 3D spheroids. These techniques mainly include colorimetric, microscopic, spectroscopic, mathematical, genomic/metabolomic as well as chip-based procedures that were reported and used in the past years in literature (see Figure 8).[82]

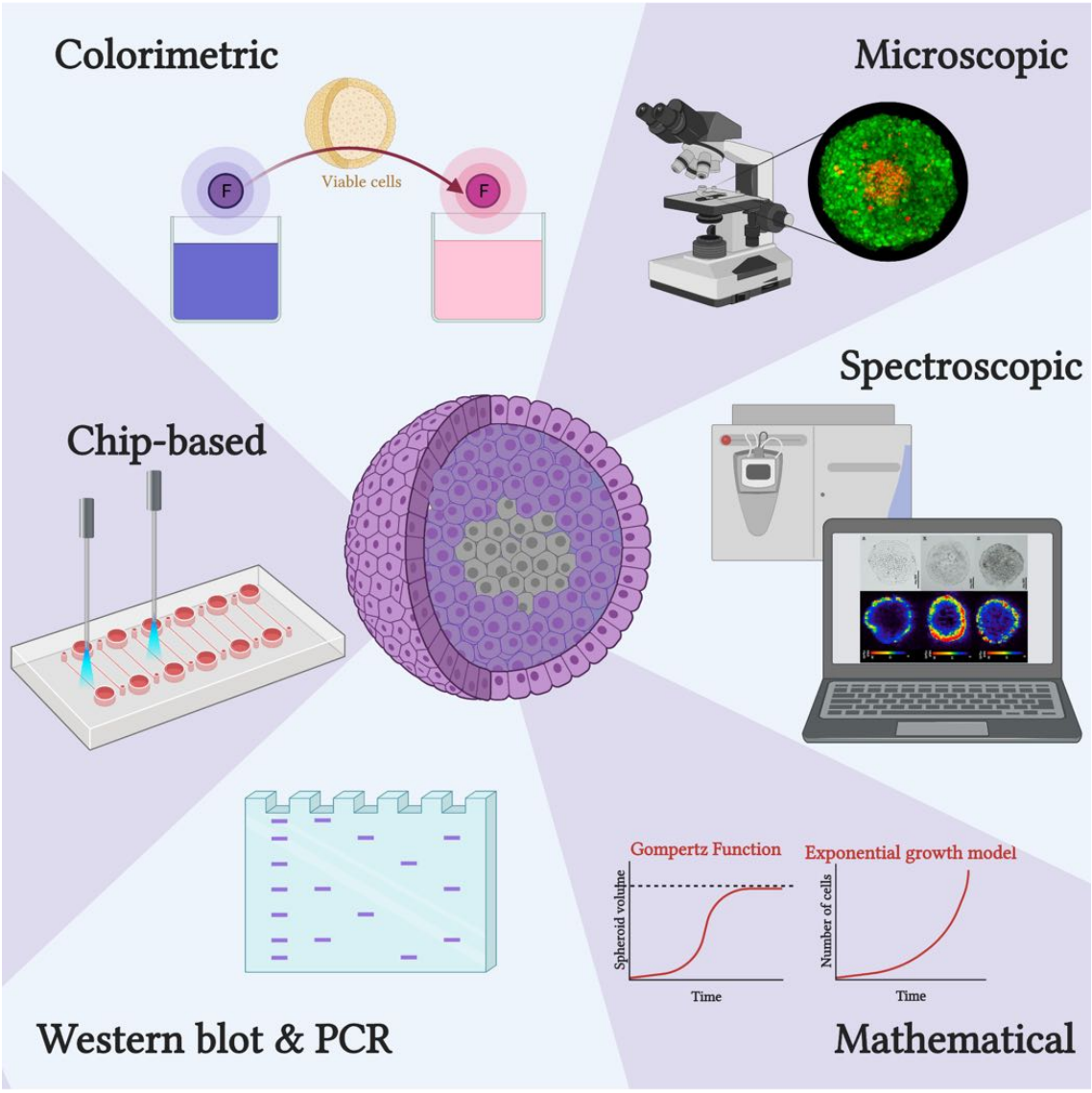

Figure 8: Schematic overview of analytical methods in 3D spheroid cultures. Created with BioRender.com.

1.1.5.1 Microscopy techniques

Optical (e.g., bright field,[83] dark field,[84] phase contrast,[85] and fluorescence[86]) microscopic techniques are precious approaches for characterizing spheroid size, morphology, and internal organization, as shown in Figure 9. Optical microscopes equipped with digital cameras are usually used to study spheroid growth and allow the observation and analysis of internal organization of cells in each layer.[87] To accomplish these tasks, antibodies that specifically target proteins (e.g., caspase-3, HIF, Ki-67) or biomarkers (e.g., EF5, pimonidazole) are used to characterize the cellular microenvironment or state (proliferating, senescent or apoptotic). Furthermore, fluorescent microscopy is an important type of optical microscopy that can be used to perform fluorescence-based viability assays for the determination live and dead cell distribution within 3D spheroids. For instance, Calcein-AM and Ethidium-homodimer 1 are commonly used cellular markers for this purpose. In addition, other stains as hematoxylin and eosin (H&E), Masson's trichrome, and toluidine blue are often applied for histological analysis by optical microscopy. In terms of assessing of the therapeutic effect in 3D spheroids, fluorescence microscopy is a very beneficial procedure for the evaluation of pharmaceutical dispersion within spheroids when auto-fluorescent drugs are used (e.g., doxorubicin or epirubicin). This method has also been applied to determine penetration distances of molecules through a spheroid, both in its free form or encapsulated in a nanocarrier.[88,89] Currently, confocal laser scanning microscopy (CLSM) is the most employed microscopic fluorescent modality to characterize spheroids.[90] However, analysis of the 3D cellular aggregates with high spatial resolution is still challenging. CLSM sometimes does not support the visualization of thick specimens due to limited light penetration and the working distance of the commonly used objectives (e.g., water immersion objectives).

Therefore, more specialized fluorescence-based techniques are often used for the imaging the distinct cell layers present in the interior of 3D spheroids as, e.g. light-sheet-based fluorescence microscopy (LSFM),[91-93] two-photon microscopy,[94] and multiphoton microscopy.[95] The recent combination of adaptive optics with lattice light-sheet technology (AO-LLSM)[96] is ideal for tissue imaging tasks, as tissue-induced aberrations can be corrected, resulting in four-dimensional (4D) movies with unachievable clarity. This so-called "4D cell biology" approach (3D tissue culture, 4D imaging, and image analytics) allows quantitative high spatiotemporal resolution analysis of subcellular interactions within 3D spheroids.[97]

Electron microscopy (scanning and transmission) allows the acquisition of images of 3D spheroids with high magnification and resolution, revealing details at the nanoscale level. Among other applications, electron microscopy enables the observation of cellular topography and microarchitecture (e.g., cytoskeleton) that are involved in cell-to-cell

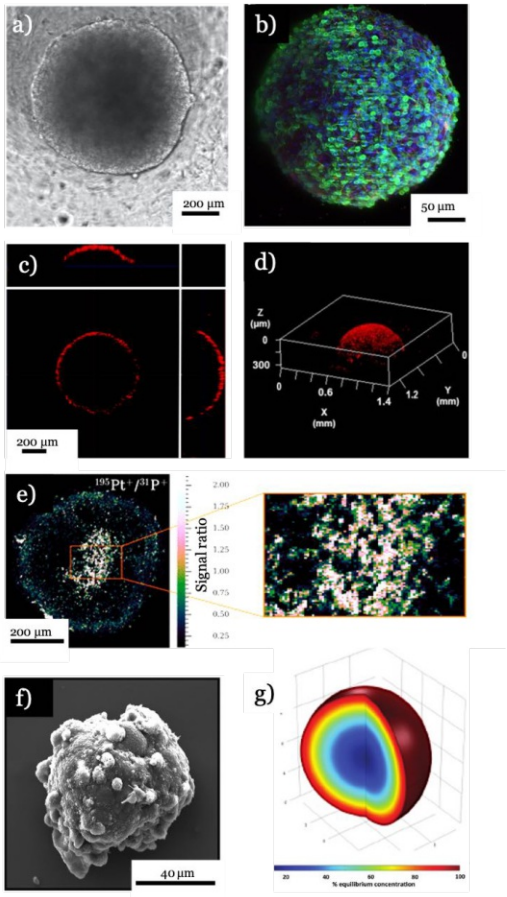

Figure 9: a) Bright-field micrographs of a HepG2 spheroid after 6 days of cultivation. b) Image of a neural aggregate using LSFM. From [92]. c) Orthogonal projection and d) 3D reconstruction of a CLSM image of a tumor spheroid. From [81]. e) High-resolution LA-ICP-MS image of $^{195}Pt^{+}/^{31}P^{+}$ signal ratio distribution in a colon cancer tumor spheroid, after treatment with oxaliplatin. [From 114]. f) SEM micrograph of a HepG2 spheroid. [From 97]. g) Computational models of oxygen gradients formed in a spheroid. From [121].

interactions.[98] Furthermore, the loss of these physical interactions and the formation of apoptotic bodies can also be studied using this type of microscopy.[46,82,99-103]

1.1.5.2 Colorimetric techniques

Colorimetric techniques are based on chemical assays that rely on the enzymatic conversion of a solute within the subcellular compartments of a cell (cytoplasm or mitochondria) to assess the cytotoxic or metabolic effects of a therapeutic agent. Colorimetric assays for examining spheroids include the alamarBlue®,[104] acid phosphatase,[85] lactate dehydrogenase,[105] MTS,[89] MTT,[106] and WST-8 assays.[107] The reaction product is quantified by measuring its absorbance, fluorescence, or luminescence at a specific wavelength and is proportional to e.g., the number of metabolic active cells.[108,109] However, special care needs to be taken in the analysis of the results obtained through these colorimetric assays since the experimental protocols available are usually optimized for monolayer cultures. In spheroids, the limited mass transport may prevent a homogeneous distribution of the solute, leading to inaccurate results.

1.1.5.3 Spectroscopic techniques

As an alternative to colorimetric assays, other spectroscopic techniques have been applied for cellular viability analysis within spheroids, including luminescence, tissue dynamic spectroscopy (TDS), fourier transform infrared (FT-IR) imaging, and proton-induced X-ray emission (PIXE).[110] These techniques allow the characterization of cellular population in spheroids by taking advantage of their inherent properties, as cellular density and motility, the distribution of of deoxyribonucleic acid (DNA),

adenosine triphosphate (ATP), proteins, metabolites as well as inorganic elements such as copper and zinc.[111-113] Laser ablation in combination with ICP-MS has a leading role in bioimaging and elemental mapping of biological systems with sufficiently high spatial resolution. This method has proven to be a sensitive way to assess the spatially resolved metal distribution in histological structures.[114,115]

1.1.5.4 Immunoblotting and gene expression

Western blot (also called immunoblotting) and quantitative Polymerase Chain Reaction (qPCR) are widely used techniques to evaluate the presence of proteins and gene expression patterns in 3D spheroids. Western blot is used to evaluate the presence of specific proteins in cell lysates. Cellular homogenates are obtained by harvesting 3D spheroids by chemical lysis, using a buffer that contains a detergent (e.g., sodium dodecyl sulfate (SDS)), or mechanical lysis as e.g., sonication.[116] Spheroids, owing to their complexity and cellular density, may need a longer incubation periods with lysis buffer than 2D cell cultures, in order to lyse all cells.[117] However, Western blot is a semi-quantitative method and should be complemented with a more quantitative analysis such as qPCR. Spheroid sample preparation for qPCR analysis is very similar to Western blot analysis, in particular, cellular aggregate disruption and the preparation of a cellular homogenate. Western blot and qPCR analysis of spheroids allows the identification of different proteins that play essential roles in, e.g. tumor progression, the analysis of therapeutic efficacy, or to verify the efficacy of gene therapy (e.g., RNA interference) in spheroids.[118,119]

1.1.5.5 Mathematical modelling

The characteristic properties of 3D tumor spheroids, as their (i) round shape, (ii) exponential growth kinetics, (iii) layered organization, and (iv) metabolite gradients are used to develop mathematical models that are capable of extracting relevant biological data.[28] For instance, initial exponential growth of spheroids can be obtained by mathematical models as the exponential growth model (Equation (1)) and the Gompertzian Function (Equation (2)), which are described as follows:

$$n(t) = N_0 exp^{\lambda t} \qquad (1)$$

$$x(t) = K exp^{\log\left(\frac{x(o)}{K}\right)} exp^{-\alpha t} \quad (2)$$

where the exponential model correlates with the number of cells at time t ($n(t)$), the initial cell number (N_o), and the growth constant (λ).[120] The Gompertz function predicts spheroid growth ($x(t)$) by associating the 3D spheroids volume (x) with the initial spheroid volume ($x(o)$) and the tumor growth rate constant (α).[121] This model can predict the spheroid volume plateau (K) after extended periods of culture (see Figure 8). Recently developed mathematical models are able to predict 3D spheroid growth in accordance with the gradient of nutrients, oxygen, and pH. Computational modeling as finite element simulations enables an *in silico* analysis of different metabolic phases and distribution of molecules inside spheroids, as shown in Figure 9g.[122] In addition to these advances, improvements in image analysis software and image processing algorithms have provided the opportunity to better follow up and analyze spheroid growth. In this context, the software MATLAB® (The MathWorks, Inc., USA) provides an automatic method to reconstruct the 3D microstructure and

calculate spheroid volume over time using simple 2D microscopic images as, e.g., bright-field.[123-126]

1.1.5.6 On-chip analysis techniques

Small and well-defined dimensions of microfluidic networks in sub-millimeter range enable the use of parallel cell culture arrangements to execute experiments simultaneously. To investigate spheroid samples in a reproducible manner, optical accessibility, integration of sensors as well as high-content analysis under various treatment regimens are essential for real-time monitoring and end-point analysis of 3D microtissues. Despite advancements in the past few years, standard microscopy-based methods are still the most common analysis techniques on-chip. For instance, viability and the distinct morphology of spheroids can be assessed using optical microscopy, fluorescence microscopy, or CLSM. Projected areas of green (live) and red (dead) cell regions are quantified as ratios after drug treatment (see Figure 10a).[127] Non-fluorescent assessment of viability, area, or sphericity can also be performed using image processing programs as e.g., ImageJ and MATLAB®, by measuring spatiotemporal changes in morphology on-chip.[82] Microfluidic culturing systems also offer the possibility to integrate sensors close to the cellular assemblies. For instance, electrode-based biosensors were implemented on a hanging drop-based microfluidic chip for the real-time monitoring of glucose uptake and lactate secretion, as shown in Figure 10b.[128] This microfluidic concept was also integrated into another device for electrical impedance spectroscopy.[129] Two pairs of platinum electrode inlays were

deposited on glass and placed lateral to the spheroid hanging drop culture in a way that each pair had various distances to it (see Figure 10c). Spheroid size induced changes in the electrical field resulted then in subsequent alterations of impedance. In another publication, a chip platform was fabricated to measure extracellular acidification, oxygen consumption, temperature, and electrical impedance.[130] As shown in Figure 10d, thin-layered deposited microelectrodes were embedded below each microwell to measure the chamber pH and the oxygen consumption of HepG2 spheroids.

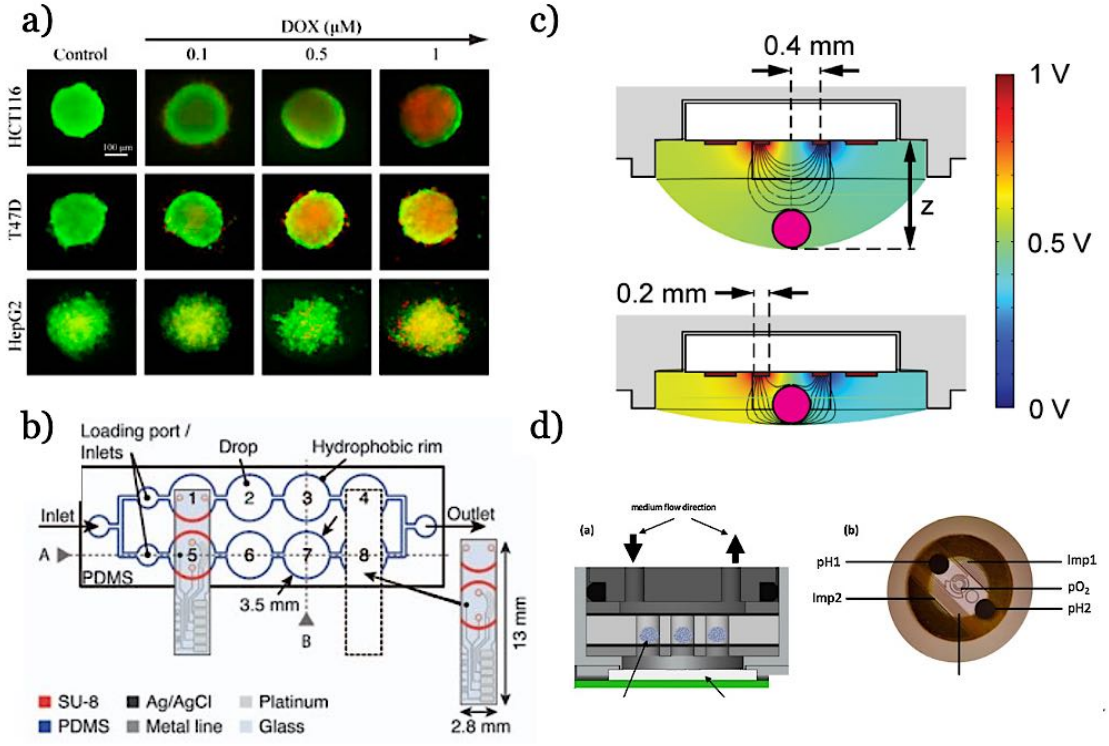

Figure 10: a) Live/dead staining images of doxorubicin treated HCT116, T47D, and HepG2 tumor spheroids. From [126]. b) Schematic sketch of the hanging drop device having eight hanging drop sites of 3.5 mm diameter and the orientation of the biosensor on the chip for lactate and glucose measurements. From [127]. c) Measurement of electrical impedance changes for two different drop heights (700 and 1400 µm). From [128]. d) Microfluidic sensor chip measuring the pH of the microenvironment (pH1 and pH2 sensors), oxygen consumption (pO_2 amperometric sensor), temperature (T), as well as impedance (Imp1 and Imp2). From [129].

In summary, a wide variety of techniques are available to screen and investigate distinctive features of 3D spheroids, such as microarchitecture, physiology, metabolic activity, secretion of biomarkers, gene expression patterns, and drug responses. These data fundamentally contribute to drug discovery process using 3D spheroids and highlight the potential of cellular aggregates to be used as *in vitro* models for the small- and large-scale screening of new compounds.

In the next section, the current status and the potential of spheroid cell culture models within the respective stages of drug discovery are discussed in more detail to emphasize the role of this technology for drug screening applications.

1.1.6 The Multifaceted Roles of Spheroids in Drug Discovery

Drug discovery is a long, winding, and complex road with growing difficulty in each step. The unique features of spheroid cell cultures would allow their integration into the drug discovery procedure, starting from disease modeling to toxicity profiling and tissue engineering, as illustrated in Figure 11.

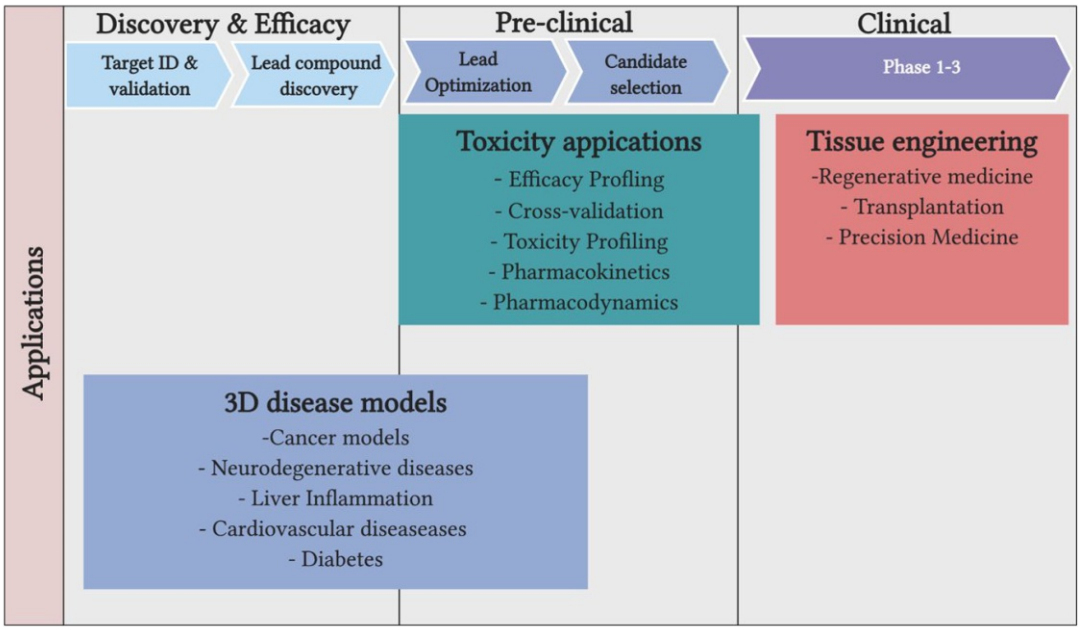

Figure 11: Potential applications of 3D spheroid cultures durung during discovery. Created with BioRender.com.

1.1.6.1 Disease modelling

To accomplish the growing therapeutic criteria for mimicking relevant human diseased states, the establishment of physiological models has become increasingly important in drug discovery programs.[131] 3D spheroid cultures provide fundamental insights into development, homeostasis, and pathogenesis and offer new translational approaches for diagnosing and treating diseases compared to 2D cultures. In the past, spheroids were used to investigate various disease mechanisms of e.g., liver steatosis,[132] insulin

resistance,[133] Alzheimer's disease,[134] drug-induced liver injury,[135] cardiomyopathy,[136] diabetes,[137] and a number of cancer models.[138] For instance, especially 3D models have gained popularity in elucidating tumor biology since 2D models are insufficient to address questions regarding indolent disease, metastatic colonization, dormancy, relapse, and the evolution of drug resistance.[139]

1.1.6.2 Target identification and validation

Target identification and validation is often the rate-limiting step in pre-clinical drug discovery. The function and therapeutic effect of a potential target (gene/protein) have first to be identified and modulated before proceeding to hit compound screening. In best case, a target should be efficacious, safe, and meet clinical and commercial requirements.[140,141] Due to similarities of gene expression patterns between 3D models and *in vivo*, spheroids can accelerate target identification and validation.[142] For instance, gene expression analysis of mesothelioma spheroid models showed primary causes of chemoresistance in malignant pleural mesothelioma and acquired increased chemoresistance than 2D monolayer cultures.[143]

1.1.6.3 Screening for hit identification

Cell-based assay screening is the beginning for identifying hit compounds in early-stage drug discovery. A "hit" is described as a compound that has the required activity in a screen. The main motive involves the identification of particular molecules that interact with a specific drug target. In the past three decades, target-based HTS has been the dominating approach in hit identification due to the simplicity, relatively low costs, and high-efficiency of HTS-compatible cellular assays. However, in recent years,

there has been a revival in phenotypic screening, driven by factors as (i) the necessity for innovative strategies and continuous improvement in the productivity of pharmaceutical R&D, (ii) more productive phenotypic screens for discovering first-in-class drugs,[144] and (iii) advanced and feasible detection technologies to perform phenotypic screens with high throughput.[145,146] Especially spheroids cultured in ULA plates have gained popularity in oncology due to easy-to-use protocols, high-throughput microplate formats (e.g., 384-well and 1,536-well), and compatibility with automation and multi-parametric read-out systems. As example, multicellular colon cancer spheroids with inner hypoxia were used to screen 1,600 compounds with documented clinical history, resulting in identifying five compounds that selectively and efficiently target the hypoxic cell population.[147]

1.1.6.4 Efficacy profiling for lead identification and optimization

Once identified in a screen, hits are further evaluated during a hit-to-lead phase for drug-likeness, possible toxicity, metabolism, and stability-related risks. Once confirmed, lead optimization is the next step to generate lead candidate compounds with improved potency, reduced off-target activities, and required physicochemical and metabolic functions. The main challenge includes the need of cost-effective *in vitro* models that can reliably predict efficacy, toxicity, and pharmacokinetics of compounds in humans. It is considered that spheroid models have the potential to play an important role in lead identification and to reduce the use of animal testing for pre-clinical studies.[7] In some cases, it has been already shown to assess drug responses more accurately than 2D models allowing personalized targeted approaches to identify the mechanisms of diseases and to select the most effective drug for patients.[148,149] For instance, patient-derived spheroids were used as a predictive tool to identify the best

therapy for 120 patients with HER2-negative breast cancer of all stages. Results showed that the spheroid model reproduced the optimal guideline treatment recommendations for HER2-negative breast cancer in contrast to human monolayer cultures.[150]

1.1.6.5 Toxicity profiling for candidate selection

Drug-induced toxicities and resulting side effects are significant causes of drug attrition and withdrawal from the market.[151] Reasons for adverse drug reactions include off-target interactions or excessive binding mechanisms of the drug molecule to cells. To address these challenges, spheroid cell culture models are considered a powerful technology in assessing drug-induced toxicity.[152] As an example, 3D liver spheroids can help to study drug-induced liver injury, adverse effects, and cytotoxicity since human liver metabolizing enzymes are completely diverse from an animal liver. In particular, human primary hepatocyte spheroids were found to be phenotypically stable and retained morphology, viability, and liver-specific functions for at least five weeks, enabling chronic toxicity assessment. This was specifically demonstrated by identifying chronic toxicity of fialuridine after repeated dosing which was not possible to detect in 2D models.[135]

1.1.6.6 Pharmacokinetics and pharmacodynamics profiling for candidate selection

As mentioned above, poor pharmacokinetic and pharmacodynamic modeling are key factors for drug attrition. Spheroid models, particularly liver spheroids, liver organoids, and multi-organ-on-chips, can help to investigate the pharmacokinetic

profiles of molecules. Several versions of liver-on-a-chip systems are capable of measuring metabolic drug clearance rates, which were compared with literature-reported values.[153-155] Although the integration of multiple tissue types into one device, termed as body-on-a-chip, can be advantageous for comprehending the kinetics and dynamics of drugs, the establishment of screening-compatible body-on-a-chip systems is still challenging due to known allometric scaling issues and the need for different cell media compositions.[156-158]

1.1.6.7 Tissue engineering

Spheroid cultures of specific stem cells have already been used for disease treatment. For instance, spheroid models were acquired to treat idiopathic pulmonary fibrosis in mice by implanting adult lung stem cells. The microtissues from healthy lung tissue explants recapitulated the stem cell niche and developed mature lung epithelial phenotypes leading to decreased inflammation and fibrosis.[159] 3D organoids from stem cells or organ progenitors could therefore provide a promising source of autologous tissue for transplantation and tissue engineering.[160]

1.1.7 Life is...3D? Current Status and Future Trends of Spheroid Culture Platforms

The increasing demand and broad application areas for drug discovery and tissue engineering are considered to promote spheroid cultures in the next upcoming years. For instance, the global 3D cell culture market was valued at USD 1.4 billion in 2019 with an annual growth rate of 11.3%.[161] In addition, the development of different assay technologies and the expected advent of 3D-optimized assays, protocols, and kits positively impact market development. Currently, the biotechnology and pharmaceutical industry accounts for the largest revenue share and is expected to achieve considerable volume increases in the next years whereas, research laboratories are the fastest growing sector.

In recent years, especially scaffold-free spheroid culture systems have gained attention from researchers seeking ease of entry into 3D culture. The emergence of cell-repellent systems as ULA plates has been a significant contributor in supporting this trend, establishing a momentum behind spheroids that have promoted many additional developments and innovations. A variety of surface coatings are used to generate ULA plates, but the effect is basically the same; ULA and cell repellent plates are currently the most popular approach to generate single spheroids per well, but other formats may be better suited in creating a large number of spheroids (e.g., microfluidic devices), enhanced size uniformity, specific cell types or niche applications. The leading vendors of standard spheroid culture consumables purchased are Corning, Thermo-Fisher Scientific, and InSphero with strong variations in throughput, as shown in Table 4.

Table 4: Vendors of scaffold-free spheroid-culture platforms on the 3D cell culture market.

Company	Platform	Method	Max. number of spheroids/plate	Static	Dynamic	Origin
300microns	Statarrays© Dynarrays©	ULA	16,224 500	+ -	- +	Germany
Agilent	Seahorse XFe96 Spheroid Microplate	ULA	96	+	-	USA
AMSbio	Lipidure Coat Low Adhesion Plate	ULA	96	+	-	UK
Corning	Costar® ULA plates Elplasia™	ULA ULA	384 2,885	+	-	USA
faCellitate	BIOFLOAT™	ULA	96			Germany
Greiner Bio-one	CELLSTAR®	ULA	384	+	-	Austria
ibidi	µ-Slide Spheroid Perfusion	ULA	84	+	+	Germany
Kugelmeiers	Sphericalplate 5D	ULA	9,000	+	-	Switzerland
MicroTissues	3D Petri Dish®	Liquid overlay micromolding	6,144			USA
MoBiTec	PrimeSurface	ULA	96	+	-	Germany
n3D BioSciences	Bio-Assembler	Magnetic Levitation	96	+	-	USA
InSphero	GravityPLUS™ Gravity TRAP	Hanging drop ULA	96 96	+ +	- -	Switzerland
Organogenix	NanoCulture plate	Imprinted ECM network	384	+	-	Japan
PerkinElmer	CellCarrier® Spheroid ULA microplate	ULA	96			USA
ScreenIn3D	ONCO-Chip^{3D}	ULA	n.a.	+	-	UK
STEMCELL Technologies	AggreWell™	ULA	4,700	+	-	Canada
Thermo-Fisher Scientific	Nunclon™	ULA	96	+	-	USA

The majority of the presented platforms are still based on static spheroid-culturing conditions, while perfused dynamic cultures are rare and nearly non-existent. A variety of perfused spheroid culture platforms has been published in the last decade, but ready-to-use microfluidic devices have not entered the market so far, which shows the great potential of user-friendly, medium-to high-throughput microfluidic screening applications (see Figure 12). It is important to note that standard bioassay protocols and screening methods have to be performed without any effort on-chip to ensure successful implementation into mainstream laboratory routines. Despite the growing

interest and broad range of culturing products of 3D spheroids in the past years, the highest proportion of research activities still relates to validation and improvements of cell culture and assay parameters as cell viability (live/dead) assessment, morphology measurements (area, perimeter, diameter, roundness, etc.) and cell proliferation which indicates the requirement for validation and optimization of spheroid cultivation parameters.[162]

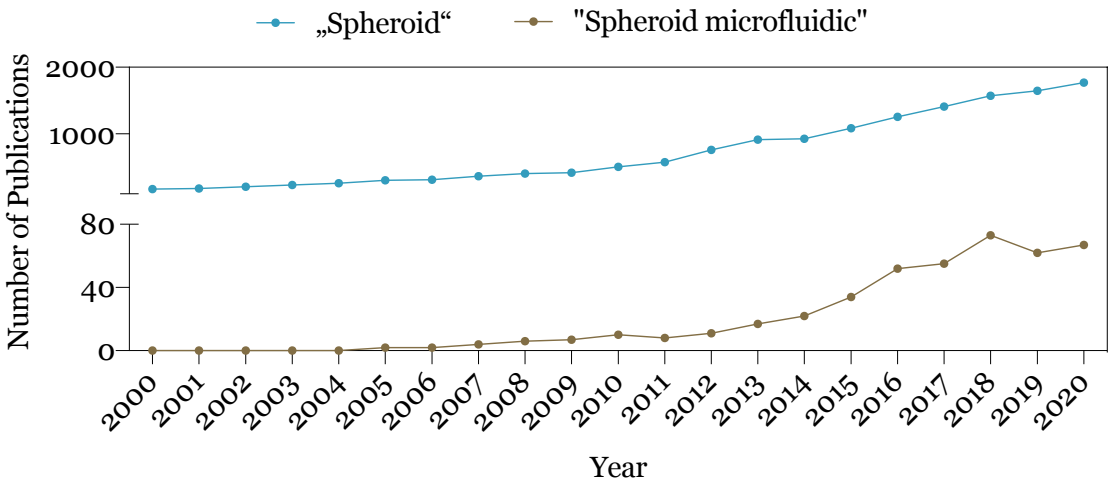

Figure 12: Number of publications about spheroids, and microfluidic spheroid platforms over the past twenty years obtained by PubMed research (https://pubmed.ncbi.nlm.nih.gov) using keywords “Spheroid” and ”Spheroid microfluidic”.

1.1.8 The Edge of Dimensionality: Critical Quality Parameters of 3D Spheroids

Despite the increasing trend of spheroid technology in pharmaceutical screening, several challenges impede the dissemination of spheroids in the industry. Critical factors such as spheroid size, spheroid age, and the choice of the generation method affect proliferative and functional features and micromilieu conditions. These aspects are directly linked to the complex cell-cell and cell-matrix interactions that affect RNA and protein expression, biomarker secretion, morphology, compound penetration, drug binding, drug bioactivity, and ultimately leading to abbreviations in treatment response (see Figure 13).

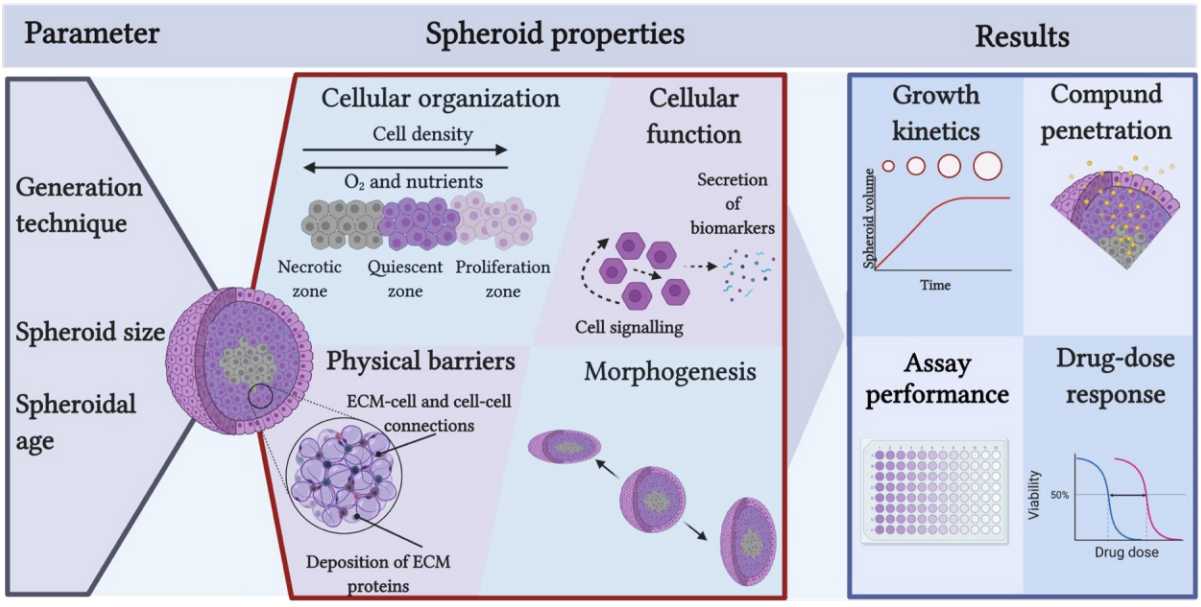

Figure 13: Impact of critical spheroid quality parameters during cultivation and drug screening on microtissue properties and consequential test results. Created with BioRender.com.

1.1.8.1 Bioassay protocols

The lack of standardized assays for spheroid imaging and assaying hinders the reproducible data output and automation for drug discovery. In contrast to 2D cell cultures, there is a limited amount of information in the form of adapted assay protocols and technologies to analyze compounds in 3D cell cultures,[82,160] As an example, CLSM, as one of the most applied fluorescence microscopy method, has a limited penetration depth that limits the imaging of larger spheroids.[163] Further, colorimetric assays (e.g., alamarBlue®), which are the standard method of choice for evaluating the cytotoxicity of therapeutics, must be performed carefully because a homogeneous distribution of the solute are difficult to control in 3D cell structures and highly influences test results. Additionally, 3D structure staining may require protocol optimization compared to the 2D equivalent. In general, the larger and tighter the spheroid, the more extended and complex it will be to complete cell stainings. Improvements in commercial assay performance including throughput, read-out precision and standardized analysis procedures are necessary for the broad acceptance of spheroid cultures for screening of potential compounds.

1.1.8.2 Spheroid generation method

Every spheroid generation technique has its advantage and limitation, as described above, but effort, material costs, scalability, reproducibility, automatization, and compatibility with available assay read-outs are areas of great concern.[164,165] Depending on the protocol used, spheroids differ in morphology, dimension, and abundance leading to limited comparability of the same spheroid models generated with distinctive techniques.[166]

1.1.8.3 Spheroid size

Spheroid size poses a bottleneck for HTS due to the resulting variations in quality parameters such as differences in gradient-based diffusion modes of oxygen and nutrients towards the spheroid core and the internal organization of proliferative and necrotic cells, as previously described in the literature.[167-169] Additionally, these factors strongly depend on the specific cell type, seeding density, and culture time. As the spheroid becomes larger, it becomes more difficult for nutrients and oxygen to reach the spheroid center, which can lead to a hypoxic core. Depending on the assay, this may or may not be desirable. The optimization of cell seeding density and spheroid size plays a leading role in the aggregation time of single cells to spheroids and maintaining spheroid cultures post-seeding in terms of media change, maximal culture time, assay protocols, etc.).

1.1.8.4 Spheroidal aging

Since cellular functions and proliferation stages alter during cultivation period, time-points for drug screening procedures have to be adequately defined to ensure reproducible and comparable outcomes. In addition to deviations in the spheroid microarchitecture, the extension of cultivation periods affects the fraction of different cell populations of distinctive proliferative stages in multicellular spheroids, leading to heterogeneous cell responses during drug exposure. These variations in culturing conditions can result in unreproducible therapeutics responses and consequently, making the comparability of drug exposure studies a problematic task. Monitoring spheroid functions and drug-response over time will therefore help in determining the ideal culture periods for each application.[170]

1.2 Aims of the Thesis

Many scientific studies confirmed that organotypic 3D cell structures have a decisive influence on the behavior of living cells. Improvements of cell model systems should avoid expensive animal experiments and replace the currently existing and inadequate *in vitro* analysis of 2D cell cultures. Nevertheless, one major limitation of using 3D culture in drug screening lies in the technical aspects of assay protocols, spheroid complexity, and cultivation conditions.

The main objective of this thesis involves the validation, investigation, and control of critical spheroid parameters as well as the establishment of novel analysis approaches and instrumentation to circumvent the limitations of 3D cultures in pre-clinical drug screening. First, the comparative evaluation of bioassay parameters and spheroid cultivation periods on generated data outcome during anti-cancer drug screening in a static 3D tumor model has to be evaluated. Based on these studies, the optimized 3D spheroid model is considered to evaluate tissue clearance and cytotoxicity by high-performance analytical approaches to increase predictability during the industrial drug development. Last, to enhance the biological complexity of 3D spheroids models, a perfused spheroid-on-a-chip platform has to be established that enables the rapid production of spheroids of defined sizes under perfused microphysiological conditions. With the help of this tool, various cell type (primary or cancer cell line) can be established, treated, and analyzed as an *in vitro* high-throughput model for pharmaceutical drug screening applications.

This thesis is written as a cumulative work and involves all original research articles (published manuscripts 1-4) of the applicant, Christoph Eilenberger, as first author to

address the challenges of reproducibility, standardization, and optimization of 3D spheroid systems in drug discovery.

1.3 Methodology

To generate 3D spheroids under static conditions, various ultra-low attachment surfaces were used. For example, the anti-fouling properties of surface layer (S-layer) proteins served as a novel ultra-low attachment biomaterial for the formation of functional spheroids of reproducible sizes. The bacterial S-layer protein SbpA displays strong cell-repellent behavior when recrystallized on planar surfaces enabling 3D cell aggregation in standard microwell plates (manuscript 1 and 2). In another publications, standardized ULA-pates with neutrally charged hydrogels as well as biocompatible low-adhesive 2-(methacryloyoxy)ethyl phosphorylcholine (MPC) polymers were used for the generation of 3D spheroids (manuscripts 3 and 4).

To evaluate and optimize the impact of assay time of a commercially available bioassay on drug screening results, spheroid viability and growth were determined by the alamarBlue® viability assay, fluorescent live/dead staining as well as the measurement of spheroid size by phase-contrast microscopy.

For analysis of the effects of spheroidal age on anti-cancer drug response, organotypic functions and microarchitecture of spheroids were obtained by enzyme linked immunosorbent assays (ELISA), immunocytochemistry, and transmission electron microscopy (TEM). To investigate spheroid size and morphology, bright-field images were taken by live-cell microscopy equipped with temperature, CO_2, and O_2 control and a high-resolution camera. For morphometric analysis, micrographs were converted to 8-bit, threshold was adjusted, and area, perimeter, roundness, and solidity were determined by an image processing software (ImageJ). In case of diffusivity-, drug penetration-, or paracellular-transport studies, fluorescent intensity

values of respective test compounds within the inner region of spheroids were measured and analyzed.

Aside from basic fluorescence microscopy-based imaging techniques, advanced spectroscopic methods were used to quantify and localize spatial distribution and internalization of compounds in spheroids. Inductively coupled plasma mass spectrometry (ICP-MS) together with laser ablation (LA-ICP-MS) have been used to offer fast, sensitive, and selective tracking of a metal-based therapeutic supramolecular complex in human liver spheroids. After respective time points, retention and clearance of cerium oxide nanoparticles-based supramolecular complex in histological sections of HepG2 spheroids were analyzed using ICP-MS and LA-ICP-MS. These insights are of great importance for monitoring clearance mechanisms to understand the pharmacokinetics of the nanodrug. Additionally, cytotoxicity and anti-inflammatory effects of the supramolecular complex were investigated by ATP-based viability assay and ELISA. To characterize stability and composition, the morphology of the supramolecular complex, analytical approaches such as TEM, UV-Vis spectroscopy, dynamic light scattering (DLS), and differential scanning calorimetry (DSC) were applied.

In order to precisely manipulate spheroid size as a critical spheroid quality factor, a microfluidic spheroid platform was designed, developed, and fabricated by micromachining and soft-lithography techniques. The microfluidic multi-sized spheroid microarray was fabricated by double casting of the polymer PDMS using a computerized numerical control (CNC) milled master mold composed of polymethylmethacrylate (PMMA). The established spheroid chip technology could be operated without the need for any pump and relied on gravity-driven bi-directional perfusion. Flow speed was modulated by adjusting the tilting angle and speed of a

conventional laboratory rocker. Characterization of microfluidic flow characteristics was performed by Computational Fluid Dynamics (CFD) analysis and mathematical modelling. The established spheroid microarray was validated for its potential application in life science in terms of morphometric and metabolic parameters of multi-sized spheroids by using a bright-field and fluorescent live-cell imaging system under continuous perfusion for 12 days.

1.4 Overview of the Research Articles

1.4.1 Manuscript 1

Title: Optimized alamarBlue assay protocol for drug dose-response determination of 3D tumor spheroids.

Authors: Eilenberger C, Kratz SRA, Rothbauer M, Ehmoser EK, Ertl P, Küpcü S.

Published: *MethodsX*. 2018, 5, 781-787. doi: 10.1016/j.mex.2018.07.011.

Summary: The redox indicator dye alamarBlue® is a widely used commercially available bioassay to assess cellular viability in a single-step procedure. Since 3D spheroids cultures are more heterogeneous in proliferation states and diffusion barriers than 2D cultures, data interpretation is more challenging, and the performance of each bioassay has to be validated before screening. In this manuscript, the wide-used alamarBlue® proliferation/viability assay protocol was optimized to identify critical steps during assaying and enhance analysis precision for toxicological drug screening approaches.

Author contribution: Eilenberger C performed the measurements and processed the experimental data. Rothbauer M, Ehmoser EK, Ertl P, Küpcü S were involved in planning and supervised the work. Eilenberger C wrote the paper with input from all authors.

1.4.2 Manuscript 2

Title: Effect of spheroidal age on sorafenib diffusivity and toxicity in a 3D Hepg2 spheroid model.

Authors: Eilenberger C, Rothbauer M, Ehmoser EK, Ertl P, Küpcü S.

Published: *Scientific Reports*. 2019, 9(1), 4863. doi: 10.1038/s41598-019-41273-3.

Summary: Spheroid cultivation time or "spheroidal age" is considered a critical quality parameter that impacts drug diffusivity and toxicity in 3D cell culture models. HepG2 spheroids were generated and cultivated on a self-assembled ultra-low attachment nano-bio interface and characterized regarding time-resolved alterations in morphology, tissue-specific functionality as well as anti-cancer drug responses. It was demonstrated that spheroidal aging directly influences anti-cancer drug resistance due to a time-resolved progression of spheroid microarchitecture and tissue-specific functions that impact the outcome of drug uptake and efficacy studies.

Author contribution: Eilenberger C conceived experimental designs and performed experiments with Rothbauer M and Küpcü S. Eilenberger C analyzed data with support from Rothbauer M, Ehmoser EK, Ertl P and Küpcü S. Eilenberger C and Rothbauer M wrote the manuscript in consultation with Ehmoser EK, Ertl P, Küpcü S.

1.4.3 Manuscript 3

Title: Cytotoxicity, retention, and anti-inflammatory effects of a CeO_2 nanoparticle-based supramolecular complex in a 3D liver cell culture model.

Authors: Eilenberger C, Selinger F, Rothbauer M, Lin Y, Limbeck A, Schädl B, Grillari J, Kavok NS, Klochkov VK, Malyukin YV, Margitich V and Ertl P.

Published: *ASC Pharmacology and Translational Science*. 2021, 4(1), 101-106. doi: 10.1021/acsptsci.0c00170.

Summary: Time-resolved analysis by LA-ICP-MS of HepG2 spheroids revealed a spatiotemporal distribution of the supramolecular complex, including cerium oxide nanoparticles and mefenamic acid, and limited clearance from the internal spheroidal microtissue over eight days in cultivation. The results demonstrated the rapid uptake, distribution, and biostability of the supramolecular complex within the HepG2 liver spheroid model as well as a significant anti-inflammatory response at non-cytotoxic levels.

Author contribution: Eilenberger C, Selinger F, Lin Y, and Schädl B performed experiments and analyzed data with support from Rothbauer M, Limbeck A, Grillari J, Margitich V and Ertl P. Kavok NS, Klochkov VK, Malyukin YV designed and synthesized the supramolecular complex. The manuscript was written through contributions of all authors.

1.4.4 Manuscript 4

Title: A microfluidic multi-size spheroid array for multi-parametric screening of anti-cancer drugs and blood-brain barrier transport properties.

Authors: Eilenberger C, Rothbauer M, Selinger F, Gerhartl A, Jordan C, Harasek M, Schädl B, Grillari J, Weghuber J, Neuhaus W, Küpcü S, and Ertl P.

Published: *Advanced Science*. 2021, 202004856. doi: 10.1002/advs.202004856.

Summary: Variations in 3D spheroid size as a critical quality parameter and consequential altered cell responses often lead to non-reproducible and unpredictable pharmaceutical drug screening results. In this manuscript, a microfluidic platform is presented that accommodates up to 360 microtissues of five different dimensions in parallel in a microtiter-plate format, supporting a range of human tissue models, including liver, lung, colon, skin, and cell components of the blood-brain barrier (BBB). The presented device allows the testing of single and combinatorial anti-cancer drug doses in tumor spheroids as well as passive and active transport mechanisms in a 3D BBB model. Compatibility and throughput of the platform were validated to produce and measure multi-sized spheroids using high-content screening, accelerating optimization protocols of an *in vitro* model, and ultimately increasing predictive accuracy of pre-clinical drug screening.

Author contribution: Eilenberger C, Rothbauer M, Selinger F, Gerhartl A and Neuhaus W conceived and planned the experiments. Jordan C, Harasek M planned and carried out the simulations. Eilenberger C, Selinger F, Gerhartl A, Schädl B

performed the experiments. Eilenberger C analyzed the data and Rothbauer M, Selinger F, Gerhartl A, Neuhaus W, Grillari J Küpcü S, Weghuber J and Ertl P contributed to the interpretation of the results. Eilenberger C, Rothbauer M and Ertl P wrote the paper with input from all authors.

1.5 Scientific Contribution of the Dissertation and Conclusion

Implementing 3D spheroids in drug discovery can cut R&D costs, shorten development time, and achieve meaningful test results. Reproducibility is a prerequisite to yield comparable studies, but the degree to which the phenotype and growth of a specific cell type are altered is rarely adequately defined. In this thesis, critical spheroid quality parameters and analytical methods were validated and established to increase predictability in academic and industrial *in vitro* drug research.

To investigate the influence of assay time, a test protocol for determining drug dose responses of 3D tumor spheroids was optimized to increase assay reproducibility (Eilenberger *et al*, *MethodsX*, 2018). Since the formation of metabolic gradients and the diffusion barriers within 3D cell culture models can reduce the precision of bioassays, it is key to adapt viability tests to the respective cell model. The standard alamarBlue® protocol was validated and optimized to improve toxicological drug screening precision for 3D tumor spheroid cultures. It was shown that, in contrast to 2D cultures, assay precision increased tremendously by a 12-fold extension of alamarBlue® incubation time accompanied by a reduction of up to 88% to a standard deviation range of 4-10% and thus, increasing reliability of results.

Another article (Eilenberger *et al*, *Sci. Rep.*, 2019) showed, for the first time, that spheroidal aging represents a critical quality variable that influences the diffusivity and toxicity of clinical-relevant anti-cancer agent (sorafenib) in 3D cell culture models. It was presented that aging of tumor spheroids affects the effectiveness of the drug, which

was significantly indicated by a 4-fold change in IC_{50} values between early-stage and late-stage spheroids.

Next, an optimized hepatic spheroid model was used to study the potential cytotoxicity and anti-inflammatory effects as well as drug retention of a pre-clinical therapeutic cerium oxide nanoparticle-based supramolecular complex (Eilenberger *et al*, *ACS Pharmacol. Transl. Sci.*, 2021). The study was performed in cooperation with Farmak JSC, an international pharmaceutical company and manufacturer of therapeutic products. To assess nanoparticle distribution inside the 3D liver tissue, an LA-ICP-MS approach was employed to determine the spatiotemporal allocation of ^{140}Ce ions. A microtissue clearance study, performed by LA-ICP-MS in 3D spheroids in this regard for the first time, confirmed stable localization of cerium oxide nanoparticles in the tissue construct for eight days after treatment, lacking an effective clearance mechanism as demonstrated in several previous *in vivo* studies. These results showed that *in vitro* 3D spheroid models can serve as an alternative to animal testing at earlier stages of drug development.

To simulate the biological niche of a tissue or a tumor in the body as realistically as possible, one detrimental part of the dissertation involves the development of an *in vitro* 3D cell culture platform that enables the generation, cultivation, and analysis of a variety of spheroid sizes under high-content conditions (Eilenberger *et al*, *Adv. Sci.*, 2021). The presented biochip accommodated up to 360 spheroids on a microtiter-plate format and was validated for its potential in life science in terms of morphometric and metabolic analysis of four different well-established cancer and non-cancerous cell lines under continuous perfusion. As anti-cancer treatment and blood-brain barrier penetration are considered two areas of great interest in industrial and academic research, those applications serve as prime examples for spheroid size validation on-

chip. Results exhibited spheroid size-related IC_{50} values variations of 160% during the screening of the anti-cancer drugs cisplatin and doxorubicin. A further application includes compound uptake studies in a perfused BBB model on-chip, showing that smaller BBB-spheroids reveal an 80% higher compound penetration than larger spheroids, which revealed spheroid size-related changes on paracellular transport properties.

In conclusion, validation of 3D cell culture- and assay conditions would improve quality, efficacy, and usability in pre-clinical research, contributing to reduce drug attrition rates and unnecessary animal tests, following the 3R concept (Replacement, Reduction, Refinement). To accomplish these tasks, identification, and optimization of critical spheroid quality parameters would gain the relevance and acceptance of spheroids in drug discovery in simplifying complex 3D-cell-based readouts and techniques.

To date, official guidelines, methodologies, or quality standards for cultivating and testing spheroid or organoid cultures are not defined yet. Despite the elevated use of 3D cultures in basic research, no harmonization framework exists that outlines distinct guides to enhance the scientific comparability and reliability of advanced 3D cell systems. For instance, drug testing using organoids as an alternative to animal models in Europe is described in a very generic “Guideline on the principles of regulatory acceptance of 3Rs testing approaches” (EMA/CHMP/CVMP/JEG-3Rs/450091/2012) by the European Medicines Agency (EMA), that do not include specific quality parameters or methodologies for better harmonization.[171] In this context, improvements in bioprocess design and robust specifications of starting materials and

the critical quality attributes (CQA) in compliance with current good manufacturing practices (GMP) guidelines have to be established that covers all aspects of production, personnel, and documentation.

Widely accepted standardized protocols and guidelines are therefore considered essential tools to overcome current reliability issues reducing the variability of cellular systems from group to group. Consequently, a collective effort should be made to set clear guidelines for bringing the technology closer to the clinic.

To accelerate these processes in the future, data from spheroids, organoids, or organ-on-a-chips must be acknowledged by regulatory authorities as accepted pre-clinical models to obtain physiologically relevant data from early on and to support the use of those models.[172,173] Additionally, data acquired from spheroid/organoid cultures need to be validated using existing human data since differences between 3D and 2D models have already been shown in a variety of studies, however, only a small set of experiments confirmed that the efficacy and toxicity of drugs in 3D models could be related to a clinical context.[150,174,175]

In summary, the presented articles in this thesis contributed new insights into the quality control, analysis, production, and cultivation of 3D spheroids in pre-clinical drug development. This knowledge allows a better prediction and identification of possible sources of error in drug screening using 3D cultures in future experimental settings.

CHAPTER 2

Optimized alamarBlue Assay Protocol for Drug Dose-Response Determination of 3D Tumor Spheroids

MethodsX 5 (2018) 781–787

Contents lists available at ScienceDirect

MethodsX

journal homepage: www.elsevier.com/locate/mex

Protocol Article

Optimized alamarBlue assay protocol for drug dose-response determination of 3D tumor spheroids

Christoph Eilenberger[a,b], Sebastian Rudi Adam Kratz[a], Mario Rothbauer[a,*], Eva-Kathrin Ehmoser[b], Peter Ertl[a], Seta Küpcü[b]

[a] *Institute of Applied Synthetic Chemistry and Institute of Chemical Technologies and Analytics, Faculty of Technical Chemistry, Vienna University of Technology, Vienna Getreidemarkt 9/163, 1060 Vienna, Austria*
[b] *Institute of Synthetic Bioarchitectures, Department of Nanobiotechnology, University of Natural Resources and Life Sciences, Vienna, Muthgasse 11, 1190 Vienna, Austria*

A B S T R A C T

The assessment of drug-dose responses is vital for the prediction of unwanted toxicological effects in modern medicine. Three-dimensional (3D) cell cultures techniques can provide *in vivo*-like spheroids and microtissues that resemble natural tumor function. However, formation of necrotic core and diffusion limitation of chemical compounds within these models can reduce the reproducibility and precision of standard bioassay protocols used to test two-dimensional (2D) cell cultures. Nonetheless, the accurate prediction of detrimental effects of test compounds based on functional bioassays is essential for the development of new efficient therapeutic strategies. For instance, alamarBlue® is a widely-used commercially available redox indicator dye that can evaluate metabolic activity and cellular health status in a single-step procedure however, suitability and optimization of this bioassay must be determined for each individual application scenario. Here, we optimized the standard alamarBlue® proliferation/viability protocol for tumor spheroid cultures to enhance assay precision during toxicological drug screening.

We optimized the original protocol of alamarBlue® assay that usually suggests an incubation time of 2–4 hours. The key modifications of the protocol for spheroid cultures are as follows:

- Aspiration of cell culture medium before drug exposure.
- Replacement of drug-supplemented medium with 10% (v/v) alamarBlue® reagent mixed with culture medium.
- Increase of incubation period to 24 h at 37 °C protected from light.

* Corresponding author.
E-mail address: mario.rothbauer@tuwien.ac.at (M. Rothbauer).

https://doi.org/10.1016/j.mex.2018.07.011

ARTICLE INFO
Method name: AlamarBlue proliferation assay
Keywords: Cell culture, Tumor spheroids, AlamarBlue, Metabolic activity, Dose-response
Article history: Received 9 April 2018; Accepted 12 July 2018; Available online 23 July 2018

Specifications Table

Subject area	• *Pharmacology, Toxicology and Pharmaceutical Science*
More specific subject area	*Cell biology, Tissue engineering*
Method name	*AlamarBlue proliferation assay*
Name and reference of original method	[1–3]
Resource availability	https://www.thermofisher.com/at/en/home/references/protocols/cell-and-tissue-analysis/cell-profilteration-assay-protocols/cell-viability-with-alamarblue.html

Method details

Preparation and generation of spheroid cultures

Materials

- Cell culture facility equipped with a CO_2 incubator, laminar flow hood, bright-field microscope, a centrifuge and a cell counter.
- Plastic consumables: cell culture dishes and flasks, serological pipettes, syringes and centrifuge tubes.
- Hepatocellular carcinoma cells (HepG2).
- Cell culture medium: Minimal essential medium supplemented with 10% v/v of fetal bovine serum, 1%vol. of 20 mM L-glutamine and 1%vol. of 100 mM penicillin and streptomycin.
- Dulbecco's Phosphate Buffered Saline (PBS) 1X (pH 7.1–7.4).
- Trypsin-EDTA solution (0.25%).
- Trypan blue stain 0.4%.

Procedure

Cells taken for experiments should be at log-phase of growth, approx. 60–80 % confluent. Amounts of media given for 75 cm^2 cell culture flasks. All media applied to cells should be pre-warmed to 37 °C. (*Note*: Spheroid cultivation time, as well as morphology, can vary for different cell types. Therefore, initial cell seeding density should be pre-screened to identify the optimal cell density.)

1 Remove medium from cell culture. Wash the cells with PBS.
2 Detach cells using 5 mL trypsin solution. Incubate for at least 5 min at 37 °C until cells detach from the surface.
3 Add 5 mL of cell culture medium.
4 For trypsin removal transfer the suspension into 15 mL Falcon tube and centrifuge for 5 min at 294×*g*.
5 Gently remove supernatant and add 5 mL fresh medium.
6 Push the cell solution through a needle by using a syringe to dissociate larger aggregates into individual cells.
7 Mix 10 μL cell solution and 10 μL Trypan Blue in an Eppendorf tube and transfer 10 μL of the mix to a cell counter slide.

8 Measure cell number and viability and adjust the suspension to a cell density between 5.000 and 25.000 cells/mL.
9 For monolayer culture pipette 15.000 HepG2 cells/mL in each flat-bottom well of a tissue culture-treated 96-microwell plate.
10 For spheroid generation add 200 μL of cell suspension at a concentration of 15.000 cells/mL to each well of cell-repellant microwell plates. For our experiments, U-bottom 96-well plates were coated by a self-assembled anti-fouling nanobiointerface based on surface layer proteins as reported elsewhere [4,5].
11 Centrifuge the microwell plate for 10 min at 294 x g (*Note:* optional step; generates more uniformly shaped spherical spheroids for HepG2 cells).
12 Incubate cell cultures at 37 °C in 5% CO_2 humidified atmosphere for 6 days. (*Note:* Experiments showed that medium exchange has no influence on cell viability of the spheroid. Therefore, fresh medium has not to be added).

AlamarBlue® protocol for drug dose-response evaluation

To assess dose-dependent toxic effects on HepG2 cells, the FDA-approved anti-liver cancer drug sorafenib was chosen. The compound inhibits tumor-cell proliferation and tumor angiogenesis and increases the rate of apoptosis [6]. (*Note*: Drug-dose response can vary for different cell types and drugs therefore, different responses must be pre-screened for 2D and 3D cultures.)

Materials

- Spectroscopic plate reader, CO_2 incubator.
- Plastic consumables: cell culture microplates and flasks, serological pipettes, syringes.
- Cell culture media.
- Sorafenib Stock solution (1 mM) in DMSO.
- AlamarBlue® reagent.

Procedure

1 Sorafenib was stored as 10 mM aliquots in DMSO at −20 °C and diluted to a working concentration in respective cell culture medium before drug exposure of HepG2 spheroids.
2 For determining the effect of a test agent on cell growth, ensure correct controls are included (e.g. untreated control, background fluorescence of phenol-red containing-medium, background fluorescence of alamarBlue®-containing medium).
3 After cultivation time of 6 days, remove cell culture medium gently by syringe and add diluted test compounds to wells and incubate cells. (*Note:* Remove liquids gently by using a syringe. Be aware to hold the needle in the opposite direction of the spheroid otherwise, it can be aspirated or destroyed; Cultivation time can vary based on cell concentration and type and should be initially checked for spheroid uniformity and shape).
4 In our experiments, cells were treated with different concentrations of sorafenib (0–1000 μmol/L) in triplicates for 24 h.
5 Incubate cell cultures at 37 °C and 5% CO_2.
6 After incubation, aspirate compounds gently with a syringe to avoid interference with the proliferation assay due to physical cell damage.
7 Prepare fresh cell culture medium and add alamarBlue® in an amount equal to 10% of the total volume. Mix the alamarBlue® reagent by shaking.
8 Add 200 μL of alamarBlue® -containing medium mix to each well.
9 Incubate spheroid cell cultures for 24 h at 37 °C protected from light.
10 Measure cytotoxicity/proliferation using fluorescence spectrophotometry and read fluorescence at excitation wavelength of 560 nm and emission wavelength of 590 nm.

To calculate percent difference in reduction between treated and control cells in cytotoxicity/proliferation assays use the following formula:

$$\%\,\text{viability} = \frac{\text{Experimental RFU with chemical compound}}{\text{Untreated cell control RFU value}} \times 100$$

Qualitative evaluation of spheroid viability

Materials

- Inverted fluorescence microscope coupled with data analysis software.
- Syringe, needle, Eppendorf tubes.
- 4 mM Calcein acetoxymethyl (AM) in dimethyl sulfoxide (DMSO).
- 2 mM Ethidium- homodimer-1.
- PBS 1×.

Procedure

1 Mix 2 μL of 4 mM Calcein AM and 4 μL of 2 mM Ethidium homodimer-1 and fill up with PBS to a final volume of 1 mL.
2 After drug exposure, remove cell culture medium.
3 Wash spheroids with 200 μL PBS.
4 Remove the PBS gently by syringe.
5 Add 100 μL of the staining solution.
6 Incubate the cells for 30 min at 37 °C and protect from light.
7 Monitor live/dead cells by using a fluorescence microscope with respective fluorescence filter for Calcein AM (ex 485 nm, em 530 nm) and ethidium bromide EthD-1 (ex530 nm, em 645 nm).

Method validation

First, we tested spheroid uniformity as well as the response of the alamarBlue® assay for 2D cell culture and 3D spheroids viability measurements. Uniform HepG2 spheroid size was observable after centrifugation with a spheroid diameter of 887.3 ± 30 μm. In addition, HepG2 spheroids exhibited a

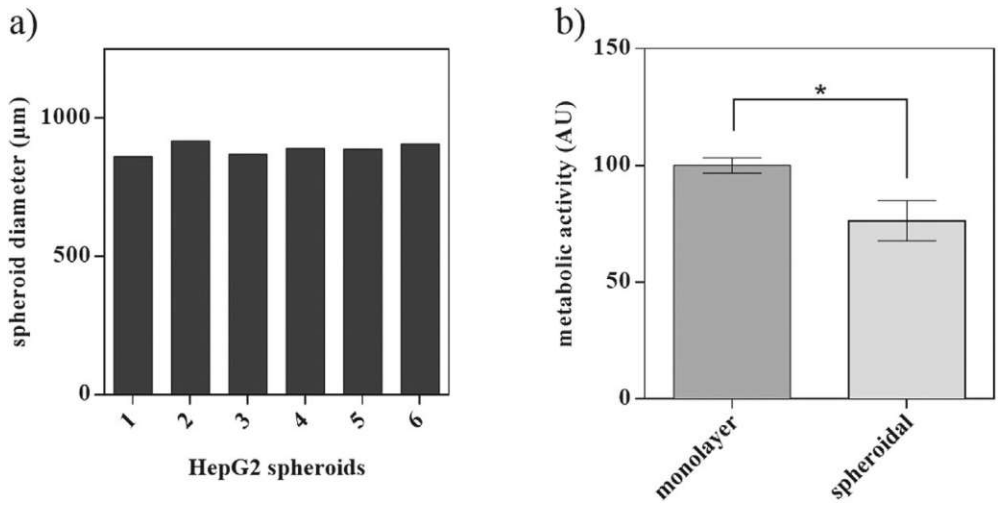

Fig. 1. (a) Uniformity of six different HepG2 spheroid samples at an initial seeding density of 15.000 cells/mL at day 6 post-seeding. (b) Metabolic activity of monolayer compared to spheroidal cultures after 4 h incubation with alamarBlue® at day 6 post-seeding (n = 3; *p < 0.05). Data points are expressed as mean values ± SD.

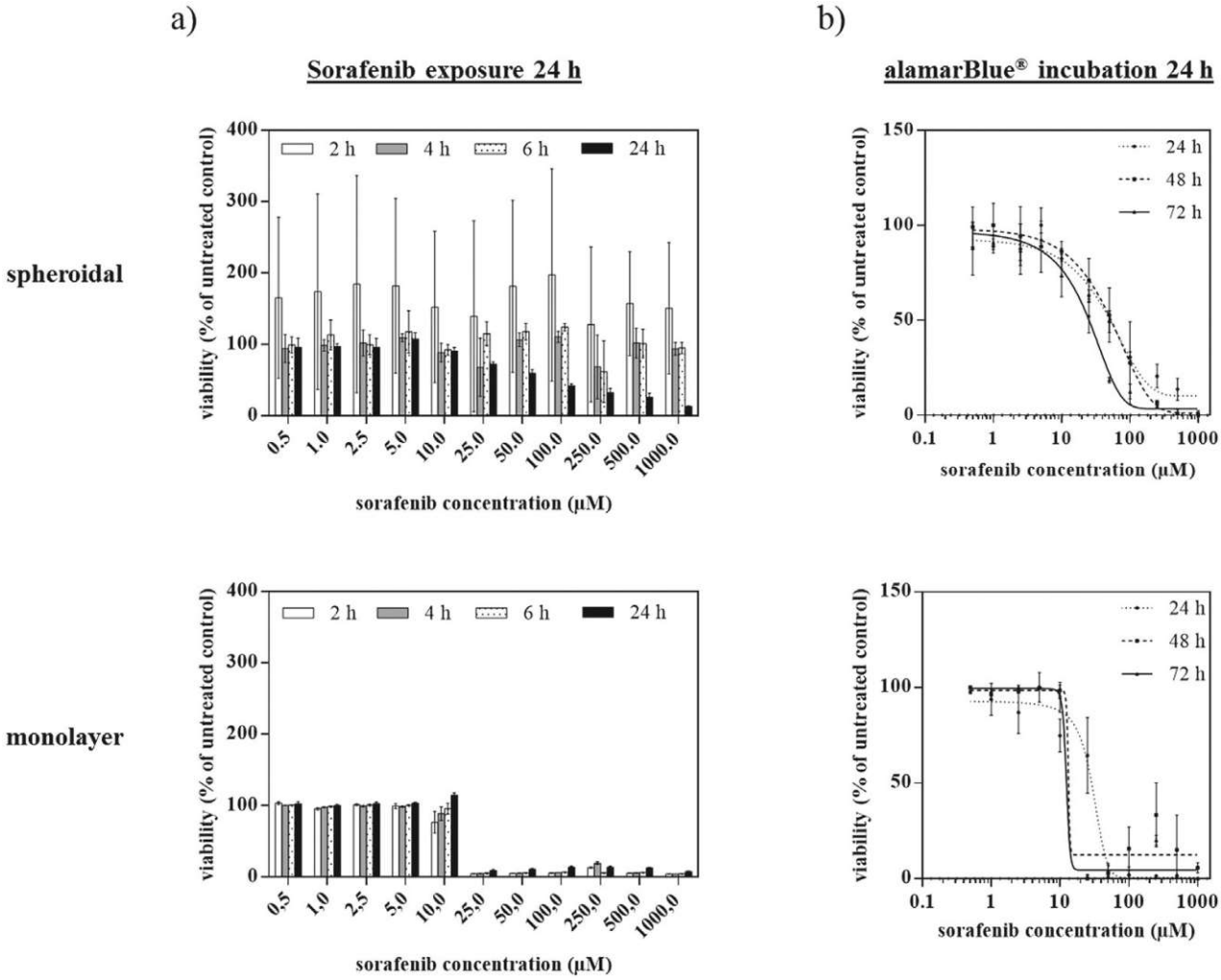

Fig. 2. (a) Sorafenib dose-response after 24 h of exposure for 2–24 h alamarBlue® incubation of HepG2 spheroids and monolayer cultures day 6 post-seeding (n = 3). (B) Dose-response of 24 h, 48 h and 72 h of HepG2 spheroid and monolayer cultures for sorafenib concentrations up to 1 mM using the optimized alamarBlue® assay protocol after day 6 post-seeding (n = 3). Data points are expressed as mean values ± SD.

24% decrease in metabolic activity compared to 2D cell culture after 4 h of incubation (Fig. 1). This effect stemming from spheroidal cultivation must be considered carefully for a comparative analysis of 2D and 3D cultures using alamarBlue® assay.

Next, we generated uniformly-sized HepG2 spheroids in 96-well microtiter plates and exposed them to several doses of the anti-liver cancer drug sorafenib. An alamarBlue® assay after 6 h and 24 h was performed to assess the influence of the incubation time on fluorescence intensity of HepG2 spheroids. Fig. 2 shows the measurement results comparing 2D monolayer with 3D spheroidal cultures of HepG2 cells. As shown in Fig. 2a, an extended incubation time of alamarBlue®-containing medium resulted in a significant improvement of assay reliability starting at a drug concentration of 50 µM ($p < 0.05$). It should also be noted that the assay precision increased tremendously by 12-fold extension of alamarBlue® incubation time with an overall reduction of standard deviation range to 4–10%. In comparison, 2D monolayer cultures displayed similar comparable precision and reliability for any alamarBlue® incubation time. Fig. 2b shows that optimization of the protocol for 3D spheroid cultures has a higher impact on the reliability and precision of the alamarBlue® bioassay than longer exposure to drugs. For instance, no significant difference was observable for HepG2 spheroids exposed to sorafenib concentrations below 250 µM ($p > 0.05$). In comparison, 2D monolayer cultures showed a significant difference in drug-dose response between 24 h and longer exposure times already around 10 µM. Overall, these results indicate that the optimized protocol

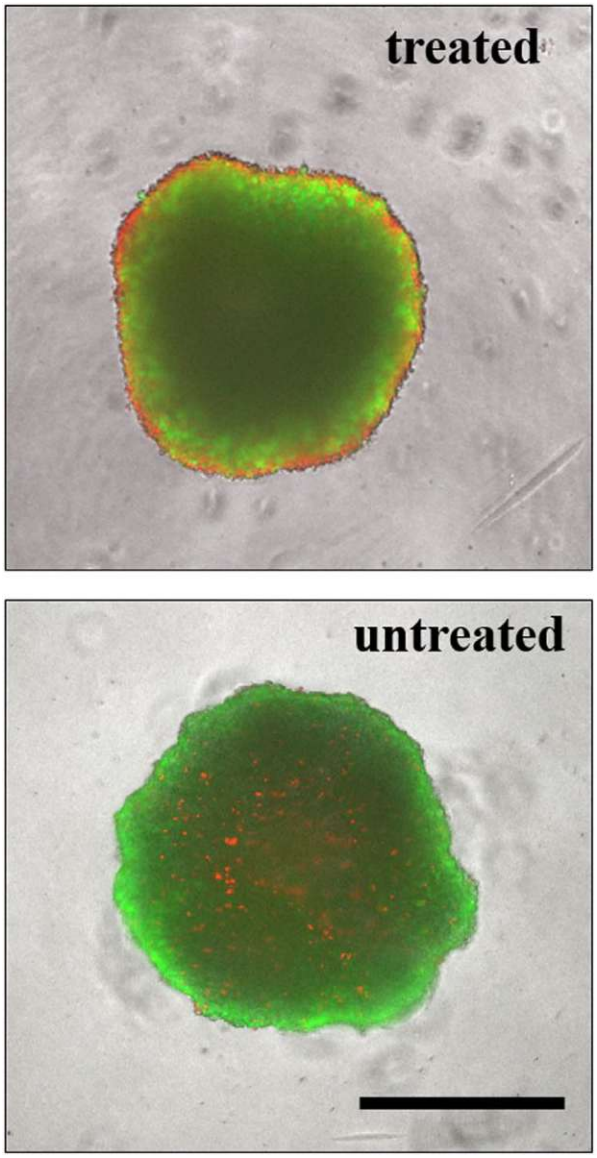

Fig. 3. Fluorescence images of 100 μM Sorafenib-treated (top panel) and untreated (bottom panel) HepG2 spheroids after 6 days post-seeding using a calcein AM (green fluorescence) and ethidium bromide (red fluorescence) LIVE/DEAD assay. Live cells are monitored green and dead cells red. Scale bar, 500 μm.

with an extension of incubation time to 24 h results in an improved and more reliable drug-dose response for 3D HepG2 spheroids. To confirm these viability results assayed by alamarBlue®, we compared the metabolic results with a LIVE/DEAD fluorescent viability kit. Fig. 3 shows morphological changes of HepG2 spheroids treated with 100 μM sorafenib for 24 h, analyzed with a LIVE/DEAD Viability/Cytotoxicity Kit for mammalian cells. The kit measures the cell viability based on the integrity of cell membranes similar to other dye-exclusion assays. The live cells are stained by Calcein AM, which emits green fluorescence light (517 nm) when excited by blue light (494 nm), while the dead cells are stained by Ethidium homodimer-1, which emit red fluorescence light (617 nm) when excited by green light (528 nm). Treated HepG2 spheroids displayed bright red fluorescent signal at the spheroid edges which corresponds to drug-induced apoptosis in comparison to untreated spheroids, which showed bright green fluorescent signal at the edges corresponding to living cell populations. Overall, this quantitative staining corresponds well with the optimized alamarBlue® assay protocol with a cell viability of 100 ± 9% for untreated and 42 ± 3% for treated HepG2 spheroids.

In summary, precise and reliable analysis of cell viability and proliferation for 3D cell cultures remains a challenging task. Here, we optimized the alamarBlue® assay standard protocol to result in a more precise and reliable assay for drug efficacy testing in spheroid cultures using an optimized fluorescence-based metabolic assay.

Acknowledgement

M.R. acknowledges the European Union's Horizon 2020 research and innovation program for funding under grant agreement No. 685817.

References

[1] J. O'Brien, I. Wilson, T. Orton, F. Pognan, Investigation of the Alamar Blue (resazurin) fluorescent dye for the assessment of mammalian cell cytotoxicity, Eur. J. Biochem. 267 (17) (2000) 5421–5426.
[2] G.R. Nakayama, M.C. Caton, M.P. Nova, Z. Parandoosh, Assessment of the Alamar Blue assay for cellular growth and viability in vitro, J. Immunol. Methods 204 (2) (1997) 205–208.
[3] R. Hamid, Y. Rotshteyn, L. Rabadi, R. Parikh, P. Bullock, Comparison of alamar blue and MTT assays for high through-put screening, Toxicol. In Vitro 18 (5) (2004) 703–710.
[4] M. Rothbauer, P. Ertl, B. Theiler, M. Schlager, U.B. Sleytr, S. Küpcü, Anisotropic crystalline protein nanolayers as multi-functional biointerface for patterned co-cultures of adherent and non-adherent cells in microfluidic devices, Adv. Mater. Interfaces 2 (1) (2015) 8020–8030.
[5] S. Moreno-Flores, S. Küpcü, 2D protein arrays induce 3D in vivo-like assemblies of cells, Soft Matter 11 (7) (2015) 1259–1264.
[6] J.C. Wei, F.D. Meng, K. Qu, Z.X. Wang, Q.F. Wu, L.Q. Zhang, Q. Pang, C. Liu, Sorafenib inhibits proliferation and invasion of human hepatocellular carcinoma cells via up-regulation of p53 and suppressing FoxM1, Acta Pharmacol. Sin. 36 (2) (2015) 241–251.

CHAPTER 3

Effect of Spheroidal Age on Sorafenib Diffusivity and Toxicity in a 3D HepG2 Spheroid Model

SCIENTIFIC REPORTS

OPEN

Effect of Spheroidal Age on Sorafenib Diffusivity and Toxicity in a 3D HepG2 Spheroid Model

Christoph Eilenberger[1,2], Mario Rothbauer[1], Eva-Kathrin Ehmoser[2], Peter Ertl[1] & Seta Küpcü[2]

Received: 23 July 2018
Accepted: 4 March 2019
Published online: 19 March 2019

The enhanced predictive power of 3D multi-cellular spheroids in comparison to conventional monolayer cultures makes them a promising drug screening tool. However, clinical translation for pharmacology and toxicology is lagging its technological progression. Even though spheroids show a biological complexity resembling native tissue, standardization and validation of drug screening protocols are influenced by continuously changing physiological parameters during spheroid formation. Such cellular heterogeneities impede the comparability of drug efficacy studies and toxicological screenings. In this paper, we demonstrated that aside from already well-established physiological parameters, spheroidal age is an additional critical parameter that impacts drug diffusivity and toxicity in 3D cell culture models. HepG2 spheroids were generated and maintained on a self-assembled ultra-low attachment nanobiointerface and characterized regarding time-dependent changes in morphology, functionality as well as anti-cancer drug resistance. We demonstrated that spheroidal aging directly influences drug response due to the evolution of spheroid micro-structure and organo-typic functions, that alter inward diffusion, thus drug uptake.

Despite the growing number of available anti-cancer drugs and various management regimes, some cancer types still remain without effective treatment strategies[1]. One of these cancer types is hepatocellular carcinoma (HCC), which is currently the second leading cause of cancer-related death with over 800.000 new cases diagnosed worldwide[2]. Even though, radiotherapy, resection, liver transplantation, and systemic chemotherapy represent the state-of-the-art treatment[3], 60% of patients are still relapsing after surgery due to the aggressiveness of hepatocellular carcinoma[4,5]. This high incident of cancer recurrence demands the development of novel and more effective anti-cancer drugs. During the drug development process cytotoxicity tests based on conventional two-dimensional (2D) *in vitro* cell-based followed by *in vivo* animal models and clinical trials are routinely performed to assess the efficacy of novel drug candidates[6]. Despite a large number of early drug candidates, only 10% of compounds progress successfully through clinical phases, with a high prevalence of drug failures at late-stage clinical trials, thus generating enormous expenses before discontinuation[7]. One reason for this unsatisfactory situation is based on the inability to reliable identify promising candidates for use in early-stage clinical trials[8]. It is generally accepted that the majority of drug failures in later stages are in part caused by overestimation of data derived from 2D *in vitro* cell culture tests, where the unnatural cellular microenvironment leads to alterations in drug response levels[9].

To overcome these drawbacks, one promising strategy is based on the establishment of three-dimensional (3D) cell cultures such as multi-cellular spheroids. These *in vivo*-like cell aggregates are surrounded by natural extra-cellular matrix (ECM) that promote direct cell-cell interaction, and thus recapitulate structures and functions of the native organs and tissue[10–12]. In cancer research, multi-cellular spheroids can be used to simulate intact human tumors featuring similar tissue architectures that are composed of cells of different phenotypes including proliferating, non-proliferating and necrotic subpopulations[13,14]. Since multi-cellular spheroids based on human-derived cells display adequate chemical and physical parameters influencing cell biology such as oxygen tension, compactness, apoptosis inhibition[15], damage repair[16], and permeability[17], they are also a good

[1]Institute of Applied Synthetic Chemistry and Institute of Chemical Technologies and Analytics, Faculty of Technical Chemistry, Vienna University of Technology, Getreidemarkt 9, 1060, Vienna, Austria. [2]Institute of Synthetic Bioarchitectures, Department of Nanobiotechnology, University of Natural Resources and Life Sciences, Vienna, Muthgasse 11, 1190, Vienna, Austria. Christoph Eilenberger and Mario Rothbauer contributed equally. Correspondence and requests for materials should be addressed to M.R. (email: mario.rothbauer@tuwien.ac.at) or P.E. (email: peter.ertl@tuwien.ac.at)

candidate to replace animal testing due to their improved predictive capability[18]. Any reduction of animal tests is not only ethically desirable but would also reduce one of the main cost-drivers in drug development process[19]. For these reasons, multi-cellular spheroids are extensively used as promising *in vitro* models for evaluating therapeutic anti-cancer strategies including chemotherapy[20,21], antibody-based immunotherapy[22], gene therapy[23] and combinatorial therapies[24].

Despite the many advantages of multi-cellular spheroids over monolayer cultures[25–28], some limitations still prevent the integration of 3D cell culture models into mainstream drug discovery pipelines. For instance, the lack of standardization in cell culture protocols often leads to variations in structure and composition of the established multi-cellular spheroids, all known to heavily affect the outcome of drug delivery and efficacy studies[29]. It is important to note that the selected culturing method significantly influences spheroid size, shape, density, surface topography and microstructure that may alter their behavior[30]. In addition to variations in structure, multi-cellular spheroids also comprise of cell populations in different proliferative stages including proliferation, quiescence and apoptosis, which leads to heterogeneous cell responses during chemical and physical treatments, thus making the comparability of drug exposure studies a difficult task[31,32].

To ensure reproducible generation of multi-cellular spheroids and to increase the reliability of *in vitro* 3D-cell based assays, a set of quality parameters including area, perimeter, solidity and roundness have been introduced to increase the reproducibility of toxicity tests, efficacy studies and drug penetration assessments[33]. Although the benefits of these quality parameters in multi-cellular spheroid cultures are well established, the influence of spheroid cultivation time, also referred to as spheroidal age, on dose-response relationships in drug screening studies still remains an underestimated factor. The present work sets out to provide a better understanding how spheroidal age influences the outcome of drug screening studies using multi-cellular spheroids. In the present work, we specifically investigate how spheroidal age modulates diffusivity, resistance and toxicity of sorafenib, an FDA-approved multi-kinase inhibitor against liver cancer. Our 3D hepatocellular carcinoma spheroid model is generated using a novel protein-based nanobiointerface that reliably eliminates cell-surface interactions over long periods of time. Our self-assembled nanobiointerface is based on the S-layer protein SbpA derived from *Lysinibacillus sphearicus* CCM 2177 and exhibits outstanding cell-repulsive and anti-fouling properties[34–36], thus effectively promoting the formation 3D HepG2 spheroids in microwells without the need of any external forces. We show that spheroid quality remains constant over 18 days in culture in the presence of SbpA-coated protein surfaces, while ultrastructural morphology and organo-specific metabolic evaluations are used to differentiate between early-stage, mid-stage and late-stage spheroids. Following the identification of spheroidal ages, drug diffusivity, toxicity and resistance are determined in an attempt to describe the interplay between spheroidal age and efficacy of drugs when employing *in vitro* 3D cell culture models.

Materials and Methods

S-layer Coating of Microwell Plates. Proteins were isolated from *Lysinibacillus sphaericus* CCM 2177 (SbpA) and subsequently purified as reported elsewhere[37]. To reconstitute the S-layer protein solution, 5 mg of lyophilized protein was dissolved in guanidine hydrochloride (5 M in 50 mM Tris-(hydroxymethyl)aminomethane x HCl buffer, pH 7.2) and dialyzed against Milli-Q-water (Millipore, Austria) for 1 h at 4 °C. Afterward, the protein solution was centrifuged at 1300 rpm for 15 min at 4 °C to remove self- assembly products. The concentration was adjusted to 100 μg/mL in a recrystallization buffer (0.5 mM Tris-(hydroxymethyl)aminomethane, 10 mM $CaCl_2$, pH 9), 250 μL of the solution were added to U-bottom 96-well tissue culture plates (Greiner-Bio-One, Austria) and incubated over night at room temperature.

Cell Culture and Spheroid Generation. Hepatocellular carcinoma cells (HepG2, HB-8065, ATCC, USA) were cultivated in minimal essential medium (MEM, Sigma-Aldrich, Austria) supplemented with 10% fetal bovine serum (FBS, Gibco, USA), 1% GlutaMax™ (Life Technologies, Thermo Fisher Scientific, USA) and 1% antibiotic/antimycotic solution (Sigma-Aldrich, Austria). The cells were cultivated in 75 cm^2 cell culture flasks at 37 °C in 5% CO_2 humidified atmosphere as adherent monolayers. For spheroid generation, trypsinized cells were pelleted at 1250 rpm for 5 min (Megastar 1.6R, VWR) prior homogenization through a syringe to separate larger cell clusters into individual cells. Cells were seeded at an initial cell concentration of 10.000, 5.000 and 3.000 cells per well in SbpA-coated 96-well microtiter plates (Greiner Bio-one, Germany) and centrifuged at 1250 rpm for 10 minutes.

Albumin and Urea Secretion. Spheroid medium supernatants of day 1, 3, 6, 9, 12, 15 and 18 were collected, centrifuged at 1250 rpm for 10 minutes to remove cell debris and stored at −20 °C until sample analysis. The amount of human serum albumin (HSA) secreted into the culture medium was determined by Human Albumin ELISA Kit (Abcam, UK) according to the manufacturer's protocol. For ELISA, the supernatant was diluted 1:100 in dilution buffer. Urea was measured using a colorimetric assay kit from BioVision (Germany) according to the manufacturer's protocol.

Cytochrome P_{450} 3A4 and metabolic activity. HepG2 spheroids at different incubation times (1, 3, 6, 9, 12, 15 and 18 days) were washed with 1X phosphate buffered saline (PBS; Sigma-Aldrich, Austria), 50 μL of 3 μM P450-Glo™ substrate (Promega, Germany) were added to individual microtissues and incubated for 1 hour at 37 °C, 5% CO_2. Then, 25 μL of substrate medium were transferred to a 96-white plate and CYP 3A4 activity was measured according to the manufacturer's protocol. The remaining microtissues were used to quantify spheroid viability by CellTiter-Glo® 3D Cell Viability Assay (Promega, Germany).

Transmission Electron Microscopy (TEM). Spheroids were fixed in 4% formaldehyde solution (Carl Roth, Austria) at 4 °C and embedded in agarose (2% in Caco buffer) as previously reported[38]. The ultrathin

sections were observed with a transmission electron microscope (FEI Tecnai G2 20, FEI, Netherlands) operating at 120 kV and images were acquired with an FEI Eagle 4 K camera (Nikon, Japan).

Histology. HepG2 spheroids were washed with 1X PBS (Sigma-Aldrich, Austria) after 3, 6, 12 and 18 days of incubation fixed with 4% paraformaldehyde in PBS (pH 7.6) at 4 °C and stored in PBS. For histological analysis, the HepG2 spheroids were cut in 3-μm serial sections, deparaffinized in xylene and rehydrated in a graded alcohol series. Histological staining was performed with hematoxylin and eosin (H&E).

For hypoxia-induced-factor-1α (HIF-1α) immunohistochemistry staining, rehydrated sections were placed in a rack filled with 10 mM sodium citrate buffer pH 6.0 (Sigma-Aldrich, Austria) and heated at 100 °C for 20 minutes by a vegetable steamer for antigen retrieval. Protein blocking was conducted by 5% BSA in 10X Tris-buffered saline pH 7.6 (TBS; Sigma-Aldrich, Austria) for 1 hour and incubated with primary anti-HIF-1α mAb (1:50; Abcam, Germany) at 4 °C overnight. Samples were washed 3X with TBS, followed by incubation with secondary antibody Alexa Fluor® 488 (1:200; Abcam, Germany) for one hour at room temperature. Nuclei were counterstained with DAPI (1:1000; Thermo-Fischer, Austria). Bright field images were acquired by bright field microscope (IX71, Olympus, Germany) equipped with a digital camera (XC10, Olympus, Germany) and Olympus IX 83 Live-cell microscope using DAPI (Ex: 350/Em: 470) and GFP (Ex: 488/Em: 519) fluorescence bandpass filters.

Drug Screening. For monolayer culture, HepG2 cells were seeded at 3.000 cells per well in 96-well flat bottom plates and incubated for 6 days. Prior drug exposure, the monolayer reached a confluency of approximately 80%. For 3D culture, S-layer coated 96-well U-bottom plates were seeded at a cell density of 3.000 cells per well and incubated for 6 days. Drug exposure was carried out with different concentrations of sorafenib diluted in DMSO. Cells were treated with different concentrations of sorafenib (0–100 μM) in triplicates and incubated for 24 and 48 hours at 37 °C and 5% CO_2. For analysis, AlamarBlue® reagent (Invitrogen, Austria) was added directly to medium (10% v/v) and incubated overnight at 37 °C. Fluorescence was measured at ex/em 560/595 nm and absorbance was measured at 565 nm and 595 nm (Infinite F200, Tecan, Austria). The cytotoxicity index was determined using the untreated cells as a negative control and the IC_{50} was extrapolated from the dose-response graph. For dose-age responses, HepG2 spheroids were treated with 100 μM sorafenib for 24 h up to 12 days of incubation.

Quantitative Live/Dead assay. For determination of spheroid viability, a fluorescence LIVE/DEAD® Viability/Cytotoxicity assay (Life Technologies, Austria) was used. Micrographs were taken by using an inverted fluorescence optical microscope (TE2000, Nikon, Japan) equipped with a digital camera (DS-Qi1MC, Nikon, Japan) using TRITC (Ex: 540/Em: 605) and GFP (Ex: 488/Em: 519) fluorescence bandpass filters.

Compound Diffusion. HepG2 spheroids were incubated for 3 and 12 days and treated with rhodamine B (Roth, Germany) diluted to a final concentration of 100 μM in cell culture media. Fluorescence micrographs were taken every minute to monitor diffusion towards the spheroid core until fluorescence intensity profile of the spheroid reached the same level as fluorescence background. Intensity values of spheroid at 3 different depths were taken using ImageJ (NIH, USA) and monitored over time.

Statistical and image analysis. Data were expressed as mean ± standard deviation (SD). All experiments were done independently in triplicates. Statistical significance among the experimental groups was determined with Student's t-test. A P value < 0.05 was considered statistically significant (*). Graphs were plotted using Prism 6 (GraphPad software, USA). Micrographs were analyzed using ImageJ (NIH, USA). Spheroid cultivation was monitored over 18 days with an inverted fluorescence optical microscope (TE2000, Nikon, Japan) equipped with a digital camera (DS-Qi1MC, Nikon, Japan). Spheroid area, perimeter, solidity roundness and diameter were measured by using the BioVoxxel Image Processing and Analysis Toolbox for ImageJ (Biovoxxel, Germany). Drug penetration distances were determined by analyzing the RGB profile of fluorescence micrographs using ImageJ (see also Fig. S3).

Results and Discussion

HepG2 spheroid formation and cultivation. Spheroid uniformity and quality including morphology, ultrastructure and organo-typic functionality are all crucial parameters and need to be optimized when using a novel protein-based cell-repulsive nanobiointerface for spheroid generation and long-term cultivation. Figure 1a shows the workflow used to generate the nanobiointerface inside the microtiter plate wells and generation of multi-cellular spheroids for drug toxicity measurements. Initial optimization investigates spheroid shape after 6 days in culture using increasing cell-seeding densities ranging from 3.000, 5.000 and 10.000 HepG2 cells per well. The dependence of spheroid shape on seeding density is illustrated in Fig. 1b where highest spheroid solidity and roundness (>0.9) is observed at a seeding density of 3.000 cells/well. Higher seeding densities resulted in inhomogeneous cell aggregates and unfavorable shape and size variations. Another important aspect of our dose-age relationship study is the long-term stability of HepG2 spheroids when cultivated over a period of 18 days on top of the self-assembled nanobiointerface. Results shown in Fig. 1c demonstrate that only in the presence of an initial seeding density of 3.000 cells per well no deformations in spheroid shape are obtained in long-term cultivations. As a result, the seeding density of 3.000 cells/well is chosen in the presence of our cell-repulsive protein nanobiointerface for all subsequent experiments.

Evaluation of HepG2 spheroids based on morphology. In a next set of experiments, additional key parameters of spheroid morphology including area, perimeter, solidity, roundness and diameter are monitored over a period of 18 days, as shown in Fig. 2.

At day 1 post-seeding individual HepG2 cells spontaneously self-assembled to an irregular shaped cell aggregate (see also Fig. 1c), exhibiting an area of 0.43 ± 0.027 mm^2, a perimeter of 6.31 ± 3.18 mm, a solidity of

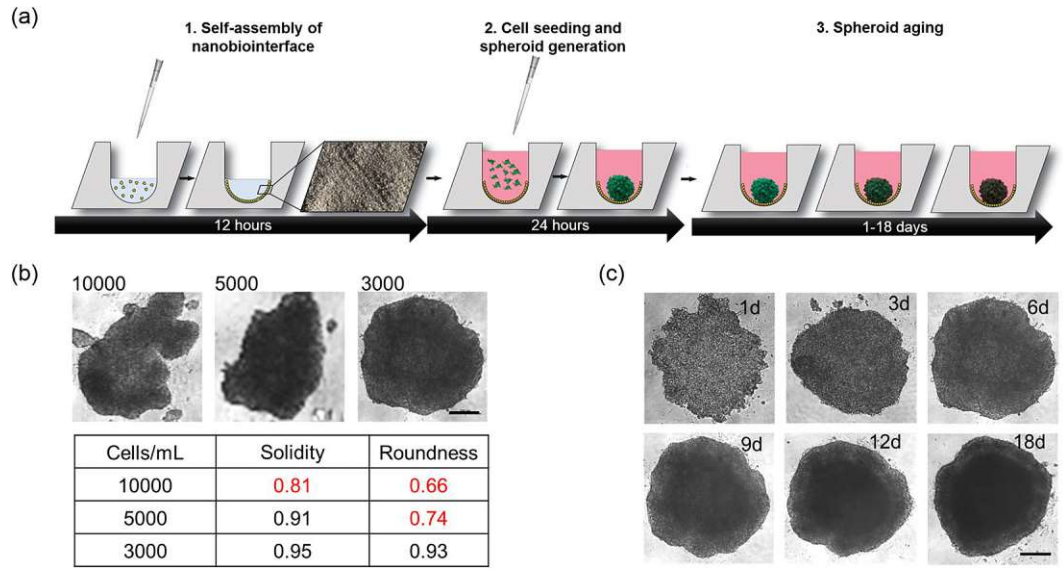

Cells/mL	Solidity	Roundness
10000	0.81	0.66
5000	0.91	0.74
3000	0.95	0.93

Figure 1. (**a**) Schematic workflow including time line of spheroid generation using self-assembled nanobiointerface. After seeding, cells form single multicellular spheroids for drug toxicity studies, based on different spheroid ages. (**b**) Phase-contrast optical micrographs show the impact of initial seeding density of HepG2 cells on spheroid solidity and roundness 6 days post-seeding. (**c**) Phase-contrast optical micrographs show the long-term evaluation of HepG2 spheroid shape at an initial seeding density of 3000 cells/well over a cultivation duration of 18 days. Scale bars, 200 µm.

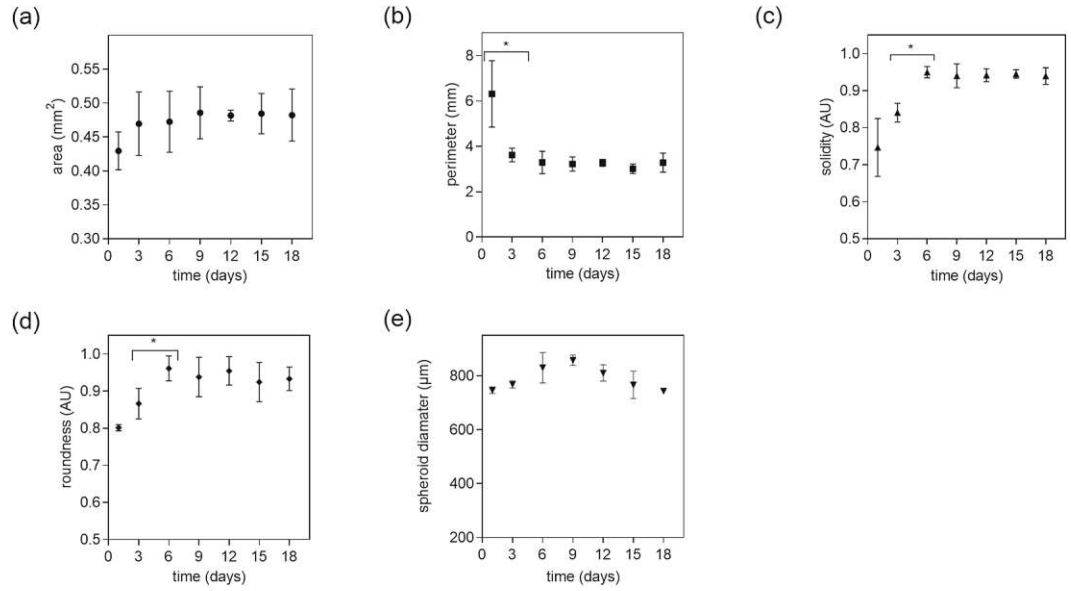

Figure 2. Influence of cultivation time on (**a**) area, (**b**) perimeter, (**c**) solidity (**d**) roundness and (**e**) diameter of HepG2 spheroids at a seeding density of 3000 cells/well. Error bars represent ± SD (n = 3) and *p < 0.05.

0.75 ± 0.25 and a roundness of 0.80 ± 0.01. At day 3 post-seeding spheroid area, solidity and roundness showed a slight increase, whereas a significant reduction in perimeter at the same time is observed ($p < 0.05$). The perimeter as an indicator for surface roughness decreased significantly within the first 3 days but remained constant over the remaining cultivation period. At day 6, a significant increase in spheroid solidity and roundness was noted, while perimeter and area remained at similar values (see Table S1). After day 6 no significant change in morphological parameters are evident ($p > 0.05$). Interestingly spheroid area did not increase significantly over time and remained in the range of 0.42 to 0.5 mm^2. These results reveal that proper spheroid shape is reached at day 6 post-seeding and remained constant for a period of 3 weeks. This initial decrease in spheroid perimeter to 3.29 mm ± 0.5 mm and simultaneous increase of solidity to 0.95 ± 0.02 and a roundness of 0.93 ± 0.02 is consistent with literature on well-shaped spheroids exhibiting a roundness and a solidity above 0.9[31]. Spheroid diameter increased for the first 9 days from 746 ± 12 µm to 857 ± 19 µm and stayed stable for the following days of culture

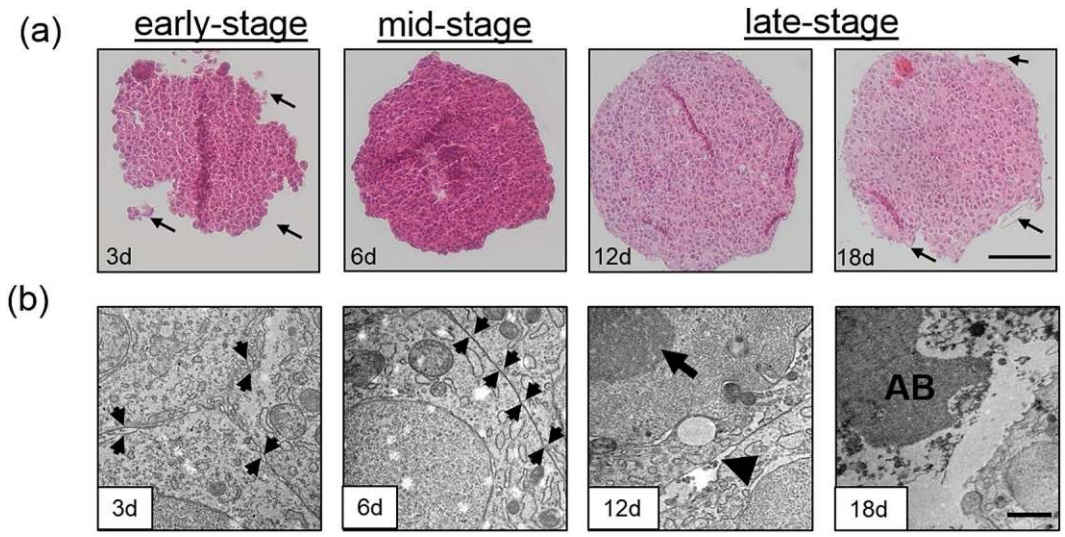

Figure 3. (**a**) Hematoxylin and eosin stained thin sections of early-stage spheroids at day 3 with loosely connected cell clusters (black arrows), mid-stage spheroids at day 6 with smooth spheroid surfaces and late-stage HepG2 spheroids starting at day 12 post-seeding with disintegrated spheroid surfaces (arrow). (**b**) Transmission electron microscopy micrographs of early-stage spheroids at day 3 with extracellular space between plasma membranes (black arrows), mid-stage spheroids at day 6 with tight junctions (black arrows) and late-stage HepG2 spheroids starting at day 12 post-seeding with blebbing of the cell surface (arrowhead), condensed chromatin (arrow) and apoptotic bodies (AB). Scale bar, 100 µm (top panel) and 1 µm (bottom panel).

with 810 ± 30 µm for day 12, respectively. At day 15 and 18 spheroid diameter decreased to 766 ± 51 µm and 743 ± 10 µm indicating the start of spheroid disintegration. In the context of our dose-age relationship study, we therefore defined early-stage, mid-stage and late-stage HepG2 spheroids based on obtained differences in perimeter, solidity and roundness between days 3 to 5, 6 to 12 and 15 to 18, respectively.

Histological and ultrastructural evaluation of HepG2 spheroid morphology. A known drawback of aged spheroids is necrotic core formation, which is an unwanted phenomenon resulting from the accumulation of metabolic waste products and insufficient diffusion of oxygen/nutrients starting at a spheroid diameter above 200 to 500 µm[39,40]. To assess the overall structural architecture, HepG2 spheroid solidity and compactness was investigated in more detail using histochemistry and transmission electron microscopy (TEM). Histological and ultra-structural analysis as shown Fig. 3a,b demonstrates that early-stage HepG2 spheroids are loosely packed cell clusters interstitial spaces between individual cells, while mid-stage spheroids (day 6) display tight cellular junctions and an overall condensed spherical morphology with intact and smooth outer spheroid surfaces. Importantly, both early-stage and mid-stage spheroids revealed equally distributed chromatin in the nucleus as well as intact cytoplasm, thus indicating viable HepG2 cells. In contrast, late-stage spheroids at day 18 displayed typical apoptotic characteristics with loss of integrity of the outermost lining layer, specialized inter- and intra-cellular structures such as cell-cell contacts, shrinking of cytoplasm, membrane blebbing and formation of membrane-bound apoptotic bodies[41]. Nuclear shrinking and chromatin condensation, also referred as pyknosis, is observed in the cell nucleus and represents a hallmark of apoptosis[42]. Additionally, disintegration of the outmost surface was observable for late-stage spheroids. These results further confirm our above definition of late-staged spheroids between days 12 and 18 in culture where the formation of necrotic cores in late-stage apoptotic spheroids takes place (see also Fig. S1).

Evaluation of secretion of organo-specific metabolites. In addition to spheroid morphology, their organo-specific functionality is also an essential indicator for physiologically relevant 3D cell culture models. It is important to highlight that native liver tissue shows a highly specialized architecture and unique organization on a cellular level with highly specialized intercellular structures, so-called bile canaliculi, which are formed by plasma membranes of adjoining cells accounting for 15% of hepatocyte's total plasma membrane surface[43]. To verify liver-specific ultrastructural intercellular morphology and metabolic functions of our HepG2 spheroids over an 18-day cultivation period, additional TEM measurements and metabolic assays were performed to assess the formation of bile canaliculi, albumin and urea secretion. Electron transmission microscopy results revealed that after day 6 post-seeding bile canaliculi with integrated luminal microvilli are present in mid and late-stage HepG2 spheroids as seen in Fig. 4a,b, while in early-stage spheroids only loosely associated cells are found that form softly packed aggregates lacking bile canaliculi. Both, mid-stage and late-stage spheroids displayed proper structural liver-specific phenotypes containing lumenized bile canaliculi that increase in diameter over time. In addition to the formation of specialized cellular structures, liver-specific metabolic activity including albumin secretion and urea excretion is evaluated in subsequent experiments. Since human CYP 3A4 has a major role in

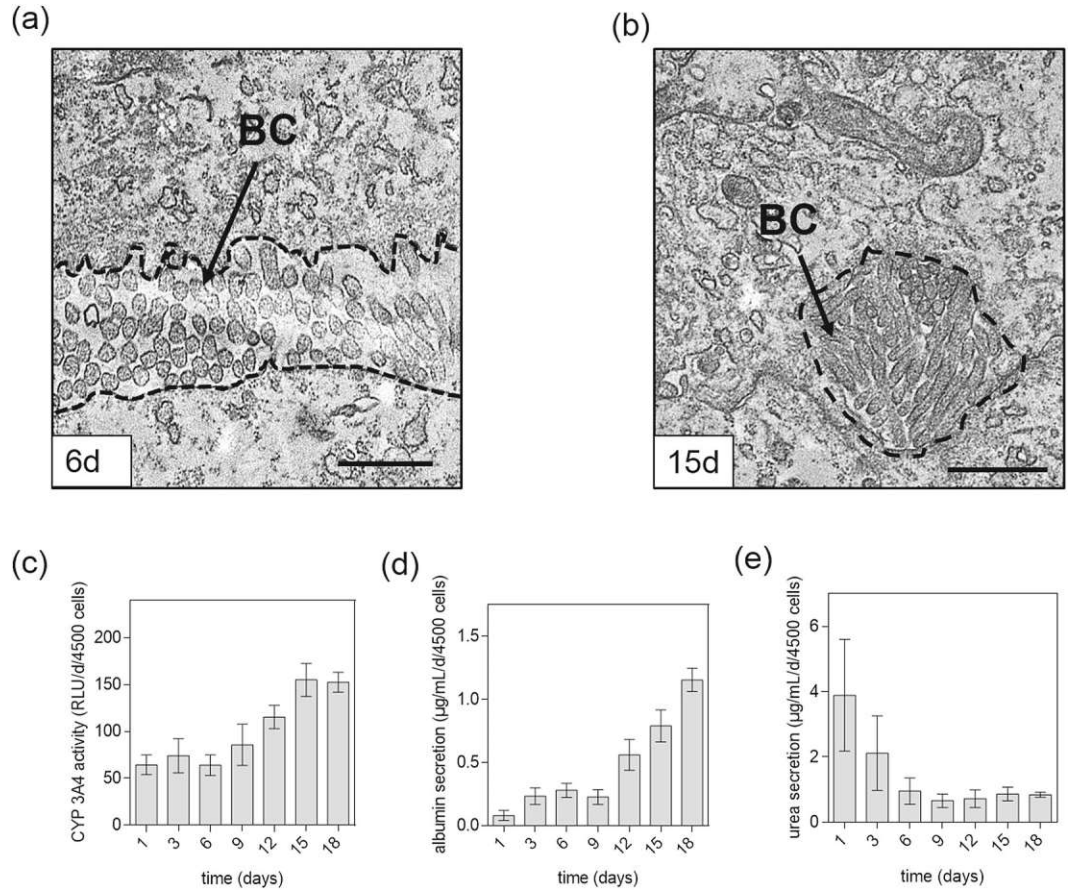

Figure 4. Transmission electron micrographs of HepG2 spheroids after (**a**) 6 days post-seeding and (**b**) 15 days post-seeding with organo-typic bile canaliculi (BC). Scale bars, 2 µm. (**c**) Activity of CYP 3A4 of HepG2 spheroids over time and secretion of (**d**) albumin and (**e**) urea of HepG2 spheroids over a cultivation period of 18 days. Error bars indicate ± SD (n = 3).

biotransformation and oxidation of bioactive compounds such as sorafenib[44], the liver-specific enzymatic activity of CYP 3A4 was additionally monitored over incubation time of 18 days. As shown in Fig. 4c, CYP 3A4 activity remained constant for HepG2 spheroids until day 6 around 69 ± 5 RLU per day and 4500 cells. An increase of enzymatic activity was observable between day 6 to day 15 by 3-fold whereas values for HepG2 spheroids for day 18 did not further increase. In addition, Fig. 4d shows that initially, HepG2 spheroids secreted very low levels of albumin with 0.08 ± 0.1 µg/mL, 0.23 ± 0.07 µg/mL, 0.28 ± 0.06 µg/mL and 0.23 ± 0.05 µg/mL per day at day 1 to day 9, while gradual increase of albumin secretion is obtained with mid-stage and late-stage spheroids peaking at 1.15 ± 0.10 µg/mL per day at day 18. In contrast to albumin, urea concentration as shown in Fig. 4e in the collected supernatant samples decreased gradually over 18 days exhibiting an average excretion rate between 0.84 and 0.94 µg/mL per day and 4500 cells for mid-stage and late-stage spheroids. Even though tissue architecture may be changing for central zones of late-stage spheroids, these functional liver-specific evaluations suggest that between day 9 and 18 HepG2 spheroids display increased liver-specific activity compared to early stages.

Since our spheroid evaluation study also indicated that in the presence of an initial cell seeding density of 3.000 cells per well, HepG2 spheroids can be considered as organo-typic starting at day 6 to day 9 post-seeding, differences in dose-response relationships between mid-stage HepG2 spheroids and 2D monolayer culture are examined in follow-on experiments. Both 2D and 3D liver cell culture models were exposed to increasing concentrations of sorafenib ranging from 0 µM to 100 µM for a period of 24 h and 48 h. Figure 5a shows the concentration-dependent inhibitory effects of sorafenib after 24 hours of drug exposure resulting in IC_{50} values for HepG2 spheroids and monolayer cultures of 47.77 ± 3.12 µM and 29.14 ± 1.14 µM, respectively. However, similar sorafenib dose-response curves are obtained for both HepG2 spheroids and 2D monocultures when exposure times are increased from 24 to 48 hours. Figure 5b shows cell viabilities in the presence of increasing sorafenib concentrations, exhibiting IC_{50} values 8.40 µM and 7.66 µM ($p > 0.05$) for spheroid and 2D monocultures, respectively. In other words, the required drug concentration necessary to inhibit 50% of the cells in HepG2 spheroids decreases from approximately 60 µM after 24 hours to 15 µM after 48 hours exposure, which translates to an overall 75% decrease. Following the same trend, an extended exposure time of 24 hours leads to a 95% decrease from 100 µM to 5 µM inhibitory concentration in the presence of 2D monolayer culture. Obtained IC_{50} values and p-values for both cell-culture methodologies are listed in Table 1 showing no statistical difference in growth inhibition after 48 hours. These results were also confirmed by Live/Dead viability assay based on Calcein AM and

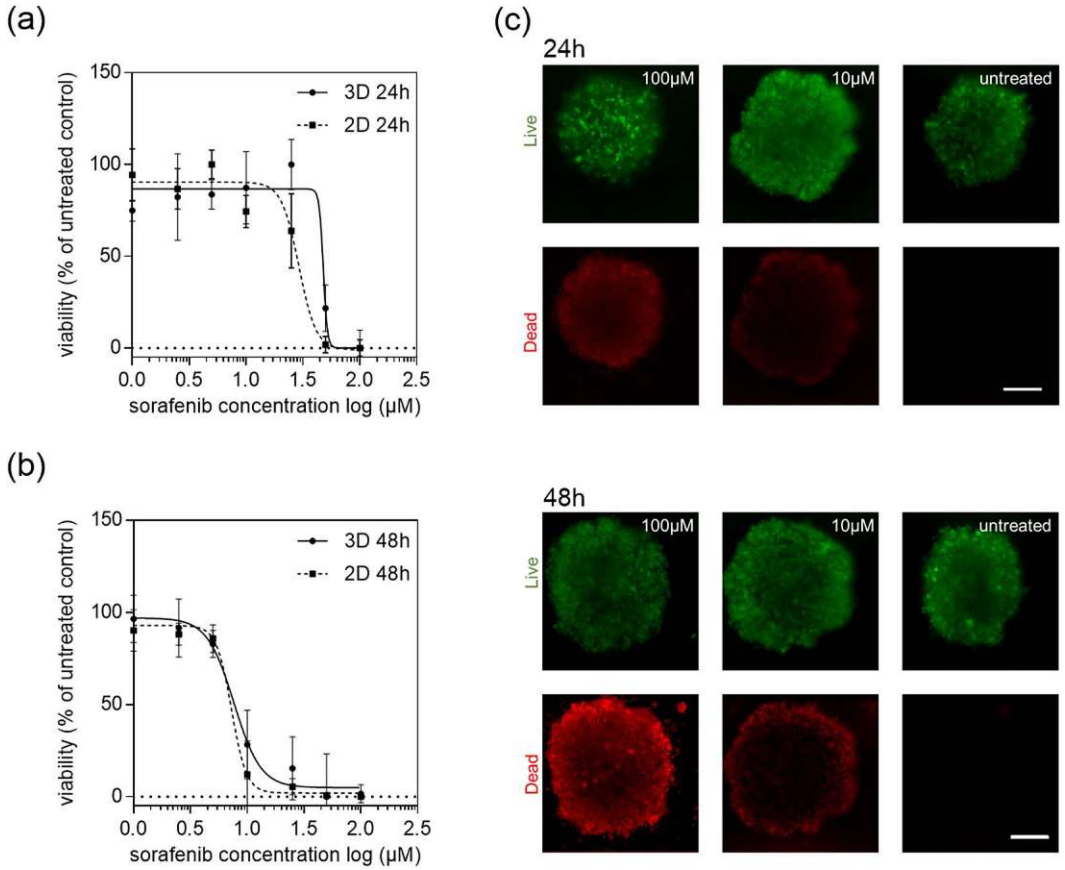

Figure 5. Sorafenib dose-response curves of HepG2 monolayers (2D) and spheroids (3D) after exposure time of (**a**) 24 hours and (**b**) 48 hours at day 6 post-seeding with (**c**) corresponding Live/Dead fluorescent micrographs. Error bars represent ± SD (n = 3).

Sorafenib exposure time (hours)	3D (µM)	2D (µM)	p-value
24	47.77 ± 3.12	29.14 ± 1.14	<0.05
48	8.40 ± 1.20	7.66 ± 1.02	>0.05

Table 1. Half-maximal inhibitory concentration (IC_{50}) of sorafenib for HepG2 spheroid (3D) and monolayer culture (2D) after 24 hours and 48 hours of drug exposure.

ethidium bromide as shown in Fig. 5c and compared to the dose-response behavior of HepG2 monolayer cultures (see Fig. S2 for Live/Dead images). This phenomenon can be attributed to several factors including (a) reduction of drug diffusivity into the spheroids, (b) the presence of quiescence cells and hypoxic areas within the core region of spheroids, (c) altered gene expression, (d) enhanced cell-cell contact and (e) the presence of ECM[45].

Next, the influence of spheroidal aging on drug diffusivity and resistance was investigated to gain a better understanding of the impact of culture time on drug efficacy. In a final set of experiments, early, mid-stage and late-stage HepG2 spheroids were subjected to a 24-hour treatment of 100 µM sorafenib. Results based on time-resolved monitoring of cell viability are shown in Fig. 6a where sorafenib toxicity reduced the viability of our HepG2 spheroids to 65%, 77%, 86% at day 3, 4, and 5 post-seeding in comparison to untreated controls (overall relative standard deviation, RSD = 6%, n = 6). Surprisingly, already during the transition phase from early-stage spheroids (day 3) to mid-stage spheroids (day 5) showed an increase in drug resistance and reduced toxicity. After a cultivation period of 5 days, mid-stage HepG2 spheroids displayed no significant cytotoxic effect of sorafenib with viability values of 90.80%, 96.30% and 100.13% over the following 6 days ($p > 0.05$, overall RSD = 10%, n = 9). Interestingly, these results correlate well with the emergence of organo-typic microstructures and increased metabolic activities that start with the emergence of spheroid maturity around day 6. To verify the importance of spheroidal age on the outcome of drug toxicity studies, a comparative analysis of dose-response relationships of sorafenib between early (day 3) and late-stage (day 12) spheroids were conducted in a final set of experiments. Figure 6b shows spheroid age-related dose-response curves obtained after 3 days and 12 days in culture resulting in elevated drug resistance to 100 µM sorafenib in late-stage spheroids.

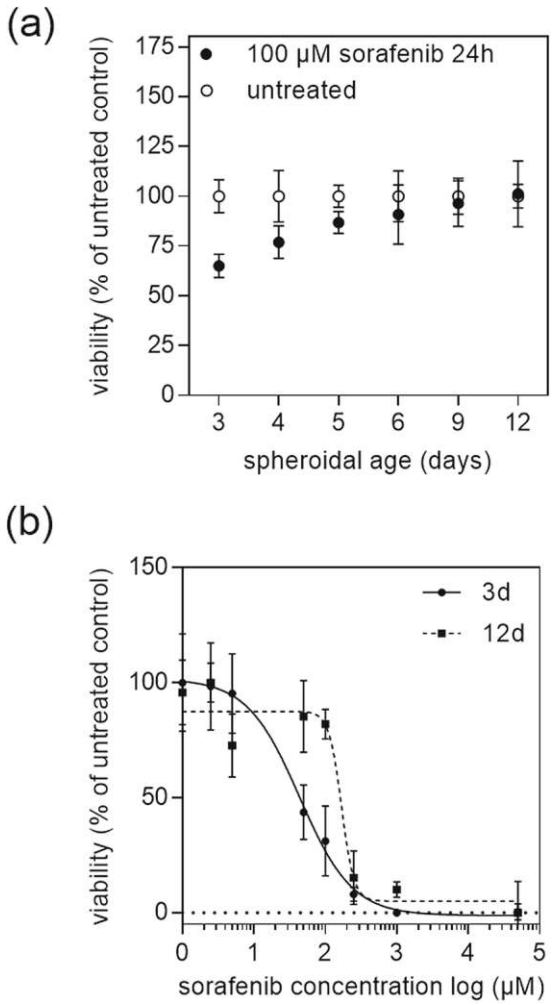

Figure 6. (**a**) Impact of spheroid age on viability of HepG2 spheroids after exposure to 100 µM sorafenib for 24 hours. (**b**) Sorafenib concentration-dependent response of 3 - and 12 days post-seeded HepG2 spheroids after an exposure period of 24 hours. Error bars represent ± SD (n = 3), *p < 0.05.

Spheroidal age (days)	Mean IC_{50} value (µM)	SD
3	43.75	±1.34
12	168.7	±1.26

Table 2. Dose-age dependence of 3D HepG2 spheroids after 3 -and 12 days post-seeding.

Additionally, IC_{50} values listed in Table 2 show that late-stage HepG2 spheroids displayed elevated IC_{50} values of 168.70 ± 1.26 µM in comparison to early HepG2 spheroids of 43.75 ± 1.34 µM. This means when using late-stage spheroid a 4-fold higher concentration of sorafenib needs to be applied to reach approximately 50% inhibition of the cells compared to an early-stage HepG2 spheroid.

To investigate this age-related effect in more detail, drug penetration depth of sorafenib was analyzed using a fluorescent dye-exclusion assay (e.g. Live/Dead cytotoxicity assay). Results from our drug penetration study show the formation of an apoptotic outer rim at a sorafenib concentration of 100 µM for early and late-stage HepG2 spheroids as seen in Fig. 7a. The observed apoptotic edge is caused by the strong cytotoxic effect of the drug on the outer-most cell layers since fluorescent intensity profile analysis of spheroid cross-sections shows highest intensities of dead cells (red channel for necrotic cells) near the outer rim of the spheroid and decreases gradually towards the spheroid core. Late-stage spheroids exhibit an even higher intensity at the rim caused by the more compact outer cell layers of otherwise properly formed spherical structures. However, when calculating the drug diffusion distance as a ratio between living and dead cells a significant decrease in diffusion distance from around 30 ± 3 µm in mid-stage spheroids (up to day 9) to 18 ± 2 µm for late-stage spheroids (after day 12 post seeding) is evident as shown in Fig. 7b. To quantify inward diffusion distance in more detail, rhodamine B was chosen as a model molecule that features molecular weight like sorafenib. As shown in Fig. 7d, early stage HepG2 spheroids display a 4.2-fold higher diffusivity towards molecules of molecular weight around 470–480 g/

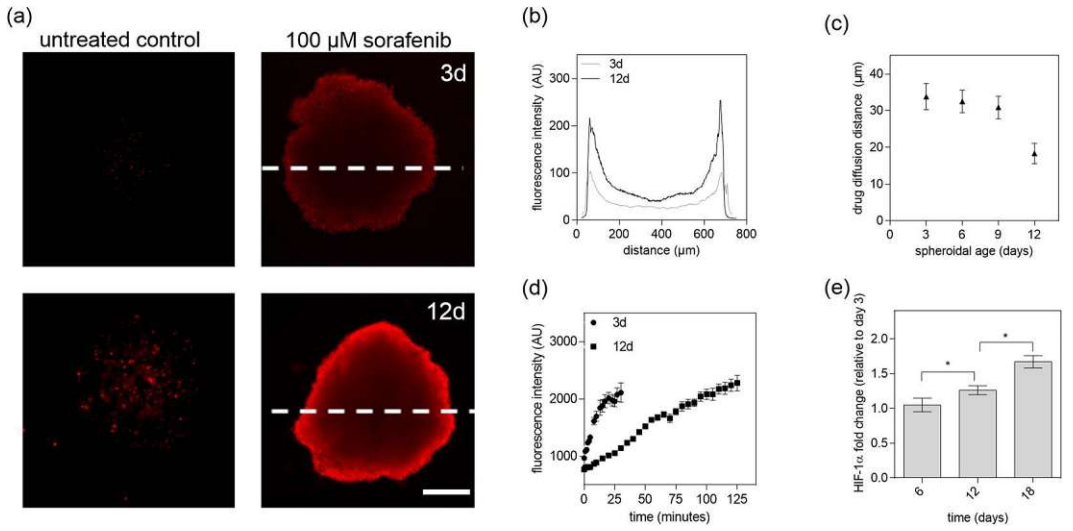

Figure 7. (**a**) Fluorescence images of early- (top panel) and late-stage (bottom panel) HepG2 spheroids with necrotic edges (red) after 24 hours of sorafenib exposure at a concentration of 0 µM and 100 µM. Scale bar, 200 µm. (**b**) Fluorescence intensity profile of early- and late-stage HepG2 spheroid images after treatment of 100 µM sorafenib for 24 hours. (**c**) Drug diffusion distance of sorafenib at a concentration of 100 µM after 24 hours exposure with respect to spheroidal age of HepG2 spheroids. Error bars represent ± SD (n = 4). (**d**) Inward diffusion of the fluorophore rhodamine B of early and late-stage HepG2 spheroids. (**e**) Fluorescence intensity fold change of HIF-1α immunohistochemical stained HepG2 spheroids relative to day 3 after cultivation time of 6, 12 and 18 days post-seeding. Error bars represent ± SD (n = 4) and *p < 0.05.

mol already plateauing after 30 and 125 minutes in the central core region of HepG2 spheroids respectively. In addition, further histochemical evaluation of central spheroid regions confirmed that HIF-1 positive hypoxic cells were gradually increasing with 100% hypoxia-positive cells at day 18 post-seeding (see Fig 7e and S4). Overall these results point at different penetration depths of bioactive compounds between early, mid-stage and late-stage spheroids, due to changes of organotypic architecture and function of HepG2 spheroids. This limited drug diffusion into the inner regions in aged tumor models significantly decreases the efficacy of chemotherapeutic drugs.

Conclusion

In vitro multi-cellular spheroid models have become a promising tool in drug discovery and development, but comparability and reproducibility remain a pressing issue. Additionally, the lack of standardization, scalability, and compatibility with current screening systems has led to large lab-to-lab discrepancies and inconsistent data outcome in drug studies even when using the same tissue type[46]. As a consequence, the reproducible generation of multi-cellular spheroids including shape, size, cell density and morphology, is key in increasing the reliability of *in vitro* 3D-cell based assays. In the present work, we have investigated the impact of spheroidal age on drug efficacy to gain a deeper understanding how methodological inconstancies influence the outcome of drug screening studies.

Using a protein-based nanobiointerface, we were able to establish HepG2 spheroids of similar size, shape and morphologies, while structural evaluation showed the formation of liver-specific morphologies over an 18-day cultivation period. Based on our ultrastructural and organo-typic functional investigations, distinctly different spheroid phases were identified including an early (day 3 to 6), mid-stage (day 6 to 12) and late stage (day 15 to 18) development. The three spheroidal development stages show significant differences in cell-to-cell interactions, specialized microstructures such as bile canaliculi formation, and metabolic activists including albumin and urea secretion. Results from our initial spheroidal aging study revealed a decreased sorafenib toxicity of following a 24-hour exposure with early, mid-stage and late-stage HepG2 spheroids. In fact, a 4-times higher sorafenib doses are needed to exhibit similar toxic effects in late-stage spheroids when compared to early-stage spheroids. To investigate this age-related effect in more detail, drug penetration depths were analyzed resulting in a significant decrease in diffusion distance from 31 ± 3 µm in mid-stage spheroids (up to day 9) to 18 ± 3 µm for late-stage spheroids. This phenomenon can be explained through intercellular interactions and physical limitations such as higher interstitial fluid pressure, which is known to restrict drug transport into deeper regions of the spheroid and thus leads to enhanced resistance to chemotherapeutics[33]. Additionally, increasing cell densities as natural diffusion barriers as well as biological limitations of complex *in vitro* models (e.g. apoptosis due to limited membranes permeability, an increasing acidic microenvironment and hypoxia in the central spheroid core regions)[47] have been linked to reduced efficacy of radio -and chemotherapies[48,49]. Independent of the reasons for the observed drug transport limitations, our study has clearly demonstrated that spheroidal age needs to be considered as an important variable for future drug sensitivity tests using spheroid-based *in vitro* models.

References

1. Savage, P. & Mahmoud, S. Development and economic trends in cancer therapeutic drugs: a 5-year update 2010–2014. *Br J Cancer* **112**, 1037–1041, https://doi.org/10.1038/bjc.2015.56 (2015).
2. Cidon, E. U. Systemic treatment of hepatocellular carcinoma: Past, present and future. *World J Hepatol* **9**, 797–807, https://doi.org/10.4254/wjh.v9.i18.797 (2017).
3. Gomaa, A. I. & Waked, I. Recent advances in multidisciplinary management of hepatocellular carcinoma. *World J Hepatol* **7**, 673–687, https://doi.org/10.4254/wjh.v7.i4.673 (2015).
4. Minagawa, M. *et al.* Extension of the frontiers of surgical indications in the treatment of liver metastases from colorectal cancer: long-term results. *Ann Surg* **231**, 487–499 (2000).
5. Nordlinger, B. *et al.* Surgical resection of colorectal carcinoma metastases to the liver. A prognostic scoring system to improve case selection, based on 1568 patients. Association Française de Chirurgie. *Cancer* **77**, 1254–1262 (1996).
6. Edmondson, R., Broglie, J. J., Adcock, A. F. & Yang, L. Three-dimensional cell culture systems and their applications in drug discovery and cell-based biosensors. *Assay Drug Dev Technol* **12**, 207–218, https://doi.org/10.1089/adt.2014.573 (2014).
7. DiMasi, J. A. & Grabowski, H. G. Economics of new oncology drug development. *J Clin Oncol* **25**, 209–216, https://doi.org/10.1200/JCO.2006.09.0803 (2007).
8. Ocana, A., Pandiella, A., Siu, L. L. & Tannock, I. F. Preclinical development of molecular-targeted agents for cancer. *Nat Rev Clin Oncol* **8**, 200–209, https://doi.org/10.1038/nrclinonc.2010.194 (2010).
9. Breslin, S. & O'Driscoll, L. Three-dimensional cell culture: the missing link in drug discovery. *Drug Discov Today* **18**, 240–249, https://doi.org/10.1016/j.drudis.2012.10.003 (2013).
10. O'Brien, L. E., Zegers, M. M. & Mostov, K. E. Opinion: Building epithelial architecture: insights from three-dimensional culture models. *Nat Rev Mol Cell Biol* **3**, 531–537, https://doi.org/10.1038/nrm859 (2002).
11. Sutherland, R. M. Cell and environment interactions in tumor microregions: the multicell spheroid model. *Science* **240**, 177–184 (1988).
12. Hagios, C., Lochter, A. & Bissell, M. J. Tissue architecture: the ultimate regulator of epithelial function? *Philos Trans R Soc Lond B Biol Sci* **353**, 857–870, https://doi.org/10.1098/rstb.1998.0250 (1998).
13. Teicher, B. A. *et al.* Tumor resistance to alkylating agents conferred by mechanisms operative only *in vivo*. *Science* **247**, 1457–1461 (1990).
14. Kobayashi, H. *et al.* Acquired multicellular-mediated resistance to alkylating agents in cancer. *Proc Natl Acad Sci USA* **90**, 3294–3298 (1993).
15. Frankel, A., Buckman, R. & Kerbel, R. S. Abrogation of taxol-induced G2-M arrest and apoptosis in human ovarian cancer cells grown as multicellular tumor spheroids. *Cancer Res* **57**, 2388–2393 (1997).
16. Dubessy, C., Merlin, J. M., Marchal, C. & Guillemin, F. Spheroids in radiobiology and photodynamic therapy. *Crit Rev Oncol Hematol* **36**, 179–192 (2000).
17. Kim, T. H., Mount, C. W., Gombotz, W. R. & Pun, S. H. The delivery of doxorubicin to 3-D multicellular spheroids and tumors in a murine xenograft model using tumor-penetrating triblock polymeric micelles. *Biomaterials* **31**, 7386–7397, https://doi.org/10.1016/j.biomaterials.2010.06.004 (2010).
18. Knight, A. Systematic reviews of animal experiments demonstrate poor contributions toward human healthcare. *Rev Recent Clin Trials* **3**, 89–96 (2008).
19. Astashkina, A., Mann, B. & Grainger, D. W. A critical evaluation of *in vitro* cell culture models for high-throughput drug screening and toxicity. *Pharmacol Ther* **134**, 82–106, https://doi.org/10.1016/j.pharmthera.2012.01.001 (2012).
20. Durand, R. E. & Olive, P. L. Resistance of tumor cells to chemo- and radiotherapy modulated by the three-dimensional architecture of solid tumors and spheroids. *Methods Cell Biol* **64**, 211–233 (2001).
21. Yip, D. & Cho, C. H. A multicellular 3D heterospheroid model of liver tumor and stromal cells in collagen gel for anti-cancer drug testing. *Biochem Biophys Res Commun* **433**, 327–332, https://doi.org/10.1016/j.bbrc.2013.03.008 (2013).
22. Herter, S. *et al.* A novel three-dimensional heterotypic spheroid model for the assessment of the activity of cancer immunotherapy agents. *Cancer Immunol Immunother* **66**, 129–140, https://doi.org/10.1007/s00262-016-1927-1 (2017).
23. Deng, X. B. *et al.* Inhibition of mesothelioma cancer stem-like cells with adenovirus-mediated NK4 gene therapy. *Int J Cancer* **137**, 481–490, https://doi.org/10.1002/ijc.29391 (2015).
24. Kashif, M. *et al. In vitro* discovery of promising anti-cancer drug combinations using iterative maximisation of a therapeutic index. *Sci Rep* **5**, 14118, https://doi.org/10.1038/srep14118 (2015).
25. Sutherland, R., Carlsson, J., Durand, R. & Yuhas, J. Spheroids in Cancer Research. *Cancer Research* **41**, 2980–2984, https://doi.org/10.1007/978-3-642-82340-4 (1981).
26. Bertuzzi, A., Fasano, A., Gandolfi, A. & Sinisgalli, C. Necrotic core in EMT6/Ro tumour spheroids: Is it caused by an ATP deficit? *J Theor Biol* **262**, 142–150, https://doi.org/10.1016/j.jtbi.2009.09.024 (2010).
27. Achilli, T. M., McCalla, S., Meyer, J., Tripathi, A. & Morgan, J. R. Multilayer spheroids to quantify drug uptake and diffusion in 3D. *Mol Pharm* **11**, 2071–2081, https://doi.org/10.1021/mp500002y (2014).
28. Bokhari, M., Carnachan, R. J., Cameron, N. R. & Przyborski, S. A. Culture of HepG2 liver cells on three dimensional polystyrene scaffolds enhances cell structure and function during toxicological challenge. *J Anat* **211**, 567–576, https://doi.org/10.1111/j.1469-7580.2007.00778.x (2007).
29. Hoffmann, O. I. *et al.* Impact of the spheroid model complexity on drug response. *J Biotechnol* **205**, 14–23, https://doi.org/10.1016/j.jbiotec.2015.02.029 (2015).
30. Härmä, V. *et al.* Quantification of dynamic morphological drug responses in 3D organotypic cell cultures by automated image analysis. *PLoS One* **9**, e96426, https://doi.org/10.1371/journal.pone.0096426 (2014).
31. Zanoni, M. *et al.* 3D tumor spheroid models for *in vitro* therapeutic screening: a systematic approach to enhance the biological relevance of data obtained. *Sci Rep* **6**, 19103, https://doi.org/10.1038/srep19103 (2016).
32. Mellor, H. R. *et al.* The influence of tumour microenvironmental factors on the efficacy of cisplatin and novel platinum(IV) complexes. *Biochem Pharmacol* **70**, 1137–1146, https://doi.org/10.1016/j.bcp.2005.07.016 (2005).
33. Gong, X. *et al.* Generation of Multicellular Tumor Spheroids with Microwell-Based Agarose Scaffolds for Drug Testing. *PLoS One* **10**, e0130348, https://doi.org/10.1371/journal.pone.0130348 (2015).
34. Moreno-Flores, S. & Küpcü, S. 2D protein arrays induce 3D *in vivo*-like assemblies of cells. *Soft Matter* **11**, 1259–1264, https://doi.org/10.1039/c4sm02278e (2015).
35. Rothbauer, M., Küpcü, S., Sticker, D., Sleytr, U. B. & Ertl, P. Exploitation of S-layer anisotropy: pH-dependent nanolayer orientation for cellular micropatterning. *ACS Nano* **7**, 8020–8030, https://doi.org/10.1021/nn403198a (2013).
36. Rothbauer, M. *et al.* Anisotropic Crystalline Protein Nanolayers as Multi- Functional Biointerface for Patterned Co-Cultures of Adherent and Non-Adherent Cells in Microfluidic Devices. *Advanced Materials Interfaces* **2**, 8020–8030, https://doi.org/10.1002/admi.201400309 (2015).
37. Ilk, N. *et al.* Molecular characterization of the S-layer gene, sbpA, of Bacillus sphaericus CCM 2177 and production of a functional S-layer fusion protein with the ability to recrystallize in a defined orientation while presenting the fused allergen. *Appl Environ Microbiol* **68**, 3251–3260 (2002).
38. Ucisik, M. H., Küpcü, S., Debreczeny, M., Schuster, B. & Sleytr, U. B. S-layer coated emulsomes as potential nanocarriers. *Small* **9**, 2895–2904, https://doi.org/10.1002/smll.201203116 (2013).

39. Nath, S. & Devi, G. R. Three-dimensional culture systems in cancer research: Focus on tumor spheroid model. *Pharmacol Ther* **163**, 94–108, https://doi.org/10.1016/j.pharmthera.2016.03.013 (2016).
40. Hirschhaeuser, F. *et al*. Multicellular tumor spheroids: an underestimated tool is catching up again. *J Biotechnol* **148**, 3–15, https://doi.org/10.1016/j.jbiotec.2010.01.012 (2010).
41. Krysko, D. V., Vanden Berghe, T., D'Herde, K. & Vandenabeele, P. Apoptosis and necrosis: detection, discrimination and phagocytosis. *Methods* **44**, 205–221, https://doi.org/10.1016/j.ymeth.2007.12.001 (2008).
42. Elmore, S. Apoptosis: a review of programmed cell death. *Toxicol Pathol* **35**, 495–516, https://doi.org/10.1080/01926230701320337 (2007).
43. Boyer, J. L. Bile formation and secretion. *Compr Physiol* **3**, 1035–1078, https://doi.org/10.1002/cphy.c120027 (2013).
44. Ghassabian, S. *et al*. Role of human CYP3A4 in the biotransformation of sorafenib to its major oxidized metabolites. *Biochem Pharmacol* **84**, 215–223, https://doi.org/10.1016/j.bcp.2012.04.001 (2012).
45. Yamada, K. M. & Cukierman, E. Modeling tissue morphogenesis and cancer in 3D. *Cell* **130**, 601–610, https://doi.org/10.1016/j.cell.2007.08.006 (2007).
46. Haibe-Kains, B. *et al*. Inconsistency in large pharmacogenomic studies. *Nature* **504**, 389–393, https://doi.org/10.1038/nature12831 (2013).
47. Brown, J. M. & Giaccia, A. J. The unique physiology of solid tumors: opportunities (and problems) for cancer therapy. *Cancer Res* **58**, 1408–1416 (1998).
48. Lyng, H., Haraldseth, O. & Rofstad, E. K. Measurement of cell density and necrotic fraction in human melanoma xenografts by diffusion weighted magnetic resonance imaging. *Magn Reson Med* **43**, 828–836 (2000).
49. Méndez-Blanco, C., Fondevila, F., García-Palomo, A., González-Gallego, J. & Mauriz, J. L. Sorafenib resistance in hepatocarcinoma: role of hypoxia-inducible factors. *Exp Mol Med* **50**, 134, https://doi.org/10.1038/s12276-018-0159-1 (2018).

Acknowledgements
The authors acknowledge the TU Wien University Library for financial support through its Open Access Funding Program. The authors thank Andrea Scheberl for preparing the ultra-thin sections for transmission electron microscopic investigations. We also thank Heinz Redl, the Ludwig-Boltzmann Institute of Experimental and Clinical Traumatology and especially, Barbara Schädl for preparing the histological sections.

Author Contributions
C.E., M.R., S.K. and P.E. conceived the experiments; C.E., M.R. and S.K. performed the experiments; C.E., M.R. and S.K. analyzed the data; C.E., M.R., E.-K.E., S.K. and P.E. conceived wrote the manuscript.

Additional Information
Supplementary information accompanies this paper at https://doi.org/10.1038/s41598-019-41273-3.

Competing Interests: The authors declare no competing interests.

Publisher's note: Springer Nature remains neutral with regard to jurisdictional claims in published maps and institutional affiliations.

Supplementary Information

Effect of Spheroidal Age on Sorafenib Diffusivity and Toxicity in a 3D HepG2 Spheroid Model

Christoph Eilenberger, Mario Rothbauer, Eva-Kathrin Ehmoser, Peter Ertl and Seta Küpcü

Supplementary Table 1: HepG2 spheroid shape evolution over time at an initial seeding density of 3000 cells per well. After day 6 post-seeding the cell aggregates can be considered as compact spherical spheroids (>0.9). Values above 0.9 are displayed in red.

Day	Area (mm^2)	Perimeter (mm)	Solidity	Roundness
1	0.43	6.31	0.75	0.80
3	0.47	3.62	0.84	0.87
6	0.47	3.29	0.95	0.93
9	0.49	3.22	0.94	0.94
12	0.48	3.28	0.94	0.95
18	0.48	3.28	0.94	0.93

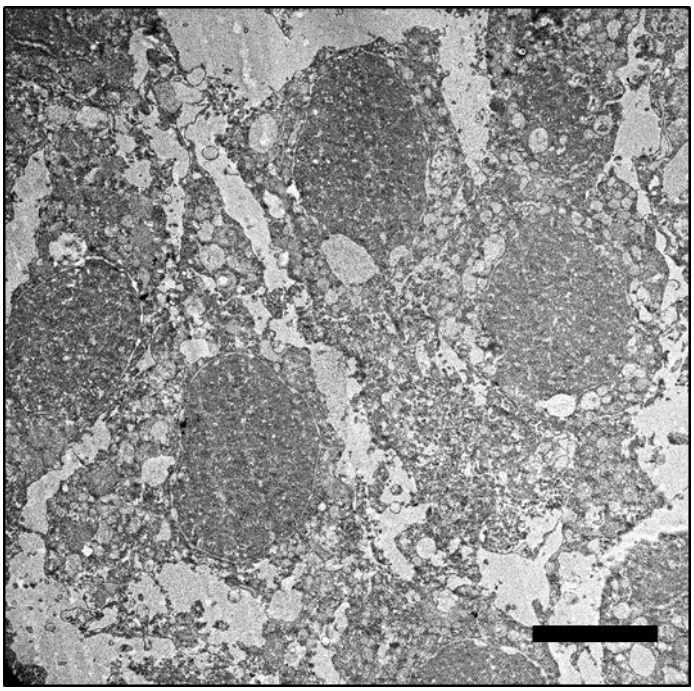

Figure S1: Transmission electron microscopy micrograph of late-stage HepG2 spheroids at day 18 post-seeding with extruded cell fragments, indicating apoptosis. Based on this observation, very late-stage spheroids were considered as apoptotic and not taken into account for following age-drug response experiments. Scale bar, 5 µm.

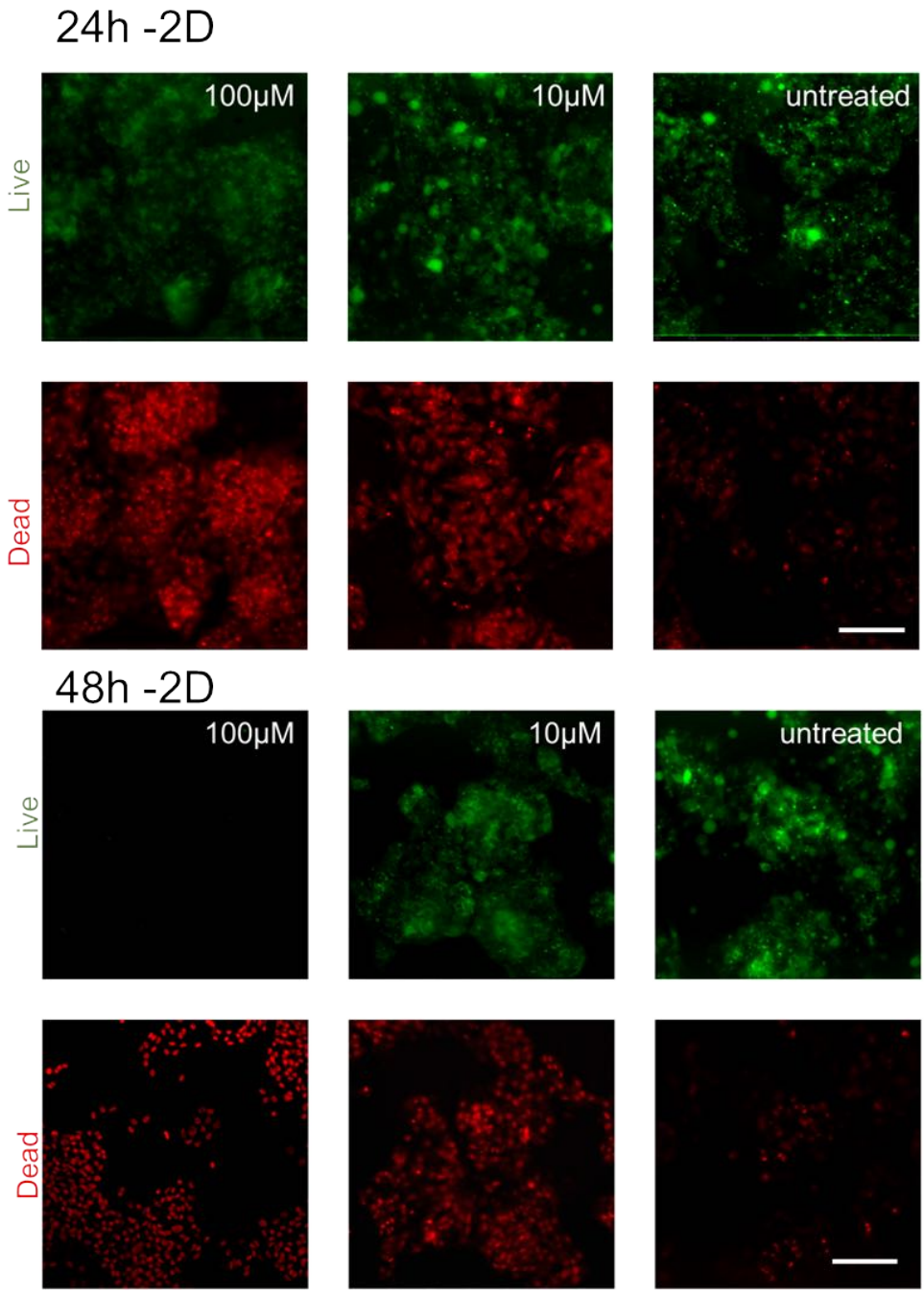

Figure S2: Live/Dead staining of HepG2 monolayer after exposure time of 24 and 48 hours with 100 µM, 10 µM and 0 µM sorafenib at day 6 post-seeding. Scale bars, 200 µm.

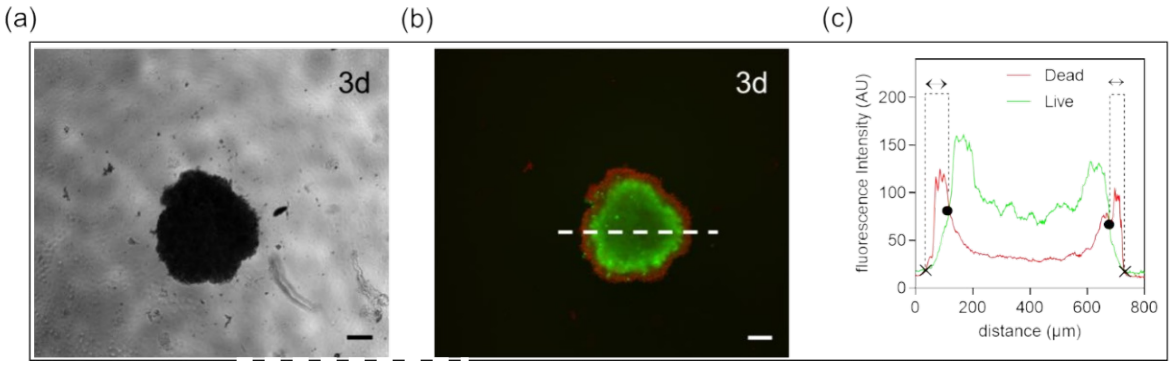

Figure S3: (a) Bright field and **(b)** fluorescence micrographs of a live (green)–dead (red) assay on HepG2 spheroids after 3 days of incubation. Scale bar, 200 µm. **(c)** The RGB profiles for both channels show the distribution of live and dead cells in the HepG2 spheroid. The drug diffusion distances (dotted line) were calculated by measuring the length of the red fluorescence signal that overlaps the green signal at the outer rim (between • and x), indicating inward diffusion of the cytotoxic drug sorafenib.

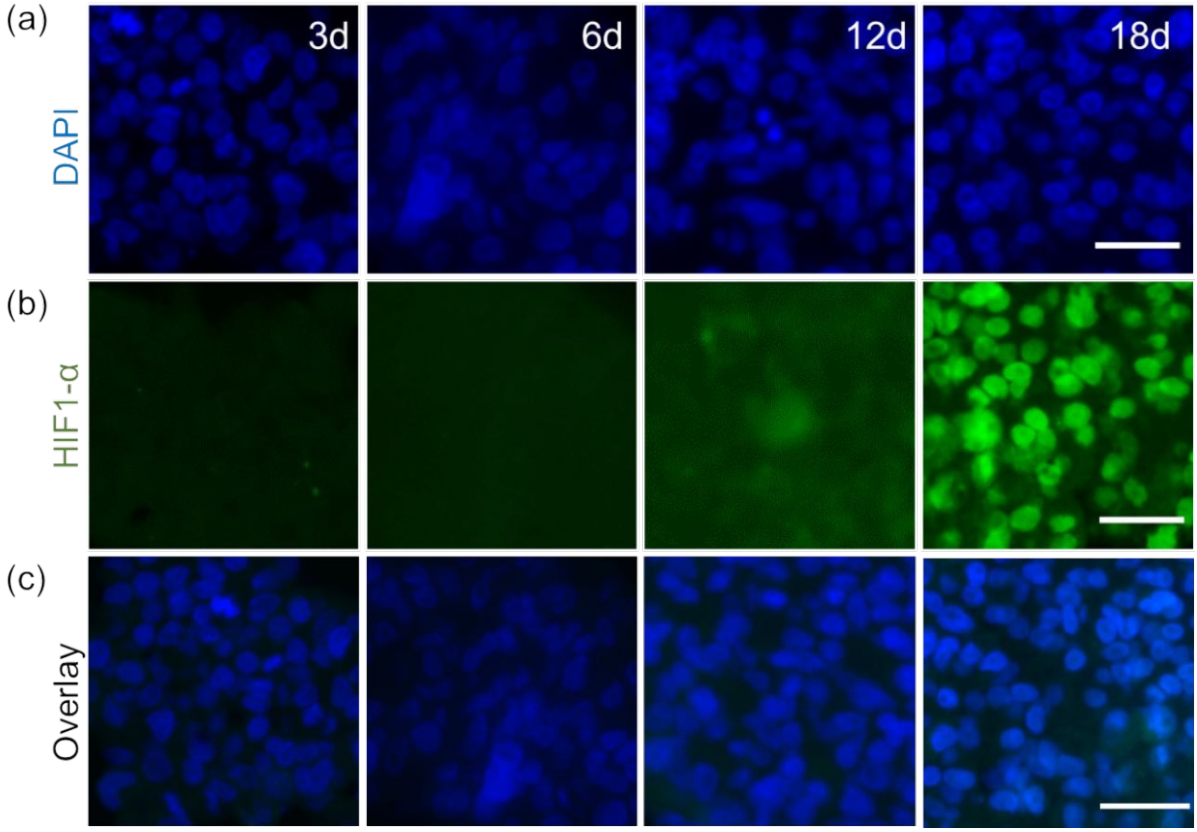

Figure S4: Hypoxic core formation of HepG2 spheroids over a cultivation time of 18 days illustrated by **(a)** fluorescence-stained cell nuclei, **(b)** immunohistochemical staining with anti-HIF1-α mAb and **(c)** an overlay of both channels. Scale bar, 20 µm.

CHAPTER 4

Cytotoxicity, retention, and anti-inflammatory effects of a CeO_2 nanoparticle-based supramolecular complex in a 3D liver cell culture model

ACS Pharmacology & Translational Science

pubs.acs.org/ptsci

Letter

Cytotoxicity, Retention, and Anti-inflammatory Effects of a CeO_2 Nanoparticle-Based Supramolecular Complex in a 3D Liver Cell Culture Model

Christoph Eilenberger, Florian Selinger, Mario Rothbauer, Yiji Lin, Andreas Limbeck, Barbara Schädl, Johannes Grillari, Nataliya S. Kavok, Vladimir K. Klochkov, Yuri V. Malyukin, Victor Margitich, and Peter Ertl*

Cite This: *ACS Pharmacol. Transl. Sci.* 2021, 4, 101−106

Read Online

ACCESS | Metrics & More | Article Recommendations | Supporting Information

ABSTRACT: Both cerium oxide (CeOx) nanoparticles and mefenamic acid (MFA) are known anti-inflammatory agents with hepatoprotective properties and are therefore prescribed for one of the major diseases in the world, nonalcoholic fatty liver disease (NAFLD). To study the potential cytotoxicity and anti-inflammatory effects as well as drug retention of a potential therapeutic CeOx/MFA supramolecular complex, a well-standardized hepatic (HepG2) spheroid model was used. Results showed that the highest cytotoxicity for the CeOx/MFA supramolecular complex was found at 50 μg/mL, while effective doses of 0.1 and 1 μg/mL yielded a significant decrease of TNF-α and IL-8 secretion. Time-resolved analysis of HepG2 spheroids revealed a spatiotemporal distribution of the supramolecular complex and limited clearance from the internal microtissue over a period of 8 days in cultivation. In summary, our results point at rapid uptake, distribution, and biostability of the supramolecular complex within the HepG2 liver spheroid model as well as a significant anti-inflammatory response at noncytotoxic levels.

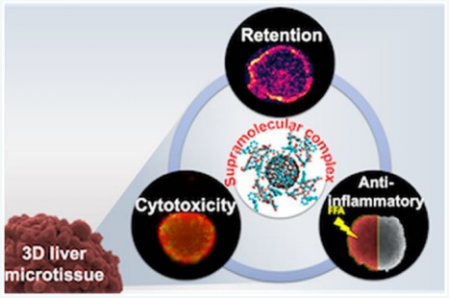

KEYWORDS: *supramolecular complexes, 3D spheroid models, NAFDL, drug delivery*

In the past decade, nanoparticle-based drug delivery systems have become increasingly popular in therapeutic and pharmaceutical applications due to their increased bioavailability, lower drug consumption rates, reduced side effects, and the ability to deliver drugs to a targeted region in the body.[1,2] A more recent development trend involves the engineering of functional nanomaterials based on supramolecular principles to create modular platforms with tunable chemical, mechanical, and biological properties.[3] Such supramolecular building blocks may combine inorganic nanomaterials with therapeutic agents to take advantage of their combinatorial effect for the treatment of severe diseases.[4−6] For instance, a supramolecular system based on cerium dioxide nanoparticles (CeO_2NPs) known for its antioxidant and hepatoprotective properties and nonsteroidal anti-inflammatory drugs (NSAIDs) such as mefenamic acid (MFA) can serve as promising nanodrug candidates for liver-related diseases.[7] Among liver diseases, nonalcoholic fatty liver disease (NAFLD) represents a major degenerative liver disorder with a global prevalence of 24%.[8,9] In fact, despite recent progress in the understanding of the pathogenesis of this common disease, there is still no approved medication for treating NAFLD.[10] In the current study, we investigate in detail the effects of a supramolecular hybrid nanocarrier consisting of a CeO_2NP core modified with MFA and a hydroxypropyl-β-cyclodextrin (HPβ-cyclodextrin) polymer shell on cellular viability, microtissue distribution and retention, as well as cytokine secretion using a three-dimensional (3D) HepG2 human liver spheroid model. The development and application of human 3D tissue models such as the generation of pathophysiological liver systems for drug pharmacokinetics and toxicity follow the international trend to overcome limitations of current animal models that do not represent, e.g., the human pathology of NAFLD.[11] Additionally, these *in vitro* 3D models are in line with recent efforts to promote alternatives to animal experiments according to the "3Rs" concept due to the ability to reproduce a cellular phenotype *in vivo*.[12,13]

Primary experiments set out to verify the feasibility and reproducibility of our 3D liver cell culture model for the evaluation of the cytotoxicity, retention, and anti-inflammatory effects of the supramolecular complex. In particular, the quality

Received: October 15, 2020
Published: December 8, 2020

of HepG2 spheroids was initially evaluated in terms of spheroid size, intracellular ATP concentration, and cellular viability over a defined cultivation time of 6 days. It is important to note that spheroid diameter and cellular aging are known factors to influence the outcome of drug testing results, thus highlighting the need for the reliable generation of identical spheroids.[14] Reproducibility results shown in Figure 1

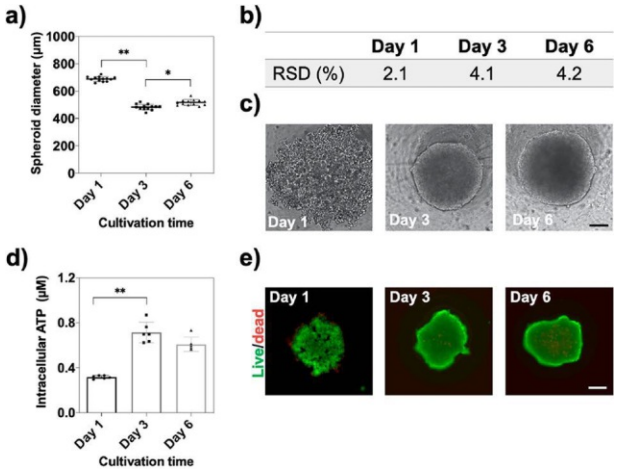

Figure 1. (a) HepG2 spheroid diameter (μm) over a cultivation period of 6 days postseeding, n = 12, ±SD, *p < 0.05, **p < 0.01. (b) Table of relative standard deviations (RSDs%) of respective HepG2 spheroid cultivation times of 1, 3, and 6 days. (c) Phase-contrast micrographs of HepG2 spheroids at day 1, day 3, and day 6 of cultivation. Scale bar, 100 μm. (d) Time-resolved intracellular ATP concentration of HepG2 spheroids over a cultivation time of 6 days postseeding, n = 6, ±SD, **p < 0.01. (e) Corresponding live (green)/dead (red) fluorescent micrographs. Scale bar, 200 μm.

demonstrate similar spheroid diameters for 6 days exhibiting respective RSDs of 2.1, 4.1, and 4.2% using an initial seeding density of 15 000 cells/mL. Additionally, intracellular ATP concentration as an indicator of viability increased significantly between day 1 and day 3 and remained constant for the remaining cultivation period, thus pointing at a highly metabolic active cell model. These results were further confirmed by live/dead viability assays based on calcein-AM and ethidium bromide staining.

In a next step, the composition, morphology, thermal properties, and size distribution of the supramolecular complex were characterized by transmission electron microscopy (TEM), UV−vis spectroscopy, and dynamic light scattering (DLS) to verify the successful formation of a stable hybrid nanostructure. The supramolecular complex (SMC) consists of the zinc salt of mefenamic acid (ZnMFA), hydroxypropyl-β-cyclodextrin (HPβ-CD), and cerium dioxide nanoparticles (see Figure S-1) in a ratio of 1:6:1 (ZnMFA/HPβ-CD/CeO_2NP). The morphology and size of the CeO_2NP-based supramolecular complex were characterized in water by TEM and DLS, respectively. Electron microscopy (TEM) analysis of CeO_2NPs shown in Figure S-1c revealed that the particles exhibit a spherical morphology in the size range of 2−3 nm. DLS measurements were performed to measure the average size distribution of the assembled SMC of ZnMFA, HPβ-CD, and CeO_2NP indicated by hydrodynamic diameters in a size range of 5−9 nm as shown in Figure S-1d. Absorption spectra of MFA, ZnMFA, and SMC in methanol revealed two characteristic bands in the UV spectral range (see Figure S-1e). The first band maxima undergo a bathochromic shift at 279.3−283.1−289.5 nm, while a hypsochromic shift at 350.7−344.9−336.8 nm was observed for the second band maxima, for MFA−ZnMFA−SMC, respectively. Similarly, a band maxima in aqueous solution revealed a shift at 285.5 and 335 nm (see Figure S-1f), thus pointing at the presence of ZnMFA within the supramolecular complex. Another important parameter to consider is the degradation characteristics of the supramolecular complex, which describe the connection between temperature and complex stability. Figure S-1g shows differential scanning calorimetry (DSC) curves for SMC and its components ZnMFA and HPβ-CD. The ZnMFA curve reveals two endothermic peaks at 106 and 120 °C, which point at a two-stage degradation process. The observed strong exothermic peak at 162°C can be associated with the thermal destruction of ZnMFA to MFA, while the endothermic peak at 250 °C is typical for MFA exhibiting a polymorph transition from form 1 to form 2.[15] In turn, temperatures above 250 °C resulted in MFA destruction. Importantly, DSC patterns for HPβ-CD and SMC revealed similar features, while DSC curves for pure SMC did not show any characteristic peaks for ZnMFA, which indicates the absence of unbound HPβ-CD and ZnMFA. In other words, DSC results confirmed that the individual components are strongly associated with each other, thus resulting in the formation of a stable supramolecular complex.

Following the physical and chemical characterization of the supramolecular complex, potential cytotoxicity was evaluated using a HepG2 3D spheroid model in subsequent experiments. The results in Figure 2a illustrate the time dose−response

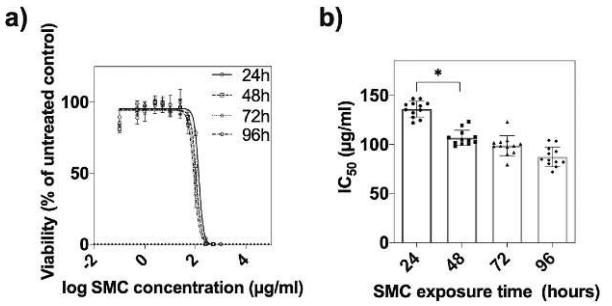

Figure 2. (a) SMC dose−response curves of HepG2 spheroids after drug exposure times of 24, 48, 72 and 96 h at day 6 postseeding. Error bars represent ±SEM (n = 12). (b) Corresponding IC_{50} values at respective exposure times. Error bars represent ±SD (n = 12), *p < 0.05.

relationship of the nanodrug indicating half-maximal inhibitory concentrations (IC50s) of the supramolecular complex of 136.4 ± 7.8, 108.3 ± 6.1, 101.1 ± 7.0, and and 87.5 ± 10.3 μg/mL after effective exposure times of 24, 48, 72, and 96 h, respectively. These results were additionally substantiated using cell viability staining (see also Figure S-2). Interestingly, IC50 values did not change significantly after 48 h of treatment in our 3D HepG2 spheroid model and remained stable, as shown in Figure 2b. As a result of this time−dose relationship study, a maximal exposure period of 48 h in the presence of the supramolecular complex was defined for all subsequent experiments.

An important aspect of any nanodrug study is concerned with bioavailability including accumulation, retention, and

https://dx.doi.org/10.1021/acsptsci.0c00170
ACS Pharmacol. Transl. Sci. 2021, 4, 101−106

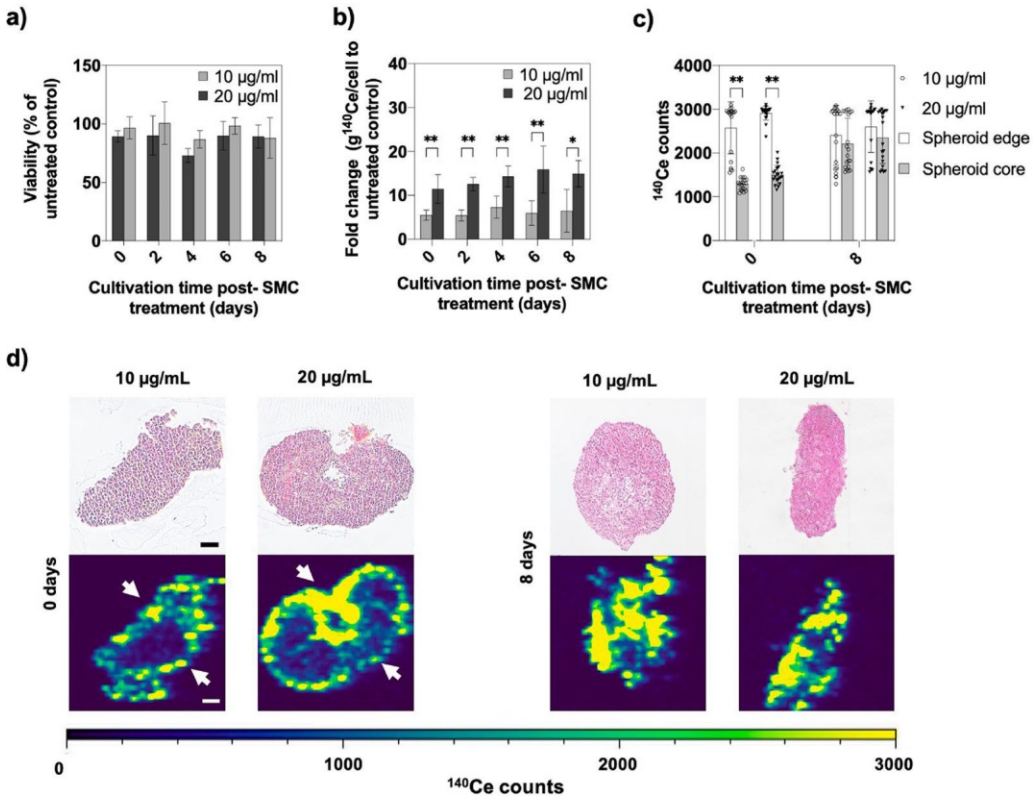

Figure 3. (a) Cellular viability of HepG2 spheroids after 0, 2, 4, 6, and 8 days of exposure at SMC concentrations of 20 and 10 μg/mL, $n = 3 \pm$ SD. (b) Quantitative analysis of isotope ^{140}Ce detected by ICP-MS in 3D HepG2 spheroids incubated with 0, 10, and 20 μg/mL of SMC, $n = 6 \pm$ SD, $^{*}p < 0.05$, $^{**}p < 0.01$. (c) Cerium distribution in HepG2 spheroids after 0 and 8 days post-treatment with 10 and 20 μg/mL of SMC. ^{140}Ce counts of the spheroid edge (50 μm from outer spheroid rim) and spheroid core (150 μm from outer rim), $n = 20 \pm$ SD, $^{**}p < 0.01$. (d) Microscopic image of H&E stained HepG2 spheroid thin sections and isotope distribution of ^{140}Ce from edges (arrows) to core after incubation with SMC for 48 h with 10 and 20 μg/mL after 0 days (left) and 8 days (right) post-treatment. Scale bar, 100 μm. LA-ICP-MS images were obtained with a laser spot size of 10 μm.

clearance from the tissue of interest. Consequently, tissue retention was analyzed using 3D HepG2 microtissues to evaluate the cellular internalization capacity of the supramolecular complex. Time-resolved retention of SMC in the HepG2 spheroid model was assessed following a 48 h treatment regime at reduced predetermined IC50 concentrations of 10 and 20 μg/mL. Microtissues were subsequently analyzed after each medium exchange step (e.g., every second day) over a cultivation period of 8 days postexposure (see also Scheme S-1). Initial viability studies shown in Figure 3a indicated no significant cytotoxic effects on the HepG2 spheroids as a result of 48 h of exposure during the 8 day post-treatment period. Next, entire 3D cell constructs were quantified and double-normalized to the spheroid cell number and untreated control after each media change to assess nanoparticle retention in the HepG2 microtissues (see Figure 3b). Over 8 days, apparent dose-dependent differences between 10 and 20 μg/mL were observed, resulting in an approximately 7-fold higher internal amount of ^{140}Ce ions present after 48 h of exposure of 10 μg/mL of SMC to an untreated control. In turn, a 20 μg/mL concentration resulted in an approximately 3-times higher amount of ^{140}Ce ions within treated spheroids. Interestingly, despite periodic medium replacement and washing steps, the concentration profile of CeO_2NPs inside the microtissues remained stable for both nanodrug concentrations, thus indicating the ability of SMC to accumulate and remain in the liver microtissue. For instance, a fold change of 5.5 ± 1.2 and 11.5 ± 3.3 g of ^{140}Ce per cell relative to untreated control was found at day 0 post-treatment, while similar values of 6.4 ± 1.9 and 14.9 ± 3.0 of g ^{140}Ce per cell were obtained after 8 days for 10 and 20 μg/mL of SMC, respectively. These results are in good correlation with published *in vivo* studies using rats, where CeO_2NPs accumulated mainly in the liver after administration and were still detectable after 8 weeks and, in some cases, up to 5 months.[16,17] In an attempt to assess cerium oxide nanoparticle distribution inside our 3D liver tissue analogues in more detail, laser ablation inductively coupled plasma mass spectrometry (LA-ICP-MS) was employed to determine the spatiotemporal allocation of ^{140}Ce ions within the liver tissue structure. Results shown in Figure 3c display the amount of ^{140}Ce ions in the spheroid edge and core at day 0 and day 8 following a 48 h administration of two nanodrug concentrations. While ^{140}Ce ion intensities of 2578 ± 595 and 2911 ± 161 counts for both 10 and 20 μg/mL SMC concentrations were similar in the outer cell layers of the spheroid after 48 h of exposure (day 0), significant lower intensities of 1285 ± 139 and 1595 ± 214 counts were found in the core of the spheroid. Moreover, following 8 days post-treatment with SMC, no significant differences of ^{140}Ce ion counts throughout the entire 3D cell constructs (e.g., from the edge to the core of the spheroid) were observed as illustrated in Figure 3d. In comparison,

https://dx.doi.org/10.1021/acsptsci.0c00170
ACS Pharmacol. Transl. Sci. 2021, 4, 101−106

analysis of the two-dimensional (2D) monolayer culture revealed a random distribution of ^{140}Ce across the culture area over the whole cultivation period, as shown in Figure S-3. These results clearly suggest spatiotemporal alterations and stable localization of nanoceria within the 3D HepG2 liver model, since even after repeated washing procedures, only limited clearance took place.

In a final set of experiments, the anti-inflammatory property of the mefenamic-acid-carrying supramolecular nanoceria complex was investigated using ELISA to determine the secretion of relevant cytokines, including TNF-α, IL-6, and IL-8. Prior to our nanodrug efficacy study, however, the ability of high concentrations of free fatty acids (FFAs) to induce inflammatory responses that are similar to those observed in patients with NAFLD and nonalcoholic steatohepatitis (NASH) was investigated in the 3D liver spheroid model.[18] Since the main fatty acids are palmitic acid and oleic acid in the human body, our human hepatic HepG2 model was incubated with a mixture of these FFAs to induce an inflammatory response that causes steatosis *in vitro*.[19,20] Figure 4a confirmed

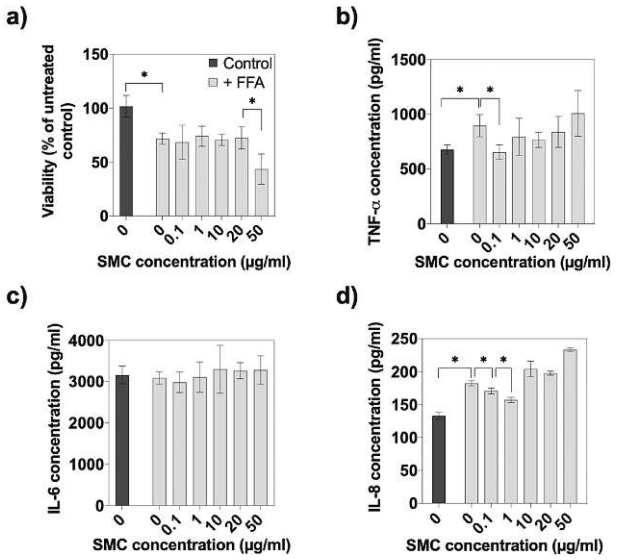

Figure 4. (a) Dose–response effects of the supramolecular complex on the viability of HepG2 spheroids treated with 600 μM FFA, $n = 3 \pm$ SD, $^*p < 0.05$. Secretion of (b) TNF-α, (c) IL-6, and (d) IL-8 of healthy and FFA treated HepG2 spheroids to evaluate the anti-inflammatory effect of SMC, $n = 3 \pm$ SD, $^*p < 0.05$.

the hepatoxicity of fat overloading via FFA as indicated by an overall reduction of viability of 33.5 ± 16.9% for FFA-exposed HepG2 spheroids in comparison to healthy controls. Importantly, the cellular viability of SMC treated healthy spheroids remained stable at a concentration range of 0.1 to 20 μg/mL and slightly decreased at 50 μg/mL. Results of the final evaluation of the anti-inflammatory effects of the supramolecular nanoceria complex are shown in Figure 4b–d, where the release of three selected cytokines after 24 h of FFA exposure was monitored. While significantly elevated TNF-α and IL-8 secretion was observed in the presence of FFA, no effect on IL-6 production was detected, thus effectively eliminating IL-6 from the panel of cytokine markers. Also, SMC exposure to spheroids did not produce an additional anti-inflammatory impact at any concentration on IL-6 secretion (see Table S-2). However, notable reductions of the other proinflammatory factors were discovered at 0.1–1 μg/mL SMC concentrations, resulting in a decreased TNF-α release of 31 ± 1.7% at 0.1 μg/mL and a stepwise reduction of IL-8 secretion by 6.4 ± 3.6 and 13.9 ± 0.7% at 0.1 and 1 μg/mL, respectively. In other words, the initial inflammatory response induced by the excess of free fatty acids yielded an increased TNF-α and IL-8 cytokine production, which was significantly reduced by SMC treatment, thus indicating the hepatoprotective function of the nanodrug. These results correlate with the known anti-inflammatory capacities of both, CeO_2NPs and MFA, in the literature.[16,21–24]

In conclusion, the investigated mefenamic-acid-carrying nanoceria-based supramolecular complex showed encouraging results leading to a significant reduction of an anti-inflammatory response in the presence of noncytotoxic levels of the nanodrug in our HepG2 liver spheroid model. Although the positive effects of both MFA and nanoceria have long been established in liver-related diseases, their combination and application in the form of a supramolecular complex are still in its infancy. Additionally, our clearance study confirmed stable localization of cerium oxide nanoparticles in the tissue construct lacking an effective clearance mechanism, as demonstrated in several previous *in vivo* studies. In this respect, the application of LA-ICP-MS has proven to be a valuable bioimaging tool for sample-specific high-resolution visualization in the field of drug delivery and tissue engineering. The presented differences in nanoparticle allocation in 2D and 3D HepG2 cultures support the hypothesis that spheroids' enhanced dimensionality and complexity can imitate transport processes closer to the *in vivo* situation than monolayer cultures. These results also mean that spheroidal *in vitro* 3D tissue models can serve as an alternative to animal testing at earlier stages of drug development. The translation to a more advanced 3D hepatic coculture model, including human primary hepatocytes combined with nonparenchymal cells, may be beneficial to investigate experimentally the intercellular effects of fat accumulation and inflammation in the liver as well as to study the complex phenotype of NAFLD in more detail. Further investigations not covered in our study need to examine the extent to which clearance mechanisms are influenced by particle load and dose rate as well as a broader evaluation of the antilipotoxic role of the supramolecular complex, thus providing a more detailed understanding of their nanobiology interactions.

■ ASSOCIATED CONTENT

Supporting Information

The Supporting Information is available free of charge at https://pubs.acs.org/doi/10.1021/acsptsci.0c00170.

Experimental section, supramolecular complex characterization, LIVE/DEAD staining of HepG2 microtissues, LA-ICP-MS analysis, experimental workflow of clearance study and ELISA data analysis (PDF)

■ AUTHOR INFORMATION

Corresponding Author

Peter Ertl – *Institute of Chemical Technologies and Analytics and Institute of Applied Synthetic Chemistry, Faculty of Technical Chemistry, Vienna University of Technology, 1060 Vienna, Austria; SAICO Biosystems KG, 1060 Vienna, Austria; Austrian Cluster for Tissue Regeneration, 1200*

Vienna, Austria; orcid.org/0000-0002-7625-2445; Email: peter.ertl@tuwien.ac.at

Authors

Christoph Eilenberger – *Institute of Chemical Technologies and Analytics and Institute of Applied Synthetic Chemistry, Faculty of Technical Chemistry, Vienna University of Technology, 1060 Vienna, Austria; SAICO Biosystems KG, 1060 Vienna, Austria; Austrian Cluster for Tissue Regeneration, 1200 Vienna, Austria*

Florian Selinger – *Institute of Chemical Technologies and Analytics and Institute of Applied Synthetic Chemistry, Faculty of Technical Chemistry, Vienna University of Technology, 1060 Vienna, Austria; SAICO Biosystems KG, 1060 Vienna, Austria; Austrian Cluster for Tissue Regeneration, 1200 Vienna, Austria*

Mario Rothbauer – *Institute of Chemical Technologies and Analytics and Institute of Applied Synthetic Chemistry, Faculty of Technical Chemistry, Vienna University of Technology, 1060 Vienna, Austria; SAICO Biosystems KG, 1060 Vienna, Austria; Austrian Cluster for Tissue Regeneration, 1200 Vienna, Austria; Medical University of Vienna, Department of Orthopedics and Trauma Surgery, Karl Chiari Lab for Orthopaedic Biology, 1090 Vienna, Austria*

Yiji Lin – *Institute of Chemical Technologies and Analytics and Institute of Applied Synthetic Chemistry, Faculty of Technical Chemistry, Vienna University of Technology, 1060 Vienna, Austria*

Andreas Limbeck – *Institute of Chemical Technologies and Analytics and Institute of Applied Synthetic Chemistry, Faculty of Technical Chemistry, Vienna University of Technology, 1060 Vienna, Austria*

Barbara Schädl – *Ludwig-Boltzmann-Institute for Experimental and Clinical Traumatology, 1200 Vienna, Austria; Austrian Cluster for Tissue Regeneration, 1200 Vienna, Austria*

Johannes Grillari – *Ludwig-Boltzmann-Institute for Experimental and Clinical Traumatology, 1200 Vienna, Austria; Austrian Cluster for Tissue Regeneration, 1200 Vienna, Austria; University of Natural Resources and Life Sciences, Dept. of Biotechnology, Institute for Molecular Biotechnology, 1190 Vienna, Austria*

Nataliya S. Kavok – *Institute for Scintillation Materials, STC "Institute for Single Crystals", 61001 Kharkiv, Ukraine*

Vladimir K. Klochkov – *Institute for Scintillation Materials, STC "Institute for Single Crystals", 61001 Kharkiv, Ukraine*

Yuri V. Malyukin – *Institute for Scintillation Materials, STC "Institute for Single Crystals", 61001 Kharkiv, Ukraine*

Victor Margitich – *Farmak JSC, Kiev 04080, Ukraine*

Complete contact information is available at: https://pubs.acs.org/10.1021/acsptsci.0c00170

Author Contributions

C.E., F.S., Y.L, and B.S. performed experiments and analyzed data with support from M.R., A.L., J.G., V.M., and P.E. N.K., V.K., and Y.M. designed and synthesized the supramolecular complex. The manuscript was written through contributions of all authors.

Notes

The authors declare the following competing financial interest(s): Work in this paper was partially supported by funding from Farmak JSC who also produced the supramolecular complex in cooperation with the Institute for Scintillation Materials. All experiments were performed by the Technical University of Vienna in cooperation with SAICO Biosystems.

■ ACKNOWLEDGMENTS

The authors thank Lukas Brunnbauer from the Institute of Chemical Technologies and Analytics at the Vienna University of Technology for performing the LA-ICP-MS analysis of the monolayer samples. The authors acknowledge the TU Wien University Library for financial support through its Open Access Funding Program.

■ REFERENCES

(1) Fu, L., Chung, R., and Shi, B. (2019) Upconversion Nanoparticle-Based Strategy for Crossing the Blood-Brain Barrier to Treat the Central Nervous System Disease. *Methods Mol. Biol. 2054*, 263–282.

(2) Zheng, Y., Li, Z., Chen, H., and Gao, Y. (2020) Nanoparticle-based drug delivery systems for controllable photodynamic cancer therapy. *Eur. J. Pharm. Sci. 144*, 105213.

(3) Webber, M. J. (2016) Engineering responsive supramolecular biomaterials: Toward smart therapeutics. *Bioeng Transl Med. 1*, 252–266.

(4) Wu, Y. L., Yin, H., Zhao, F., and Li, J. (2013) Multifunctional hybrid nanocarriers consisting of supramolecular polymers and quantum dots for simultaneous dual therapeutics delivery and cellular imaging. *Adv. Healthcare Mater. 2*, 297–301.

(5) Rozou, S., and Antoniadou-Vyza, E. (1998) An improved HPLC method overcoming Beer's law deviations arising from supramolecular interactions in tolfenamic acid and cyclodextrins complexes. *J. Pharm. Biomed. Anal. 18*, 899–905.

(6) Wang, L., Li, L. L., Fan, Y. S., and Wang, H. (2013) Host-guest supramolecular nanosystems for cancer diagnostics and therapeutics. *Adv. Mater. 25*, 3888–3898.

(7) Carvajal, S., Perramón, M., Oró, D., Casals, E., Fernández-Varo, G., Casals, G., Parra, M., González de la Presa, B., Ribera, J., Pastor, Ó., Morales-Ruíz, M., Puntes, V., and Jiménez, W. (2019) Cerium oxide nanoparticles display antilipogenic effect in rats with non-alcoholic fatty liver disease. *Sci. Rep. 9*, 12848.

(8) Kanuri, G., and Bergheim, I. (2013) In vitro and in vivo models of non-alcoholic fatty liver disease (NAFLD). *Int. J. Mol. Sci. 14*, 11963–11980.

(9) Younossi, Z., Anstee, Q. M., Marietti, M., Hardy, T., Henry, L., Eslam, M., George, J., and Bugianesi, E. (2018) Global burden of NAFLD and NASH: trends, predictions, risk factors and prevention. *Nat. Rev. Gastroenterol. Hepatol. 15*, 11–20.

(10) Lam, B., and Younossi, Z. M. (2010) Treatment options for nonalcoholic fatty liver disease. *Ther. Adv. Gastroenterol. 3*, 121–137.

(11) Takahashi, Y., Soejima, Y., and Fukusato, T. (2012) Animal models of nonalcoholic fatty liver disease/nonalcoholic steatohepatitis. *World J. Gastroenterol 18*, 2300–2308.

(12) Tannenbaum, J., and Bennett, B. T. (2015) Russell and Burch's 3Rs then and now: the need for clarity in definition and purpose. *J. Am. Assoc Lab Anim Sci. 54*, 120–132.

(13) Eilenberger, C., Kratz, S. R. A., Rothbauer, M., Ehmoser, E. K., Ertl, P., and Küpcü, S. (2018) Optimized alamarBlue assay protocol for drug dose-response determination of 3D tumor spheroids. *MethodsX 5*, 781–787.

(14) Eilenberger, C., Rothbauer, M., Ehmoser, E.-K., Ertl, P., and Küpcü, S. (2019) Effect of Spheroidal Age on Sorafenib Diffusivity and Toxicity in a 3D HepG2 Spheroid Model. *Sci. Rep. 9*, 4863.

(15) Adam, A., Schrimpl, L., and Schmidt, P. C. (2000) Some physicochemical properties of mefenamic acid. *Drug Dev. Ind. Pharm. 26*, 477–487.

(16) Oró, D., Yudina, T., Fernández-Varo, G., Casals, E., Reichenbach, V., Casals, G., González de la Presa, B., Sandalinas, S.,

Carvajal, S., Puntes, V., and Jiménez, W. (2016) Cerium oxide nanoparticles reduce steatosis, portal hypertension and display anti-inflammatory properties in rats with liver fibrosis. *J. Hepatol. 64*, 691−698.
(17) Heckman, K. L., DeCoteau, W., Estevez, A., Reed, K. J., Costanzo, W., Sanford, D., Leiter, J. C., Clauss, J., Knapp, K., Gomez, C., Mullen, P., Rathbun, E., Prime, K., Marini, J., Patchefsky, J., Patchefsky, A. S., Hailstone, R. K., and Erlichman, J. S. (2013) Custom cerium oxide nanoparticles protect against a free radical mediated autoimmune degenerative disease in the brain. *ACS Nano 7*, 10582−10596.
(18) Chavez-Tapia, N. C., Rosso, N., and Tiribelli, C. (2012) Effect of intracellular lipid accumulation in a new model of non-alcoholic fatty liver disease. *BMC Gastroenterol. 12*, 20.
(19) Grishko, V., Rachek, L., Musiyenko, S., Ledoux, S. P., and Wilson, G. L. (2005) Involvement of mtDNA damage in free fatty acid-induced apoptosis. *Free Radical Biol. Med. 38*, 755−762.
(20) Chiu, H. C., Kovacs, A., Ford, D. A., Hsu, F. F., Garcia, R., Herrero, P., Saffitz, J. E., and Schaffer, J. E. (2001) A novel mouse model of lipotoxic cardiomyopathy. *J. Clin. Invest. 107*, 813−822.
(21) Rainsford, K. D. (2007) Anti-inflammatory drugs in the 21st century. *Subcell. Biochem. 42*, 3−27.
(22) Madrigal-Perez, V. M., García-Rivera, A., Rodriguez-Hernandez, A., Ceja-Espiritu, G., Briseño-Gomez, X. G., Galvan-Salazar, H. R., Soriano-Hernandez, A. D., Guzman-Esquivel, J., Martinez-Fierro, M. L., Newton-Sanchez, O. A., Olmedo Buenrostro, B. A., Rodriguez-Sanchez, I. P., López-Lemus, U. A., Lara-Esqueda, A., and Delgado-Enciso, I. (2015) Preclinical analysis of nonsteroidal anti-inflammatory drug usefulness for the simultaneous prevention of steatohepatitis, atherosclerosis and hyperlipidemia. *Int. J. Clin Exp Med. 8*, 22477−22483.
(23) Utzeri, E., and Usai, P. (2017) Role of non-steroidal anti-inflammatory drugs on intestinal permeability and nonalcoholic fatty liver disease. *World J. Gastroenterol 23*, 3954−3963.
(24) Li, Y., Hou, X., Yang, C., Pang, Y., Li, X., Jiang, G., and Liu, Y. (2019) Photoprotection of Cerium Oxide Nanoparticles against UVA radiation-induced Senescence of Human Skin Fibroblasts due to their Antioxidant Properties. *Sci. Rep. 9*, 2595.

Supplementary Information

Cytotoxicity, retention, and anti-inflammatory effects of a CeO_2 nanoparticle-based supramolecular complex in a 3D liver cell culture model

Christoph Eilenberger, Florian Selinger, Mario Rothbauer, Yiji Lin, Andreas Limbeck, Barbara Schädl, Johannes Grillari, Nataliya S. Kavok, Vladimir K. Klochkov, Yuri V. Mayukin, Victor Margitich and Peter Ertl

Experimental Section

Supramolecular complex synthesis

Supramolecular complex was synthesized in three step procedure: 1) synthesis of CeO_2 NPs colloidal solution; 2) synthesis of ZnMFA:CeO_2NPs complex; 3) synthesis of ZnMFA:CeO_2NPs:HPβ-CD complex. The CeO_2NPs colloidal solution was prepared as described elsewhere [176].

Synthesis of ZnMFA:CeO_2NPs complex:

75 ml of the Zn-MK ethanol solution (0.2 mg/ml) was mixed with 75 ml of the CeO_2NPs aqueous solution (0.2 mg/ml) followed by stirring until an opalescent solution was formed. Then, 75 ml of distilled water was added to obtain transparent colorless solution. The solution was poured into a round bottom flask and evaporated to 30 ml using a rotary evaporator at a bath temperature of 50oC. During evaporation, the alcohol was completely removed. The resulting aqueous ZnMFA:CeO_2NPs solution contains 0.5 mg/ml ZnMFA in a complex with 0.5 mg/ml CeO_2 NPs.

Synthesis of ZnMFA:CeO_2NPs:HPβ-CD complex:

30 ml of the ZnMFA: CeO_2NP complex solution was added to 9 ml of an aqueous solution of HPβ-CD (10 mg/ml). The solution was stirred for 10 minutes and left in the dark at room temperature for 24 hours. The solution was evaporated to dryness using a rotary evaporator to obtain a bright-yellow powder which is soluble in water. The powder was dried in a desiccator over $CaCl_2$.

Characterization of the supramolecular complex

Transmission electron microscopy (TEM) was performed using a TEM-125K electron microscope (Selmi, Ukraine) and a 100 kV electron beam. For sample preparation, 200 mesh carbon-coated Cu were used. A 2 µL drop of the test solution was deposited to a

grid and the solvent allowed to evaporate. Absorption spectra were measured using a "Specord 200" spectrometer (Analytik Jena, Germany). The temperature of experiments was 25°C. Hydrodynamic diameters were measured using a ZetaPALS/BI-MAS analyzer (Brookhaven Instruments Corp., USA) operated in the phase analysis light scattering mode. Measurements were carried out at the scattering angle of 90° and laser emission at 659 nm. The temperature of experiments was 25°C.

Cell Culture

Hepatocellular carcinoma cells (HepG2; HB-8065, ATCC, USA) were cultivated in Minimal Essential Media (Sigma-Aldrich, Austria) and supplemented with 10% fetal bovine serum (Sigma-Aldrich, Austria) and 1% antibiotic/antimycotic solution (Sigma-Aldrich, Austria) to a confluency of approx. 60-80 % under cell culture conditions at 37°C and 5% CO_2.

Spheroid Generation

Cells for spheroid production were obtained from monolayer cultures. After rinsing with phosphate buffer (1X PBS, Sigma-Aldrich, Austria) and treatment with trypsin/EDTA (Sigma-Aldrich, Austria), cell suspension was centrifuged at 1250 rpm for 5 min, adjusted to a cell density of 15.000 cells/ml and 200 µl were pipetted to each well of the U-bottom ultra-low attachment plate (Corning, Austria). Cells were incubated at 37°C and 5% CO_2 humidified atmosphere and media was changed every 48h.

Intracellular ATP determination

For cell viability determination 3D spheroids were treated with CellTiter-Glo® 3D Reagent and RealTime-Glo™ MT Cell Viability Assay (Promega, Austria) according to manufacturer's protocol.

Live/dead staining

Spheroid viability was qualitatively evaluated using a commercially available fluorescence assay (LIVE/DEAD® Viability/Cytotoxicity Assay, Life Technologies, Austria).

Image acquisition

Phase-contrast micrographs of HepG2 spheroids were analyzed and spheroid diameters were measured using Olympus' CellSense Standard® software. Live/dead cells were monitored by a fluorescence microscope (IX83, Olympus, Germany) with fluorescein optical filter (ex 485, em 530) and rhodamine filter (ex 530 nm, em 645 nm).

Inductively coupled plasma mass spectrometry (ICP-MS)

After respective time points, HepG2 spheroids were washed with 1X PBS and fixed with 4% Paraformaldehyde (Sigma-Aldrich, Austria) for 48 hours. Spheroids were embedded in Paraffin and cut into 4 µm sections for histological staining with hematoxylin and eosin (H&E). For ^{140}Ce retention analysis in a 2D monolayer model, microscope glass slides (VWR, Austria) were coated with 0.25 µg/ml Collagen I (from rat tail, Sigma-Aldrich, Austria), and HepG2 cells were seeded at an initial density of 10^5 cells/ml. HepG2 cells were incubated for 2 days at 37°C and 5% CO_2 until a confluency of approx. 80% was reached prior drug exposure with SMC. After respective

time points, HepG2 monolayer were washed with 1X PBS, fixed with 4% Paraformaldehyde (Sigma-Aldrich, Austria) for 15 minutes and stored in 1X TBS buffer (Sigma-Aldrich, Austria) until proceeding with analysis.

For sample ablation a 213 nm frequency quintupled Nd:YAG laser (New Wave 213, ESI, Fremont, CA) was used. Samples are placed into a washout cell with washout times below one second. Ablated material is transported with a Helium gasflow to the coupled iCAP Qc ICP-MS instrument (ThermoFisher Scientific, Germany). The gas flow is mixed with Argon as make-up gas upon introduction to the plasma. For data acquisition the Qtegra software was provided by the manufacturer. Elemental images were acquired through the usage of Epina ImageLab 2.99.

A detailed description of the laser and measurement parameters can be found in Table S-1. Generally, all parameters were held constant with the exception of the laser scan speed and laser spot diameter. For imaging measurements, a spot diameter of 10 µm with a laser scan speed of 30 µm/s was chosen, whereas quantitative measurements were performed with a 40 µm laser spot diameter and 120 µm/s laser scan speed.

Table S-1: Summary of instrumental parameters used for LA-ICP-MS measurements

LA-ICP-MS		*ICP-MS*	
Wavelength	213 nm	Plasma power	1550 W
Pulse duration	4 ns	Cool gas flow	14 L/min
Laser repetition rate	20 Hz	Auxiliary gas flow	0.8 L/min
Laser Fluence	11 J/cm²	Cones	Ni
Laser scan speed	30 - 120 µm/s (imaging/ quantitative)	Monitored isotopes	27Al, 29Si, 31P, 64Zn, 67Zn, 68Zn, 140Ce, 142Ce
Laser spot diameter	10 - 40 µm (imaging/ quantitative)	Dwell time per isotope	10 ms
Carrier gas flow (He)	650 mL/min	Mass resolution (m/Δm)	300

For the quantification a dried droplet calibration approach was applied. Throughout the experiment ultra-pure water with a resistivity of 18 MΩ obtained from a Barnstead EASYPURE II water system (ThermoFisher Scientific, Marietta, OH, USA) was used for dilutions. The standards contained a cerium single standard solution (ThermoFisher, Germany) and di-sodium hydrogen phosphate dodecahydrate (p.a., Carl Roth, Germany) to calibrate cerium and phosphorus respectively. Six solutions with cerium concentration ranging from 0.3 µg/l to 100 µg/l and di-sodium hydrogen phosphate dodecahydrate concentration ranging from 10 µg/l to 3000 µg/l were produced. 1 µL of each standard was pipetted on a glass substrate which was precoated with octadecyltrichlorosilane to make the surface hydrophobic and subdue the coffee-ring effect.

For sample ablation, a 213 nm frequency quintupled Nd:YAG laser (New Wave 213, ESI, Fremont, CA) was used. Ablated material was transported with Helium gasflow to the coupled iCAP Qc ICP-MS instrument (Thermo Fisher Scientific, Germany). For data acquisition the Qtegra software was provided by the manufacturer. Elemental images were acquired through the usage of Epina ImageLab 2.99. For quantification a dried droplet calibration approach was applied. Raw data was normalized to ^{31}P signal

of one spheroid and respective ATP content per cell. For imaging measurements, a spot diameter of 10 µm with a laser scan speed of 30 µm/s was chosen, whereas quantitative measurements were performed with a 40 µm laser spot diameter and 120 µm/s laser scan speed.

Quantification of cytokine secretion

After 5 days of spheroid cultivation, inflammation was induced by 600 µM free fatty acids (FFA; at a molecular ration of 2:1 for oleic: palmitic acid) for 24 hours. Media was changed and HepG2 spheroids were treated with SMC for 48h. After cultivation, spheroid supernatants were collected and frozen at -20°C until ELISA of Human IL-6, Human IL-8 and Human TNF- alpha (Abcam, Germany). ELISA was performed according to the manufacturer's protocols.

Statistical Analysis

Statistical significance among the experimental groups was determined with Student's t-test. A P value $p<0.05$ was considered statistically significant (*). Graphs were plotted and statistical analysis was performed using Prism 8.2.1 (GraphPad Software, USA).

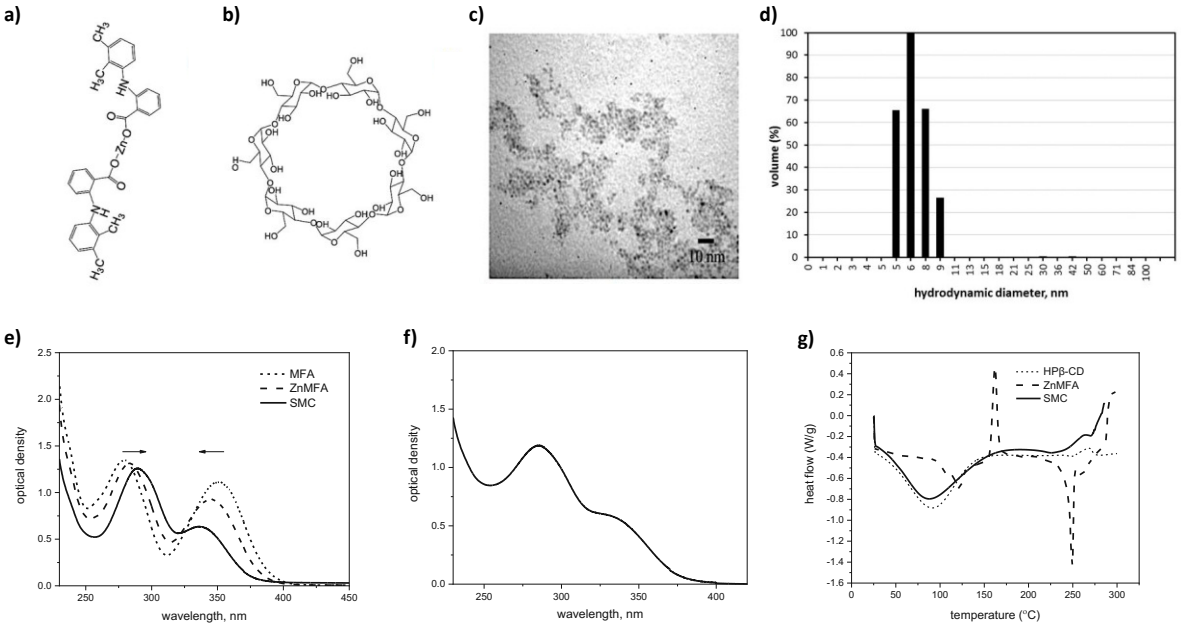

Figure S-1: a) Structural formulas of zinc salt of mefenamic acid, **b)** hydroxypropyl-β-cyclodextrin and **c)** TEM image of CeO_2 nanoparticles. **d)** Size Distribution (DLS) of a colloidal dispersion of the supramolecular complex (SMC) in water. UV/VIS absorption spectra of **e)** mefenamic acid (MFA), zinc salt of mefenamic acid ZnMFA and SMC in methanol and **f)** of SMC in water. **g)** Differential scanning calorimetry DSC curves for SMC and its components.

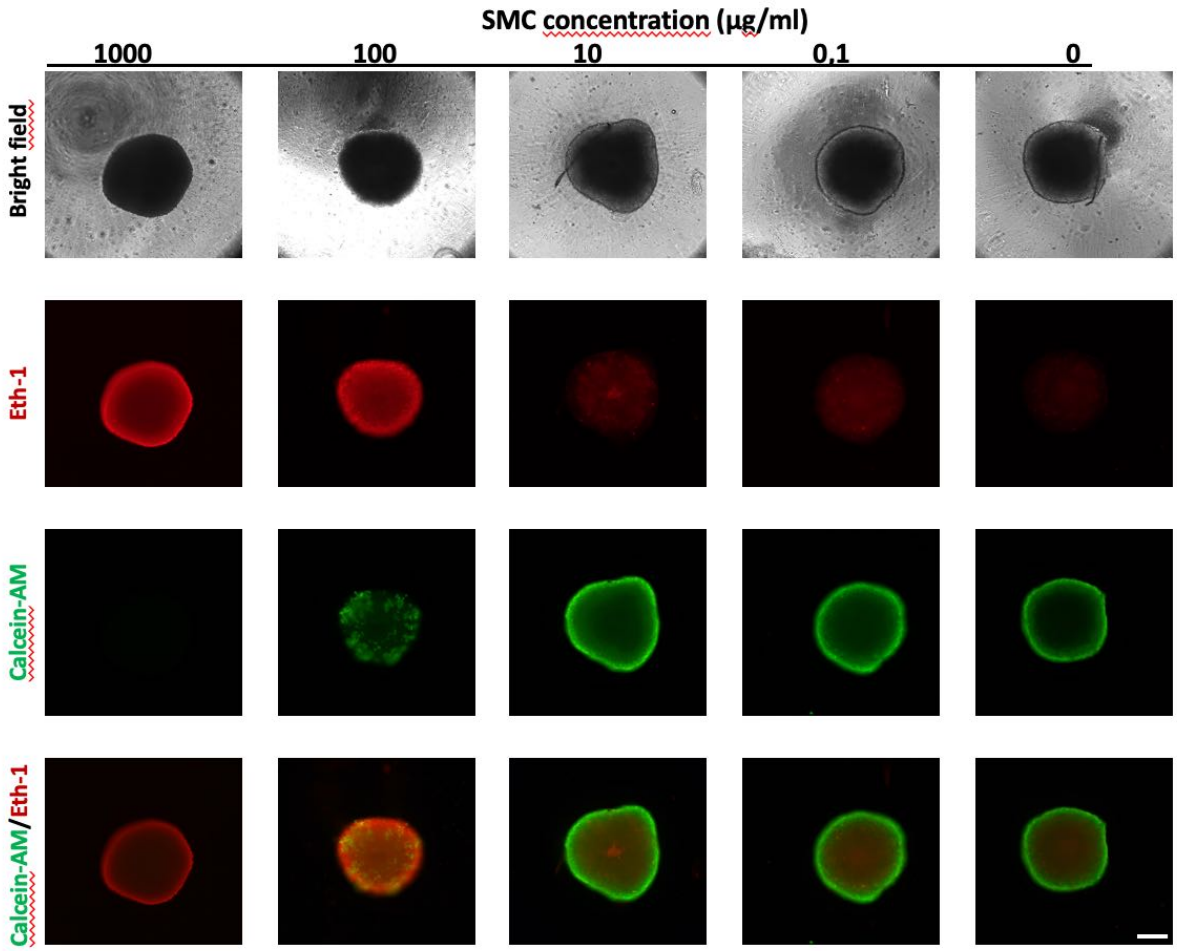

Figure S-2: Bright field and fluorescence micrographs of a live (green)–dead (red) assay on HepG2 spheroids after exposure time 96 hours with 1000 µg/ml, 100 µg/ml, 10 µg/ml and 0.1 µg/ml and 0 µg/ml SMC at day 6 post-seeding. Scale bars, 200 µm.

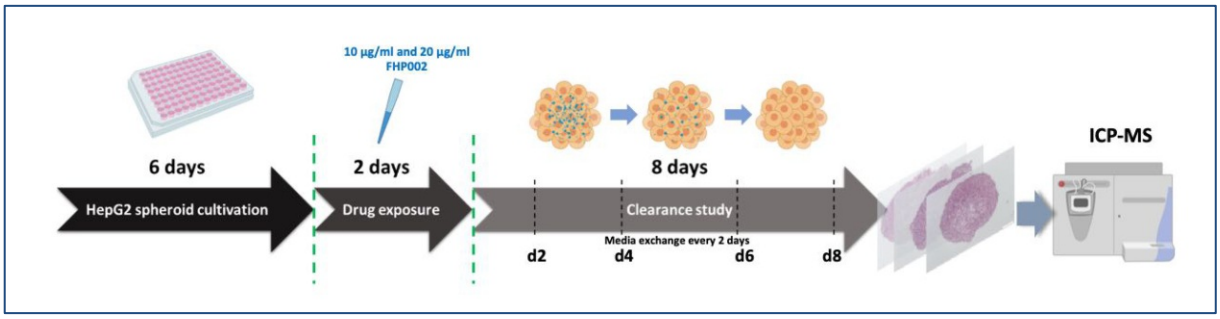

Scheme S-1: Schematic workflow of nanodrug retention study including HepG2 spheroid cultivation, exposure of 10 µg/ml and 20 µg/ml of supramolecular complex, periodic washing steps of spheroids with cell culture media for 8 days post-treatment, histology followed by quantification of ^{140}Ce by ICP-MS. The figures were exported under a paid subscription. Created with BioRender (www.biorender.com).

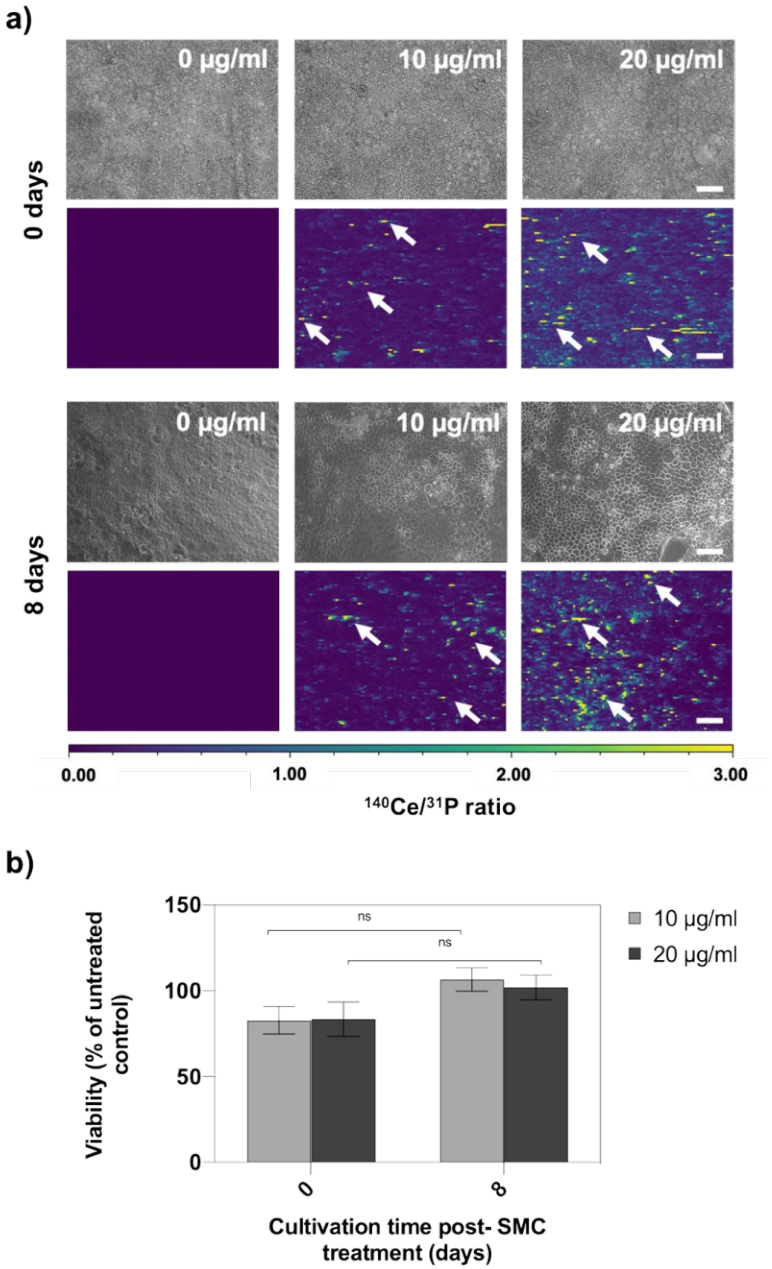

Figure S-3: a) Bright-field and LA-ICP-MS micrographs of $^{140}Ce/^{31}P$ signal ratio distribution in HepG2 monolayer culture after 0- and 8-days post-treatment with 0, 10, and 20 µg/ml SMC. Scale bar, 100 µm. **b)** Cellular viability of HepG2 monolayer culture after 0- and 8-days of exposure at SMC concentrations of 10 µg/ml and 20 µg/ml, n=3 ± SD.

Table S-2: Table of the anti-inflammatory capacity of the supramolecular complex in an untreated and free fatty acid (FFA) treated HepG2 spheroid model.

Inflammatory factor	*control (pg/ml)*	*+ FFA (pg/ml)*	*Effective nanodrug doses (µg/ml)*	*+ FAA +SMC (pg/ml)*	*p-value (treated vs. inflamed)*	*Reduction of cytokine secretion (%)*
TNF-α	676.5 ± 44.0	895.1 ± 100.5	0.1	653.6 ± 67.3	p< 0.05	30.9 ± 1.7
IL-6				No effect		
IL-8	133.1 ± 5.2	182.4 ± 3.8	0.1	170.6 ± 4.6	p< 0.05	6.4 ± 3.6
			1.0	157.0 ± 4.0	p< 0.01	13.9 ± 0.7

References

(1) Vladimir K., K.; Anna V., G.; Olga O., S.; Yuri V., M. Colloids and Surfaces A: Physicochemical and Engineering Aspects 2012, 409, 176-182.

CHAPTER 5

A microfluidic multi-size spheroid array for multi-parametric screening of anti-cancer drugs and blood-brain barrier transport properties

RESEARCH ARTICLE

ADVANCED SCIENCE Open Access

www.advancedscience.com

A Microfluidic Multisize Spheroid Array for Multiparametric Screening of Anticancer Drugs and Blood–Brain Barrier Transport Properties

Christoph Eilenberger, Mario Rothbauer, Florian Selinger, Anna Gerhartl, Christian Jordan, Michael Harasek, Barbara Schädl, Johannes Grillari, Julian Weghuber, Winfried Neuhaus, Seta Küpcü, and Peter Ertl**

Physiological-relevant in vitro tissue models with their promise of better predictability have the potential to improve drug screening outcomes in preclinical studies. Despite the advances of spheroid models in pharmaceutical screening applications, variations in spheroid size and consequential altered cell responses often lead to nonreproducible and unpredictable results. Here, a microfluidic multisize spheroid array is established and characterized using liver, lung, colon, and skin cells as well as a triple-culture model of the blood-brain barrier (BBB) to assess the effects of spheroid size on (a) anticancer drug toxicity and (b) compound penetration across an advanced BBB model. The reproducible on-chip generation of 360 spheroids of five dimensions on a well-plate format using an integrated microlens technology is demonstrated. While spheroid size-related IC_{50} values vary up to 160% using the anticancer drugs cisplatin (CIS) or doxorubicin (DOX), reduced CIS:DOX drug dose combinations eliminate all lung microtumors independent of their sizes. A further application includes optimizing cell seeding ratios and size-dependent compound uptake studies in a perfused BBB model. Generally, smaller BBB-spheroids reveal an 80% higher compound penetration than larger spheroids while verifying the BBB opening effect of mannitol and a spheroid size-related modulation on paracellular transport properties.

1. Introduction

The costs of drug development increase exponentially, starting at the late stage of preclinical testing using in vivo models followed by lengthy clinical trials.[1] In addition to the increased financial burden, the majority of initially identified compounds with potential health benefits are steadily eliminated during clinical phase periods one, two, and three. This high drug failure rate in the pharmaceutical development cycle has mainly been attributed to the lack of predictability in the early preclinical phase testing using standard in vitro and in vivo models. Similar situations have also been reported by other industries that regularly develop new chemicals for consumer use, including cosmetics, agro-food, and consumer goods.[2] To improve the predictability of preclinical in vitro models, recent efforts of pharmaceutical companies are based on implementing complex 3D biological systems such as multicellular spheroid and organoid technologies. Since multicellular spheroid systems are able to mimic

C. Eilenberger, Dr. M. Rothbauer, F. Selinger, Dr. C. Jordan, Prof. M. Harasek, Prof. P. Ertl
Faculty of Technical Chemistry
Vienna University of Technology
Getreidemarkt 9, Vienna 1060, Austria
E-mail: mario.rothbauer@meduniwien.ac.at; peter.ertl@tuwien.ac.at

Dr. M. Rothbauer
Karl Chiari Lab for Orthopaedic Biology
Department of Orthopedics and Trauma Surgery
Medical University of Vienna
Währinger Gürtel 18-20, Vienna 1090, Austria

The ORCID identification number(s) for the author(s) of this article can be found under https://doi.org/10.1002/advs.202004856

DOI: 10.1002/advs.202004856

A. Gerhartl, Dr. W. Neuhaus
AIT Austrian Institute of Technology GmbH
Center Health and Bioresources
Competence Unit Molecular Diagnostics
Giefinggasse 4, Vienna 1210, Austria

B. Schädl, Dr. J. Grillari
Ludwig-Boltzmann-Institute for Experimental and Clinical Traumatology
Donaueschingenstraße 13, Vienna 1200, Austria

Dr. J. Grillari
Institute for Molecular Biotechnology
Department of Biotechnology
University of Natural Resources and Life Sciences
Muthgasse 18, Vienna 1190, Austria

Prof. J. Weghuber
School of Engineering
University of Applied Sciences Upper Austria
Stelzhamerstraße 23, Wels 4600, Austria

human (patho)physiologies, they are considered a promising alternative to bridge the gap between preclinical tests and in vivo outcomes by eliminating unsuitable agents early on.[3,4] As a result, the application of multicellular spheroid systems in industrial settings can potentially lead to significantly lower pharmaceutical development costs by shortening development time, providing meaningful and representative test results.[5]

Despite the many potentials of using multicellular spheroid systems as advanced in vitro models, including 1) more predictive and reproducible toxicity and efficacy tests, 2) early exclusion of drug candidates in the drug development pipeline, 3) the possibility to perform substance testing on relevant human disease models, and 4) a reduction of animal studies, thus following the 3R principle (e.g., replacing, reducing, refining animal testing),[6] some distinct limitations still remain. The main drawback of using complex multicellular spheroid systems in the drug development process is the lack of standardization and harmonization across the industry leading to significant variations in spheroid morphologies,[7,8] cell numbers and ratios used, medium compositions, and cultivation/assay times,[9] which essentially eliminates a meaningful comparison between different end-users and laboratories. Recently, we have shown that spheroid age variations and lack of reproducible uniformity impact the outcome of drug delivery and efficacy studies,[10] thus preventing the integration of this promising technology into mainstream drug discovery pipelines. It is important to highlight that the generated size of multicellular spheroids, which ranges in the hundreds of microns in diameter (e.g., 100 to 1000 µm), can be considered a primary critical parameter that influences gradient distributions of oxygen, growth factors, nutrition (e.g., sugar, peptides, proteins), ions, and pH as well as guiding the elimination of metabolic wastes inside the spheroid, thus tissue size heavily impacts all aspects of cellular functions.[11–13] Taken into a pharmaceutical context, the altered mass transport properties in differently sized spheroids further modulate penetration, distribution, and retention of drugs directly and impact spheroid (size-related) drug response.[12] As an example, larger tumor spheroids are known to display higher chemoresistance due to i) increased contact-mediated resistance, ii) exclusion of drugs, and iii) their content of proliferating and hypoxic cells resulting from more pronounced nutrient and oxygen gradients.[14,15] Additional reports indicated spheroid size-related biological effects such as altered protein production as albumin secretion,[16] amount of cancer stem cell accumulation in tumor spheroids,[17] shifts in differentiation pattern in human embryoid bodies,[18] as well as cell-type-specific tissue stiffness variations (e.g., loose vs tight cell aggregates).[19]

To date, a number of methods for multicellular 3D spheroid generation exist, including nonadhesive surfaces,[20,21] spinner flasks,[22] scaffold supports,[23] acoustic tweezers,[24] hanging drops,[25,26] microwells,[27–29] as well as various microfluidic devices.[30,31] Among these, only the hanging drop technology and microwell-based methods combined with precision fabrication techniques such as lithography, 3D-printing, and computerized numerical control milling can achieve homogenous spheroids with controllable sizes.[26] Despite their ability to generate uniform spheroid sizes, these techniques are highly laborious and, at times, technical challenging, thus limiting their scalability. Alternatively, in recent years, microfluidics technology has been used to produce chip designs capable of controlling spheroid size and growth dynamics.[27,32–35] Unfortunately, most microfluidic spheroid technologies still lack automatic generation and cultivation of 3D spheroids as well as the formation of different-sized spheroids on a single chip-platform, which is needed to account for size-dependent compound toxicities, drug responses, and biological phenomena. Consequently, to meet the growing demand for medium-throughput and high-content multicellular spheroid systems, next-generation microfluidic devices need to offer 1) optimal tissue culture conditions including tight control of medium composition and gas exchange, 2) simple and robust cell loading procedures, 3) parallel spheroid production of different sizes, and 4) dynamic medium perfusion as well as 5) simple operation with reproducible tissue maintenance.[36] To address these challenges, we have developed a microfluidic multisize spheroid array capable of culturing 3D multicellular spheroids with high reproducibility in medium-to high-throughput formats using a wide range of different tissue types.

In this study, we demonstrate the reliable and reproducible generation of 90 multiple-sized spheroids on a single chip and the formation of 360 spheroids on a "microtiter plate"-based platform layout as shown in Figure S1 (Supporting Information). To ensure medium-throughput capability, gravity-driven perfusion is selected, whereby flow velocities are adjusted by an embedded flow restrictor in combination with tilting angle and speed of a conventional laboratory rocker. Additionally, medium reservoirs are arranged at a 9 mm pitch to be compatible with standard multichannel pipettes for 96-well microtiter plates. The microfluidic multisize spheroid array shown in **Figure 1**A is therefore comprised of three main components: i) six microfluidic culture channels in a standard 96-well plate footprint each containing 15 individual microwells with five diameters of 1000, 900, 700, 500, and 300 µm, ii) perfusion connectors incorporated into the cover layer that interconnect the inlets and outlets of the channels with medium reservoirs and air bubble traps, and iii) a pair of medium reservoirs for each culture channel that can be filled using a multichannel pipettor to enable straightforward and simple cell seeding as well as facile retrieval of supernatant and cellular material. A rendered cutaway of the platform is seen in Figure S2 (Supporting Information) and shows the different microfluidic layers, which are constructed using soft lithography from polydimethyl siloxane (PDMS). The main feature of the microfluidic multi-sized spheroid array highlighted in Figure 1B, however, is the integration of different-sized microwells of defined semispherical geometry capable of reliably trapping increasing cell numbers. Spontaneous cell aggregation within 24 hours is accomplished by surface modification using a biocompatible low-adhesive 2-(methacryloyoxy)ethyl phosphorylcholine (MPC) polymer. Initial performance evaluation of

Prof. J. Weghuber
FFoQSI GmbH-Austrian Competence Centre for Feed and Food Quality Safety and Innovation
Technopark 1C, Tulln 3430, Austria
Dr. S. Küpcü
Institute of Synthetic Bioarchitectures
Department of Nanobiotechnology
University of Natural Resources and Life Sciences
Vienna, Muthgasse 11, Vienna 1190, Austria

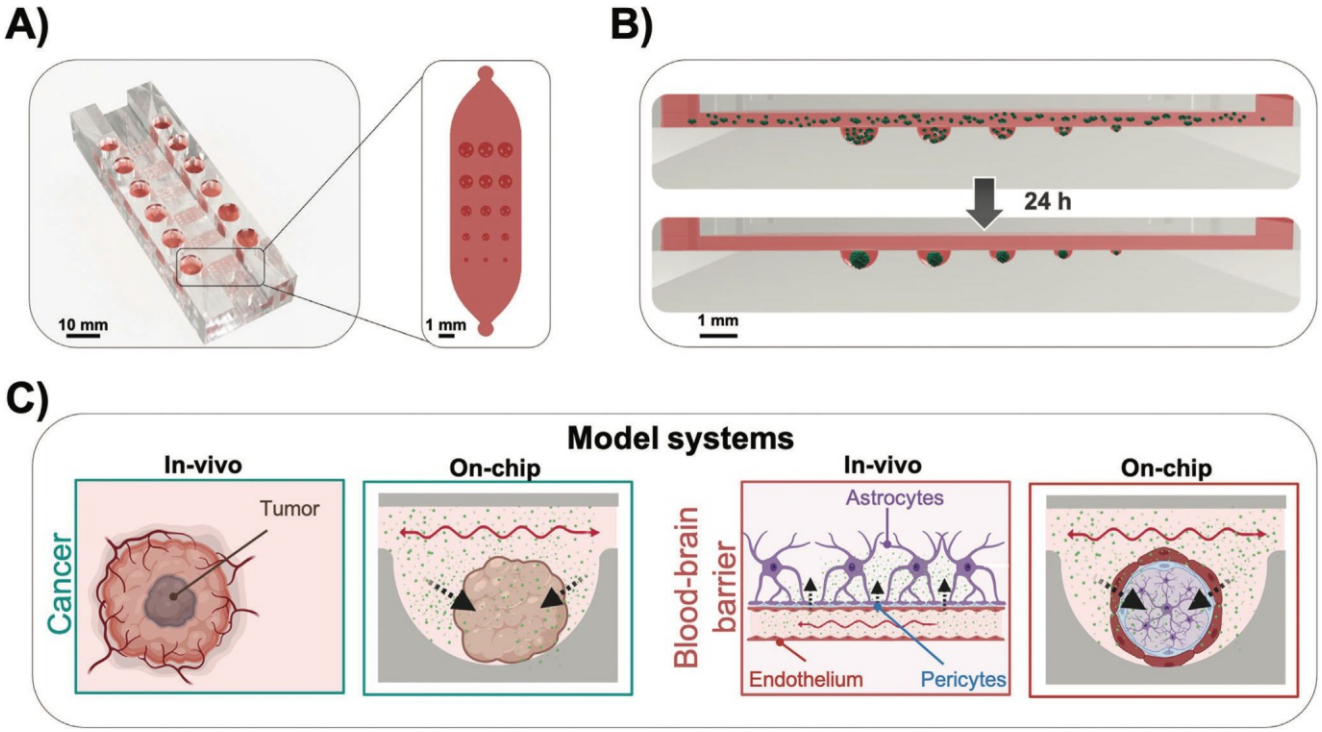

Figure 1. A) A cutaway rendering of the microfluidic spheroid array showing six microfluidic channels, each containing 15 spheroids with five different sizes and respective medium reservoirs, which can be addressed by multichannel pipettes. B) Workflow of parallel on-chip spheroid generation within 24 h. C) Overview of the established cell model systems, including spheroid tumor models and 3D BBB models for pharmaceutical screening applications. Arrows indicate diffusion of anticancer drugs or active and passive transport across the BBB in vivo and on the chip.

our microfluidic multisize spheroid array biochip includes a comparison of morphometric and metabolic parameters using four different well-established cancer and noncancerous cell lines cultured under continuous perfusion for 12 d. Practical applications of the microfluidic multicellular spheroid technology involve a) an anticancer screening approach and b) a blood–brain barrier drug penetration study as outlined in Figure 1C. Here, we demonstrate that our multisize spheroid platform is compatible with the standard software and hardware of a high-content live-cell imaging system by analyzing spheroid size, morphology, cellular activity, hypoxia levels, transport of fluorescent-labeled compounds, and drug-dose responses.

In summary, our study focuses on the establishment of a variety of in vitro spheroid-based spheroid models used i) to optimize cell culture conditions, including seeding densities and coculture cell ratios, ii) to evaluate two clinically relevant anticancer drugs for therapy optimization studies and iii) to investigate active and passive transport across the blood–brain barrier. Thus, our microfluidic multisize spheroid array closes a critical technological gap, enabling rapid and easy production of spheroids of defined size and cell types.

2. Results and Discussion

2.1. Identification of Best Microwell Dimensions for the Formation of Multisized Spheroids

Although cell trapping in microcavities is by far the most popular technique to generate spheroids in microfluidic devices, this approach results in high variability of spheroid quality, thus hindering standardization and comparability. To evaluate whether a specific geometric feature allows precise control over the formation of reproducible, uniformly sized and single multicellular spheroids of defined dimensions, various well shapes and geometries were investigated. In total, five geometries with varying dimensions as shown in **Figure 2**A, including flat-bottom wells (cylinder of 100 and 500 µm depth), spherical caps, elliptic paraboloids, and hemispheres were evaluated on their ability to generate uniform spheroids reproducibly. After 3 d postseeding, the total number of individual spheroids formed, spheroid roundness, center-to-center distance, and size controllability of HepG2 spheroids were compared using bright-field micrographs as depicted in Figure 2B (see also Figure S3, Supporting Information). Results of this comparative study are shown in **Table 1**, indicating that only hemispherical dimensions using a microlens design fostered the formation of single spheroids in every microwell diameter (total of 15 wells). In contrast, wells with sharper or flatter curvatures and cylindrical shapes revealed a higher probability of multiple spheroid formations in each cavity, thus decreasing accuracy. These results clearly eliminate flat-bottom shapes and favor round-bottom shapes to ensure reliable formation of a single spheroid within each well. To assess the influence of round-bottom microwell shapes on the quality of spheroid morphology in more detail, each spheroids' roundness was determined using cylinders (100 and 500 µm depth), a spherical cap, and a hemisphere shape. Results reveal that both the hemispherical- and the spherical cap-shapes generate highly reproducible, round HepG2 spheroids in each

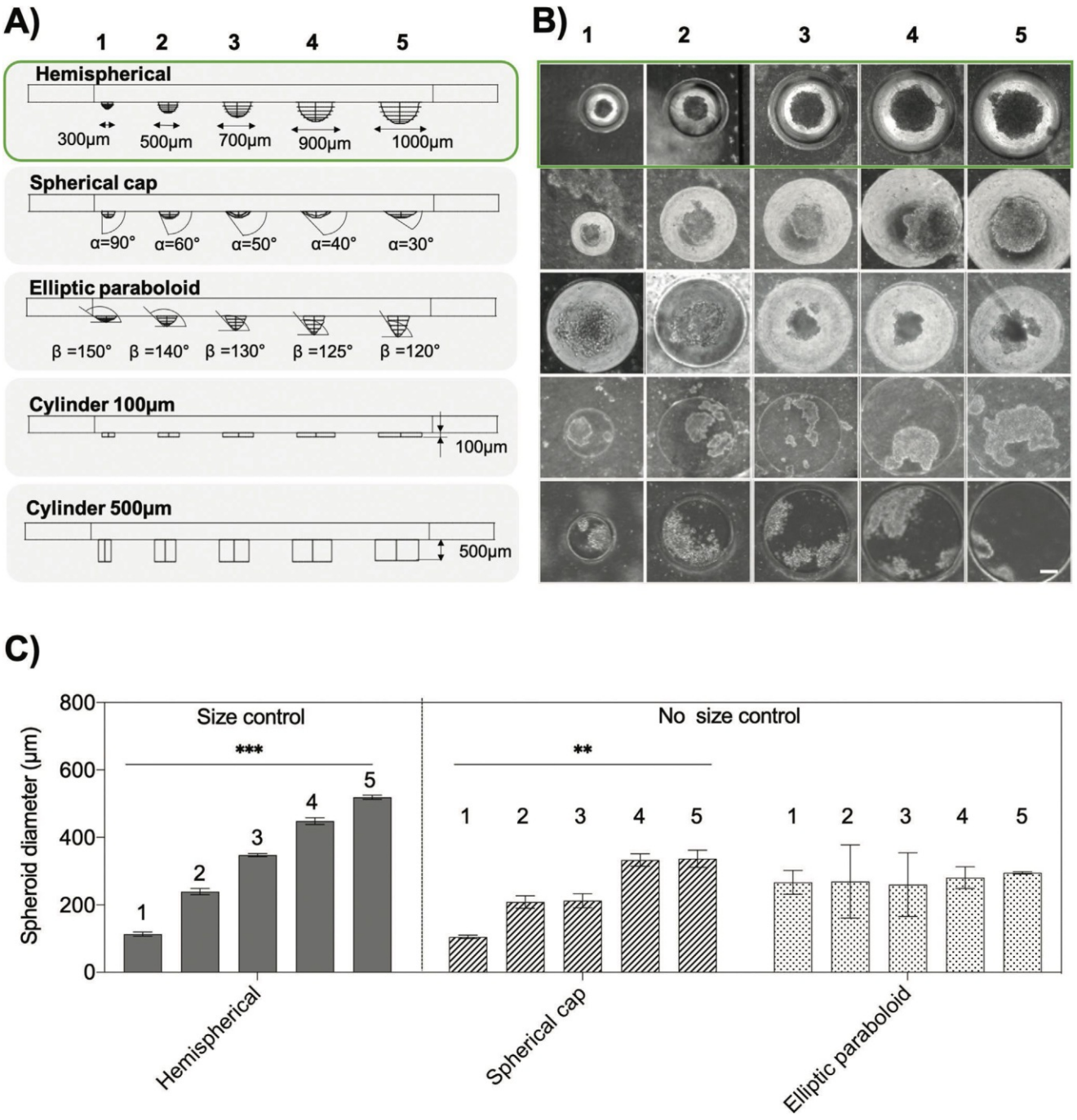

Figure 2. A) Cross-sections of CNC milled microwells of different geometries, including hemispherical microlenses, spherical caps, elliptic paraboloids, and cylinders. B) Bright-field micrographs of HepG2 spheroids after three days of on-chip cultivation. Scale bar, 100 µm. C) Optimization of microwells by evaluating the controllability of HepG2 sizes in terms of different microwell geometries, $n = 3–6 \pm$ SD. Statistical analysis was performed using the mixed-effects analysis (**$p < 0.0021$, ***$p < 0002$).

well diameter, exhibiting an overall roundness factor of 0.95 ± 0.04 and 0.94 ± 0.03, respectively. In contrast, spheroids located in flat-bottom cylinder shapes with depths of 100 and 500 µm exhibited decreased roundness with factors of 0.57 ± 0.07, 0.49 ± 0.07 for each respective shape. Additionally, spheroids formed in elliptical paraboloid-shaped wells revealed comparable roundness factors of hemispherical and cap-shaped wells only at wider polar angles of 150° and 140°. Interestingly, with an increasing polar angle, a reduction in roundness below 0.9 was observed. It is important to note that only spheroids with a roundness above 0.9 are considered as regular spherical-shaped spheroids as described in literature.[37] This means that both of the cylindrical shapes generated irregular, noncircular HepG2 spheroids.

Table 1. Optimization of microwells by evaluating a number of spheroids per well, spheroid roundness, and spheroid center-to-microwell center-distances. Data are expressed as mean value ± SD for $n = 3$. Underlined values are considered as the most optimal shape parameter.

Parameter		Hemispherical	Spherical cap	Elliptic paraboloid	Cylinder 100 µm	Cylinder 500 µm
Spheroid number per well (optimum: 1.0)	1	1.0 ± 0.0	1.0 ± 0.0	1.0 ± 0.0	2.3 ± 0.6	1.3 ± 0.6
	2	1.0 ± 0.0	1.3 ± 0.3	1.0 ± 0.0	2.7 ± 1.2	1.7 ± 0.6
	3	1.0 ± 0.0	1.0 ± 0.0	1.0 ± 0.0	6.3 ± 2.1	2.7 ± 0.6
	4	1.0 ± 0.0	1.3 ± 0.5	1.3 ± 0.6	6.0 ± 1.7	3.7 ± 1.2
	5	1.0 ± 0.0	1.7 ± 0.6	1.0 ± 0.0	7.7 ± 1.5	3.0 ± 1.0
Roundness per well [AU] (optimum ≥ 0.9)	1	1.0 ± 0.0	0.9 ± 0.0	0.9 ± 0.0	0.5 ± 0.0	0.5 ± 0.2
	2	1.0 ± 0.1	0.9 ± 0.0	1.0 ± 0.0	0.6 ± 0.1	0.5 ± 0.0
	3	0.9 ± 0.0	0.9 ± 0.0	0.8 ± 0.0	0.6 ± 0.1	0.5 ± 0.1
	4	0.9 ± 0.0	0.9 ± 0.0	0.8 ± 0.0	0.7 ± 0.1	0.5 ± 0.0
	5	0.9 ± 0.0	1.0 ± 0.0	0.7 ± 0.0	0.5 ± 0.0	0.5 ± 0.1
Center-to-center distance per well [µm] (optimum = 0 µm)	1	5.4 ± 6.6	47.3 ± 25.7	27.3 ± 19.1	76.1 ± 26.4	89.3 ± 25.60
	2	16.3 ± 8.0	55.4 ± 33.9	23.3 ± 17.7	138.4 ± 54.1	121.6 ± 31.7
	3	18.5 ± 7.5	31.7 ± 0.1	4.8 ± 1.7	228.2 ± 54.8	244.7 ± 26.3
	4	10.3 ± 2.0	40.0 ± 5.5	26.3 ± 29.6	280.4 ± 146.5	316.5 ± 59.6
	5	10.1 ± 6.3	53.9 ± 32.3	23.9±20.9	376.0 ± 113.6	410.0 ± 12.7

Final microfluidic microwell array evaluation involved reliable localization of spheroids and size control measures, which are essential aspects for automation, signal processing, and image analysis in medium- to high-throughput screening applications. While flat bottom layouts yielded the highest center-to-center distances (e.g., from 410 µm to 89 µm in 500 µm cylinders), hemispherical wells showed the lowest center-to-center variations with distances of 10.1 ± 6.3, 10.3 ± 2.0, 18.5 ± 7.5, 16.3 ± 8.0, and 5.4 ± 6.6 µm from the largest (1000 µm) to the smallest (300 µm) cavity. Based on the results above, only hemispherical, spherical cap, and elliptic paraboloid shapes were evaluated for spheroid size controllability in subsequent experiments. Results in Figure 2C demonstrate that only hemispherical cavities/microwell shapes are able to reliably generate spheroids of increasing sizes in a linear fashion exhibiting diameters of 113.1 ± 6.3, 239.3 ± 9.4, 347.5 ± 4.7, 448.4 ± 10.2, and 519.2 ± 6.4 µm. In turn, elliptical paraboloid- and spherical cap-shaped cavities resulted in an irregular and less controllable spheroids formation (no linear increase and correlation). In summary, our highly optical, transparent hemispherical microwell design based on "microlens" dimensions is ideally suited to generate spheroids of defined sizes, geometric features, and similar locations within a microfluidic spheroid array.

2.2. Characterization of Dynamic Culture Conditions Using a Bidirectional Hydrostatic Flow

Supply and continuous perfusion of cell culture medium were achieved by gravity-induced bidirectional fluid circulation using an automated tilting motion of the microfluidic multisized spheroid array, as shown in **Figure 3**A. Some advantages of this pumpless-flow strategy are the ability i) to adjust flow profiles by modifying the tilting angle and speed, ii) to reduce bubble formation, and iii) to reproduce pulsating nature of blood circulation, as depicted in Figure 3B. Since gravity-driven perfusion results in rapid flow profile changes within the microchannel network, flow restrictors are additionally embedded underneath each medium reservoir to increase the hydraulic resistances of the microfluidic channel, thus passively controlling flow velocities. To estimate fluid velocities and shear forces of the continuous bi-directional microfluidic flow under different operating conditions, computational fluid dynamics (CFD) simulations and experiments were performed. Initially, flow rates (at a period of 60 s) were determined in silico to assess three different gravity-flow protocols using a fixed tilting angle of 1° in the presence of increasing tilting speeds. Results of our fluid dynamics study are shown in Figure 3B, where reproducible net flow rates of 0.4, 1.0, and 2.1 µL min^{-1} were estimated using tilting speeds of 1, 3, and 4 rpm, respectively. An additional increase of pulsation rates from 0.01 to 0.05 Hz yielded maximal flow rates ranging from 17.4 to 70 µL min^{-1}. To validate these computational results, fluid column heights in the reservoirs were measured at defined tilting angles to calculate hydrostatic pressures and resulting flow velocities. As an example, **Table 2** shows no significant differences of simulated versus measured flow rates at increasing tilting angles and a fixed tilting speed of 1 rpm, which points to the ability to reliably control flow velocities between 15.7 ± 9.2 and 176.0 ± 33.9 µL min^{-1}. It is important to note that this elevated flow regime provided homogenous distribution of cell suspension during cell loading and trapping in microwells and efficiently removed nontrapped cells

Table 2. Experimental versus in silico data of maximum flow rates as a function of tilting angles at a constant frequency of 1 rpm. Data are expressed as mean value ± SD for $n = 6$.

Flow rate [µL min^{-1}]	Tilting angle				
	1°	3°	5°	7°	10°
Experimental	15.7 ± 9.2	57.6 ± 22.9	90.0 ± 28.6	126.3 ± 33.1	176.0 ± 33.9
Simulation	17.9 ± 0.0	53.8 ± 0.08	89.5 ± 0.1	125.1 ± 0.1	175.4 ± 0.2

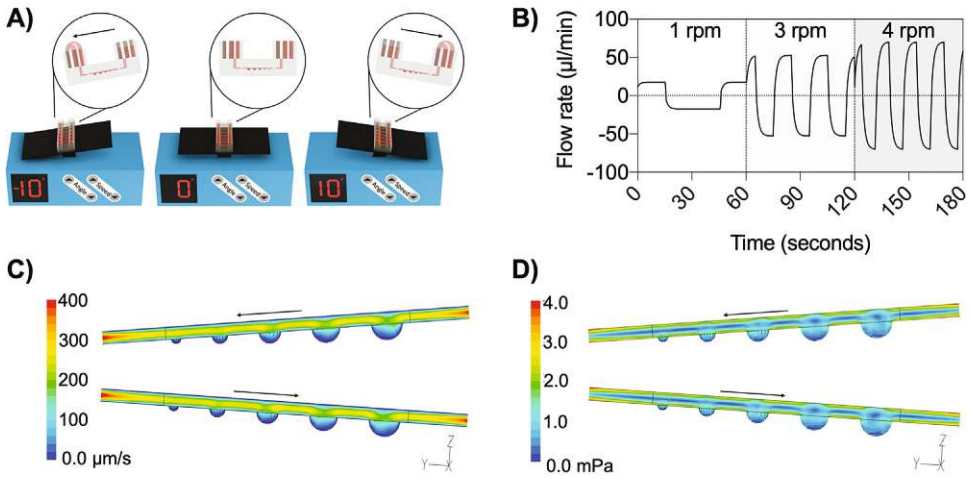

Figure 3. A) Tilting schemes of the microfluidic spheroid array system by gravity-driven flow. B) Flow profiles at tilting speeds of 1, 3, and 4 rpm at a fixed angle of 1°. C) Flow velocity and D) shear stress at a constant tilting speed of 1 rpm at a tilting inclination angle of 1° in spheroid culture channels.

in the antiadhesive coated microchannel network. To further estimate generated flow rates and shear forces present inside the cavities where spheroids reside, additional CFD simulations were performed. Results of 3D CFD simulations (see Figure 3C,D) reveal a 75% to 80% reduction in fluid velocity of 37.9 ± 16.1 µm s^{-1} in the microwells and a shear stress reduction to 1.4 ± 0.2 mPa (at a tilting angle of 1° and 1 rpm). Moreover, fluid streamlines fully enveloped the entire spheroid without indication of turbulences, thus pointing at an efficient medium turnover inside the growth compartment, as shown in Figure S4 (Supporting Information). Notably, microwell flow velocity and shear stress increased to 72.06 ± 30.8 µm s^{-1} and 2.9 ± 0.4 mPa as well as 109.2 ± 46.6 µm s^{-1} and 4.2 ± 0.6 mPa with rising tilting frequencies of 3 and 4 rpm, when keeping tilting angle constant (data not shown). These results demonstrate that pumpless gravity-driven flow is able to tune flow velocities inside the cavities and spheroids, which is needed to identify optimum cell culture conditions.

2.3. On-Chip Generation of Multitissue Spheroids and Characterization of Linear Size-Control Strategy

Since differences in tissue types and growth can result in inconsistent assessments between multiple spheroid cell-line cultures, initial testing of seeding densities is crucial to describe the cell type-specific behavior regarding spheroid size and cellular growth. One important aspect of those evaluations is the capability to assess direct relationships between initial cell seeding concentrations and spheroid sizes as well as linear spheroid size separation to ensure a broad range of dimensions on one chip. To evaluate spheroid growth rates in terms of diameter and spheroid size separation under continuous bidirectional perfusion, a panel of standardized cancer cell lines and human fibroblasts were recorded over a 12 d incubation period. **Figure 4** shows measured spheroid diameters after 3 d in culture using lung, liver, colon, and skin cell cultures in the presence of increasing seeding densities to shed light on the relationship between initial cell seeding concentrations and spheroid sizes. Interestingly, cell type-dependent spheroid diameters were already obtained after 3 d in on-chip culture ranging from a minimum to a maximum diameter of 66. 2 ± 12.6 µm to 581.4 ± 58.4 µm for lung (A540), 142.6 ± 37.6 µm to 596 ± 50.5 µm for liver (HepG2), 86.2 ± 20.0 µm to 828.7 ± 49.5 µm for colon (Caco-2) and 75.6 ± 30.3 µm to 229.2 ± 27.1 µm for skin (NHDF) spheroids. This means that by varying initial cell seeding densities a) an extensive range of spheroid sizes can be reliably generated, and b) cell line-specific growth differences can be readily evaluated using our microfluidic multisize spheroid array. For instance, looking at lung A549 spheroid growth rates revealed that smaller spheroids exhibited a substantially larger size change over a 12 d cultivation period of 45% in 500 µm diameter wells than the 30% size expansion obtained with spheroids grown in 1000 µm diameter wells (see also Figure S5, Supporting Information). In turn, liver (HepG2) and colon (Caco-2) spheroids exhibited a well diameter-independent increase of size of approximately 50% and 30%, respectively. In contrast to lung and colon epithelial cells, dermal fibroblast spheroids showed a tendency to get more compact over time where spheroid diameters in 1000, 900, 700, 500, and 300 µm wells decreased by 20.6 ± 9.9%, 16.3 ± 9.5%, 17.6 ± 6.6%, 31.0 ± 12.1%, and 24.6 ± 15.8%, respectively.

As a first practical application of the microfluidic multisize spheroid array, a seeding density optimization study was conducted using a one-way ANOVA and linear regression analyses to evaluate growth differences between the different tissue spheroid models. Initial ANOVA results showed significant differences among all evaluated seeding densities with calculated p-values between $p < 0.0332$ and $p < 0.0001$, which pointed at a reliable spheroid generation of 270 spheroids in all chips. Next, optimal seeding protocols for increasing well sizes were evaluated on day three using linear regression analysis. **Table 3** lists the calculated R^2-values of each replicate value that indicate a linear trend with increasing seeding densities. This means that optimal seeding densities in terms of statistical significance and spheroid-to-well linearity were obtained at concentrations of 3 × 10^6 cells mL^{-1} for HepG2, Caco-2, and NHDF spheroids as well as 1 × 10^6 cells mL^{-1} for A549 spheroids. As a consequence of these results, the above-optimized seeding protocols were used for all subsequent experiments. Interestingly, individual slopes

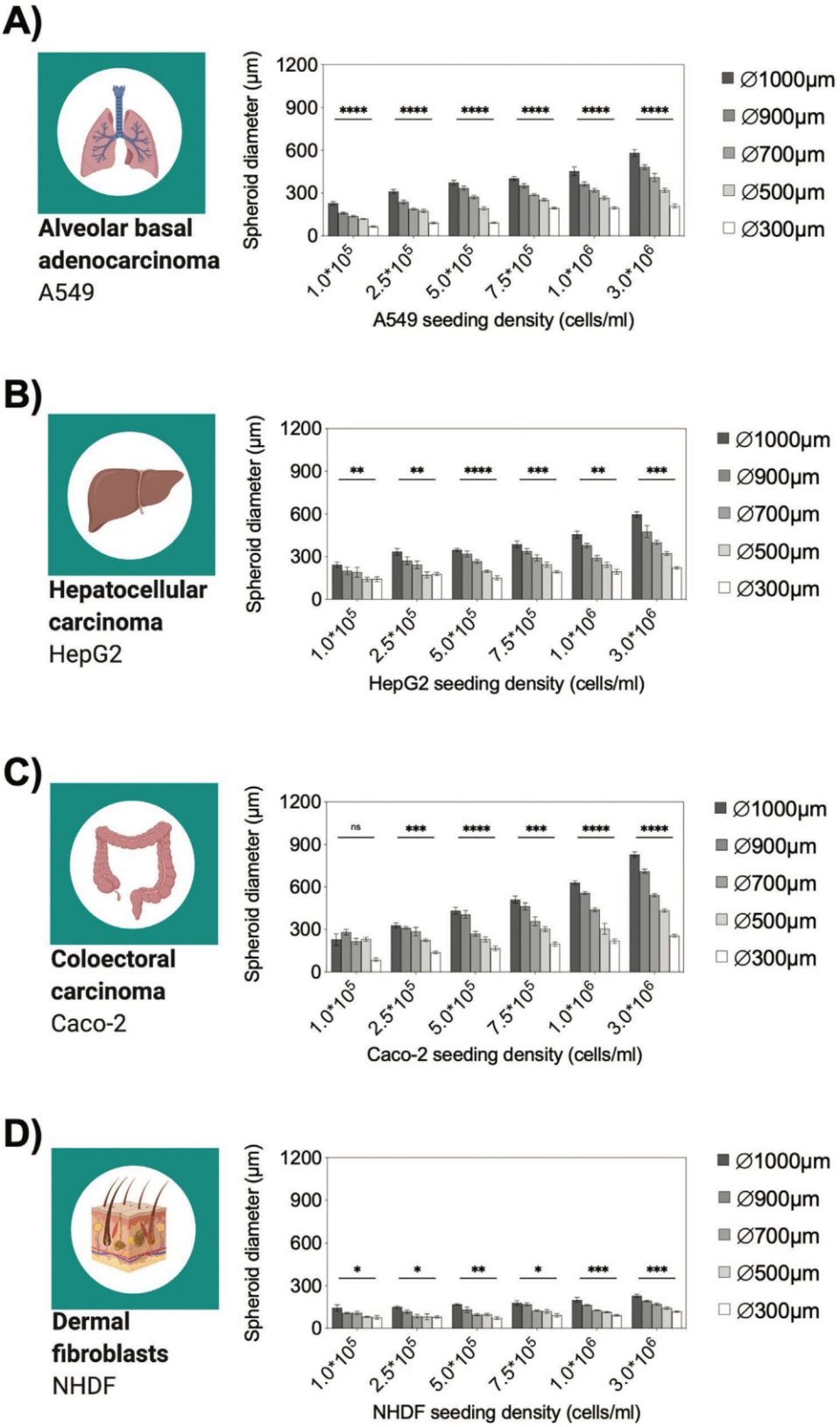

Figure 4. Analysis of spheroid diameters of A) A549, B) HepG2, C) Caco-2 and D) NHDF spheroids at different initial seeding densities after 3 d postseeding under continuous perfusion in the microfluidic spheroid array device, $n = 6–9 \pm$ SD. Statistical analysis was performed using mixed-effects analysis (*$p < 0.0332$, **$p < 0.0021$, ***$p < 0.0002$, ****$p < 0.0001$).

Table 3. Linear regression analysis and goodness-of-fit (R^2) values of generated sizes after 3 d postseeding of A549, HepG2, Caco-2, and NHDF spheroids in respect to initial seeding densities Statistical significance of respective slopes was determined by analysis of covariance (ANCOVA). Data are expressed as mean value ± SD for $n = 6$. Underlined values are considered as the most optimal seeding density.

	Seeding density [cells mL^{-1}]						
Cell line	1.0×10^5	2.5×10^5	5.0×10^5	7.5×10^5	1.0×10^6	3.0×10^6	*p*-value of slopes
A549	0.8336	0.8388	0.8251	0.8725	0.8938	0.8747	$P < 0.0001$
HepG2	0.2701	0.4697	0.8278	0.6739	0.7988	0.8345	$P < 0.0001$
Caco-2	0.1977	0.7552	0.7915	0.8140	0.9175	0.9662	$P < 0.0001$
NHDF	0.3463	0.3968	0.5596	0.5502	0.7430	0.7935	$P = 0.1387$

of the spheroid size separation can be tailored by simply adjusting initial seeding densities, thus enabling on-demand spheroid size generation depending on initial seeding densities and microwell sizes.

2.4. Multiparametric Monitoring of Multitissue Spheroids On-Chip

Using the above-optimized cell seeding densities for the five tissue types, time-resolved images of individual spheroids were taken to investigate morphology changes, esterase activity shifts, and hypoxia occurrence in the next set of experiments (see **Figure 5**A).To validate the spheroid quality of generated lung (A549), colon (Caco-2), liver (HepG2), and skin (NHDF) spheroid cultures according to optimized seeding protocols, spheroid area, perimeter, roundness, and solidity were tested in detail to determine cell-type-specific morphological differences. Results in Figure 5B show significant changes of spheroid areas among presented cell lines and microlens diameters in the range from 0.005 to 0.6 mm^2 and a direct proportional linear decrease with well diameter for A549, Caco-2, and HepG2 spheroids. In turn, NHDF spheroids showed no significant area change in all microwell sizes. In the next step, individual spheroid perimeters were determined to quantify spheroid surface structure and smoothness. Here, significant variations in the topographic structures were found between all four cell lines, where Caco-2 cells revealed the most unregular morphologies as indicated by perimeters in a range of 3.3 ± 0.3 mm. Interestingly, A549 lung and HepG2 liver cells displayed similar perimeters of 1.6 ± 0.2 and 2.3 ± 0.7 mm, respectively. Similar results were obtained in other well dimensions too. An alternative to size-related spheroid quality parameter, roundness and solidity of spheroids determines the ability to form tight well-defined round cell aggregates. Results shown in Figure 5B indicate the absence of significant roundness and solidity differences for all cell lines, thus pointing at the generation of stable and reproducible spheroids for various cell lines and tissue types.

To demonstrate that the platform's capability of performing functional fluorescent-based assays in a size-and cell type-specific manner, we next monitored time-resolved changes of esterase activity and hypoxia levels on-chip. A panel of the previously characterized cell lines was cultivated and evaluated on-chip with metabolic indicators using calcein-AM as an intracellular esterase-activity sensing solution and a reversible fluorogenic hypoxia reagent that responds to the low oxygen environment in the cell. Due to the high permeability of calcein-AM, no size-dependent differences in intracellular esterase activity were determined, except for Caco-2 cells at day three ($P = 0.0295$), as shown in Figure 5C. However, differences in overall fluorescence intensity values, thus esterase activities, were cell-line specific with significantly lower levels observable for Caco-2 cells compared to the other cell lines. In detail, A549, HepG2, and NHDF spheroids showed mean intensities of 50.5 ± 8.8, 54.3 ± 8.9, and 41.0 ± 8.0 kAU after 3 d postseeding respectively, in contrast to significantly lower ($P < 0.0001$) signal levels of Caco-2 spheroids of 24.9 ± 4.3 kAU. In addition, identification of time-dependent metabolic activity variations was also achieved. For example, after incubation for 12 d on-chip, calcein intensity changes were only significantly elevated in NHDF spheroids, while constant fluorescent values were monitored for epithelial cell lines. These results correlate to reported variations in calcein-AM and consequently intracellular esterase activities for different cell lines.[38]

Final spheroid quality evaluation involved the investigation of hypoxic conditions for a cultivation period of 12 d on-chip. Results shown in Figure 5D reveal the presence of hypoxic conditions in all spheroids after a 12 d cultivation period. High hypoxia signals of 21.1 ± 0.9 kAU were already detected at day 3 for primary fibroblast spheroids, followed by a 235% increase in hypoxia to fluorescent intensity of 70.6 ± 1.7 kAU at day 12. The parallel increase of metabolic activity in the presence of hypoxia signals confirms the reported stimulating effect of hypoxia on dermal fibroblasts during wound healing.[39–41] In contrast, epithelial tumor spheroids exhibited significantly lower hypoxic condition levels in all spheroid sizes ($P = 0.0004$) of 42.9 ± 15.7 kAU, 52.8 ± 4.5 kAU, and 16.9 ± 5.5 kAU for A549, HepG2, and Caco-2 spheroids respectively, after 12 days postseeding. Even though cancer spheroids had the highest spheroid diameters, none of the investigated models showed hypoxia on day three, indicating higher hypoxia resilience than primary fibroblasts. Considering that healthy lung alveoli face approximately 100–110 mmHg of pO_2 in contrast to a healthy colon, which is normoxic below ten mmHg pO_2,[42] these differences in metabolism and susceptibility toward hypoxia are not surprising and described as a response of cell models to in vitro culture conditions. Summarizing these results, we demonstrated that our microfluidic spheroid array system is capable of performing multiparametric prescreenings of critical spheroid parameters (as morphology, metabolic activity, and hypoxia) that are ultimately revealing cell type-, spheroid size-, and time-specific differences.

2.5. Spheroid Size-Dependent Tissue Diffusivity and Toxicity of Anticancer Drugs

In the next set of experiments, the effects of anticancer drug treatment scenarios on increasing spheroid sizes were evaluated to assess toxicity shifts resulting from diffusion-limited drug penetration. As a practical example, doxorubicin (DOX), a well-known anticancer drug (e.g., lung and ovarian cancers), was employed to assess the ability of the microfluidic multisize spheroid array to study size-dependent drug resistance of growing solid tumors.

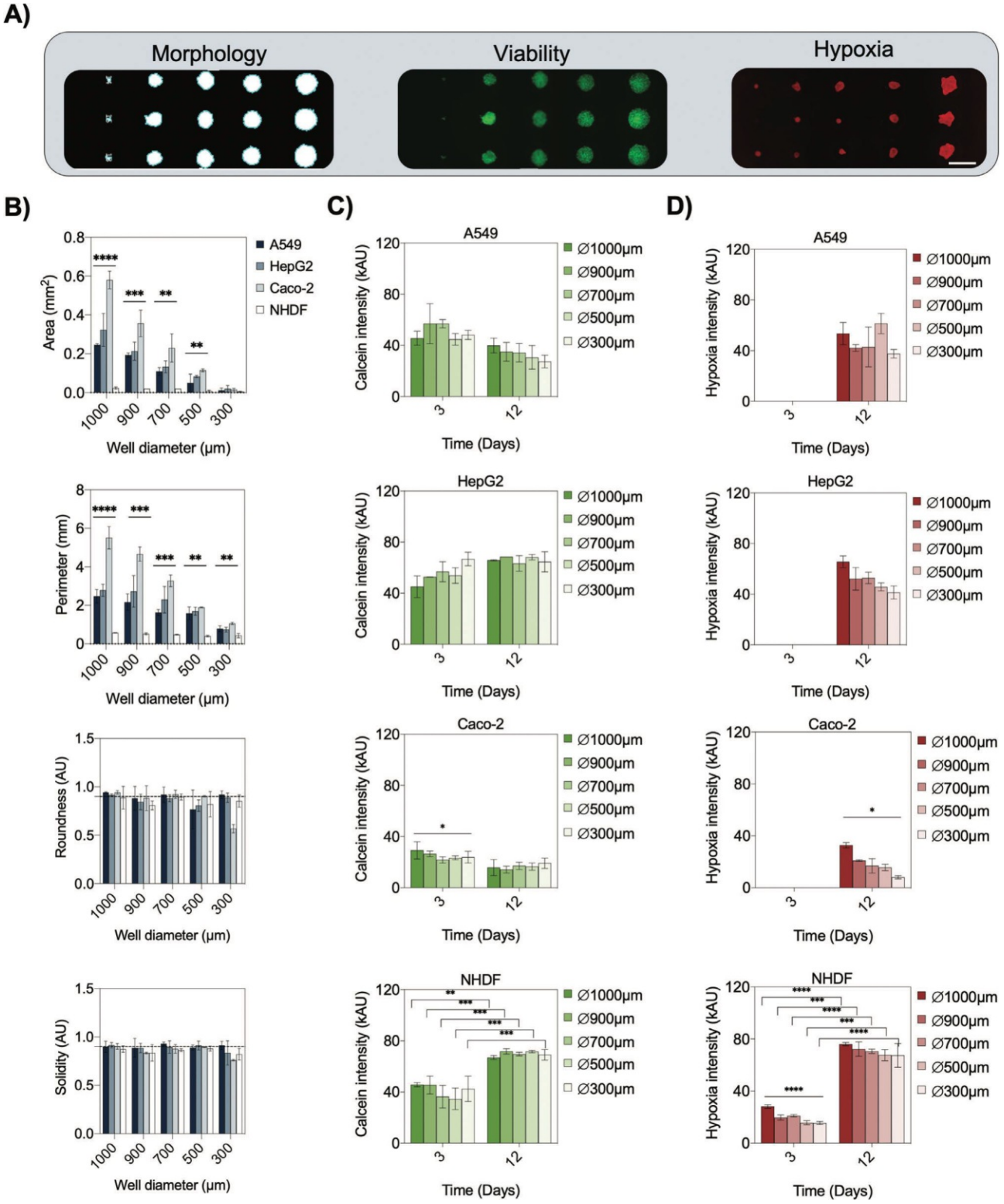

Figure 5. A) Representative bright-field and fluorescent micrographs to evaluate morphology, intracellular esterase-activity, and hypoxia during cultivation of spheroids in the microfluidic array. Scale bar, 1 mm. B) Morphometric analysis of area, perimeter, roundness, and solidity of A549, HepG2, Caco-2, and NHDF spheroids with different sizes, $n = 3 \pm$ SD. Statistical analysis was performed using the one-way ANOVA (*$p < 0.0332$, **$p < 0.0021$, ***$p < 0002$, ****$p < 0.0001$). C) Calcein and D) Hypoxia fluorescence intensities of the four cell lines at day 3 and 12 postseeding on-chip of different sizes, as indicated in each graph, $n = 3 \pm$ SD. Statistical analysis was performed using one-way ANOVA and Holm-Sidak's multiple comparisons test (*$p < 0.0332$, **$p < 0.0021$, ***$p < 0.0002$, ****$p < 0.0001$).

Initially, multisized lung cancer spheroids (A549 cell line) were treated over 4 h with the autofluorescent drug DOX to determine time-resolved diffusion. Results shown in **Figure 6**A (see also images in Figure S7, Supporting Information) reveal i) a Gompertzian growth at a DOX concentration of 100×10^{-6} M, ii) a continuous exponential growth at 10×10^{-6} M, and iii) a linear increase at 1×10^{-6} M. Additionally, significant lower signals were observed for 1×10^{-6} M DOX in larger spheroids, thus verifying a size-dependent diffusion barrier resulting in increasing diffusivities over time of 2.1 ± 0.4 kAU h^{-1} in 1000 µm, 2.4 ± 0.4 kAU h^{-1} in 900 µm, 3.0 ± 0.5 kAU h^{-1} in 700 µm, 3.0 ± 0.4 kAU h^{-1} in 500 µm and 3.3 ± 0.3 kAU h^{-1} in 300 µm wells ($P < 0.0001$). Overall, diffusivity results considering all DOX concentrations and spheroid dimensions indicated an indirect proportional correlation between spheroid size and drug transport.

Since drug combinations are often used in cancer therapy, the synergistic effects of doxorubicin (DOX) and cisplatin (CIS) medications are investigated on-chip to identify the optimal concentration ratio for, e.g., lung cancer treatment. To evaluate a potential application of the microfluidic multisize spheroid array for cancer therapy optimization studies, dose-depended effects of CIS and DOX combinations, multisized A549 spheroids were stained with Hoechst and ethidium-homodimer-1 and imaged after 24 h of drug exposure. Spheroid viabilities were calculated as the ratio of cell nuclei to dead cells (see Figure S8, Supporting Information) using background-subtracted images. Results in Figure 6B show obtained size-dependent drug dose relationships of CIS and DOX. Interestingly, at higher CIS concentrations of 1—500×10^{-6} M, smaller sized-spheroids such as 300 µm diameter displayed higher drug sensitivity than 900 µm diameter spheroids, while higher DOX concentrations resulted in similar toxicities independent of each spheroid size. Additionally, calculated Hill slopes from the sigmoidal dose–response curves suggest faster cellular responses to increasing CIS concentrations (e.g., Hill slope of -1.2 and -4.5) than DOX (e.g., Hill slope of -0.8 to -1.1). Furthermore, a size-dependent comparison of IC_{50} values (see Figure S9, Supporting Information) between larger (e.g., 474.0. ± 64.3, 364.7 ± 41.7, 320 ± 31.2, 266.6 ± 26.7 µm) and smallest (e.g., 197.2 ± 23.1 µm in 300 µm wells) A549 lung cancer spheroids revealed that a 1.5 to 2.7-fold higher CIS and a 2.3 to 6.9-fold higher DOX concentration is needed to reach a 50% inhibition of spheroid viability, thus confirming the influence of spheroids size on drug response. To finally evaluate the ability of the microfluidic multi-size spheroid array to accomplish therapy optimizations, the effect of combinatorial drug concentrations on increasing tumor sizes was investigated to identify the best CIS:DOX ratio capable of eliminating all tumor spheroids independent of their sizes. Results in Figure 6C are represented as a heat map to better visualize A540 spheroid viabilities in the presence of reciprocal CIS:DOX mixtures. Remarkably, only in the presence of 0.1–5 $\times 10^{-6}$ M CIS and 500–50 $\times 10^{-6}$ M DOX mixtures, size-independent anticancer effects were obtained for all spheroid sizes. All other drug combinations resulted in size-related toxicity variations, as shown in Table S1 (Supporting Information). It is important to highlight that spheroid sizes significantly impact toxicities in the presence of the pure drugs CIS and DOX even at high concentrations of 500×10^{-6} M, while the synergistic combinatorial effect of CIS:DOX ratio ($5{:}50 \times 10^{-6}$ M) effectively eliminates tumor spheroids using reduced drug concentrations (e.g., factors of 1 for CIS and 10 for DOX).

Table 4. Linear regression analysis and goodness-of-fit (R^2) values of generated sizes of BBB spheroids after six days postseeding, including human primary astrocytes (hA), human primary pericytes (hP), and immortalized hCMEC/D3 (BEC) in a ratio of 1:1:3 in respect to initial seeding densities. Statistical significance of respective slopes was determined by analysis of covariance (ANCOVA). Data are expressed as mean value ± SD for $n = 6$. Underlined values are considered as the most optimal seeding density.

	Seeding densities [cells mL^{-1}]				
BBB triple-culture	1.0×10^6	2.0×10^6	3.0×10^6	5×10^6	*p*-value of slopes
hA:hP:BEC (1:1:3)	0.9071	0.8389	0.9096	<u>0.9318</u>	$P = 0.0009$

2.6. Spheroid Size-Dependent Compound Penetration across an Advanced 3D Blood–Brain Barrier Model

Since compound permeability across biological barriers constitutes an important aspect in the pharmaceutical drug development process, an advanced 3D blood-brain barrier (BBB) model was established on-chip to monitor brain-penetrating drugs. Although altered BBB functions are observed in several diseases of the central nervous system, little is known about possible tissue size-dependent effects on barrier function, which could severely limit the reproducibility of current in vitro spheroid models.[43] A scheme of the microfluidic spheroid triple-culture consisting of human brain endothelial cells, pericytes, and astrocytes is shown in Figure 1C (right panel). The major advantage of the 3D model over commonly used in vitro models, including, e.g., transwells, is based on direct cell–cell contact allowing increased cell-to-cell interactions, which, in turn, leads to enhanced BBB integrity.[44] Thus, cell numbers, ratios, and sizes may influence barrier function. To investigate the ability of the microfluidic multisized spheroid array to reliably induce the formation of BBB spheroids, human primary astrocytes (hA) and human primary pericytes (hP) were cultivated with immortalized hCMEC/D3 (human cerebral microvascular endothelial cell line D3; BEC). Initial cell density optimization was conducted using a ratio of 1:1:3 (hA:hP:BEC) to evaluate the generation of 3D BBB spheroids on-chip under continuous perfusion for 6 d postseeding. Results in **Table 4** show reliable production of multisize spheroids using seeding densities above 3×10^6 cells mL^{-1} with optimal size-linearity at 5×10^6 cells mL^{-1} ($P = 0.0002$, $R^2 = 0.9096$). The results further highlight the ability of the microfluidic platform for cell culture optimization studies. To confirm the spontaneous formation and structural organization of different-sized BBB triple-cultures on the microfluidic spheroid array, each cell type was pre-labeled with cell labeling fluorescent dyes to visualize human astrocytes, human pericytes, and BECs, as shown in Figure S10 (Supporting Information). As observed in previous studies,[45,46] astrocytes were mostly located in the spheroid core, covered by hP, and surrounded by an endothelial cell layer indicating directed self-organization of all three cell types within differently sized spheroids.

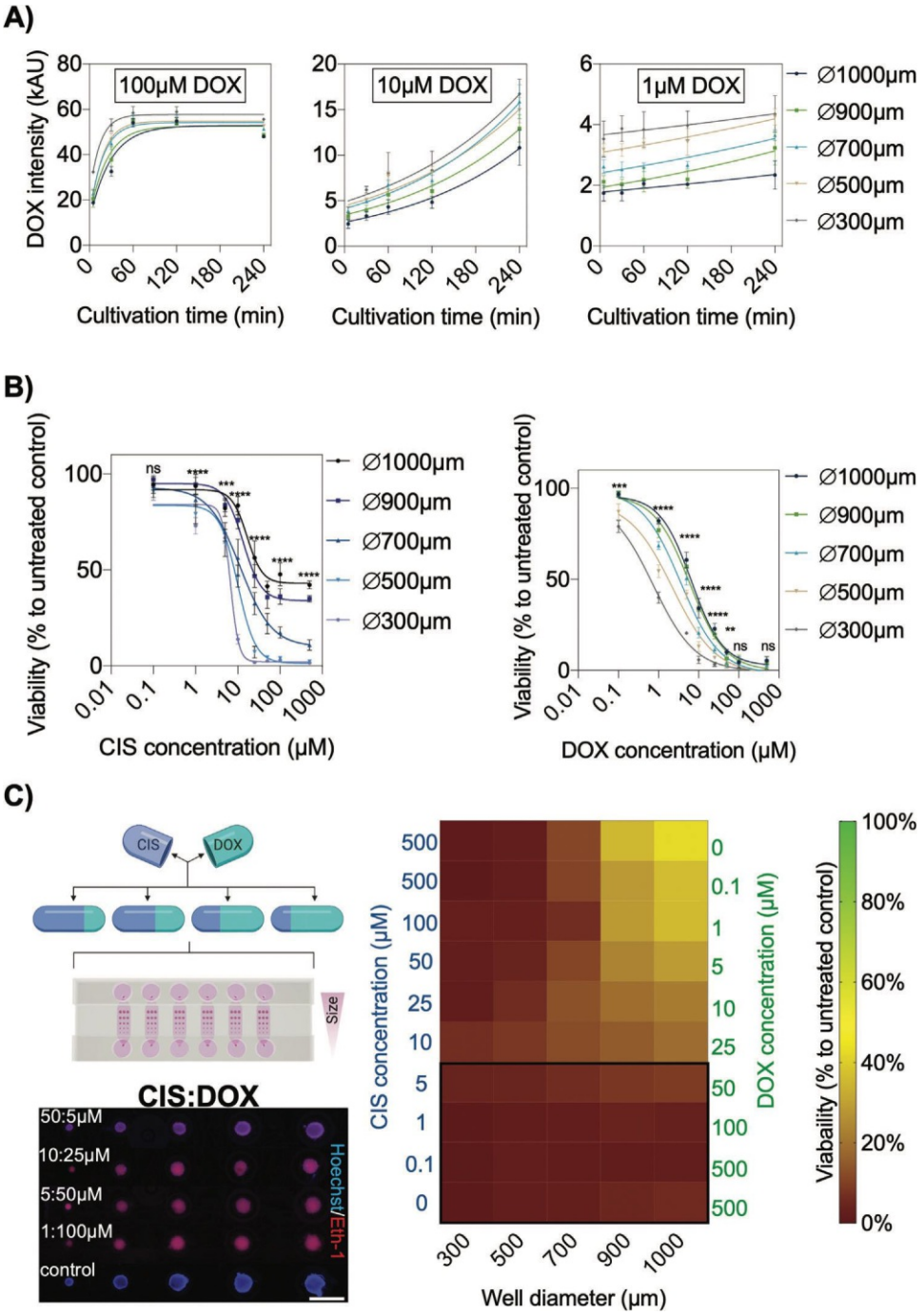

Figure 6. A) Monitoring of on-chip A549 spheroid penetration of 100×10^{-6} M, 10×10^{-6} M, and 1×10^{-6} M doxorubicin (DOX) over a cultivation period of 4 h, $n = 6 \pm$ SD. B) Dose-response relationships of CIS and DOX treated A549 spheroids of different sizes (generated in 1000, 900, 700, 500, and 300 µm microwells) in the spheroid array chip for 24 h using a dye exclusion assay (Hoechst; cell nuclei and ethidium homodimer-1; dead cells), $n =$ 4–6 ± SD. Statistical analysis of respective CIS and DOX concentrations was performed using the mixed-effects model. (*$p < 0.0332$, **$p < 0.0021$, ***$p < 0.0002$, ****$p < 0.0001$). C) Combinatorial on-chip drug screening of CIS and DOX in correlation to untreated controls after 24 h exposure of A549 spheroids of various dimensions, $n = 3$–6 ± SD. Corresponding fluorescent micrographs of treated different-sized A549 spheroids of CIS:DOX for 24 h to screen drug toxicity by staining cell nuclei (Hoechst; blue) and dead cells (Ethidium homodimer-1; red). Scale bar, 1 mm.

Table 5. Efficient Permeability P_e of BBB spheroids of different sizes and cell ratios after 1 and 4 h of cultivation with 10×10^{-6} M FD4. Data are expressed as mean value ± SD for $n = 6$.

BBB seeding ratio (hA:hP:BEC)	Efficient permeability P_e (10^{-6} cm s^{-1})									
	1000 µm		900 µm		700 µm		500 µm		300 µm	
	1 h	4 h	1 h	4 h	1 h	4 h	1 h	4 h	1 h	4 h
1:1:3	3.3 ± 0.6	7.8 ± 1.3	4.5 ± 1.1	8.3 ± 1.1	4.9 ± 2.0	8.9 ± 2.3	5.2 ± 0.5	9.1 ± 1.3	6.2 ± 2.9	10.6 ± 2.3
1:1:2	6.0 ± 0.5	8.8 ± 1.4	7.5 ± 1.6	9.9 ± 1.4	8.1 ± 2.8	10.0 ± 1.8	8.9 ± 1.1	11.3 ± 2.1	9.9 ± 2.4	11.4 ± 3.0
1:1:1	7.0 ± 2.2	11.5 ± 2.1	9.2 ± 1.4	12.7 ± 1.4	9.6 ± 1.8	14.2 ± 1.4	10.4 ± 2.3	13.3 ± 2.8	11.1 ± 3.7	13.5 ± 1.2
5.5:1.5:3	2.9 ± 0.7	7.1 ± 1.5	4.4 ± 1.0	8.3 ± 1.9	5.1 ± 1.3	8.7 ± 2.2	4.6 ± 0.7	9.5 ± 2.3	5.4 ± 2.0	11.2 ± 1.1
1:0:0	11.5 ± 3.0	12.7 ± 1.9	11.8 ± 3.3	13.8 ± 3.3	12.1 ± 2.4	14.6 ± 2.9	12.4 ± 3.4	15.3 ± 2.6	14.1 ± 3.0	16.9 ± 3.6

In the next set of experiments, BBB spheroids were formed with varying hA:hP:BEC cell ratios (e.g., 1:1:1, 1:1:2, 1:1:3, 5.5:1.5:3, 1:4:0, and 1:0:0) and sizes to investigate the influence of spheroid size and respective cell ratio on active and passive transport mechanisms (see also Table S2, Supporting Information). Interestingly, control experiments using astrocytes and pericytes as coculture caused single-cell artifacts on the bottom of the microwells (see Figure S11A, Supporting Information), indicating that pericytes, by themselves, lack the ability to align on the surface of astrocytes showing their intrinsic function to mediate between brain endothelium and astrocytes.[45,47,48] As a result of our BBB spheroid study (see **Figure 7**A), the robust generation of a multisized spheroid triple-culture BBB model on-a-chip was demonstrated since the presence of different cell ratios showed no significant size variations independent of the employed hA:hP:BEC ratio. For instance, hA:hP:BEC ratios of 1:1:3, 1:1:2, 1:1:1, and 5.5:1.5:3 (with a total seeding density of 5×10^6 cells mL^{-1}) resulted in the generation of 475.1 ± 38.5 µm and 177.9 ± 55.5 µm in 1000 µm and 300 µm diameter hemispherical wells. In turn, significantly smaller spheroid sizes were obtained in the presence of single-cell type spheroids (hA:hP:BEC ratio of 1:0:0) despite similar cell seeding densities, thus indicating the impact of cell-to-cell interaction on spheroid growth and size. Additionally, significant differences in spheroid size-dependent well diameter were found at all cell ratios as well as the generation of single round BBB spheroids (as shown in Figure S11B,C, Supporting Information).

In the next step, time-resolved compound accumulation in spheroids of increasing sizes and six different cell type ratios was investigated for a period of 4 h following exposure to 10×10^{-6} M 4kDa FITC-dextran (FD4). As an example of this comparative study, Figure 7B shows representative high-resolution images of a single cell culture chamber containing 15 multisized BBB spheroids at a cell ratio of 1:1:3 (hA:hP:BECs) after 1 h of FD4 exposure (see also Figure S11D, Supporting Information). Fluorescent intensity profile analysis of spheroid cross-sections revealed apparent size-dependent fluorophore accumulation behavior, where FITC–dextran levels gradually decrease towards the spheroid core in the presence of larger spheroids (above 500 µm diameter wells). Results of all applied seeding ratios and sizes are shown in Figure 7C, exhibiting size-dependent FD4 compound accumulation following a 4 h exposure. In summary, independent of spheroid size, hA monoculture spheroids showed significantly higher FD4 fluorescence intensities in a range of 29.7–31.7 kAU compared to hA:hP:BEC triple-cultures, indicating the absence of a functional cell barrier in hA-spheroids. Additionally, a general size-related transport effect was revealed, suggested by a 24.6 ± 4.4% lower FD4 accumulation in large triple-culture spheroids in 1000 µm wells than in smaller spheroids in 300 µm wells. Large BBB spheroids with a 1:1:3 cell ratio constituting the highest total number of endothelial cells (3×10^6 cells mL^{-1}) exhibited a distinct barrier integrity with a low FD4 signal of 19.7 ± 2.7 kAU, which was also reflected in the efficient permeability coefficient of 3.3 ± 0.6 × 10^{-6} cm s^{-1} after 1 h of FD4 incubation (see **Table 5**). Remarkably, when shifting the ratio to 5.5:1.5:3, containing the lowest total cell numbers of pericytes (0.7×10^6 cells mL^{-1}) and brain endothelial cells (1.5×10^6 cells mL^{-1}), but the highest astrocyte fraction (2.75×10^6 cells mL^{-1}), results still showed low permeability of 2.9 ± 0.7 × 10^{-6} cm s^{-1}, which underlined the influence of each cell type on barrier properties and revealed the importance to prescreen optimal BBB spheroid models for, e.g., compound uptake studies. Furthermore, these results are in line with reported FD4 permeability coefficients of other BBB models.[49,50]

In order to analyze barrier integrity in more detail, differences in localization and continuity at the spheroid's outer rims of tight junction-associated protein zonula occludens-1 (ZO-1) were investigated by immunofluorescence staining of histological sections (see Figure 7D). Large triple-culture spheroids generated in 900 µm hemispherical wells showed increasing ZO-1 localization and thickness proportional to endothelial cell content. Additionally, small spheroids (300 µm) displayed weaker and more discontinued ZO-1 signals correlating with the elevated FD4 permeability. As expected, hA spheroids with no endothelial barrier were void of ZO-1 signal at the outermost spheroid surface with the highest FD4 permeability values. Overall, results of our microfluidic 360-spheroid array indicate that identification and pre-screening of barrier properties prior high-throughput testing should be performed multiparametric since parameters as spheroid size or cell-composition alone fail to provide conclusive evidence concerning transport properties and best performing BBB models.

Final practical evaluation of the microfluidic multisize spheroid array involved the investigation of spheroid size-related effects on FD4 accumulation in the presence of the BBB opening agent mannitol, which has been exploited as a drug and therapeutic agent delivery system for facilitating the entrance of therapeutic biologics into the brain.[51] Results of FD4 accumulation

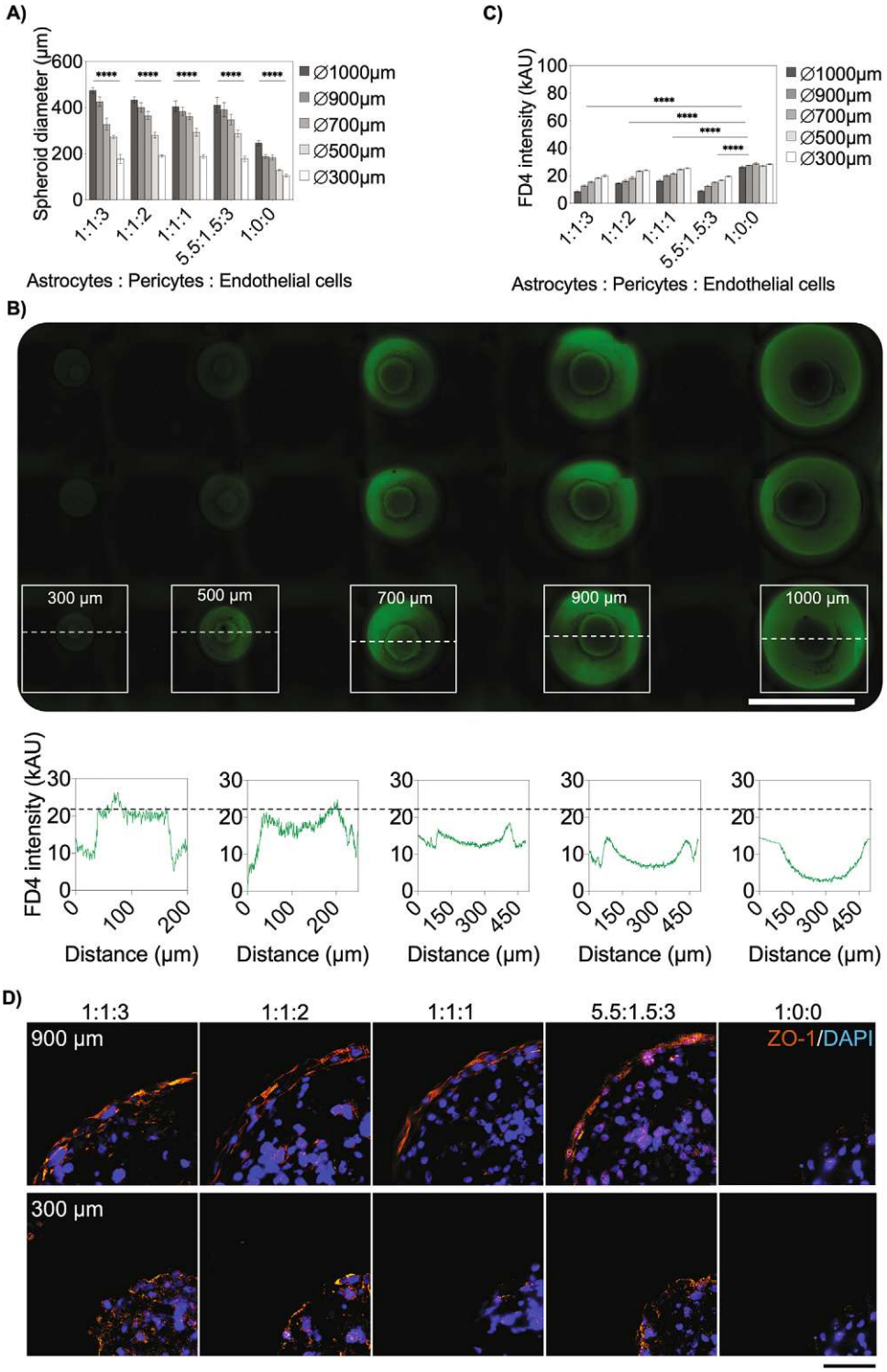

Figure 7. A) Spheroid diameters at the same total cell numbers and different seeding ratios of hA, hP, and hCMEC/D3 after 6 d postseeding, $n = 6–9 \pm$ SD. Statistical analysis was performed using the mixed-effects model. B) Fluorescence plot profiles of 4 kDa FITC-dextran (FD4) treated different-sized BBB spheroids after one hour, seeded at a cell ratio of 1:1:3. Scale bar, 1 cm. C) Mean fluorescence intensities of triple-culture spheroids of different sizes and cell ratios after 4 h of cultivation with 10×10^{-6} M FD4, $n = 9–12 \pm$ SD. Statistical analysis was performed using Dunnett's multiple comparisons test. (*$p < 0.0332$, **$p < 0.0021$, ***$p < 0.0002$, ****$p < 0.0001$). D) Immunofluorescence staining of tight-junction associated protein ZO-1 (orange) of large (900 µm) and small (300 µm) BBB spheroids of various cell seeding ratios. Cell nuclei were stained with DAPI (blue). Scale bar, 50 µm.

studies are shown in **Figure 8**A where a clinically relevant mannitol concentration (e.g., 1.6 M),[52,53] was applied as an indicator of barrier integrity loss in our BBB-chip model. For instance, a comparable FD4 signal increase of 1.6 to 2.8-fold was observed in all spheroid samples independent of the used cell ratios after a four-hour incubation period, thus confirming the barrier opening effect of mannitol. However, mannitol treatment of triple-culture spheroids resulted in an indirect proportional increase of FD4 accumulation with decreasing spheroid size. In more detail, a size-dependent variation in FD4 accumulation exhibiting an increasing mean FD4 signal fold change relative to untreated control of 1.8 ± 0.1, 1.9 ± 0.1, 2.2 ± 0.1, 2.5 ± 0.2, and 2.6 ± 0.1 was observable in smaller BBB spheroids sizes. Additional time-resolved FD4 accumulation tests using largest (1000 µm wells) and smallest BBB spheroids (300 µm wells) were conducted to assess passive uptake kinetics of untreated and mannitol-treated spheroids of varying cell ratios as shown in Figure 8B. Generally, smaller spheroids revealed $79.8 \pm 19.8\%$ significantly higher FD4 signal intensities in mannitol-treated triple-culture spheroids than larger ones (e.g., 46.6%) and untreated spheroids of similar sizes (31.2%). In contrast, astrocyte monoculture spheroids showed comparable fluorescence signals in both sizes during mannitol treatment, confirming the absence of BBB endothelium. Furthermore, results of treated spheroids showed similar FD4 transport kinetics in accumulation of $16.3 \pm 4.6\%$ and $17.8 \pm 4.0\%$ with brain endothelial (hA:hP:BEC) ratios of 1:1:3 and 5.5:1.5:3, while increased uptake levels of $28.1 \pm 0.8\%$, $29.6 \pm 9.4\%$, and $25.2 \pm 2.8\%$ were observed in spheroids consisting of smaller BEC fractions of 1:1:2, 1:1:1, and 1:0:0, respectively. Similar phenomena could also be observed after washing spheroids with PBS (w/wo mannitol) to monitor FD4 efflux. For instance, after 1× PBS, FD4 signals in larger spheroids remained stable in treated and untreated spheroids at 1:1:3 and 5.5:1.5:3 ratios, in contrast, mannitol treated spheroids of 1:1:2, 1:1:1, and 1:0:0 fractions showed significant signal reductions relative to control of $48.1 \pm 3.4\%$, 50.8 ± 4.1, and $33.2 \pm 9.0\%$, respectively. Interestingly, smaller spheroids revealed a higher signal decrease for all cell ratios in the presence of mannitol versus untreated control of approximately 74%. Overall, these paracellular tightness studies not only verify the barrier opening effect of mannitol in triple-culture BBB spheroids based on astrocytes, pericytes, and brain endothelial cells but also highlight a spheroid size-related modulation on passive, paracellular transport properties.

In the last set of experiments, active transport of compounds into our advanced 3D BBB model was investigated. Here, spheroids were treated with the potent P-gp inhibitor verapamil, which is known to inhibit efflux of the P-gp substrates rhodamine123 and doxorubicin,[54,55] to examine efflux pump activities of multisized BBB spheroids. Results in Figure 8E show compound accumulation by measuring fluorescence intensities found in the spheroid cores of increasing sizes and different cell ratios as an indicator of active efflux of rhodamine123 (RHO), doxorubicin (DOX), and 4kDa FITC-dextran (FD4) in the absence and presence of verapamil. An effective inhibition of the efflux pump activities in verapamil-treated multisized spheroids was found independent of the cell ratios, resulting in an increased accumulation compared to FD4 of 31.3%–43.8% of the P-gp substrates RHO and 8.6%-24.9% in DOX-treated multisized, triple-culture BBB spheroids. In contrast, monoculture spheroids indicated enhanced spheroid core accumulation, shown by a $66.1\% \pm 6.5\%$ increase of RHO and $47.4 \pm 8.8\%$ of DOX in correlation to FD4. These results showed that verapamil did not affect FD4 uptake, verifying an effective blockade of the ABC transporter and enabling an increased transcellular accumulation of RHO and DOX. In turn, DOX accumulation was mainly unaffected by verapamil treatment in the largest triple-culture spheroids, while little increase of fluorescence signals was found in smaller spheroids. This underlines that a spheroid size-dependent active compound accumulation was observed with clear differences in RHO, DOX, and FD4 uptake rates in the largest triple-culture spheroids (1000 µm wells) of $P = 0.0006$ in comparison to smallest spheroids (300 µm wells). These findings strongly suggest that RHO accumulation in triple-culture spheroids was enhanced at all seeding ratios and spheroid sizes due to treatment with verapamil, while DOX accumulation was mainly observed in small spheroids, thus highlighting the importance of uniform spheroid dimensions and cellular ratios for BBB compound uptake studies. Therefore, the perfused BBB spheroid chip model represents a scalable cell culture tool due to the simplicity of the approach to establish 3D aggregates and the capability to screen multiple BBB spheroid architectures for studying drug transport mechanisms on a single device.

3. Conclusion

Current 3D spheroid methodologies generate spheroids that vary in size, morphology, and complexity. This leads to challenges in obtaining standards concerning culture and assay protocols as well as output data for any given cell type and tissue model.[17] Next-generation spheroid technologies, therefore, need to ensure higher reproducibility, multiparametric analysis, compatibility of readout techniques, and better automation, to establish standardized and validated in vitro 3D tissue models with improved quality, consistency, and predictive capacity. To address these shortcomings, we designed, fabricated, and tested a microfluidic chip system capable of reliably generating a large number of spheroids of defined sizes, which can be readily integrated into pharmaceutical workflows. Overall, the device is easy to operate, robust, and potentially compatible with other technologies, such as robotic pipetting, live-cell imaging, plate readers, and laboratory tilting platforms.

To date, the majority of commercial and academic approaches for spheroid generation are still based on static culturing conditions such as ultra-low attachment plates (e.g., Aggrewell plates) or 384-hanging drop systems. Recent studies have shown that microfluidic technology has contributed significantly to spheroid research by addressing the deficiencies of static methods such as variable spheroid diameters, laborious handling, high reagent consumption, and better recapitulation of the in vivo microenvironment. Even though perfused spheroid culture platforms have been developed over the last decade,[36] these microfluidic devices have not entered the market yet. This can be attributed to extensive operational know-how requirements, the lack of scale-up and parallelization possibilities as well as limited throughput of the devices (e.g., 24 or 96 spheroids on one plate).[25,32] Here, our plug-and-play microfluidic multispheroid array in well-plate format shows great potential to enable user-friendly, medium-to-high-throughput microfluidic prescreening (e.g., culture

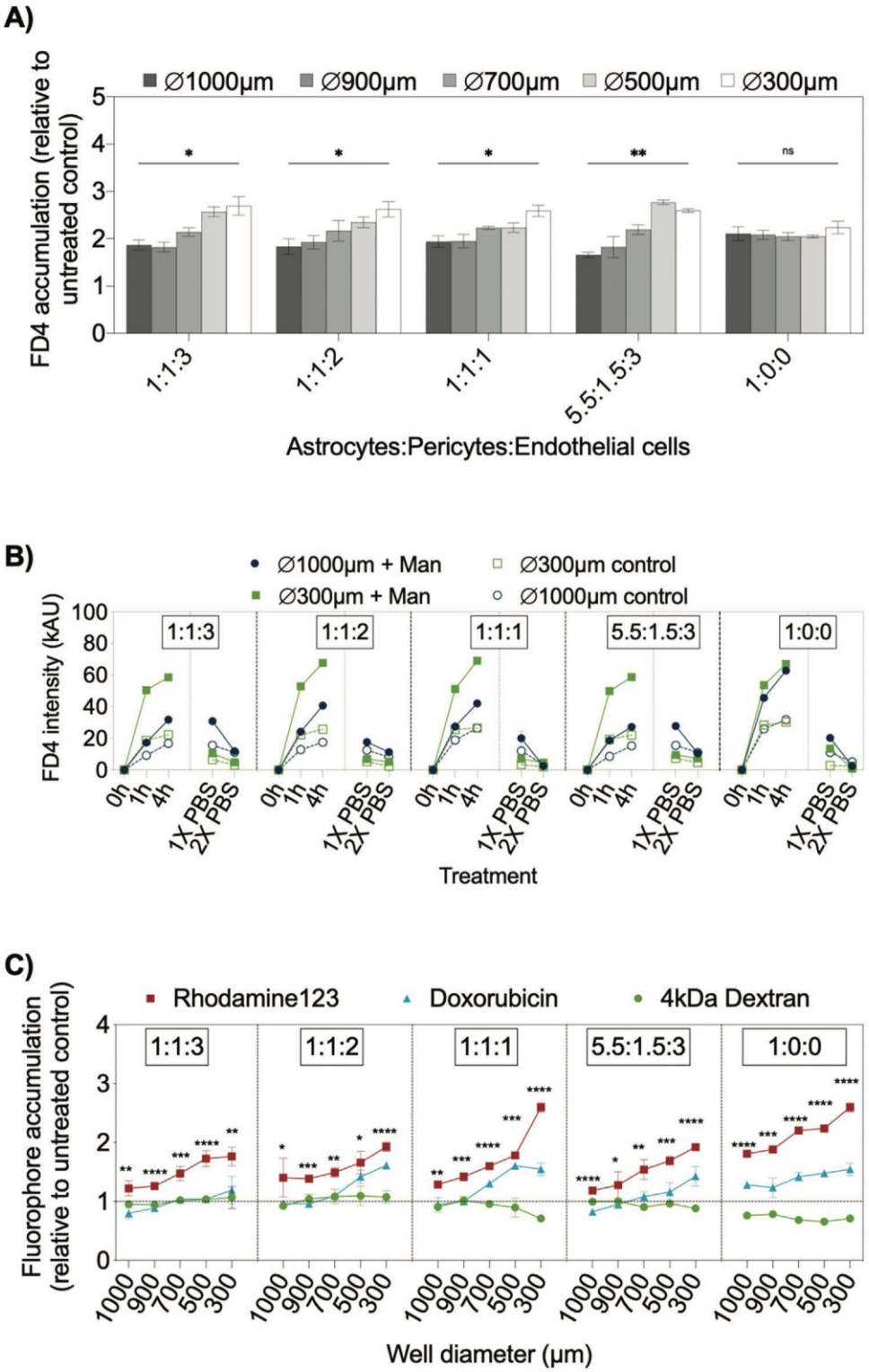

Figure 8. A) Accumulation fold change of 4 kDa-FITC dextran (FD4) of mannitol treated BBB spheroids at various cell ratios and sizes in correlation to untreated controls after 4 h of incubation. Statistical analysis was performed using one-way ANOVA, $n = 3 \pm$ SD (*$p < 0.0332$, **$p < 0.0021$, ***$p < 0.0002$, ****$p < 0.0001$). B) Time-resolved FD4 intensity profiles of largest (1000 µm) and smallest (300 µm) BBB spheroids during incubation of treated (+1.6 M mannitol) and untreated BBB spheroids, $n = 3 \pm$ SD. C) Effects of 100×10^{-6} M P-gp inhibitor verapamil on fluorophore accumulation of 10×10^{-6} M 4 kDa FITC–dextran, 10×10^{-6} M rhodamine123, 1×10^{-6} M doxorubicin after 1 h of incubation in BBB spheroids in correlation to untreated control without verapamil, $n = 3 \pm$ SD. Statistical analysis of significance between fluorophore accumulation at each spheroid size was performed by one-way ANOVA (*$p < 0.0332$, **$p < 0.0021$, ***$p < 0.0002$, ****$p < 0.0001$).

establishment and optimization) and screening applications (e.g., anticancer drug testing) of up to 360 spheroids. The presented system also allows the stacking of multiple plates on a laboratory rocker platform, permitting an easy scale-up of spheroid production and cultivation on-chip. This extent of parallelization constitutes a major improvement of throughput compared to currently reported microfluidic spheroid systems and is competitive to other mid-to-high-throughput plates. Another feature of perfused systems is that spheroids can be cultured in a dynamic micromilieu to better recapitulate the native tissue environment by controlling continuous flow and shear stress, improving spheroid function, and long-term cultivation performance.[56–59] A significant advantage includes the parallel production of 15 spheroids of five different sizes by applying only one cell density in a single pipetting step in contrast to numerous dilution series and laborious pipetting procedures that are necessary for traditional well-plate cultures. Consequently, the presented approach enables direct monitoring of spheroid size effects under various treatment scenarios on a single device, with minimum user manipulation avoiding needless pipetting errors and excessive demand of expensive culture media or test reagents. Furthermore, the presented microfluidic technology facilitates a direct automated and reproducible control of spheroid size and morphology under continuous perfusion with relative standard deviations of 12% or less in a diameter range between 90 µm and 900 µm. Nonetheless, a current drawback of our novel microfluidic spheroid array is that manual delamination of the reversible sealing and pooling of spheroids for proteomic/genomic end-point detection is still necessary. Since this time-consuming step is not feasible for automation, future design considerations include one-channel/one-size and one-chip/one-size strategies, which allow single-step harvesting/pooling procedures for more in-depth functional analysis of a uniform-sized sample population. Subsequently, any combination of four microfluidic spheroid array inserts can be used on a microplate-format and adapted to the specific research question and analytical requirements.

Overall, the results of our multisized spheroid study verified an apparent size-dependent effect of compound penetration, toxicity, and uptake. Chemotherapeutic drug transport and its uptake by tumor cells are strongly dependent on solid tumor properties, especially size, representing a crucial parameter for drug sensitivity.[60–62] Here, we demonstrated size-dependent transport kinetics of the fluorescent drug doxorubicin, known for its high efficacy in lung and ovarian cancers,[63–65] using A549 lung cancer spheroids. The impact of spheroid size was demonstrated by significant IC_{50} differences up to 160% in a single treatment regime in A549 lung cancer spheroids. Next, the synergistic therapeutic effect of cisplatin,[66,67] a DNA synthesis inhibitor, and doxorubicin,[68,69] known to inhibit the topoisomerase II (TOP2) pathway, was demonstrated by identifying the ideal ratio and minimum concentrations needed to overwhelm the cellular repair mechanisms in tumor spheroids. This combinatorial therapy aspect is particularly critical,[70–72] since both DOX and CIS exhibited severe side effects and drug resistance in clinic.[73] As a final practical example, compound permeability in BBB spheroids was screened to study BBB spheroid size effects on barrier function.[43] During the past years, different 3D BBB models and approaches have been established to mimic the BBB's biological niche by assembling spheroids with a range of distinctive ratios of hAs, hPs, and BECs into a BBB–like model.[45,46,48] For the first time, successful integration of triple-culture BBB spheroids into a microfluidic setup as well as a parallel screening of BBB spheroid size effects on self-organization and compound transport was demonstrated, representing a novel approach for future experimental design strategy optimizations. Initially, the influence of seeding densities and cell ratios on BBB spheroid sizes and compound diffusivity was evaluated in our work to establish an improved and reliable BBB model. Additionally, the penetration enhancer mannitol, which is applied in, e.g., glioblastoma patients inducing the opening of endothelial tight junctions to allow the passage of chemotherapeutics that normally cannot enter the parenchyma,[74,75] was used to demonstrate spheroid size-dependent paracellular transport kinetics. The results indicated significant differences in larger and smaller spheroids independent of the employed cell ratios during mannitol treatment. The inhibition of the P-gp efflux pump using verapamil further revealed increased accumulation of RHO and DOX in our BBB model with the exemption of smaller spheroids, where increased DOX accumulation was recorded, thus highlighting the importance of size for the optimization of BBB properties.

In conclusion, we demonstrated the compatibility, usability, and throughput of a microfluidic platform to produce and measure complex multisized spheroids, accelerating optimization and screening protocols of an advanced in vitro model and ultimately increase predictive accuracy in basic and preclinical biomedical research.

4. Experimental Section

Microfluidic Multisize Spheroid Array Fabrication: The microfluidic spheroid array chip was fabricated by double-casting of polydimethyl siloxane (PDMS). The master mold, including microwells and channel structures, was manufactured in polymethyl methacrylate (PMMA) by CNC micromilling (Denz-Biomedical, Austria). PDMS (Sylgard 184 Silicon Elastomer, Farnell, Austria) was mixed with the curing agent in a weight ratio of 10:1. The polymer was degassed in a vacuum chamber for 1 h, poured onto the PMMA structure, and baked for 2 h at 80 °C. The structure was peeled off from the PMMA matrix subsequently and was hard baked for 48 h at 90 °C. As a result, the final PDMS mold for biochip channel structure fabrication was obtained. To remove PDMS chip structures from molds properly, the surface of the PDMS mold was plasma-activated and silanized with trichloro(1H,1H,2H,2H-perfluorooctyl) silane (Sigma-Aldrich, Austria) for 10 min under vacuum and baked for 1 h at 80 °C. Molds for top layer, including reservoirs, were 3D printed by iMaterialise (Denmark). PDMS master mix was poured into 3D printed molds and baked for 2 h at 70 °C. Before bonding, each channel was coated with 0.5% wt antifouling Lipidure-CM5206 solution (AMSbio, UK) for 1 h at 80 °C. Holes of 1.5 mm diameter were punched through the reservoir layer with biopsy punchers to generate perfusion connectors between the reservoirs and the channels. The two PDMS layers (channel structure layer and top layer with reservoirs) were bonded by O_2-plasma activation for 30 s, 0.9 mbar, 200 W (Diener, Germany) and baked at 80 °C overnight.

Cell Culture Handling and Cultivation Procedures: Caco-2 (HTB-37, ATCC, USA), and normal human dermal fibroblasts (NHDF; CRL-2522, ATCC, USA) were cultured with Dulbecco's minimal essential medium (DMEM; Sigma-Aldrich, Austria) supplemented with 10% fetal bovine serum (FBS; Sigma-Aldrich, Austria) and 1% antibiotic/antimycotic solution (Sigma-Aldrich, Austria). HepG2 cells (HB-8065, ATCC, USA) were cultivated with supplemented minimal essential medium (MEM; Sigma-Aldrich, Austria) with 10% FBS and 1% antibiotic/antimycotic solution (Sigma-Aldrich, Austria), and A549 cells (CCL-185, ATCC, USA) were cultivated in Hams F12K Medium (Sigma-Aldrich, Austria) with 10% FBS

and 1% antibiotic/antimycotic solution (Sigma-Aldrich, Austria). All cell types were cultivated in T75 cell culture flasks at 37 °C in 5% CO_2 humidified atmosphere as adherent monolayers. Cells were washed with 1× phosphate-saline buffer (PBS; Sigma-Aldrich) at a confluency of 70–80%, and 0.5% trypsin–EDTA (Sigma-Aldrich, Austria) was added for 10 min to detach cells. After detachment, respective growth medium was added, and cells were centrifuged at 140 g for 5 min. Medium was removed, and the cell pellet was diluted to required cell densities. For blood-brain barrier experiments, human primary astrocytes (hA; SC-1800-5, Provitro AG, Germany) were cultured in astrocyte medium AM (ScienCell, USA) supplemented with 2% FBS (ScienCell, USA), 1% of penicillin/streptomycin (ScienCell, USA), and 1% astrocyte growth supplement (ScienCell, USA). Human primary pericytes (hP; SC-1200, Provitro AG, Germany) were cultivated in pericyte medium PM (ScienCell, USA) supplemented with 2% FBS (ScienCell, USA), 1% of penicillin/streptomycin (ScienCell, USA), and 1% pericyte growth supplement (ScienCell, USA). Human primary astrocytes and human primary pericytes were cultured on 10 µg mL^{-1} poly-L-lysine (ScienCell, USA) coated culture flasks. Human cerebral microvascular endothelial cells (hCMEC/D3; SCC066, Merck Millipore, Germany) were cultured on 0.5% gelatin-coated culture flasks (SERVA Electrophoresis GmbH, Germany) in EBM-2 (Lonza, Swiss) containing 5% FBS (Sigma-Aldrich, USA), 1% penicillin/streptomycin (Biochrom GmbH, Germany;) as well as 10×10^{-3} M HEPES (Sigma-Aldrich, USA), 5 µg mL^{-1} ascorbic acid (Sigma-Aldrich, USA) and 1 ng mL^{-1} hbFGF (Sigma-Aldrich, USA). For experimental use, astrocytes were maintained between passages 3 and 8, pericytes between passages 4 and 8, hCMEC/D3 cells between passage 21 and 32. Cells were cultivated as previously described.[76]

To visualize the location of each cell type in BBB triple-culture spheroids, hA were labeled with CellTracker Deep-red Dye (5×10^{-6} M; Thermo Fisher Scientific, USA), hP with NucBlue Live Cell Stain (1 drop; Life Technologies, USA) and hCMEC/D3 were labeled with CellTracker Orange CMDA dye (5×10^{-6} M; Thermo Fisher Scientific, USA). After cell detachment, cells were centrifuged at 300 g for 5 min and washed with DMEM without further supplements (Gibco, Thermo Fisher Scientific, USA). Cells were mixed with each dye in DMEM without further supplements (Gibco, Thermo Fisher Scientific, USA) and incubated for 30 min at 37 °C in the water bath. After centrifugation, cells were resuspended in the corresponding culture medium and the BBB spheroid formation protocol was continued.

Chip Loading and Cell Seeding Protocol: Before cell seeding, chips were filled with 70% ethanol and placed in an ultrasonic bath to remove air bubbles. Chips were sterilized by washing 3× with 200 µL of 70% ethanol and three times with 200 µL of 1× PBS (Sigma-Aldrich, Austria) supplemented with 1% of penicillin/streptomycin (Sigma-Aldrich, Austria) to clear the channel from ethanol. Chips were maintained and incubated in quadriPERM chambers (Sarstedt, Austria) filled with 2 mL 1× PBS supplemented with 1% antibiotic/antimycotic solution (Sigma-Aldrich, Austria) to avoid liquid evaporation. Prior to cell seeding, PBS was removed from all reservoirs, and preconditioned with 200 µL cell culture medium. After removal of medium, 100 µL of a cell suspension was added to each channel. The quadriPERM with the chips was placed on the rocker platform and set to a flow rate of 4 µL min^{-1} at 1° tilting angle and 1 rpm. On the next day, channels were flushed with 200 µL growth medium to remove excess cells. Growth medium in the chips was changed every 2 d.

CFD Simulation: CFD (computational fluid dynamics) modeling was carried out using Ansys Fluent 6.3.26, (www.ansys.com), a general-purpose finite volume CFD solver. The computational mesh for the 3D fluid flow problem consisted of about 120 000 hexahedral control volumes. Next, steady-state snapshots representative for the physical movement were identified and the flow geometry was oriented accordingly. Wall boundaries were treated as ideally smooth and no-slip (zero flow velocity at the wall), inlet and outlet were set to pressure boundary conditions (reference pressure $p = 1$ atm/101325 Pa at the lower fluid column). Gravity or equivalent pressure of a virtual water column was used as single fluid phase (Newtonian fluid, constant dynamic viscosity) and the flow was idealized as isothermal (reference temperature $T = 25$ °C) and incompressible (constant density). Second or higher-order discretization schemes were selected for continuity equation (mass conservation) and Navier-Stokes equations (momentum conservation). Due to the small geometrical features and the low fluid velocities, the flow can safely be considered as laminar ($Re << 1$). Simulations were carried out on the cluster server cae.zserv.tuwien.ac.at (operated by the IT department of TU Wien, www.zid.tuwien.ac.at). Base on the steady-state snapshot CFD results, correlations were derived to set up a fast 1D mass balancing tool to calculate and analyze the transient flow behavior inside the spheroid chamber.

Flow Rate Measurements: Measuring the flow rate in the chip at various tilting angles was achieved by setting an assembled platform (Rocker Platform Shaker 444-0756, VWR, Austria) on a tilting stage at a defined angle α. Medium reservoirs were filled with stained cell culture medium to ensure steady flow from the experiment's beginning. To calculate the volumetric flow rate, measurements of the angle associated change of liquid column height were made. Images from the neutral setting and the maximum angle were taken and change in liquid column height Δh was measured with ImageJ FIJI (NIH, USA), and ΔP was calculated using the tilting-dependent hydrostatic pressure difference in Equation (1):

$$\Delta P = \rho g \Delta h \tag{1}$$

and the hydrodynamic resistance R_h as shown in Equation (2) which is the sum of the hydraulic resistance of the microfluidic tissue culture channel (R_r) and both tubular connecting channels (R_t; Equations (3) and (4))

$$R_h = R_r + 2R_t \tag{2}$$

$$R_r = \frac{12\eta l}{wh^3}\left[1 - \frac{192h}{\pi^5 w}\tanh\left(\frac{\pi w}{2h}\right)^{-1}\right] \tag{3}$$

$$R_t = \frac{8\eta l}{\pi r^4} \tag{4}$$

The hydrodynamic resistance is given by the dimensions of the culture channel and the fluid properties, where l is the length, w is the width, h is the height, and η is the dynamic viscosity. The volumetric flow rates Q through the device is proportional to ΔP for a given channel hydraulic resistance Rh which is described in Equation (4):

$$Q = \Delta P R_h \tag{5}$$

Evaluation of Spheroid Esterase Activity and Hypoxia: The calcein-AM (Invitrogen, Austria) solution was prepared in growth medium for each cell type with a concentration of 0.5 µL stock per mL growth medium. Growth medium was removed from reservoirs, and 200 µL of the calcein-AM solution was added to each reservoir. After incubation of 30 min under standard cell culture conditions, the spheroids were imaged. All further calcein determinations were performed according to the same protocol with corresponding growth medium. To monitor hypoxia on-chip, 10×10^{-6} M of Image-iT Red Hypoxia Reagent (Invitrogen, Austria) was prepared in respective cell growth medium. As shown in Figure S6 (Supporting Information), culture medium was gently removed from reservoirs, and 200 µL of the 10×10^{-6} M hypoxia reagent was applied. The chip was incubated for 1 h at 37 °C and 5% CO_2 in a live-cell incubator (Pecon, Germany) and imaged using TRITC filter (ex 530 nm, em 645 nm) by IX83 live-cell microscope (Olympus, Germany).

Doxorubicin Penetration Study: After 3 d of cultivation, medium was removed from chip reservoirs and 200 µL of fresh medium supplemented with 100×10^{-6} M, 10×10^{-6} M and 1×10^{-6} M of doxorubicin (Sigma-Aldrich, Germany) was added, followed by the incubation at 37 °C and 5% CO_2 in a life cell incubator (Pecon, Germany) where real-time tracking of fluorescence intensities was performed. Images were taken after 5, 60, 120, and 460 min using a FITC filter (ex 485, em 530; IX83, Olympus, Germany).

Anticancer Drug Screening: A549 cells were seeded at a concentration of 1×10^6 cells per mL and cultivated for 3 d under standard cell culture conditions under bi-directional flow. Stock solutions of 10×10^{-3} M cisplatin (Sigma-Aldrich, Austria) in DMSO and 10×10^{-3} M doxorubicin (Sigma-Aldrich, Austria) in PBS were prepared. Doxorubicin and cisplatin

were dissolved in cell culture medium to yield concentrations of 0.5 × 10^{-6}, 1 × 10^{-6}, 5 × 10^{-6}, 10 × 10^{-6}, 25 × 10^{-6}, 50 × 10^{-6}, and 500 × 10^{-6} M for the treatment of A549 spheroids. Cell culture medium within the channels of the devices was replaced with drug containing medium and incubated for 24 h prior to cell death analyses. One channel on a separate device was used as an untreated control. Following the incubation, drug solutions were removed, and 10 µg mL^{-1} Hoechst 33342 (Invitrogen, Austria) and 4 × 10^{-6} M ethidium–Homodimer 1 (Invitrogen, Austria) applied. After incubation for 30 min, spheroids were imaged using DAPI (ex 390 nm, em 460 nm) and TRITC filters (ex 530 nm, em 645 nm). Raw fluorescence signals were processed as described in 2.11, and dose–response curves were generated by Sigmoidal-4PL nonlinear regression analysis.

Evaluation of BBB Permeability: Multicellular BBB spheroids were formed through a two-step cell seeding protocol. First, human primary astrocytes were seeded on-chip by injecting 100 µL of cell suspension into the channels and incubated overnight at 37 °C, 5% CO_2 in a cell culture incubator to allow the assembly of astrocyte spheroids. Second, human primary pericytes and hCMEC/D3 were mixed at defined ratios, and 100 µL of the cell suspension were injected into respective microchannels to form multilayered BBB spheroids and incubated for 6 d. Cells were seeded at 1:1:3, 1:1:2, 1:1:1, 5.5:1.5:3, 1:4:0, and 1:0:0 rations of astrocytes:pericytes:hCMEC/D3 at total seeding densities of 5 × 10, ^{6} 3 × 10^{6}, 2 × 10^{6} and 1 × 10^{6} cells mL^{-1}. Medium was changed every 2 d with respective medium ratios for each cell type. For real-time permeability experiments, spheroids of different cell type rations were generated at a seeding density of 5 × 10^{6} cells mL^{-1}. Spheroids were incubated with 200 µL of the paracellular marker fluorescein isothiocyanate-dextran (10 × 10^{-6} M; FD4; 4 kDa; Sigma-Aldrich, USA, 1 × 10^{-3} M stock solution of FD4 ultrafiltered with Amicon tubes with a cutoff 3 kDa to separate from residual, free FITC) in the supplemented EBM-2 medium for 4 h at 37 °C with 5% CO_2 in live-cell incubator (Pecon, Germany) and imaged after one and 4 h. For mannitol experiments, BBB spheroids were treated with 200 µL of 1.6 M D-Mannitol (Fluka, Austria) and 10 × 10^{-6} M FD4 in supplemented EBM-2 medium for 4 h and washed two times with 200 µL of 1× PBS containing 1.6 M D-Mannitol. To monitor P-gp activity, the BBB-spheroids were pretreated with 100 × 10^{-6} M of the P-gp blocker verapamil (Sigma-Aldrich, Austria) in serum-free EBM-2 for 15 min and exposed to a mixture of 100 × 10^{-6} M verapamil and 10 × 10^{-6} M rhodamine123 (Sigma-Aldrich, Austria), 100 × 10^{-6} M verapamil and 1 × 10^{-6} M doxorubicin (Sigma-Aldrich, Austria) or 100 × 10^{-6} M verapamil and 10 × 10^{-6} M FD4 for 1 h. Spheroids were treated with rhodamine123, doxorubicin, or FD4 with 0.16% DMSO (PanReac AppliChem, Austria) as control on separate chips.

To calculate the efficient permeability P_e of BBB spheroids, Equation (5) was used as described elsewhere:[77]

$$P_e = \frac{-\ln\left(1 - \frac{C_s}{C_{equilibrium}}\right)}{A_s\left(\frac{1}{V_m} + \frac{1}{V_s}\right)t} \quad (6)$$

where C_s is the FD4 intensity in the spheroid at time t, A_s is the surface area of the spheroid, V_m is the volume of medium, V_s is the volume of spheroid, and t is the incubation time. $C_{equilibrium}$ is obtained by the Equation (6):

$$C_{equilibrium} = \frac{C_m V_m + C_s V_s}{V_m + V_s} \quad (7)$$

where C_m is the FD4 intensity in the medium at time t.

Immunohistochemistry: After 6 d of culture on-chip, BBB spheroids were washed twice with 1× PBS (Sigma-Aldrich, Austria) and fixed with 4% paraformaldehyde in 1× PBS (containing Mg^{2+} and Ca^{2+}; Sigma-Aldrich, Austria) at 4 °C overnight. Individual BBB spheroids were harvested by cutting off the PDMS chip's top layer with a scalpel and transferred to Eppendorf tubes. The spheroids were embedded in paraffin and sliced into 4 µm serial sections, deparaffinized in xylene, and rehydrated in a graded alcohol series. Antigen retrieval was performed by keeping rehydrated sections in a 10 × 10^{-3} M sodium citrate buffer pH 6.0 (Sigma-Aldrich, Austria) for 20 mi at 100 °C in a steamer. Blocking was conducted by exposure to 10% goat serum with 1% BSA in 1× Tris-buffered saline pH 7.6 (TBS; Sigma-Aldrich, Austria) for 2 h at room temperature. Samples were incubated with polyclonal rabbit anti-ZO-1 (1:100; 21773-1-AP, ProteinTech, Germany) at 4 °C overnight. After washing with 1× TBS, secondary Alexa Fluor 555 goat antirabbit IgG (1:1000; A32732, Invitrogen, Austria) was applied for 1 h at room temperature. Nuclei were counterstained with DAPI (1:1000; Thermo-Fischer, Austria). Images were acquired by Olympus IX83 live-cell microscope using DAPI (Ex: 350/Em: 470) and TRITC filters (ex 530 nm, em 645 nm). Images of fluorescent immunohistochemical staining were taken using equal filter and acquisition parameters to assure comparable conditions.

Image Acquisition and Data Processing: To investigate spheroid size and morphology, bright-field images were taken using an IX83 microscope (Olympus, Austria) equipped with temperature, CO_2, and O_2 control (Peacon, Germany) and high-resolution camera (Hamamatsu, Germany). For imaging of the whole cultivation channel, MIA scans were conducted using 4× and 10× magnification. All images were processed by ImageJ (NIH, USA). For morphometric analysis, micrographs were converted to 8-bit, threshold was adjusted, and area, perimeter, roundness, and solidity were measured by the function of Analyze Particles. Roundness was calculated as described in Equation (7):

$$\text{Roundness} = \frac{4A_s}{\pi a^2} \quad (8)$$

where is the A_s is the spheroid surface area and a is the major axis of the diameter. Spheroid solidity was defined using Equation (8):

$$\text{Solidity} = \frac{A_s}{A_c} \quad (9)$$

where A_c is the convex area.

Center-to-center distances were determined mathematically by calculating the vector length between the x–y positions of the spheroid center point and the respective microwell center point. Each center point was obtained by the "Centroid" function of ImageJ. Phase-contrast micrographs of spheroids were analyzed, and spheroid diameters were measured on respective times using Olympus' CellSense Standard software. To normalize fluorescent micrographs, Image backgrounds were subtracted, and mean fluorescence intensities (sum of the fluorescent values of all the pixels in the selection divided by the number of pixels) of spheroids were measured. In the case of penetration studies of doxorubicin, rhodamine123 and 4kDa FITC-dextran, fluorescent values of the spheroid's core (150–100 µm from the edge) were measured. The Z-stack images of single immunofluorescent stained BBB spheroids were obtained using an Olympus IX83 live-cell microscope at 40× magnification. Z-stacks of optical sections were captured across the entire spheroid thickness using excitation and emission (DAPI 350/470 nm, TRITC: 530/645 nm) settings for simultaneous dual-channel recordings; approximately 20 Z-stacks per spheroid were taken. Z-stacks were processed and analyzed using the Wiener deconvolution by Olympus' CellSense Standard software.

Statistical Analysis: All experiments were carried out at n = 3–12; exact numbers are mentioned per experiment in figure captions. For statistical analysis, data sets were tested for significance using Prism software 8 (Version 8.2.1; GraphPad, USA). Statistical analysis between three or more conditions was performed using the Mixed-effects model, one-way ANOVA, Holm-Sidak's multiple comparisons test, Dunnett's multiple comparisons test, or analysis of covariance (ANCOVA). P values <0.0332 were considered as statistically significant (*p < 0.0332, **p < 0.0021, ***p < 0002, ****p < 0.0001). The data are presented as the mean ± standard deviation (SD).

Supporting Information

Supporting Information is available from the Wiley Online Library or from the author.

Acknowledgements

The authors acknowledge funding from Christian Doppler Forschungsgesellschaft (Josef Ressel Center for Phytogenic Drug Research). This project has received funding from the Innovative Medicines Initiative 2 Joint Undertaking (JU) under grant agreement No 807015 to W.N. The JU receives support from the European Union's Horizon 2020 research and innovation program and EFPIA. Schemes in the manuscript and supporting information were created with BioRender.com under paid subscription. The authors acknowledge the TU Wien University Library for financial support through its Open Access Funding Program.

Conflict of Interest

The authors declare no conflict of interest.

Author Contributions

C.E., M.R., F.S., and A.G. contributed equally to this work. C.E., M.R., F.S., A.G., and W.N. conceived and planned the experiments. C.J. and M.H. planned and carried out the simulations. C.E., F.S., A.G., and B.S. performed the experiments. C.E. analyzed the data and M.R., F.S., A.G., W.N., J.G., S.K., J.W., and P.E. contributed to the interpretation of the results. C.E., M.R., and P.E. wrote the paper with input from all authors.

Data Availability Statement

Research data are not shared.

Keywords

anticancer drugs, blood-brain barrier, in vitro tests, microfluidics, multicellular spheroids

Received: December 16, 2020
Revised: January 30, 2021
Published online:

[1] F. Hirschhaeuser, H. Menne, C. Dittfeld, J. West, W. Mueller-Klieser, L. A. Kunz-Schughart, *J. Biotechnol.* **2010**, *148*, 3.
[2] B. Zhang, M. Radisic, *Lab Chip* **2017**, *17*, 2395.
[3] R. M. Eglen, J. L. Klein, *SLAS Discovery* **2017**, *22*, 453.
[4] X. Cui, Y. Hartanto, H. Zhang, *J. R. Soc., Interface* **2017**, *14*, 20160877.
[5] C. G. Begley, J. P. Ioannidis, *Circ. Res.* **2015**, *116*, 116.
[6] M. Rothbauer, J. M. Rosser, H. Zirath, P. Ertl, *Curr. Opin. Biotechnol.* **2019**, *55*, 81.
[7] O. I. Hoffmann, C. Ilmberger, S. Magosch, M. Joka, K. W. Jauch, B. Mayer, *J. Biotechnol.* **2015**, *205*, 14.
[8] V. Härmä, H. P. Schukov, A. Happonen, I. Ahonen, J. Virtanen, H. Siitari, M. Åkerfelt, J. Lötjönen, M. Nees, *PLoS One* **2014**, *9*, e96426.
[9] C. Eilenberger, S. R. A. Kratz, M. Rothbauer, E. K. Ehmoser, P. Ertl, S. Küpcü, *MethodsX* **2018**, *5*, 781.
[10] C. Eilenberger, M. Rothbauer, E. - K. Ehmoser, P. Ertl, S. Küpcü, *Sci. Rep.* **2019**, *9*, 4863.
[11] R. Edmondson, J. J. Broglie, A. F. Adcock, L. Yang, *Assay Drug Dev. Technol.* **2014**, *12*, 207.
[12] A. Bertuzzi, A. Fasano, A. Gandolfi, C. Sinisgalli, *J. Theor. Biol.* **2010**, *262*, 142.
[13] E. V. Zagaynova, I. N. Druzhkova, N. M. Mishina, N. I. Ignatova, V. V. Dudenkova, M. V. Shirmanova, *Adv. Exp. Med. Biol.* **2017**, *1035*, 105.
[14] J. P. Ward, J. R. King, *Math. Biosci.* **2003**, *181*, 177.
[15] R. M. Sutherland, *Science* **1988**, *240*, 177.
[16] R. Glicklis, J. C. Merchuk, S. Cohen, *Biotechnol. Bioeng.* **2004**, *86*, 672.
[17] T. Ishiguro, H. Ohata, A. Sato, K. Yamawaki, T. Enomoto, K. Okamoto, *Cancer Sci.* **2017**, *108*, 283.
[18] S. H. Moon, J. Ju, S. J. Park, D. Bae, H. M. Chung, S. H. Lee, *Biomaterials* **2014**, *35*, 5987.
[19] A. Ivascu, M. Kubbies, *J. Biomol. Screening* **2006**, *11*, 922.
[20] A. P. Napolitano, D. M. Dean, A. J. Man, J. Youssef, D. N. Ho, A. P. Rago, M. P. Lech, J. R. Morgan, *BioTechniques* **2007**, *43*, 494.
[21] S. Moreno-Flores, S. Küpcü, *Soft Matter* **2015**, *11*, 1259.
[22] J. M. Yuhas, A. P. Li, A. O. Martinez, A. J. Ladman, *Cancer Res.* **1977**, *37*, 3639.
[23] V. Beachley, V. Kasyanov, A. Nagy-Mehesz, R. Norris, I. Ozolanta, M. Kalejs, P. Stradins, L. Baptista, K. da Silva, J. Grainjero, X. Wen, V. Mironov, *J. Tissue Eng.* **2014**, *5*, 204173141455656.
[24] B. Chen, Y. Wu, Z. Ao, H. Cai, A. Nunez, Y. Liu, J. Foley, K. Nephew, X. Lu, F. Guo, *Lab Chip* **2019**, *19*, 1755.
[25] O. Frey, P. M. Misun, D. A. Fluri, J. G. Hengstler, A. Hierlemann, *Nat. Commun.* **2014**, *5*, 4250.
[26] A. A. Popova, T. Tronser, K. Demir, P. Haitz, K. Kuodyte, V. Starkuviene, P. Wajda, P. A. Levkin, *Small* **2019**, *15*, 1901299.
[27] T. Tao, Y. Wang, W. Chen, Z. Li, W. Su, Y. Guo, P. Deng, J. Qin, *Lab Chip* **2019**, *19*, 948.
[28] X. Gong, C. Lin, J. Cheng, J. Su, H. Zhao, T. Liu, X. Wen, P. Zhao, *PLoS One* **2015**, *10*, e0130348.
[29] E. O. Mosaad, K. F. Chambers, K. Futrega, J. A. Clements, M. R. Doran, *Sci. Rep.* **2018**, *8*, 253.
[30] P. Sabhachandani, V. Motwani, N. Cohen, S. Sarkar, V. Torchilin, T. Konry, *Lab Chip* **2016**, *16*, 497.
[31] S. Sart, R. F. Tomasi, G. Amselem, C. N. Baroud, *Nat. Commun.* **2017**, *8*, 469.
[32] M. Marimuthu, N. Rousset, A. St-Georges-Robillard, M. A. Lateef, M. Ferland, A. M. Mes-Masson, T. Gervais, *Lab Chip* **2018**, *18*, 304.
[33] H. Byun, Y. Bin Lee, E. M. Kim, H. Shin, *Biofabrication* **2019**, *11*, 035025.
[34] W. Song, D. An, D. I. Kao, Y. C. Lu, G. Dai, S. Chen, M. Ma, *ACS Appl. Mater. Interfaces* **2014**, *6*, 7038.
[35] G. Fang, H. Lu, A. Law, D. Gallego-Ortega, D. Jin, G. Lin, *Lab Chip* **2019**, *19*, 4093.
[36] K. Moshksayan, N. Kashaninejad, M. E. Warkiani, J. G. Lock, H. Moghadas, B. Firoozabadi, M. S. Saidi, N.-T. Nguyen, *Sens. Actuators, B* **2018**, *263*, 151.
[37] M. Zanoni, F. Piccinini, C. Arienti, A. Zamagni, S. Santi, R. Polico, A. Bevilacqua, A. Tesei, *Sci. Rep.* **2016**, *6*, 19103.
[38] F. L. Miles, J. E. Lynch, R. A. Sikes, *J. Biol. Methods* **2015**, *2*, 29.
[39] V. Falanga, T. A. Martin, H. Takagi, R. S. Kirsner, T. Helfman, J. Pardes, M. S. Ochoa, *J. Cell. Physiol.* **1993**, *157*, 408.
[40] D. S. Steinbrech, M. T. Longaker, B. J. Mehrara, P. B. Saadeh, G. S. Chin, R. P. Gerrets, D. C. Chau, N. M. Rowe, G. K. Gittes, *J. Surg. Res.* **1999**, *84*, 127.
[41] M. Singh, M. Pierpoint, A. G. Mikos, F. K. Kasper, *J. Biomed. Mater. Res., Part A* **2011**, *98*, 412.
[42] L. Zheng, C. J. Kelly, S. P. Colgan, *Am. J. Physiol. Cell Physiol.* **2015**, *309*, C350.
[43] P. Prieto, B. J. Blaauboer, A. G. de Boer, M. Boveri, R. Cecchelli, C. Clemedson, S. Coecke, A. Forsby, H. J. Galla, P. Garberg, J. Greenwood, A. Price, H. Tähti, *Altern. Lab. Anim.* **2004**, *32*, 37.
[44] R. Cecchelli, V. Berezowski, S. Lundquist, M. Culot, M. Renftel, M. P. Dehouck, L. Fenart, *Nat. Rev. Drug Discovery* **2007**, *6*, 650.
[45] E. Urich, C. Patsch, S. Aigner, M. Graf, R. Iacone, P. O. Freskgård, *Sci. Rep.* **2013**, *3*, 1500.
[46] C. F. Cho, J. M. Wolfe, C. M. Fadzen, D. Calligaris, K. Hornburg, E. A. Chiocca, N. Y. R. Agar, B. L. Pentelute, S. E. Lawler, *Nat. Commun.* **2017**, *8*, 15623.

[47] B. D. Gastfriend, S. P. Palecek, E. V. Shusta, *Curr. Opin. Biomed. Eng.* **2018**, *5*, 6.
[48] G. Nzou, R. T. Wicks, E. E. Wicks, S. A. Seale, C. H. Sane, A. Chen, S. V. Murphy, J. D. Jackson, A. J. Atala, *Sci. Rep.* **2018**, *8*, 7413.
[49] L. B. Thomsen, A. Burkhart, T. Moos, *PLoS One* **2015**, *10*, e0134765.
[50] P. J. Gaillard, A. G. de Boer, *Eur. J. Pharm. Sci.* **2000**, *12*, 95.
[51] M. A. Bellavance, M. Blanchette, D. Fortin, *AAPS J.* **2008**, *10*, 166.
[52] R. C. Brown, R. D. Egleton, T. P. Davis, *Brain Res.* **2004**, *1014*, 221.
[53] M. Ikeda, A. K. Bhattacharjee, T. Kondoh, T. Nagashima, N. Tamaki, *Biochem. Biophys. Res. Commun.* **2002**, *291*, 669.
[54] F. Takata, S. Dohgu, A. Yamauchi, J. Matsumoto, T. Machida, K. Fujishita, K. Shibata, Y. Shinozaki, K. Sato, Y. Kataoka, S. Koizumi, *PLoS One* **2013**, *8*, e55166.
[55] L. Fenart, V. Buée-Scherrer, L. Descamps, C. Duhem, M. G. Poullain, R. Cecchelli, M. P. Dehouck, *Pharm. Res.* **1998**, *15*, 993.
[56] S. A. Lee, Y. No da, E. Kang, J. Ju, D. S. Kim, S. H. Lee, *Lab Chip* **2013**, *13*, 3529.
[57] J. Ruppen, L. Cortes-Dericks, E. Marconi, G. Karoubi, R. A. Schmid, R. Peng, T. M. Marti, O. T. Guenat, *Lab Chip* **2014**, *14*, 1198.
[58] Y. Jun, J. Lee, S. Choi, J. H. Yang, M. Sander, S. Chung, S. H. Lee, *Sci. Adv.* **2019**, *5*, eaax4520.
[59] Y. Y. Choi, J. Kim, S. H. Lee, D. S. Kim, *Biomed. Microdevices* **2016**, *18*, 58.
[60] A. I. Minchinton, I. F. Tannock, *Nat. Rev. Cancer* **2006**, *6*, 583.
[61] M. Sefidgar, M. Soltani, K. Raahemifar, H. Bazmara, S. M. Nayinian, M. Bazargan, *J. Biol. Eng.* **2014**, *8*, 12.
[62] W. Zhan, W. Gedroyc, X. Y. Xu, *PLoS One* **2017**, *12*, e0172276.
[63] B. Pang, X. Qiao, L. Janssen, A. Velds, T. Groothuis, R. Kerkhoven, M. Nieuwland, H. Ovaa, S. Rottenberg, O. van Tellingen, J. Janssen, P. Huijgens, W. Zwart, J. Neefjes, *Nat. Commun.* **2013**, *4*, 1908.
[64] C. W. Wang, C. L. Chen, C. K. Wang, Y. J. Chang, J. Y. Jian, C. S. Lin, C. J. Tai, *Integr. Cancer Ther.* **2015**, *14*, 546.
[65] A. Vavrova, H. Jansova, E. Mackova, M. Machacek, P. Haskova, L. Tichotova, M. Sterba, T. Simunek, *PLoS One* **2013**, *8*, e76676.
[66] Q. Hu, W. Sun, C. Wang, Z. Gu, *Adv. Drug Delivery Rev.* **2016**, *98*, 19.
[67] S. McMeekin, D. Dizon, J. Barter, G. Scambia, L. Manzyuk, A. Lisyanskaya, A. Oaknin, S. Ringuette, P. Mukhopadhyay, J. Rosenberg, I. Vergote, *Gynecol. Oncol.* **2015**, *138*, 18.
[68] E. R. Jamieson, S. J. Lippard, *Chem. Rev.* **1999**, *99*, 2467.
[69] D. Wang, S. J. Lippard, *Nat. Rev. Drug Discovery* **2005**, *4*, 307.
[70] K. H. Kim, D. Jelovac, D. K. Armstrong, B. Schwartz, S. C. Weil, C. Schweizer, R. D. Alvarez, *Gynecol. Oncol.* **2016**, *140*, 210.
[71] F. H. van Wijk, M. S. Aapro, G. Bolis, B. Chevallier, M. E. van der Burg, A. Poveda, C. F. de Oliveira, S. Tumolo, V. Scotto di Palumbo, M. Piccart, M. Franchi, F. Zanaboni, A. J. Lacave, R. Fontanelli, G. Favalli, P. Zola, J. P. Guastalla, R. Rosso, C. Marth, M. Nooij, M. Presti, C. Scarabelli, T. A. Splinter, E. Ploch, L. V. Beex, W. ten Bokkel Huinink, M. Forni, M. Melpignano, P. Blake, P. Kerbrat, C. Mendiola, A. Cervantes, A. Goupil, P. G. Harper, C. Madronal, M. Namer, G. Scarfone, J. E. Stoot, I. Teodorovic, C. Coens, I. Vergote, J. B. Vermorken, *Ann. Oncol.* **2003**, *14*, 441.
[72] M. E. Randall, V. L. Filiaci, H. Muss, N. M. Spirtos, R. S. Mannel, J. Fowler, J. T. Thigpen, J. A. Benda, G. O. G. Study, *J. Clin. Oncol.* **2006**, *24*, 36.
[73] M. A. Fuertes, C. Alonso, J. M. Pérez, *Chem. Rev.* **2003**, *103*, 645.
[74] E. C. Kaal, C. J. Vecht, *Curr. Opin. Oncol.* **2004**, *16*, 593.
[75] L. Palma, G. Bruni, A. I. Fiaschi, A. Mariottini, *J. Neurosurg. Sci.* **2006**, *50*, 63.
[76] A. Gerhartl, N. Pracser, A. Vladetic, S. Hendrikx, H. P. Friedl, W. Neuhaus, *Fluids Barriers CNS* **2020**, *17*, 19.
[77] J. B. Lee, S. H. Son, M. C. Park, T. H. Kim, M. G. Kim, S. D. Yoo, S. Kim, *J. Biotechnol.* **2015**, *205*, 93.

Supplementary Information

A microfluidic multi-size spheroid array for multi-parametric screening of anti-cancer drugs and blood-brain barrier transport properties

Christoph Eilenberger, Mario Rothbauer, Florian Selinger, Anna Gerhartl, Christian Jordan, Michael Harasek, Barbara Schädl, Johannes Grillari, Julian Weghuber, Winfried Neuhaus, Seta Küpcü and Peter Ertl

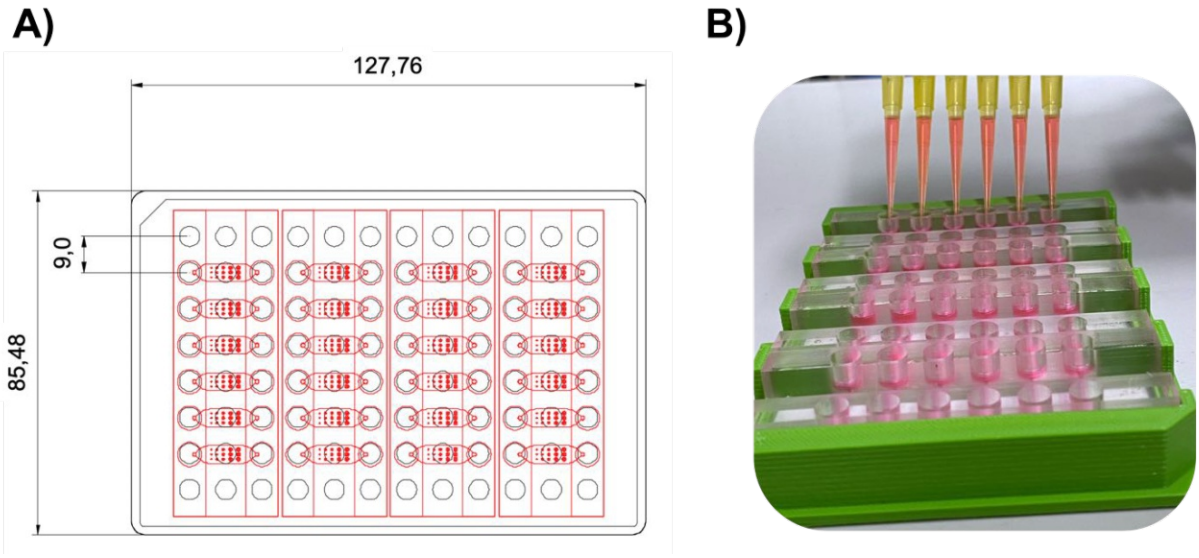

Figure SI-1: A) Design overlay of a standard 96-well microtiter plate and a panel of 4 microfluidic spheroid arrays positioned in the chip-frame showing the arrangement of media reservoirs and channel structures at a pitch of 9 mm and fitted widths of microchannels and reservoirs to microtiter well dimensions (in mm). **B)** Media reservoirs are conveniently addressable with standard multichannel pipettes and capable to generate 360 spheroids of 5 sizes in one microtiter plate design.

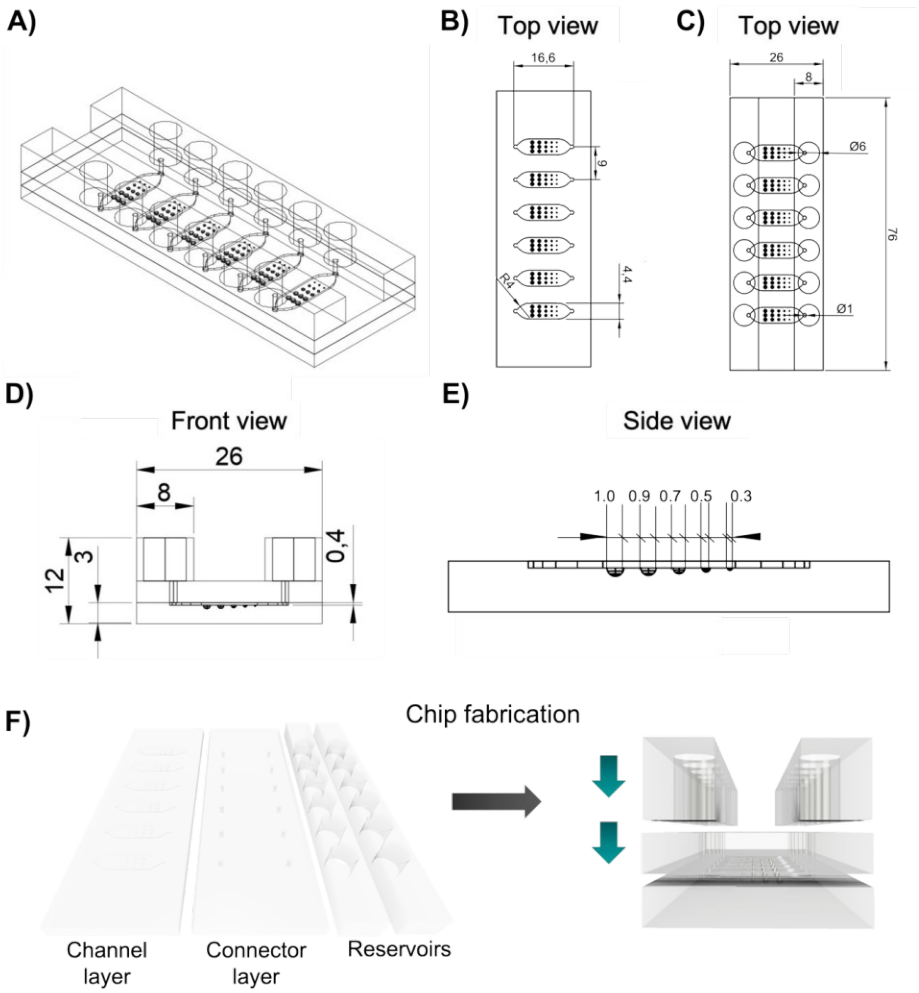

Figure SI-2: A) Three-dimensional graphical illustration of the microfluidic spheroid array including hemispherical microwells of different diameters for spheroid generation on the bottom, microfluidic connector holes and media reservoirs on the top. Engineering drafts of **B)** the top view of the entire device with media reservoirs, **C)** top view of the open channel, **D)** front view of the chip with respective heights of microchannels, micro connectors and reservoirs, and E) side view of the channel layer showing individual microwell diameters. All units are presented in mm. **F)** The platform comprises the microfluidic channel structure, a cover layers consisting of twelve connecting holes which are fluidically coupled to the reservoir layer ensuring continuous media perfusion.

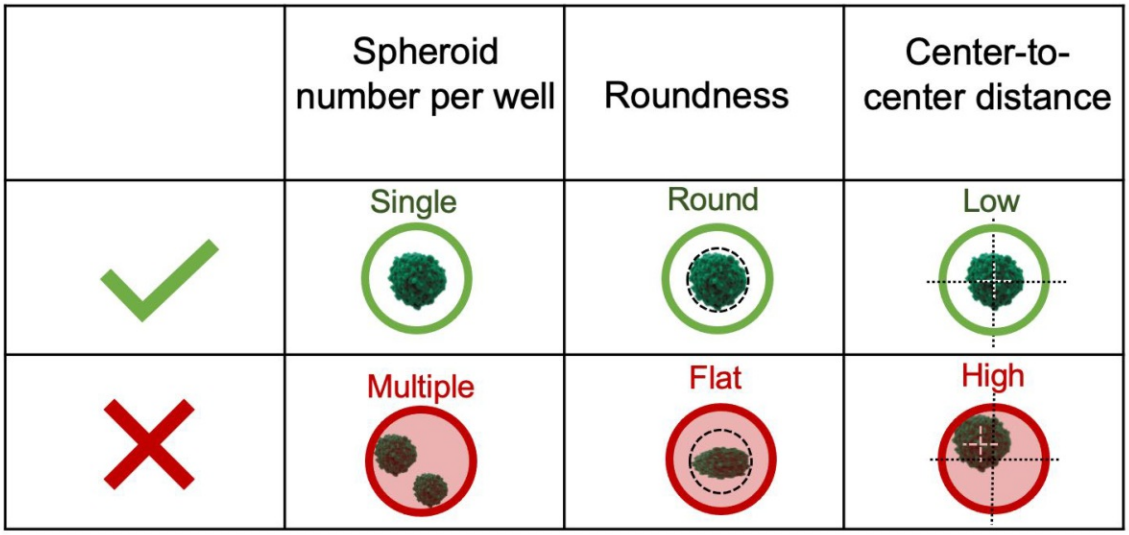

Figure SI-3: Schematic overview of the most optimal (green) and suboptimal (red) microwell quality parameters for reproducible spheroid generation and cultivation on-chip. Microwell dimensions were evaluated regarding number of spheroids per well, spheroid roundness, and spheroid center-to-microwell center-distances.

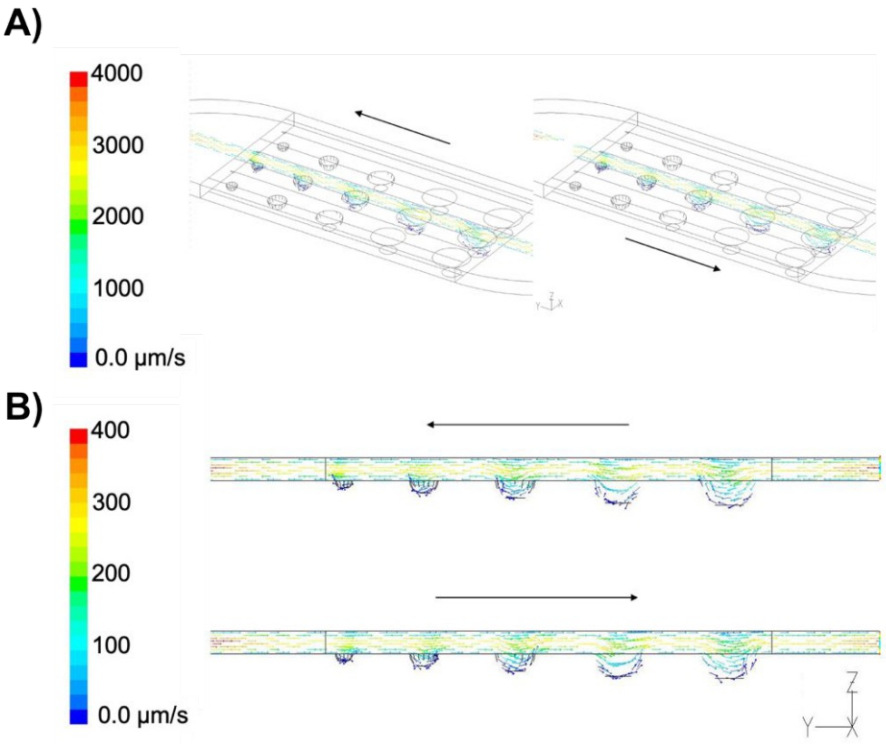

Figure SI-4: A) Top view and **B)** side view of flow velocity vector streams in spheroid array culture channels and microwells during tilting at an inclination angle of 1° and a speed of 1 rpm. Simulation was performed CFD (computational fluid dynamics)

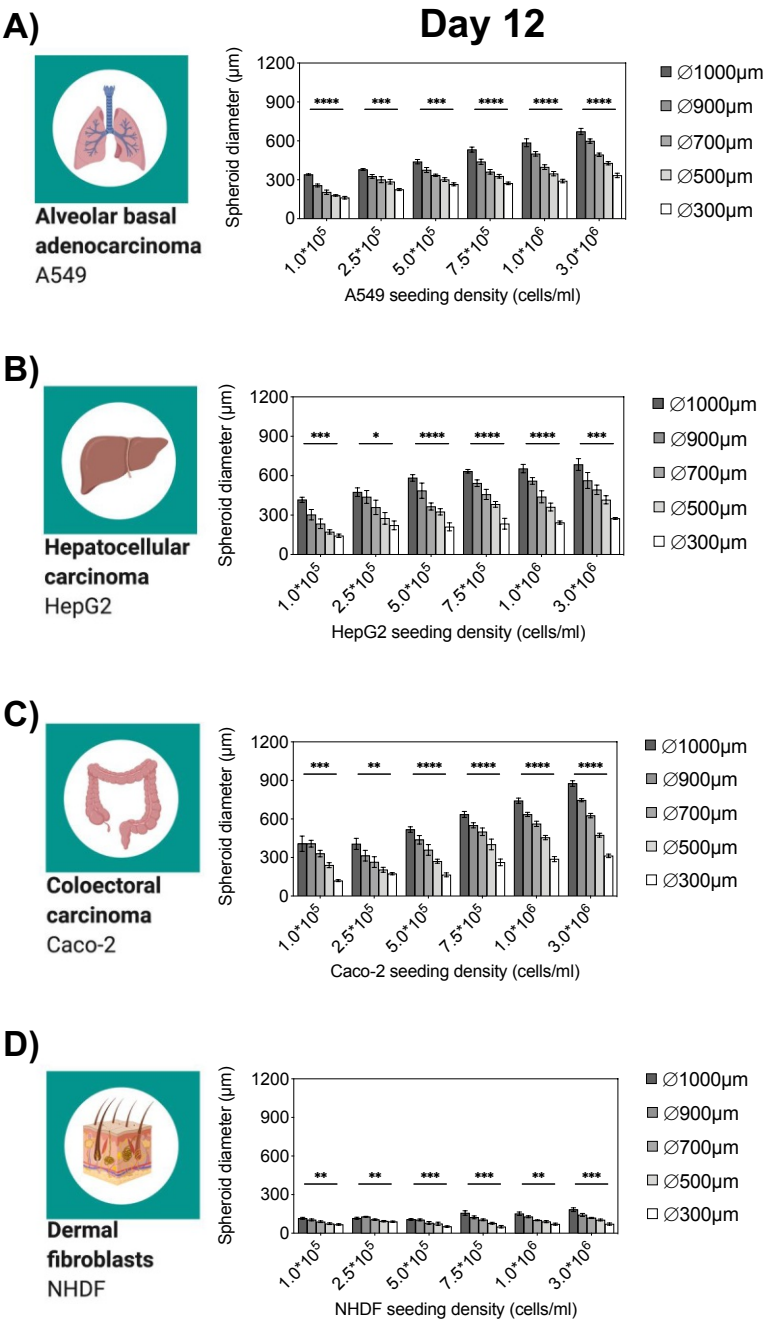

Figure SI-5: Analysis of spheroid diameters of **A)** A549, **B)** HepG2, **C)** Caco-2 and **D)** NHDF spheroids at different initial seeding densities over a cultivation period of twelve days under continuous perfusion, n=6-9 ± SD Statistical analysis was performed using Mixed-effects analysis (*p<0.0332, **p<0.0021, ***p<0.0002, ****p<0.0001).

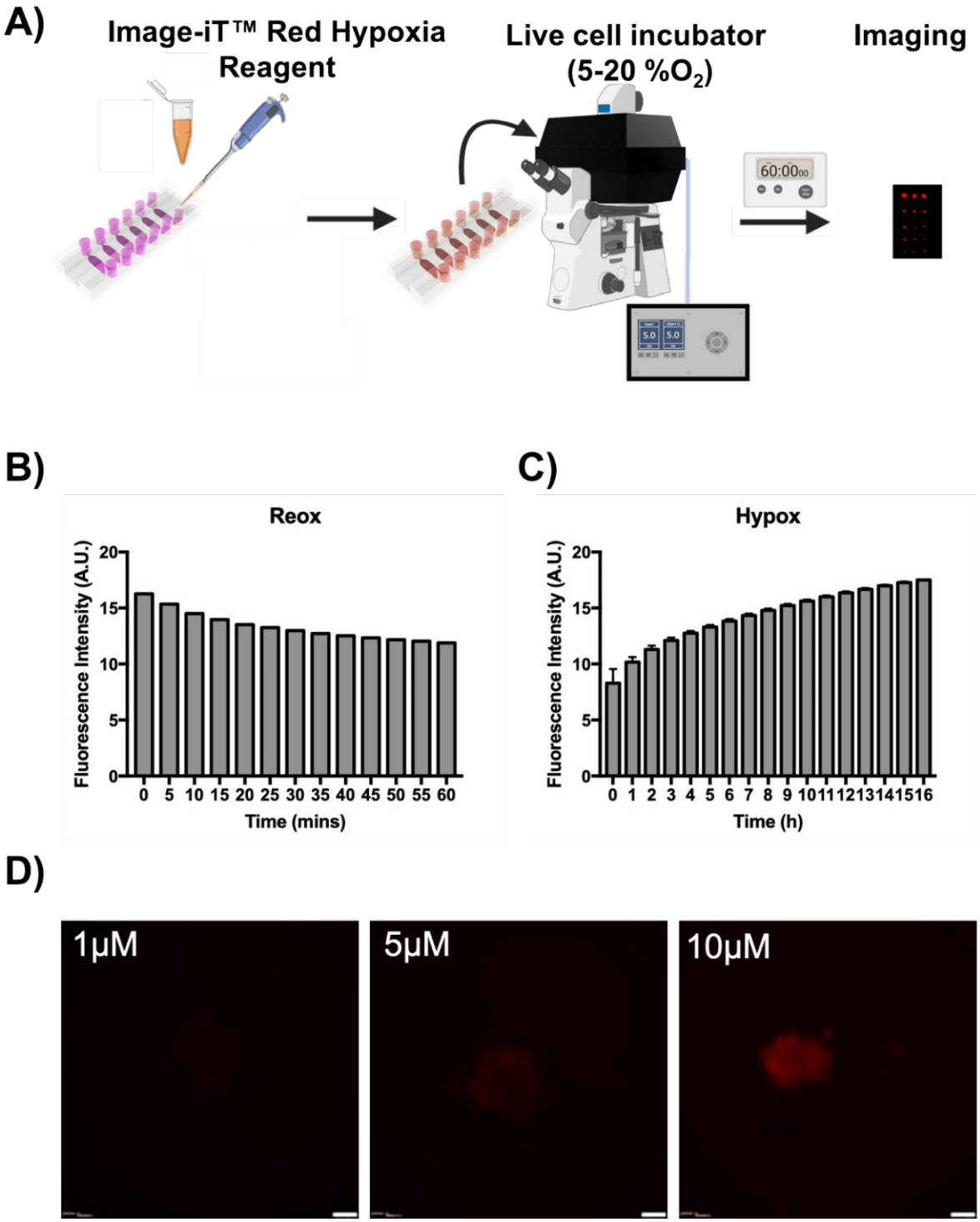

Figure SI-6: A) Experimental design of spheroid hypoxia imaging with the Image-iT™ Red Hypoxia Reagent (Invitrogen). The compound responds to increasing HIF-1alpha expression levels, appearing non-fluorescent when live cells are in an environment with normal oxygen concentrations and becomes fluorescent when oxygen levels are decreased. First, cell culture media was removed from reservoirs and and 200µl of Hypoxia reagent was added and incubated for 1 hour in live cell incubator. After 1 hour of incubation, hypoxia intensities were imaged using TRITC (Ex: 540/Em: 605) fluorescence filter. To first test the reagent sensitivity to low oxygen states, a 2D-monolayer culture of A549 cells stained with Image-iT Red Hypoxia Reagent in live cell incubator with varying oxygen levels. The graphs show the cellular response under **B)** low oxygen conditions at 5% O_2 and **C)** after restoring normal oxygen levels to 20% O_2. The monolayer cultures reacted to low oxygen conditions with a steep increase in signal emission within the first hour. After one hour of exposure, the hypoxia levels increase did not continue with this rate, n=3 ± SD. The declining rate indicates the approach of a plateau state after approximately 24 hours. Restoring oxygen levels (20% O_2) showed a decline in fluorescence intensity by a factor of about 1.4 AU within one hour. This validates that the read-out is sensitive to the decline of HIF-1a expression. **D)** For the determination of the optimal working concentration, A549 cells were seeded at a concentration of 10^4 cells/ml in an ultra-low attachment plate and cultivated at 37°C with 5% CO_2. After 7 days post-seeding A549 spheroids were treated with 1 µM, 5 µM and 10 µM of Image-iT. Red Hypoxia reagent for 1 hour. Scale bar, 200 µm. The hypoxia reagent applied to A549 spheroids showed the best results at a concentration of 10 µm. HIF-1a expression level appears to be low in spheroids under normal oxygen conditions leading to the requirement of higher reagent concentrations.

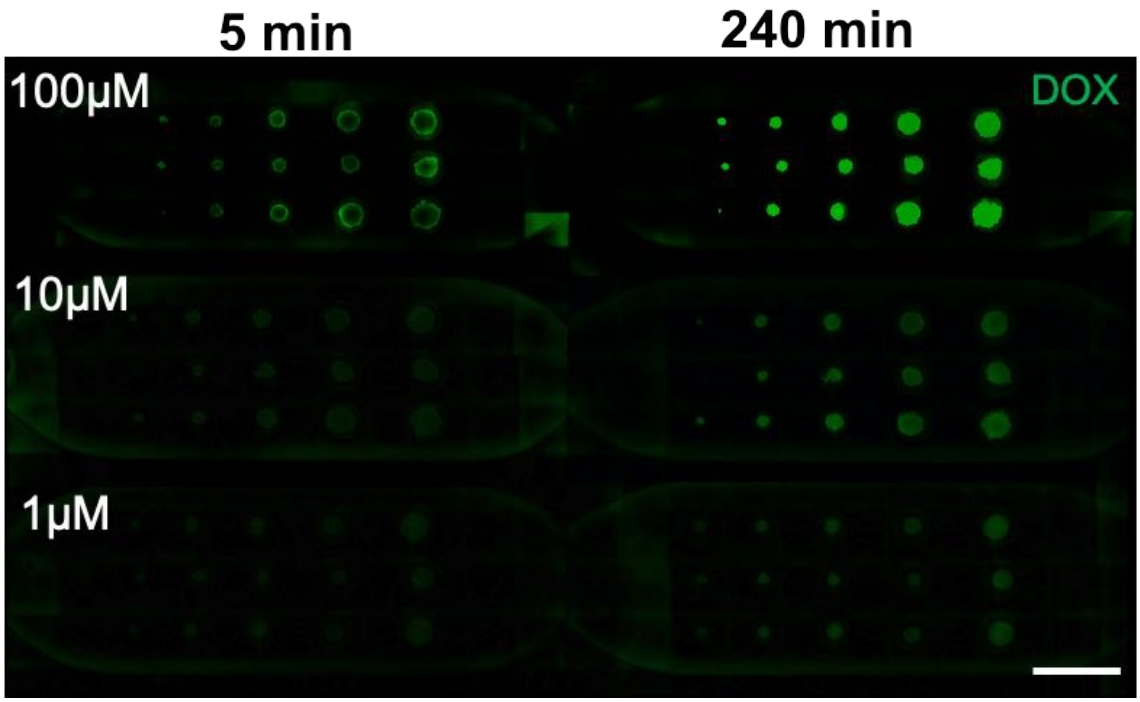

Figure SI-7: Fluorescent micrographs of treated A549 spheroids with the auto-fluorescent anti-cancer drug doxorubicin (DOX) at concentrations of 100 µM, 10 µM and 1 µM for an incubation spheroid of 240 minutes. Scale bar, 2 cm.

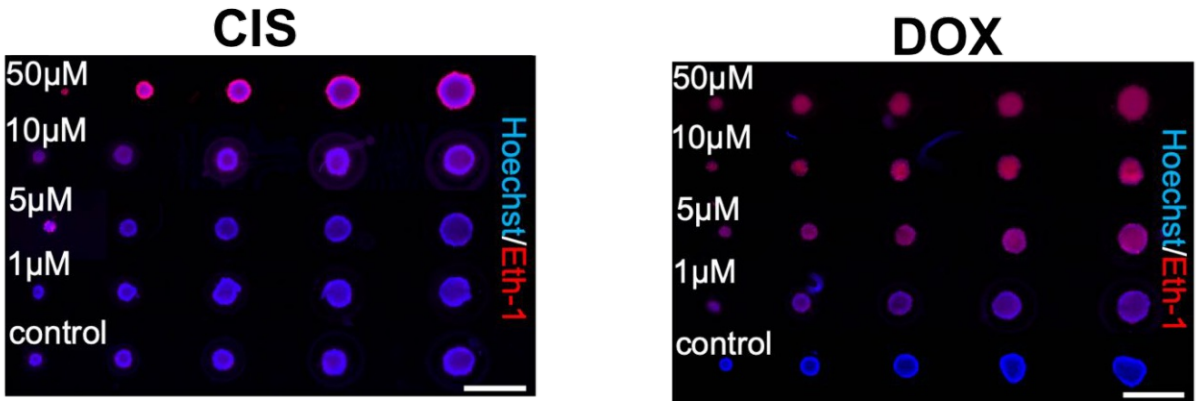

Figure SI-8: Fluorescent micrographs of treated different-sized A549 spheroids in the spheroid array chip with various doses of cisplatin (CIS) and doxorubicin (DOX)) for 24 hours to screen drug toxicity by staining cell nuclei (Hoechst; blue) and dead cells (Ethidium homodimer-1; red. Scale bar, 1 mm.

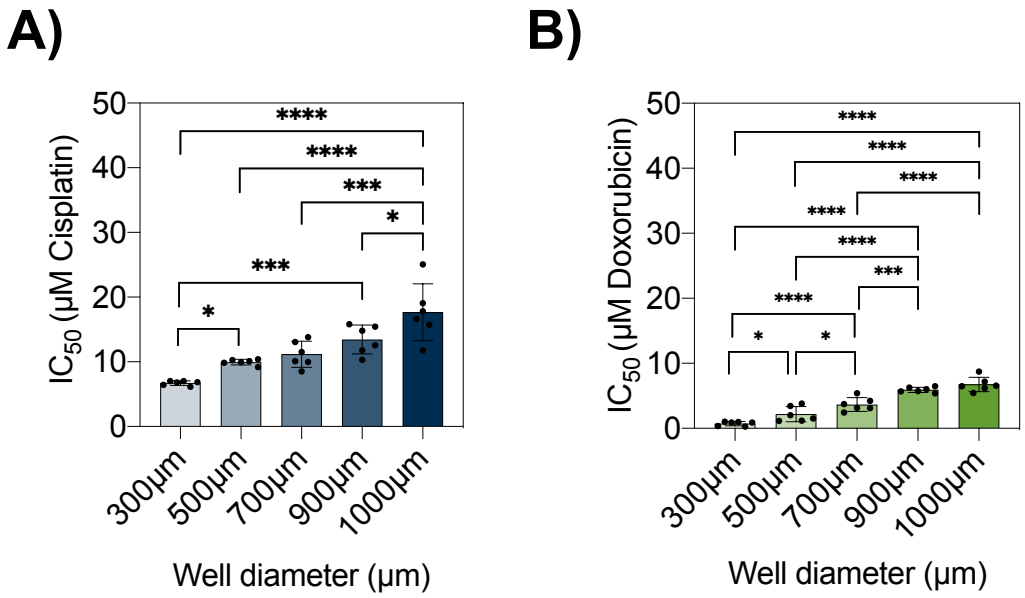

Figure SI-9: Comparative analysis of spheroid size-related effects on IC_{50} values of **A)** cisplatin and **B)** doxorubicin treated A549 spheroids, n=6 ± SD. Statistical analysis was performed using the Holm-Sidak's multiple comparisons test (*p<0.0332, **p<0.0021, ***p<0002, ****p<0.0001).

Table SI-1: Statistical analysis of combinatorial drug screening including cisplatin (CIS) and doxorubicin (DOX) by using the Mixed-effect model, n=3-6 (*p<0.0332, **p<0.0021, ***p<0002, ****p<0.0001, ns, not significant).

CIS:DOX concentrations [µM]	p - value	Summary
500:0	<0.0001	****
500:0.1	<0.0001	****
100:1	<0.0001	****
50:5	<0.0001	****
25:10	0.0004	***
10:25	0.0064	**
5:50	0.1287	ns
1:100	0.1902	ns
0.1:500	0.0556	ns
0:500	0.4062	ns

Table SI-2: Seeding densities of respective BBB cell ratios including human primary astrocytes (hA), human primary pericytes (hP) and hCMEC/D3 (BEC).

Total [cells/ml]	hA	hP	BEC
5.000.000	1	1	3
	1.000.000	1.000.000	3.000.000
5.000.000	1	1	2
	1.250.000	1.250.000	2.500.000
5.000.000	1	1	1
	1.666.667	1.666.667	1.666.667
5.000.000	5.5	1.5	3
	2.750.000	750.000	1.500.00
5.000.000	1	0	0
	5.000.000	0	0
5.000.000	1	4	0
	1.000.000	4.000.000	0

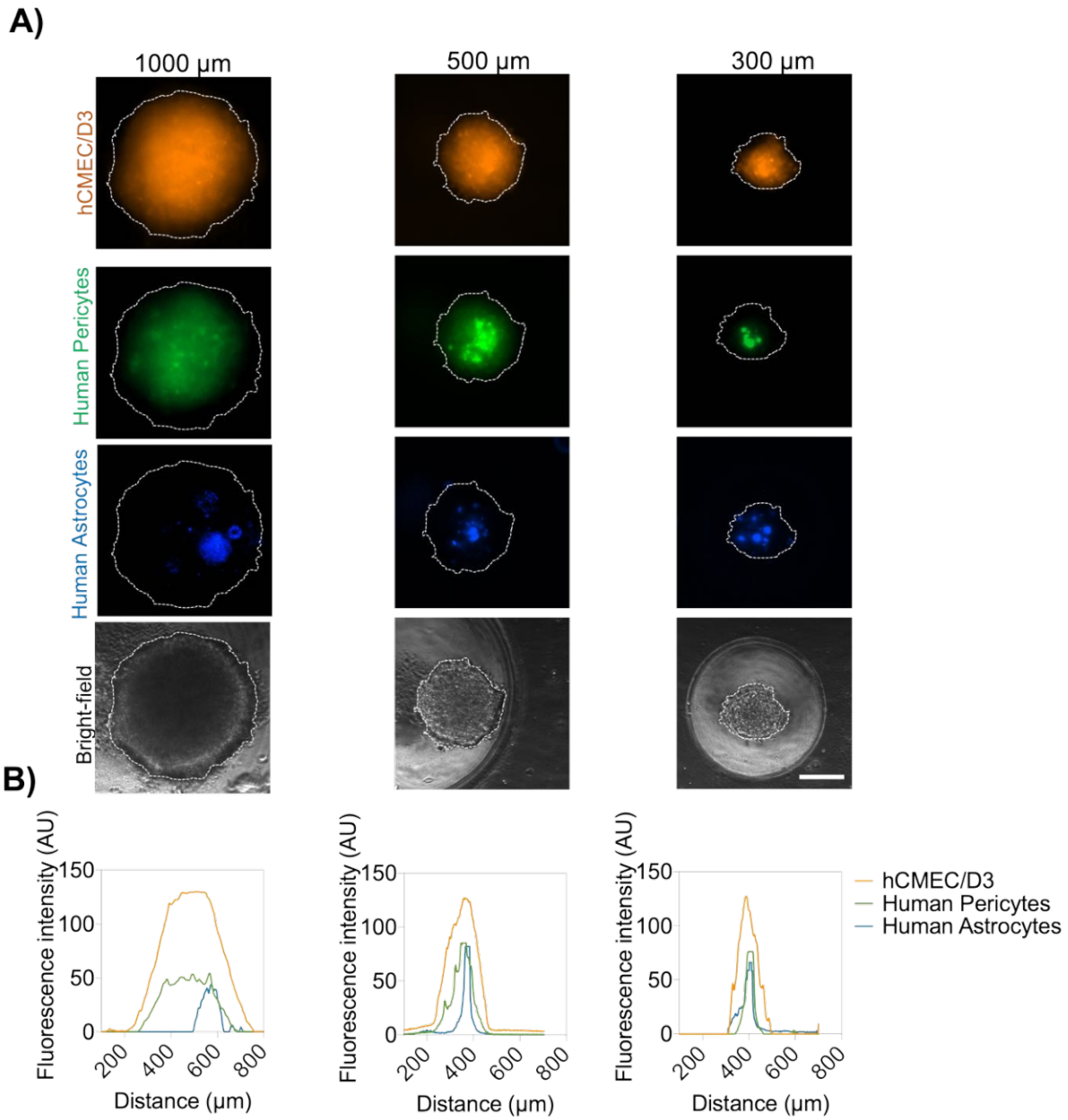

Figure SI-10: A) Fluorescent images of the internal organization of human brain endothelial cells (hCMEC/D3; orange), human pericytes (green), and human astrocytes (blue), when co-cultured to form spheroids after 6-days post-seeding at a cell ratio of 1:1:3 (hA:hP:BEC). Scale bar, 200 µm. **B)** Fluorescent intensity profiles of each labeled cell type in BBB triple-culture spheroids cultivated in 1000 µm, 500 µm, and 300 µm microwells on-chip under continuous perfusion.

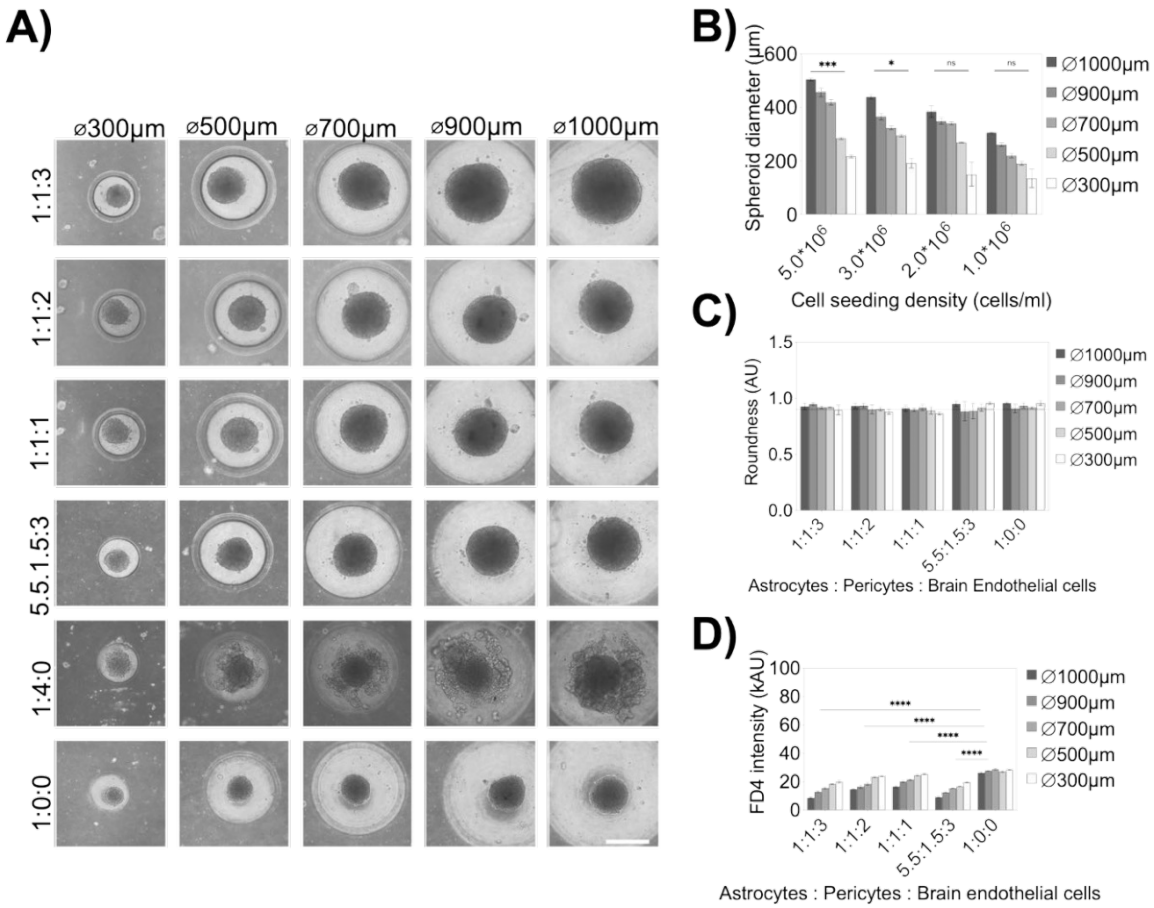

Figure SI-11: A) Bright-field micrographs of BBB spheroids after 6 days post-seeding at an initial cell density of 5*10^6 cells/ml at different cell ratios of human primary astrocytes: human primary pericytes: human brain endothelial cells. Scale bar, 500 µm. **B)** Optimization of initial seeding density for on-chip spheroid co-culture generation regarding spheroid diameters at a ratio of 1:1:3 (hA:hP:BEC), n=3-6 ± SD. Statistical analysis was performed by using the Mixed-effects model. **C)** Roundness of BBB spheroids at different spheroid diameters and seeding ratios, n=3-6 ± SD. **D)** Mean fluorescence intensities of co-culture spheroids of different sizes and cell ratios after one hour of cultivation with 10 µM 4kDa FITC-Dextran (FD4), n = 7-9 ± SD. Statistical analysis was performed by using Dunnett's multiple comparisons test. (*p<0.0332, **p<0.0021, ***p<0.0002, ****p<0.0001, ns=not significant).

References

(1) Scannell, J. W.; Blanckley, A.; Boldon, H.; Warrington, B. Diagnosing the decline in pharmaceutical R&D efficiency. *Nat Rev Drug Discov* **2012,** *11* (3), 191.

(2) "Statistics 2015 - The Pharmaceutical Industry in Germany" German Association of Research-Based Pharmaceutical Companies, 2015.

(3) Ekert, J. E.; Deakyne, J.; Pribul-Allen, P.; Terry, R.; Schofield, C.; Jeong, C. G.; Storey, J.; Mohamet, L.; Francis, J.; Naidoo, A.et al. Recommended Guidelines for Developing, Qualifying, and Implementing Complex In Vitro Models (CIVMs) for Drug Discovery. *SLAS Discov* **2020**, 2472555220923332.

(4) Kaitin, K. I. Deconstructing the drug development process: the new face of innovation. *Clin Pharmacol Ther* **2010,** *87* (3), 356.

(5) Paul, S. M.; Mytelka, D. S.; Dunwiddie, C. T.; Persinger, C. C.; Munos, B. H.; Lindborg, S. R.; Schacht, A. L. How to improve R&D productivity: the pharmaceutical industry's grand challenge. *Nat Rev Drug Discov* **2010,** *9* (3), 203.

(6) Matthews, H.; Hanison, J.; Nirmalan, N. "Omics"-Informed Drug and Biomarker Discovery: Opportunities, Challenges and Future Perspectives. *Proteomes* **2016,** *4* (3).

(7) Hay, M.; Thomas, D. W.; Craighead, J. L.; Economides, C.; Rosenthal, J. Clinical development success rates for investigational drugs. *Nat Biotechnol* **2014,** *32* (1), 40.

(8) Waring, M. J.; Arrowsmith, J.; Leach, A. R.; Leeson, P. D.; Mandrell, S.; Owen, R. M.; Pairaudeau, G.; Pennie, W. D.; Pickett, S. D.; Wang, J.et al. An analysis of the attrition of drug candidates from four major pharmaceutical companies. *Nat Rev Drug Discov* **2015,** *14* (7), 475.

(9) Cukierman, E.; Pankov, R.; Stevens, D. R.; Yamada, K. M. Taking cell-matrix adhesions to the third dimension. *Science* **2001,** *294* (5547), 1708.

(10) Breslin, S.; O'Driscoll, L. Three-dimensional cell culture: the missing link in drug discovery. *Drug Discov Today* **2013,** *18* (5-6), 240.

(11) Jensen, C.; Teng, Y. Is It Time to Start Transitioning From 2D to 3D Cell Culture? *Front Mol Biosci* **2020,** *7*, 33.

(12) Tobert, J. A. Lovastatin and beyond: the history of the HMG-CoA reductase inhibitors. *Nat Rev Drug Discov* **2003,** *2* (7), 517.

(13) Clark, M.; Steger-Hartmann, T. A big data approach to the concordance of the toxicity of pharmaceuticals in animals and humans. *Regul Toxicol Pharmacol* **2018,** *96*, 94.

(14) Arrowsmith, J. Trial watch: Phase II failures: 2008-2010. *Nat Rev Drug Discov* **2011,** *10* (5), 328.

(15) Arrowsmith, J. Trial watch: phase III and submission failures: 2007-2010. *Nat Rev Drug Discov* **2011,** *10* (2), 87.

(16) Eglen, R. M.; Randle, D. H. Drug Discovery Goes Three-Dimensional: Goodbye to Flat High-Throughput Screening? *Assay Drug Dev Technol* **2015,** *13* (5), 262.

(17) Kola, I.; Landis, J. Can the pharmaceutical industry reduce attrition rates? *Nat Rev Drug Discov* **2004,** *3* (8), 711.

(18) Pammolli, F.; Righetto, L.; Abrignani, S.; Pani, L.; Pelicci, P. G.; Rabosio, E. The endless frontier? The recent increase of R&D productivity in pharmaceuticals. *J Transl Med* **2020,** *18* (1), 162.

(19) Yamada, K. M.; Cukierman, E. Modeling tissue morphogenesis and cancer in 3D. *Cell* **2007,** *130* (4), 601.

(20) Caicedo-Carvajal, C.; Liu, Q.; Goy, A.; Pecora, A.; Suh, K. Three-Dimensional Cell Culture Models for Biomarker Discoveries and Cancer Research. *Translational Medicine* **2012**.

(21) Nath, S. a. D. G. R. Three-Dimensional Culture Systems in Cancer Research: Focus on Tumor Spheroid Model. *Pharmacology \& Therapeutics* **2016**.

(22) Edmondson, R.; Broglie, J. J.; Adcock, A. F.; Yang, L. Three-dimensional cell culture systems and their applications in drug discovery and cell-based biosensors. *Assay Drug Dev Technol* **2014,** *12* (4), 207.

(23) Sutherland, R. M. Cell and environment interactions in tumor microregions: the multicell spheroid model. *Science* **1988,** *240* (4849), 177.

(24) Achilli, T. M.; Meyer, J.; Morgan, J. R. Advances in the formation, use and understanding of multi-cellular spheroids. *Expert Opin Biol Ther* **2012,** *12* (10), 1347.

(25) Hirschhaeuser, F.; Menne, H.; Dittfeld, C.; West, J.; Mueller-Klieser, W.; Kunz-Schughart, L. A. Multicellular tumor spheroids: an underestimated tool is catching up again. *J Biotechnol* **2010,** *148* (1), 3.

(26) Sato, T.; Vries, R. G.; Snippert, H. J.; van de Wetering, M.; Barker, N.; Stange, D. E.; van Es, J. H.; Abo, A.; Kujala, P.; Peters, P. J.et al. Single Lgr5 stem cells build crypt-villus structures in vitro without a mesenchymal niche. *Nature* **2009,** *459* (7244), 262.

(27) Hofmann, C.; Obermeier, F.; Artinger, M.; Hausmann, M.; Falk, W.; Schoelmerich, J.; Rogler, G.; Grossmann, J. Cell-cell contacts prevent anoikis in primary human colonic epithelial cells. *Gastroenterology* **2007,** *132* (2), 587.

(28) Mehta, G.; Hsiao, A. Y.; Ingram, M.; Luker, G. D.; Takayama, S. Opportunities and challenges for use of tumor spheroids as models to test drug delivery and efficacy. *J Control Release* **2012,** *164* (2), 192.

(29) Friedrich, J.; Ebner, R.; Kunz-Schughart, L. A. Experimental anti-tumor therapy in 3-D: spheroids--old hat or new challenge? *Int J Radiat Biol* **2007,** *83* (11-12), 849.

(30) Curcio, E.; Salerno, S.; Barbieri, G.; De Bartolo, L.; Drioli, E.; Bader, A. Mass transfer and metabolic reactions in hepatocyte spheroids cultured in rotating wall gas-permeable membrane system. *Biomaterials* **2007,** *28* (36), 5487.

(31) Koppenol, W. H.; Bounds, P. L.; Dang, C. V. Otto Warburg's contributions to current concepts of cancer metabolism. *Nat Rev Cancer* **2011,** *11* (5), 325.

(32) Nath, S.; Devi, G. R. Three-dimensional culture systems in cancer research: Focus on tumor spheroid model. *Pharmacol Ther* **2016,** *163*, 94.

(33) Shultz, L. D.; Brehm, M. A.; Garcia-Martinez, J. V.; Greiner, D. L. Humanized mice for immune system investigation: progress, promise and challenges. *Nat Rev Immunol* **2012,** *12* (11), 786.

(34) Mestas, J.; Hughes, C. C. Of mice and not men: differences between mouse and human immunology. *J Immunol* **2004,** *172* (5), 2731.

(35) Haycock, J. W. 3D cell culture: a review of current approaches and techniques. *Methods Mol Biol* **2011,** *695*, 1.

(36) Varthya, S.; Chenchula, S.; Kumar, S.; Shobhan, B. Comparative Efficacy of 3Dimensional (3D) Cell Culture Organoids Vs 2Dimensional (2D) Cell Cultures Vs Experimental Animal Models In Disease modeling, Drug development, And Drug Toxicity Testing. *International Journal of Current Research and Review* **2019**.

(37) Allensworth, J. L.; Evans, M. K.; Bertucci, F.; Aldrich, A. J.; Festa, R. A.; Finetti, P.; Ueno, N. T.; Safi, R.; McDonnell, D. P.; Thiele, D. J.et al. Disulfiram (DSF) acts as a copper ionophore to induce copper-dependent oxidative stress and mediate anti-tumor efficacy in inflammatory breast cancer. *Mol Oncol* **2015,** *9* (6), 1155.

(38) Lee, G. Y.; Kenny, P. A.; Lee, E. H.; Bissell, M. J. Three-dimensional culture models of normal and malignant breast epithelial cells. *Nat Methods* **2007,** *4* (4), 359.

(39) Youn, B. S.; Sen, A.; Behie, L. A.; Girgis-Gabardo, A.; Hassell, J. A. Scale-up of breast cancer stem cell aggregate cultures to suspension bioreactors. *Biotechnol Prog* **2006,** *22* (3), 801.

(40) Muhitch, J. W.; O'Connor, K. C.; Blake, D. A.; Lacks, D. J.; Rosenzweig, N.; Spaulding, G. F. Characterization of aggregation and protein expression of bovine corneal endothelial cells as microcarrier cultures in a rotating-wall vessel. *Cytotechnology* **2000,** *32* (3), 253.

(41) Yoshii, Y.; Waki, A.; Yoshida, K.; Kakezuka, A.; Kobayashi, M.; Namiki, H.; Kuroda, Y.; Kiyono, Y.; Yoshii, H.; Furukawa, T.et al. The use of nanoimprinted scaffolds as 3D culture models to facilitate spontaneous tumor cell migration and well-regulated spheroid formation. *Biomaterials* **2011,** *32* (26), 6052.

(42) Nemeth, C. L.; Janebodin, K.; Yuan, A. E.; Dennis, J. E.; Reyes, M.; Kim, D. H. Enhanced chondrogenic differentiation of dental pulp stem cells using nanopatterned PEG-GelMA-HA hydrogels. *Tissue Eng Part A* **2014,** *20* (21-22), 2817.

(43) Li, J.; He, F.; Pei, M. Creation of an in vitro microenvironment to enhance human fetal synovium-derived stem cell chondrogenesis. *Cell Tissue Res* **2011,** *345* (3), 357.

(44) Giovannini, S.; Diaz-Romero, J.; Aigner, T.; Heini, P.; Mainil-Varlet, P.; Nesic, D. Micromass co-culture of human articular chondrocytes and human bone marrow mesenchymal stem cells to investigate stable neocartilage tissue formation in vitro. *Eur Cell Mater* **2010,** *20*, 245.

(45) Carlsson, J.; Yuhas, J. M. Liquid-overlay culture of cellular spheroids. *Recent Results Cancer Res* **1984,** *95*, 1.

(46) Costa, E. C.; Gaspar, V. M.; Coutinho, P.; Correia, I. J. Optimization of liquid overlay technique to formulate heterogenic 3D co-cultures models. *Biotechnol Bioeng* **2014,** *111* (8), 1672.

(47) Vinci, M.; Gowan, S.; Boxall, F.; Patterson, L.; Zimmermann, M.; Court, W.; Lomas, C.; Mendiola, M.; Hardisson, D.; Eccles, S. A. Advances in establishment and analysis of three-dimensional tumor spheroid-based functional assays for target validation and drug evaluation. *BMC Biol* **2012,** *10*, 29.

(48) Kelm, J. M.; Timmins, N. E.; Brown, C. J.; Fussenegger, M.; Nielsen, L. K. Method for generation of homogeneous multicellular tumor spheroids applicable to a wide variety of cell types. *Biotechnol Bioeng* **2003,** *83* (2), 173.

(49) Tung, Y. C.; Hsiao, A. Y.; Allen, S. G.; Torisawa, Y. S.; Ho, M.; Takayama, S. High-throughput 3D spheroid culture and drug testing using a 384 hanging drop array. *Analyst* **2011,** *136* (3), 473.

(50) Timmins, N. E.; Nielsen, L. K. Generation of multicellular tumor spheroids by the hanging-drop method. *Methods Mol Med* **2007,** *140*, 141.

(51) Sebastian, A.; Buckle, A. M.; Markx, G. H. Tissue engineering with electric fields: immobilization of mammalian cells in multilayer aggregates using dielectrophoresis. *Biotechnol Bioeng* **2007,** *98* (3), 694.

(52) Ino, K.; Okochi, M.; Honda, H. Application of magnetic force-based cell patterning for controlling cell-cell interactions in angiogenesis. *Biotechnol Bioeng* **2009,** *102* (3), 882.

(53) Liu, J.; Kuznetsova, L. A.; Edwards, G. O.; Xu, J.; Ma, M.; Purcell, W. M.; Jackson, S. K.; Coakley, W. T. Functional three-dimensional HepG2 aggregate cultures generated from an ultrasound trap: comparison with HepG2 spheroids. *J Cell Biochem* **2007,** *102* (5), 1180.

(54) Peng, W.; Unutmaz, D.; Ozbolat, I. T. Bioprinting towards Physiologically Relevant Tissue Models for Pharmaceutics. *Trends Biotechnol* **2016,** *34* (9), 722.

(55) Knowlton, S.; Onal, S.; Yu, C. H.; Zhao, J. J.; Tasoglu, S. Bioprinting for cancer research. *Trends Biotechnol* **2015,** *33* (9), 504.

(56) Young, E. W. Cells, tissues, and organs on chips: challenges and opportunities for the cancer tumor microenvironment. *Integr Biol (Camb)* **2013,** *5* (9), 1096.

(57) Whitesides, G. M.; Ostuni, E.; Takayama, S.; Jiang, X.; Ingber, D. E. Soft lithography in biology and biochemistry. *Annu Rev Biomed Eng* **2001,** *3*, 335.

(58) Gokaltun, A.; Yarmush, M. L.; Asatekin, A.; Usta, O. B. Recent advances in nonbiofouling PDMS surface modification strategies applicable to microfluidic technology. *Technology (Singap World Sci)* **2017,** *5* (1), 1.

(59) Folch, A.; Toner, M. Microengineering of cellular interactions. *Annu Rev Biomed Eng* **2000,** *2*, 227.

(60) Rothbauer, M.; Ertl, P.; Theiler, B.; Schlager, M.; Sleytr, U. B.; Küpcü, S. Anisotropic Crystalline Protein Nanolayers as Multi- Functional Biointerface for Patterned Co-Cultures of Adherent and Non-Adherent Cells in Microfluidic Devices. *Advanced Materials Interfaces* **2015,** *2* (1), 8020.

(61) El-Ali, J.; Sorger, P. K.; Jensen, K. F. Cells on chips. *Nature* **2006,** *442* (7101), 403.

(62) Nguyen, N. T.; Shaegh, S. A.; Kashaninejad, N.; Phan, D. T. Design, fabrication and characterization of drug delivery systems based on lab-on-a-chip technology. *Adv Drug Deliv Rev* **2013,** *65* (11-12), 1403.

(63) Tagle, D. A. The NIH microphysiological systems program: developing in vitro tools for safety and efficacy in drug development. *Curr Opin Pharmacol* **2019,** *48*, 146.

(64) McMillan, K. S.; McCluskey, A. G.; Sorensen, A.; Boyd, M.; Zagnoni, M. Emulsion technologies for multicellular tumour spheroid radiation assays. *Analyst* **2016,** *141* (1), 100.

(65) Chan, H. F.; Zhang, Y.; Ho, Y. P.; Chiu, Y. L.; Jung, Y.; Leong, K. W. Rapid formation of multicellular spheroids in double-emulsion droplets with controllable microenvironment. *Sci Rep* **2013,** *3*, 3462.

(66) Yoon, S.; Kim, J. A.; Lee, S. H.; Kim, M.; Park, T. H. Droplet-based microfluidic system to form and separate multicellular spheroids using magnetic nanoparticles. *Lab Chip* **2013,** *13* (8), 1522.

(67) Kwapiszewska, K.; Michalczuk, A.; Rybka, M.; Kwapiszewski, R.; Brzózka, Z. A microfluidic-based platform for tumour spheroid culture, monitoring and drug screening. *Lab Chip* **2014,** *14* (12), 2096.

(68) Kim, C.; Bang, J. H.; Kim, Y. E.; Lee, S. H.; Kang, J. Y. On-chip anticancer drug test of regular tumor spheroids formed in microwells by a distributive microchannel network. *Lab Chip* **2012,** *12* (20), 4135.

(69) Fu, C. Y.; Tseng, S. Y.; Yang, S. M.; Hsu, L.; Liu, C. H.; Chang, H. Y. A microfluidic chip with a U-shaped microstructure array for multicellular spheroid formation, culturing and analysis. *Biofabrication* **2014,** *6* (1), 015009.

(70) Liu, W.; Wang, J. C.; Wang, J. Controllable organization and high throughput production of recoverable 3D tumors using pneumatic microfluidics. *Lab Chip* **2015,** *15* (4), 1195.

(71) Frey, O.; Misun, P. M.; Fluri, D. A.; Hengstler, J. G.; Hierlemann, A. Reconfigurable microfluidic hanging drop network for multi-tissue interaction and analysis. *Nat Commun* **2014,** *5*, 4250.

(72) Wu, H. W.; Hsiao, Y. H.; Chen, C. C.; Yet, S. F.; Hsu, C. H. A PDMS-Based Microfluidic Hanging Drop Chip for Embryoid Body Formation. *Molecules* **2016,** *21* (7).

(73) Torisawa, Y. S.; Chueh, B. H.; Huh, D.; Ramamurthy, P.; Roth, T. M.; Barald, K. F.; Takayama, S. Efficient formation of uniform-sized embryoid bodies using a compartmentalized microchannel device. *Lab Chip* **2007,** *7* (6), 770.

(74) Hsiao, A. Y.; Torisawa, Y. S.; Tung, Y. C.; Sud, S.; Taichman, R. S.; Pienta, K. J.; Takayama, S. Microfluidic system for formation of PC-3 prostate cancer co-culture spheroids. *Biomaterials* **2009,** *30* (16), 3020.

(75) Ota, H.; Kodama, T.; Miki, N. Rapid formation of size-controlled three dimensional hetero-cell aggregates using micro-rotation flow for spheroid study. *Biomicrofluidics* **2011,** *5* (3), 34105.

(76) Ota, H.; Miki, N. Microtechnology-based three-dimensional spheroid formation. *Front Biosci (Elite Ed)* **2013,** *5*, 37.

(77) Chen, K.; Wu, M.; Guo, F.; Li, P.; Chan, C. Y.; Mao, Z.; Li, S.; Ren, L.; Zhang, R.; Huang, T. J. Rapid formation of size-controllable multicellular spheroids via 3D acoustic tweezers. *Lab Chip* **2016,** *16* (14), 2636.

(78) Shi, J.; Yazdi, S.; Lin, S. C.; Ding, X.; Chiang, I. K.; Sharp, K.; Huang, T. J. Three-dimensional continuous particle focusing in a microfluidic channel via standing surface acoustic waves (SSAW). *Lab Chip* **2011,** *11* (14), 2319.

(79) Bender, B. F.; Aijian, A. P.; Garrell, R. L. Digital microfluidics for spheroid-based invasion assays. *Lab Chip* **2016,** *16* (8), 1505.

(80) Eydelnant, I. A.; Uddayasankar, U.; Li, B.; Liao, M. W.; Wheeler, A. R. Virtual microwells for digital microfluidic reagent dispensing and cell culture. *Lab Chip* **2012,** *12* (4), 750.

(81) Moshksayan , K.; Kashaninejad , N.; Warkiani , M. E.; Lock , J. G.; Moghadas , H.; Firoozabadi , B.; Saidi , M. S.; Nguyen , N.-T. Spheroids-on-a-chip: Recent advances and design considerations in microfluidic platforms for spheroid formation and culture. *Sensors and Actuators B: Chemical* **2018,** *263*.

(82) Costa, E. C.; Moreira, A. F.; de Melo-Diogo, D.; Gaspar, V. M.; Carvalho, M. P.; Correia, I. J. 3D tumor spheroids: an overview on the tools and techniques used for their analysis. *Biotechnol Adv* **2016,** *34* (8), 1427.

(83) Ma, H. L.; Jiang, Q.; Han, S.; Wu, Y.; Cui Tomshine, J.; Wang, D.; Gan, Y.; Zou, G.; Liang, X. J. Multicellular tumor spheroids as an in vivo-like tumor model for three-dimensional imaging of chemotherapeutic and nano material cellular penetration. *Mol Imaging* **2012,** *11* (6), 487.

(84) Huo, S.; Ma, H.; Huang, K.; Liu, J.; Wei, T.; Jin, S.; Zhang, J.; He, S.; Liang, X. J. Superior penetration and retention behavior of 50 nm gold nanoparticles in tumors. *Cancer Res* **2013,** *73* (1), 319.

(85) Friedrich, J.; Eder, W.; Castaneda, J.; Doss, M.; Huber, E.; Ebner, R.; Kunz-Schughart, L. A. A reliable tool to determine cell viability in complex 3-d culture: the acid phosphatase assay. *J Biomol Screen* **2007,** *12* (7), 925.

(86) Ansari, N.; Müller, S.; Stelzer, E. H.; Pampaloni, F. Quantitative 3D cell-based assay performed with cellular spheroids and fluorescence microscopy. *Methods Cell Biol* **2013,** *113*, 295.

(87) Ivanov, D. P.; Parker, T. L.; Walker, D. A.; Alexander, C.; Ashford, M. B.; Gellert, P. R.; Garnett, M. C. In vitro co-culture model of medulloblastoma and human neural stem cells for drug delivery assessment. *J Biotechnol* **2015,** *205*, 3.

(88) Gaspar, V. M.; Gonçalves, C.; de Melo-Diogo, D.; Costa, E. C.; Queiroz, J. A.; Pichon, C.; Sousa, F.; Correia, I. J. Poly(2-ethyl-2-oxazoline)-PLA-g-PEI amphiphilic triblock micelles for co-delivery of minicircle DNA and chemotherapeutics. *J Control Release* **2014,** *189*, 90.

(89) Yeon, S. E.; No, d. Y.; Lee, S. H.; Nam, S. W.; Oh, I. H.; Lee, J.; Kuh, H. J. Application of concave microwells to pancreatic tumor spheroids enabling anticancer drug evaluation in a clinically relevant drug resistance model. *PLoS One* **2013,** *8* (9), e73345.

(90) Graf, B. W.; Boppart, S. A. Imaging and analysis of three-dimensional cell culture models. *Methods Mol Biol* **2010,** *591*, 211.

(91) Bruns, T.; Schickinger, S.; Wittig, R.; Schneckenburger, H. Preparation strategy and illumination of three-dimensional cell cultures in light sheet-based fluorescence microscopy. *J Biomed Opt* **2012,** *17* (10), 101518.

(92) Pampaloni, F.; Ansari, N.; Stelzer, E. H. High-resolution deep imaging of live cellular spheroids with light-sheet-based fluorescence microscopy. *Cell Tissue Res* **2013,** *352* (1), 161.

(93) Gualda, E. J.; Simão, D.; Pinto, C.; Alves, P. M.; Brito, C. Imaging of human differentiated 3D neural aggregates using light sheet fluorescence microscopy. *Front Cell Neurosci* **2014,** *8*, 221.

(94) Baek, S. K.; Makkouk, A. R.; Krasieva, T.; Sun, C. H.; Madsen, S. J.; Hirschberg, H. Photothermal treatment of glioma; an in vitro study of macrophage-mediated delivery of gold nanoshells. *J Neurooncol* **2011,** *104* (2), 439.

(95) Hwang, Y. J.; Kolettis, N.; Yang, M.; Gillard, E. R.; Sanchez, E.; Sun, C. H.; Tromberg, B. J.; Krasieva, T. B.; Lyubovitsky, J. G. Multiphoton imaging of actin filament formation and mitochondrial energetics of human ACBT gliomas. *Photochem Photobiol* **2011,** *87* (2), 408.

(96) Liu, T. L.; Upadhyayula, S.; Milkie, D. E.; Singh, V.; Wang, K.; Swinburne, I. A.; Mosaliganti, K. R.; Collins, Z. M.; Hiscock, T. W.; Shea, J.et al. Observing the cell in its native state: Imaging subcellular dynamics in multicellular organisms. *Science* **2018,** *360* (6386).

(97) Schöneberg, J.; Dambournet, D.; Liu, T. L.; Forster, R.; Hockemeyer, D.; Betzig, E.; Drubin, D. G. In *Mol Biol Cell*, 2018; Vol. 29.

(98) Moreno-Flores, S.; Küpcü, S. 2D protein arrays induce 3D in vivo-like assemblies of cells. *Soft Matter* **2015,** *11* (7), 1259.

(99) do Amaral, J. B.; Urabayashi, M. S.; Machado-Santelli, G. M. Cell death and lumen formation in spheroids of MCF-7 cells. *Cell Biol Int* **2010,** *34* (3), 267.

(100) Dolfini, E.; Roncoroni, L.; Elli, L.; Fumagalli, C.; Colombo, R.; Ramponi, S.; Forlani, F.; Bardella, M. T. Cytoskeleton reorganization and ultrastructural damage induced by gliadin in a three-dimensional in vitro model. *World J Gastroenterol* **2005,** *11* (48), 7597.

(101) Uroukov, I. S.; Patton, D. Optimizing environmental scanning electron microscopy of spheroidal reaggregated neuronal cultures. *Microsc Res Tech* **2008,** *71* (11), 792.

(102) Yoshida, D.; Noha, M.; Watanabe, K.; Sugisaki, Y.; Teramoto, A. Novel approach to analysis of in vitro tumor angiogenesis with a variable-pressure scanning electron microscope: suppression by matrix metalloproteinase inhibitor SI-27. *Brain Tumor Pathol* **2001,** *18* (2), 89.

(103) Dorst, N.; Oberringer, M.; Grässer, U.; Pohlemann, T.; Metzger, W. Analysis of cellular composition of co-culture spheroids. *Ann Anat* **2014,** *196* (5), 303.

(104) Walzl, A.; Unger, C.; Kramer, N.; Unterleuthner, D.; Scherzer, M.; Hengstschläger, M.; Schwanzer-Pfeiffer, D.; Dolznig, H. The Resazurin Reduction Assay Can Distinguish Cytotoxic from Cytostatic Compounds in Spheroid Screening Assays. *J Biomol Screen* **2014,** *19* (7), 1047.

(105) De Witt Hamer, P. C.; Jonker, A.; Leenstra, S.; Ruijter, J. M.; Van Noorden, C. J. Quantification of viability in organotypic multicellular spheroids of human malignant glioma using lactate dehydrogenase activity: a rapid and reliable automated assay. *J Histochem Cytochem* **2005,** *53* (1), 23.

(106) Ho, W. Y.; Yeap, S. K.; Ho, C. L.; Rahim, R. A.; Alitheen, N. B. Development of multicellular tumor spheroid (MCTS) culture from breast cancer cell and a high throughput screening method using the MTT assay. *PLoS One* **2012,** *7* (9), e44640.

(107) Zhang, X.; Fryknäs, M.; Hernlund, E.; Fayad, W.; De Milito, A.; Olofsson, M. H.; Gogvadze, V.; Dang, L.; Påhlman, S.; Schughart, L. A.et al. Induction of mitochondrial dysfunction as a strategy for targeting tumour cells in metabolically compromised microenvironments. *Nat Commun* **2014,** *5*, 3295.

(108) Riss, T. L.; Moravec, R. A. Use of multiple assay endpoints to investigate the effects of incubation time, dose of toxin, and plating density in cell-based cytotoxicity assays. *Assay Drug Dev Technol* **2004,** *2* (1), 51.

(109) Riss, T. L.; Moravec, R. A.; Niles, A. L. Cytotoxicity testing: measuring viable cells, dead cells, and detecting mechanism of cell death. *Methods Mol Biol* **2011,** *740*, 103.

(110) Zhang, J. Z.; Bryce, N. S.; Siegele, R.; Carter, E. A.; Paterson, D.; de Jonge, M. D.; Howard, D. L.; Ryan, C. G.; Hambley, T. W. The use of spectroscopic imaging and mapping techniques in the characterisation and study of DLD-1 cell spheroid tumour models. *Integr Biol (Camb)* **2012,** *4* (9), 1072.

(111) Sun, M.; Tian, X.; Yang, Z. Microscale Mass Spectrometry Analysis of Extracellular Metabolites in Live Multicellular Tumor Spheroids. *Anal Chem* **2017,** *89* (17), 9069.

(112) Bollard, M. E.; Stanley, E. G.; Lindon, J. C.; Nicholson, J. K.; Holmes, E. NMR-based metabonomic approaches for evaluating physiological influences on biofluid composition. *NMR Biomed* **2005,** *18* (3), 143.

(113) Schilling, F.; Düwel, S.; Köllisch, U.; Durst, M.; Schulte, R. F.; Glaser, S. J.; Haase, A.; Otto, A. M.; Menzel, M. I. Diffusion of hyperpolarized (13) C-metabolites in tumor cell spheroids using real-time NMR spectroscopy. *NMR Biomed* **2013,** *26* (5), 557.

(114) Theiner, S.; Schreiber-Brynzak, E.; Jakupec, M. A.; Galanski, M.; Koellensperger, G.; Keppler, B. K. LA-ICP-MS imaging in multicellular tumor

spheroids - a novel tool in the preclinical development of metal-based anticancer drugs. *Metallomics* **2016,** *8* (4), 398.

(115) Theiner, S.; Van Malderen, S. J. M.; Van Acker, T.; Legin, A.; Keppler, B. K.; Vanhaecke, F.; Koellensperger, G. Fast High-Resolution Laser Ablation-Inductively Coupled Plasma Mass Spectrometry Imaging of the Distribution of Platinum-Based Anticancer Compounds in Multicellular Tumor Spheroids. *Anal Chem* **2017,** *89* (23), 12641.

(116) Mahmood, T.; Yang, P. C. Western blot: technique, theory, and trouble shooting. *N Am J Med Sci* **2012,** *4* (9), 429.

(117) Mischiati, C.; Ura, B.; Roncoroni, L.; Elli, L.; Cervellati, C.; Squerzanti, M.; Conte, D.; Doneda, L.; Polverino de Laureto, P.; de Franceschi, G.et al. Changes in protein expression in two cholangiocarcinoma cell lines undergoing formation of multicellular tumor spheroids in vitro. *PLoS One* **2015,** *10* (3), e0118906.

(118) Lakka, S. S.; Gondi, C. S.; Yanamandra, N.; Olivero, W. C.; Dinh, D. H.; Gujrati, M.; Rao, J. S. Inhibition of cathepsin B and MMP-9 gene expression in glioblastoma cell line via RNA interference reduces tumor cell invasion, tumor growth and angiogenesis. *Oncogene* **2004,** *23* (27), 4681.

(119) Pettee, K. M.; Dvorak, K. M.; Nestor-Kalinoski, A. L.; Eisenmann, K. M. An mDia2/ROCK signaling axis regulates invasive egress from epithelial ovarian cancer spheroids. *PLoS One* **2014,** *9* (2), e90371.

(120) Yorke, E. D.; Fuks, Z.; Norton, L.; Whitmore, W.; Ling, C. C. Modeling the development of metastases from primary and locally recurrent tumors: comparison with a clinical data base for prostatic cancer. *Cancer Res* **1993,** *53* (13), 2987.

(121) Laird, A. K. Dynamics of growth in tumors and in normal organisms. *Natl Cancer Inst Monogr* **1969,** *30*, 15.

(122) Leung, B. M.; Lesher-Perez, S. C.; Matsuoka, T.; Moraes, C.; Takayama, S. Media additives to promote spheroid circularity and compactness in hanging drop platform. *Biomater Sci* **2015,** *3* (2), 336.

(123) Piccinini, F.; Tesei, A.; Arienti, C.; Bevilacqua, A. Cancer multicellular spheroids: volume assessment from a single 2D projection. *Comput Methods Programs Biomed* **2015,** *118* (2), 95.

(124) Achilli, T. M.; McCalla, S.; Meyer, J.; Tripathi, A.; Morgan, J. R. Multilayer spheroids to quantify drug uptake and diffusion in 3D. *Mol Pharm* **2014,** *11* (7), 2071.

(125) Goodman, T. T.; Chen, J.; Matveev, K.; Pun, S. H. Spatio-temporal modeling of nanoparticle delivery to multicellular tumor spheroids. *Biotechnol Bioeng* **2008,** *101* (2), 388.

(126) Gao, Y.; Li, M.; Chen, B.; Shen, Z.; Guo, P.; Wientjes, M. G.; Au, J. L. Predictive models of diffusive nanoparticle transport in 3-dimensional tumor cell spheroids. *AAPS J* **2013,** *15* (3), 816.

(127) Chen, Y.; Gao, D.; Liu, H.; Lin, S.; Jiang, Y. Drug cytotoxicity and signaling pathway analysis with three-dimensional tumor spheroids in a microwell-based microfluidic chip for drug screening. *Anal Chim Acta* **2015,** *898*, 85.

(128) Misun, P. M.; Rothe, J.; Schmid, Y. R. F.; Hierlemann, A.; Frey, O. Multi-analyte biosensor interface for real-time monitoring of 3D microtissue spheroids in hanging-drop networks. *Microsyst Nanoeng* **2016,** *2*, 16022.

(129) Schmid, Y.; Bürgel, S.; Misun, P.; Hierlemann, A.; Frey, O. Electrical Impedance Spectroscopy for Microtissue Spheroid Analysis in Hanging-Drop Networks. *ACS Sensors* **2016,** *1*.

(130) Alexander, F.; Eggert, S.; Wiest, J. A novel lab-on-a-chip platform for spheroid metabolism monitoring. *Cytotechnology* **2018,** *70* (1), 375.

(131) Rask-Andersen, M.; Almén, M. S.; Schiöth, H. B. Trends in the exploitation of novel drug targets. *Nat Rev Drug Discov* **2011,** *10* (8), 579.

(132) Pingitore, P.; Sasidharan, K.; Ekstrand, M.; Prill, S.; Lindén, D.; Romeo, S. Human Multilineage 3D Spheroids as a Model of Liver Steatosis and Fibrosis. *Int J Mol Sci* **2019,** *20* (7).

(133) Kozyra, M.; Johansson, I.; Nordling, Å.; Ullah, S.; Lauschke, V. M.; Ingelman-Sundberg, M. Human hepatic 3D spheroids as a model for steatosis and insulin resistance. *Sci Rep* **2018,** *8* (1), 14297.

(134) Lee, H. K.; Velazquez Sanchez, C.; Chen, M.; Morin, P. J.; Wells, J. M.; Hanlon, E. B.; Xia, W. Three Dimensional Human Neuro-Spheroid Model of Alzheimer's Disease Based on Differentiated Induced Pluripotent Stem Cells. *PLoS One* **2016,** *11* (9), e0163072.

(135) Bell, C. C.; Hendriks, D. F.; Moro, S. M.; Ellis, E.; Walsh, J.; Renblom, A.; Fredriksson Puigvert, L.; Dankers, A. C.; Jacobs, F.; Snoeys, J.et al. Characterization of primary human hepatocyte spheroids as a model system for drug-induced liver injury, liver function and disease. *Sci Rep* **2016,** *6*, 25187.

(136) Zhao, Y.; Rafatian, N.; Feric, N. T.; Cox, B. J.; Aschar-Sobbi, R.; Wang, E. Y.; Aggarwal, P.; Zhang, B.; Conant, G.; Ronaldson-Bouchard, K.et al. A Platform for Generation of Chamber-Specific Cardiac Tissues and Disease Modeling. *Cell* **2019,** *176* (4), 913.

(137) Lee, S. H.; Hong, S.; Song, J.; Cho, B.; Han, E. J.; Kondapavulur, S.; Kim, D.; Lee, L. P. Microphysiological Analysis Platform of Pancreatic Islet β-Cell Spheroids. *Adv Healthc Mater* **2018,** *7* (2).

(138) Zanoni, M.; Cortesi, M.; Zamagni, A.; Arienti, C.; Pignatta, S.; Tesei, A. Modeling neoplastic disease with spheroids and organoids. *J Hematol Oncol* **2020,** *13* (1), 97.

(139) Tanner, K.; Gottesman, M. M. Beyond 3D culture models of cancer. *Sci Transl Med* **2015,** *7* (283), 283ps9.

(140) Simon, G. M.; Niphakis, M. J.; Cravatt, B. F. Determining target engagement in living systems. *Nat Chem Biol* **2013,** *9* (4), 200.

(141) Hughes, J. P.; Rees, S.; Kalindjian, S. B.; Philpott, K. L. Principles of early drug discovery. *Br J Pharmacol* **2011,** *162* (6), 1239.

(142) Ghosh, S.; Spagnoli, G. C.; Martin, I.; Ploegert, S.; Demougin, P.; Heberer, M.; Reschner, A. Three-dimensional culture of melanoma cells profoundly affects gene expression profile: a high density oligonucleotide array study. *J Cell Physiol* **2005,** *204* (2), 522.

(143) Barbone, D.; Van Dam, L.; Follo, C.; Jithesh, P. V.; Zhang, S. D.; Richards, W. G.; Bueno, R.; Fennell, D. A.; Broaddus, V. C. Analysis of Gene Expression in 3D Spheroids Highlights a Survival Role for ASS1 in Mesothelioma. *PLoS One* **2016,** *11* (3), e0150044.

(144) Swinney, D. C.; Anthony, J. How were new medicines discovered? *Nat Rev Drug Discov* **2011,** *10* (7), 507.

(145) Feng, Y.; Mitchison, T. J.; Bender, A.; Young, D. W.; Tallarico, J. A. Multi-parameter phenotypic profiling: using cellular effects to characterize small-molecule compounds. *Nat Rev Drug Discov* **2009,** *8* (7), 567.

(146) Esch, E. W.; Bahinski, A.; Huh, D. Organs-on-chips at the frontiers of drug discovery. *Nat Rev Drug Discov* **2015,** *14* (4), 248.

(147) Senkowski, W.; Zhang, X.; Olofsson, M. H.; Isacson, R.; Höglund, U.; Gustafsson, M.; Nygren, P.; Linder, S.; Larsson, R.; Fryknäs, M. Three-Dimensional Cell Culture-Based Screening Identifies the Anthelmintic Drug Nitazoxanide as a Candidate for Treatment of Colorectal Cancer. *Mol Cancer Ther* **2015,** *14* (6), 1504.

(148) Hickman, J. A.; Graeser, R.; de Hoogt, R.; Vidic, S.; Brito, C.; Gutekunst, M.; van der Kuip, H.; Consortium, I. P. Three-dimensional models of cancer for pharmacology and cancer cell biology: capturing tumor complexity in vitro/ex vivo. *Biotechnol J* **2014,** *9* (9), 1115.

(149) Fatehullah, A.; Tan, S. H.; Barker, N. Organoids as an in vitro model of human development and disease. *Nat Cell Biol* **2016,** *18* (3), 246.

(150) Halfter, K.; Hoffmann, O.; Ditsch, N.; Ahne, M.; Arnold, F.; Paepke, S.; Grab, D.; Bauerfeind, I.; Mayer, B. Testing chemotherapy efficacy in HER2 negative breast cancer using patient-derived spheroids. *J Transl Med* **2016,** *14* (1), 112.

(151) Wilke, R. A.; Lin, D. W.; Roden, D. M.; Watkins, P. B.; Flockhart, D.; Zineh, I.; Giacomini, K. M.; Krauss, R. M. Identifying genetic risk factors for serious adverse drug reactions: current progress and challenges. *Nat Rev Drug Discov* **2007,** *6* (11), 904.

(152) Lancaster, M. A.; Knoblich, J. A. Organogenesis in a dish: modeling development and disease using organoid technologies. *Science* **2014,** *345* (6194), 1247125.

(153) LeCluyse, E. L.; Witek, R. P.; Andersen, M. E.; Powers, M. J. Organotypic liver culture models: meeting current challenges in toxicity testing. *Crit Rev Toxicol* **2012,** *42* (6), 501.

(154) Baudoin, R.; Prot, J. M.; Nicolas, G.; Brocheton, J.; Brochot, C.; Legallais, C.; Benech, H.; Leclerc, E. Evaluation of seven drug metabolisms and clearances by cryopreserved human primary hepatocytes cultivated in microfluidic biochips. *Xenobiotica* **2013,** *43* (2), 140.

(155) Chao, P.; Maguire, T.; Novik, E.; Cheng, K. C.; Yarmush, M. L. Evaluation of a microfluidic based cell culture platform with primary human hepatocytes for the prediction of hepatic clearance in human. *Biochem Pharmacol* **2009,** *78* (6), 625.

(156) Gao, D.; Liu, H.; Lin, J. M.; Wang, Y.; Jiang, Y. Characterization of drug permeability in Caco-2 monolayers by mass spectrometry on a membrane-based microfluidic device. *Lab Chip* **2013,** *13* (5), 978.

(157) Chan, C. Y.; Huang, P. H.; Guo, F.; Ding, X.; Kapur, V.; Mai, J. D.; Yuen, P. K.; Huang, T. J. Accelerating drug discovery via organs-on-chips. *Lab Chip* **2013,** *13* (24), 4697.

(158) Wikswo, J. P.; Curtis, E. L.; Eagleton, Z. E.; Evans, B. C.; Kole, A.; Hofmeister, L. H.; Matloff, W. J. Scaling and systems biology for integrating multiple organs-on-a-chip. *Lab Chip* **2013,** *13* (18), 3496.

(159) Henry, E.; Cores, J.; Hensley, M. T.; Anthony, S.; Vandergriff, A.; de Andrade, J. B.; Allen, T.; Caranasos, T. G.; Lobo, L. J.; Cheng, K. Adult Lung Spheroid Cells Contain Progenitor Cells and Mediate Regeneration in Rodents With Bleomycin-Induced Pulmonary Fibrosis. *Stem Cells Transl Med* **2015,** *4* (11), 1265.

(160) Fang, Y.; Eglen, R. M. Three-Dimensional Cell Cultures in Drug Discovery and Development. *SLAS Discov* **2017,** *22* (5), 456.

(161) "3D Cell Culture Market Size, Share & Trends Analysis Report By Technology (Scaffold Based, Scaffold Free, Bioreactors), By Application (Cancer, Drug Development), By End-use, By Region, And Segment Forecasts, 2020 - 2027," Grand View Research Inc., 2020.

(162) "3D Spheroid Culture Technology Trends 2016," 2015.

(163) St Croix, C. M.; Shand, S. H.; Watkins, S. C. Confocal microscopy: comparisons, applications, and problems. *Biotechniques* **2005,** *39* (6 Suppl), S2.

(164) Janzen, W. P. Screening technologies for small molecule discovery: the state of the art. *Chem Biol* **2014,** *21* (9), 1162.

(165) Zanoni, M.; Piccinini, F.; Arienti, C.; Zamagni, A.; Santi, S.; Polico, R.; Bevilacqua, A.; Tesei, A. 3D tumor spheroid models for in vitro therapeutic screening: a systematic approach to enhance the biological relevance of data obtained. *Sci Rep* **2016,** *6*, 19103.

(166) Raghavan, S.; Mehta, P.; Horst, E. N.; Ward, M. R.; Rowley, K. R.; Mehta, G. Comparative analysis of tumor spheroid generation techniques for differential in vitro drug toxicity. *Oncotarget* **2016,** *7* (13), 16948.

(167) Acker, H.; Carlsson, J.; Mueller-Klieser, W.; Sutherland, R. M. Comparative pO2 measurements in cell spheroids cultured with different techniques. *Br J Cancer* **1987,** *56* (3), 325.

(168) Asghar, W.; El Assal, R.; Shafiee, H.; Pitteri, S.; Paulmurugan, R.; Demirci, U. Engineering cancer microenvironments for in vitro 3-D tumor models . *Mater Today (Kidlington)* **2015,** *18* (10), 539.

(169) Groebe, K.; Mueller-Klieser, W. Distributions of oxygen, nutrient, and metabolic waste concentrations in multicellular spheroids and their dependence on spheroid parameters. *Eur Biophys J* **1991,** *19* (4), 169.

(170) Eilenberger, C.; Rothbauer, M.; Ehmoser, E. K.; Ertl, P.; Küpcü, S. Effect of Spheroidal Age on Sorafenib Diffusivity and Toxicity in a 3D HepG2 Spheroid Model. *Sci Rep* **2019,** *9* (1), 4863.

(171) Vives, J.; Batlle-Morera, L. The challenge of developing human 3D organoids into medicines. *Stem Cell Res Ther* **2020,** *11* (1), 72.

(172) Dambach, D. M.; Uppal, H. Improving risk assessment. *Sci Transl Med* **2012,** *4* (159), 159ps22.

(173) Marx, U.; Andersson, T. B.; Bahinski, A.; Beilmann, M.; Beken, S.; Cassee, F. R.; Cirit, M.; Daneshian, M.; Fitzpatrick, S.; Frey, O.et al. Biology-inspired microphysiological system approaches to solve the prediction dilemma of substance testing. *ALTEX* **2016,** *33* (3), 272.

(174) Aref, A. R.; Huang, R. Y.; Yu, W.; Chua, K. N.; Sun, W.; Tu, T. Y.; Bai, J.; Sim, W. J.; Zervantonakis, I. K.; Thiery, J. P.et al. Screening therapeutic EMT blocking agents in a three-dimensional microenvironment. *Integr Biol (Camb)* **2013,** *5* (2), 381.

(175) Gunness, P.; Mueller, D.; Shevchenko, V.; Heinzle, E.; Ingelman-Sundberg, M.; Noor, F. 3D organotypic cultures of human HepaRG cells: a tool for in vitro toxicity studies. *Toxicol Sci* **2013,** *133* (1), 67.

(176) Vladimir K., K.; Anna V., G.; Olga O., S.; Yuri V., M. The influence of agglomeration of nanoparticles on their superoxide dismutase-mimetic activity. *Colloids and Surfaces A: Physicochemical and Engineering Aspects* **2012,** *409*, 176.

Curriculum Vitae

CHRISTOPH EILENBERGER

Date of birth: 07.11.1988
Address: Weintraubengasse 19/20, 1020 Vienna, Austria
E-mail: christoph.eilenberger@tuwien.ac.at
Phone: +43 664 216 5867

PROFILE

Skilled and ambitious bioengineer with strong background in biotechnology, cell biology, tissue engineering, and pharmacology. Result-driven professional with 4 years of experience in the field of pre-clinical research and biochip industry. Extensively published in peer-reviewed journals with related expertise in cancer biology, microphysiological systems, and 3D microtissue handling and analysis. Internationally experienced and forward-thinking with exceptional communication skills and team-oriented mentality.

RESEARCH INTERESTS

- Organ-on-a-chip technologies
- Automated biomedical microsystems
- In-vitro diagnostics
- Microfabrication
- 3D cell culture models (Spheroids/Organoids)
- Tumor microenvironment
- High-throughput drug screening
- Bioassay development

EDUCATION

VIENNA UNIVERSITY OF TECHNOLOGY | 08/2017 – 09/2021
Ph.D. in Technical Chemistry
Institute of Chemical Technologies and Analytics and Institute of Applied Synthetic Chemistry, Prof. Ertl

- Dissertation: *Controlling the third dimension: Critical quality parameters of static and dynamic spheroid cultures for drug screening applications*.

UNIVERSITY OF NATURAL RESOURCES AND LIFE SCIENCES | 03/2014 – 04/2017
Master of Science in Biotechnology
Institute of Synthetic Bioarchitectures, Prof. Ehmoser

- Thesis: *Generation of individual spheroids with tissue-like features on a nano bio-interface.*
- Published thesis in an international journal and awarded with the BOKU Innovation Award (3 awards-35 applicants).

UNIVERSITY OF NATURAL RESOURCES AND LIFE SCIENCES | 09/2009 – 02/2014
Bachelor in Food – and Biotechnology
Institute of Biochemistry, Prof. Staudacher

- Thesis: *Wachstumshormone.*

UNIVERSITY OF VIENNA | 09/2008 - 09/2009
Bachelor of Science in Biology

BUNDESREALGYMNASIUM KREMS AN DER DONAU | 09/1999 – 07/2007
High school diploma

RESEARCH EXPERIENCE

PROJECT ASSISTANT | 08/2017 – 09/2021
Vienna University of Technology

- Enhanced analytical throughput by 275% for drug screening applications by the development of a novel microfluidic 3D cell culture tool; honored with the Best Overall Concept Award by the TU Wien Innovation Incubation Center (1 award -15 participants).
- Identified and examined potential quality parameters of 3D spheroid cultures by biochemical and cell-based assays, live-cell imaging, transmission electron microscopy, immunohistochemistry, and mass spectrometry.
- Authored peer-reviewed publications, presented at international conferences and engineered a patented technology.

RESEARCH SCHOLAR | 04/2021 – 09/2021
Harvard Medical School
Cancer Center, Beth Israel Deaconess Medical Center, Prof. Muranen

- Awarded with the Austrian Marshall Plan Scholarship and the Marietta-Blau Grant.
- Characterized and integrated primary breast cancer organoids into a microfluidic chip platform.

GRADUATE RESEARCH FELLOW | 02/2017 – 07/2017
Vienna University of Technology

- Proposed and implemented rapid prototyping strategies (micromachining, soft-lithography, 3D printing) by the specification, design, manufacture and quality control of microfluidic systems and integrated instrumentation.
- Compiled and revised academic papers, reports, presentations, and grants.

PROCESS ENGINEERING INTERN | 09/2015 – 10/2015
Vienna University of Technology

- Planned and compared purification efficiencies of three recombinant isoenzymes from *Pichia pastoris* by using particle-based and monolithic chromatography columns.
- Developed Design of Experiment (DoE) strategies to maximize productivity based on biochemical parameters.

BIOMEDICAL RESEARCH INTERN | 08/2013
Danube University Krems

- Developed a novel effective detection method for glyphosate from soil samples using HPLC, SPE, and ELISA.

MOLECULAR BIOLOGY RESEARCH INTERN | 06/2013
University of Natural Resources and Life Sciences

- Established sterile plant cultures, optimized PCR genotyping protocols, and identified 15 transgenic plants.

PROFESSIONAL EXPERIENCE

SCIENTIFIC CONSULTANT | 09/2017 – 04/2021
Saico Biosystems KG

- Provided expert assessments for translating academic innovations into industrial production, created reports based on strategic fit, analyzed experimental data, and pitched opportunities to senior management.

- Managed a client portfolio including startups and pharmaceutical enterprises with an annual revenue up to 250 M US Dollar.
- Planned, designed, and implemented lab-on-a-chip and 3D mammalian cell culture solutions in three non-academic and two academic institutions.
- Acquired and counseled two new clients within two years.

Teaching and Administrative Experience

- Instructed and guided students as tutor at the Vienna University of Technology (*Course no.: 163.180: Rapid prototyping of microfluidic devices*), 2019.
- Trained and mentored 1-2 interns, undergraduates, and graduate students per year, 2018 – 2021.
- Managed laboratory functions including organization, ordering, and scheduling equipment use.
- Contributed to two funded research grant proposals worth 1.66 M Euro (Christian Doppler Forschungsgesellschaft: Josef-Ressel Centre for Phytogenic Drug Research and FFG Bridge 1: TRACE-Transport of living 3D cell cultures by biochip).

Professional Development

I.E.C.T Summer School of Entrepreneurship 2018 | 16/08/2018 – 22/08/2018
I.E.C.T Herman Hauser
STARTacademy 2018 | 13/02/2018 – 16/02/2018
TU Wien Innovation Incubation Center (i^2C)

Fellowships and Awards

Marietta-Blau Grant 2020 – OeAD GmbH (Austrian Federal Ministry of Education, Science and Research)
Marshall Plan Scholarship 2020 – Austrian Marshall Plan Foundation
Best Concept Award 2018 – TU Wien Innovation Incubation Center (i^2C)
BOKU Innovation Award 2017 – tecnet equity NÖ GmbH and accent incubator GmbH

Professional Associations

Austrian Scientists & Scholars in North America (ASciNA)
European Organ-on-Chip Society (EUROoCS)
Erwin Schrödinger Society for Nanosciences
Austrian Association of Molecular Life Sciences and Biotechnology (ÖGMBT)

Metrics

- Publications: 14
- Book chapters: 1
- Patent applications: 1
- Citations: 145
- *h*-factor: 6
- Sum journal impact factor: 41.4
- Highest journal impact factor: 15.8
- Conference contributions: 7

Conference Presentations

Eilenberger, C., Rothbauer, M., Gerhartl A., Neuhaus W., Ertl, P., Microfluidic multi-sized brain organoid microarray for BBB transport screening, *European Organ-on-Chip Conference, EUROoC* **2020**, Graz, Austria, poster presentation.

Eilenberger, C., Rothbauer, M., Ertl, P., A Microfluidic multi-cellular spheroid array for biomedical applications, *European Organ-on-Chip Conference, EUROoC* **2019**, Graz, Austria, poster presentation.

Eilenberger, C., Rothbauer, M., Ertl, P. MultiSphere – Establishing a microfluidic multi-cellular spheroid array, *Organ-on-a-Chip & Tissue-on-a-Chip Europe* **2019**, Rotterdam, The Netherlands, poster presentation.

Eilenberger, C., Rothbauer, M., Ehmoser, E.K., Ertl, P., S. Küpcü, S., 3D cellular spheroid age as critical parameter for drug toxicity screenings. *10th ÖGMBT Annual Meeting* **2018**, Vienna, Austria, talk.

Eilenberger, C., Rothbauer, M., Ehmoser, E.K., Ertl, P., Küpcü, S., Impact of spheroidal age on drug toxicity and diffusivity. *21st European Congress on Alternatives to Animal Testing and 18th Annual Congress of EUSAAT* **2018**, Linz, Austria, talk.

Eilenberger, C., Rothbauer, M., Küpcü, S., Sinner, E.K., Ertl, P., Microfluidic generation and maintenance of spheroids on a self-assembled ultra-low attachment nano-biointerface. 17. *Österreichische Chemietage* **2017**, Salzburg, Austria, talk.

Eilenberger, C., Rothbauer, M., Küpcü, S., Sinner, E.K., Ertl, P., Bacterial nanointerface for the microfluidic generation of mammalian microtissue. *Lab-on-a-Chip & Microfluidics Conference* **2017**, Munich, Germany, poster presentation.

PUBLICATIONS

Top 10 peer-reviewed publications

Eilenberger, C., Rothbauer, M., Selinger, F., Gerhartl, A., Jordan, C., Harasek, M., Schädl, B., Grillari, J., Weghuber, J., Neuhaus, W., Küpcü, S., Ertl, P. A microfluidic multi-size spheroid array for multi-parametric screening of anti-cancer drugs and blood-brain barrier transport properties. *Advanced Science* **2021**, doi: 10.1002/advs.202004856.

Eilenberger, C., Selinger, F., Rothbauer, M., Lin, Y., Limbeck, A., Schädl, B., Grillari, J., Kavok, N.S., Klochkov, V.K., Malyukin, Y.V., Margitich, V., Ertl, P. Cytotoxicity, retention, and anti-inflammatory effects of a CeO_2 nanoparticle-based supramolecular complex in a 3D liver cell culture model. *ACS Pharmacology & Translational Science* **2021**, 4,1, 101-106, doi: 10.1021/acsptsci.0c00170.

Kratz, S.R.A., Bachmann, B., Spitz, S., Höll, G., Eilenberger, C., Göritz, H., Ertl, P., Rothbauer, M. A compression transmission device for the evaluation of bonding strength of biocompatible microfluidic and biochip materials and systems. *Scientific Reports* **2020**, 10, 1400, doi: 10.1038/s41598-020-58373-0.

Rothbauer, M., Höll, G., Eilenberger, C., Kratz, S.R.A., Farooq B., Schuller, P., Olmos, Calvo I., Byrne, R.A., Meyer, B., Niederreiter, B., Küpcü, S., Sevelda, F., Holinka, J., Hayden, O., Tedde, S.F., Kiener, H.P., Ertl, P. Monitoring tissue-level remodelling during inflammatory arthritis using a three-dimensional synovium-on-a-chip with non-invasive light scattering biosensing. *Lab on a Chip* **2020**, 20, 8, 1461-1471, doi:10.1039/c9lc01097a.

Eilenberger, C., Spitz, S., Bachmann, B., Ehmoser, E.K., Ertl, P., Rothbauer, M. The usual suspects 2019: Of chips, droplets, synthesis and artificial cells. *Micromachines* **2019**, 10, 285, doi:10.3390/mi10050285.

Kratz, S.R.A., Eilenberger, C., Schuller, P., Bachmann, B., Spitz, S., Ertl, P., Rothbauer, M. Characterization of four functional biocompatible pressure-sensitive adhesives for rapid prototyping of cell-based lab-on-a-chip and organ-on-a-chip systems. *Scientific Reports* **2019**, 9, 9287, doi: 10.1038/s41598-019-45633-x.

Eilenberger, C., Rothbauer, M., Ehmoser, E.K., Ertl, P., Küpcü, S. Effect of spheroidal age on sorafenib diffusivity and toxicity in a 3D HepG2 spheroid model. *Scientific Reports* **2019**, 9, 4863, doi:10.1038/s41598-019-41273-3.

Eilenberger, C., Kratz, S.R.A., Rothbauer, M., Ehmoser, E.K., Ertl, P., Küpcü, S. Optimized alamarBlue assay protocol for drug dose-response determination of 3D tumor spheroids. *MethodsX* **2018**, 5, 781-787, doi:10.1016/j.mex.2018.07.011.

Bachmann, B., Spitz, S., Rothbauer, M., Jordan, C., Purtscher, M., Zirath, H., Schuller, P., Eilenberger, C., Ali, S.F., Mühleder, S., Pringlinger, E., Harasek, M., Redl, H., Holnthoner, W., Ertl, P. Engineering of three-dimensional pre-vascular networks within fibrin hydrogel constructs by microfluidic control over reciprocal cell signaling. *Biomicrofluidics* **2018**, 12, 042216, doi:10.1063/1.5027054.

Damiati, S., Küpcü, S., Peacock, M., Eilenberger, C., Zamzami, M., Qadri, I., Choudhry, H., Sleytr, U.B., Schuster, B. Acoustic and hybrid 3D-printed electrochemical biosensors for the real-time immunodetection of liver cancer cells (HepG2). *Biosensors and Bioelectronics* **2017**, 94, 500-506, doi: 10.1016/j.bios.2017.03.045.

Book chapters
Eilenberger, C., Rothbauer, M., Ertl, P., Küpcü, S. A self-assembled antifouling nano-biointerface for the generation of spheroids. *Cell-Based Microarrays. Methods in Molecular Biology* **2018**, 1771, 251-258, Humana Press, New York, NY, doi:10.1007/978-1-4939-7792-5_20.

Patent applications
International Application PCT/EP2019/075362, European Patent Application 18195997.4, U.S. Patent Application 2020/0095526: "Production of cellular spheroids", filed September 21, 2018. Patent pending.
Inventors: Christoph Eilenberger (TU Wien), Mario Rothbauer (TU Wien), Peter Ertl (TU Wien).

SKILLS

Languages: Englisch (fluent), German (native), Italian (basic)
Software: Microsoft Office (Word, Excel, PowerPoint), Adobe CS (Photoshop, InDesign, Illustrator), GraphPad Prim, Slicer, AutoCAD, Fusion360, ImageJ.

Vienna, July 2021

Christoph Eilenberger